HYDROGEN SPILLOVER IN THE FISCHER-TROPSCH SYNTHESIS

The roles of platinum and gold as promoters for cobalt-based catalysts

THESIS

presented for the degree of

DOCTOR OF PHILOSOPHY

by

Doreen Nabaho

BSc. Eng. (Hons) Chemical Engineering, UCT, South Africa.

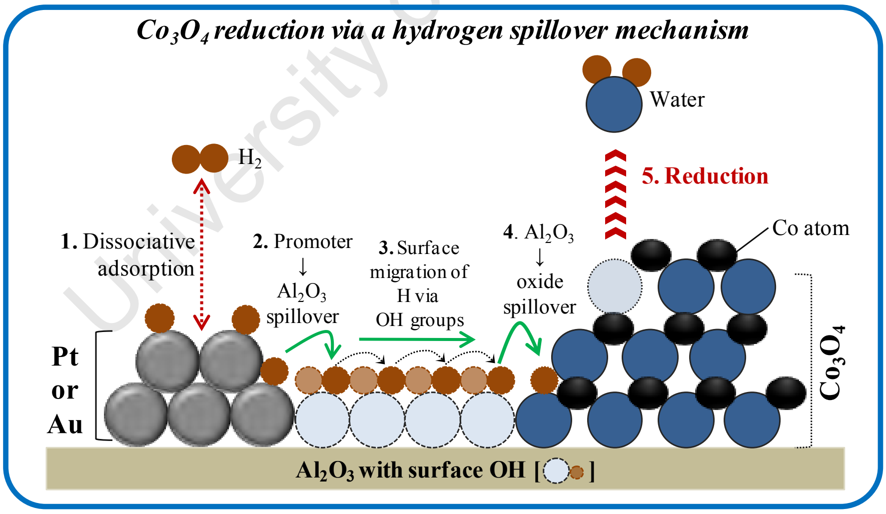

Centre for Catalysis Research
Department of Chemical Engineering
University of Cape Town
South Africa

May 2015

dedicated to my parents

Acknowledgements

Foremost, I would like to express my deepest gratitude to Prof. Eric van Steen for his unwavering support during my postgraduate studies. His vast knowledge of catalysis, curiosity, and scientific brilliance have led to a most intellectually challenging and gratifying doctoral journey. It was an honour to join the ranks of the esteemed group of doctoral candidates that thrived under his instruction.

Thanks to my co-supervisor, Prof. Michael Claeys, for his invaluable insights at various stages of this research, especially with regard to the in situ XRD work. I wish to thank Prof. Hans Niemantsverdriet at the Eindhoven University of Technology, whose kind hospitality and guidance were instrumental to the success of the XPS experiments.

The support provided by following contributors is gratefully acknowledged: Mr Mohammed Jaffer, Dr Franscious Cummings, and Dr Subelia Botha from the Electron Microscopy Units at UCT and UWC; Mrs Helen Divey, Mrs Suzanna Vasic, Ms Stephanie LeGrange and Ms Zulfa Le Riche from the Analytical Laboratory; Mr Tiny Verhoeven and Dr Kees-Jan Weststrate for the XPS work at the Eindhoven University of Technology.

I am grateful to the DST-NRF Centre of Excellence in Catalysis – c*change, for the funding that made this project possible, as well as the semester abroad and numerous local and international conferences that I was able to attend.

A wonderful group of friends has encouraged me every step of the way including Gracia, Rebecca, Tapiwa, Porogo, Christy, Martha, Nozonke, Melissa, and Rukaya. Zandi and Ntando, thank for the many inspiring chats, coffees, hikes, races - you made doing a PhD just a little more tolerable.

RW, I have been most fortunate to have you with me through the toughest parts of this journey. Thank you for keeping me motivated, for holding down the fort, and for wearing many hats including ‘editor’ and ‘therapist’. I am forever in your debt for the support during the write-up of this thesis.

Finally, and most importantly, I would like to say a big thank you to my family. Myra and Aisa, thank you for always being there and for checking up on me even though we were always so far apart. This thesis is dedicated to my mother, Dr Dinah Nahaabi and my father, Dr Wilson Were, whose patience, love and belief in me has been central to the completion of this work.

Declaration

I, Doreen Nabaho, hereby declare that the work on which this thesis is based is my original work (except where acknowledgements indicate otherwise) and that neither the whole work nor any part of it has been, is being, or is to be submitted for another degree in this or any other university. I authorise the University to reproduce for the purpose of research either the whole or any portion of the contents in any manner whatsoever.

Signature:……………………………………… Date: ……………………………………….

Synopsis

The Low Temperature Fischer-Tropsch (LTFT) synthesis involves the catalytic hydrogenation of carbon monoxide with the aim to produce long-chained hydrocarbons. Commercial cobalt-based catalysts incorporate oxidic supports that are known to negatively affect the reducibility and hinder formation of the active phase. Consequently, reduction promoters such as Pt are introduced to facilitate the reduction of cobalt during catalyst pre-treatment. However, synergistic and adverse effects of the promoter have been reported under reaction conditions including a higher site-time yield and higher selectivity towards hydrogenated products. The perspective on the operation of the Pt promoter is polarised between ‘Hydrogen spillover’, which is a so-called remote-control effect that could otherwise occur in the absence of Pt-Co contact, and ‘ligand/electronic effects’ that require direct Pt-Co coordination.

The objective of this study was to explicate the operation of Pt and Au as promoters of the Co/Al_2O_3 catalyst by decoupling hydrogen spillover from effects that require direct promoter-cobalt coordination. The analysis was subdivided into the reduction process and the Fischer-Tropsch reaction, which are the two arenas in which the actions of these promoters have been claimed. The employment of model ‘hybrid’ catalysts, which are mechanical mixtures of the monometallic constituents of the promoted catalyst, presents a novel way to investigate the role of spillover hydrogen in the Pt-Co and Au-Co catalyst systems. Thus far, no systematic investigation of the hydrogen spillover phenomenon using these catalyst systems during both reduction and under commercially relevant LTFT conditions has been encountered in the published literature. Furthermore, this study serves to contribute to the limited body of literature on the role of Au as a potential promoter for the commercial cobalt-based catalyst.

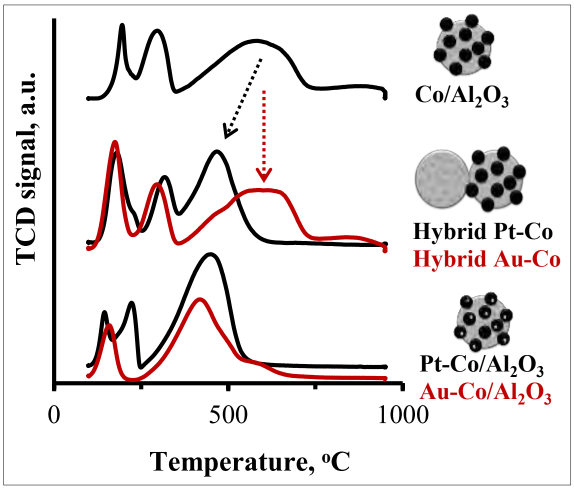

Fig. 1: Temperature-programmed reduction (TPR) profiles.

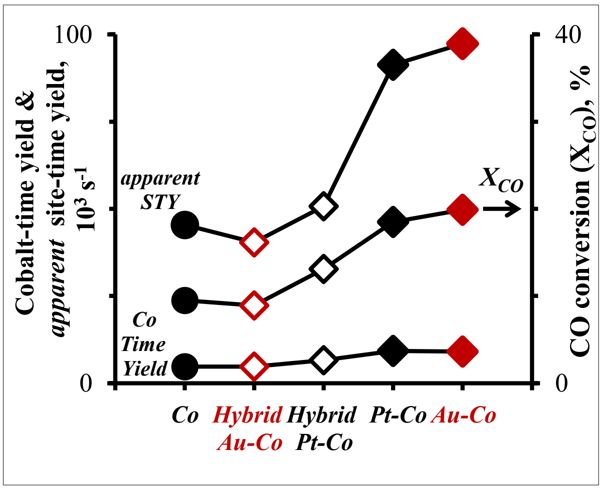

Fig. 2: Cobalt-time yield, *apparent* site-time yield, and CO conversion during the Low Temperature Fischer Tropsch reaction.

The Pt promoter improved the reducibility of Pt-Co/Al_2O_3 and that of Hybrid Pt-Co (Pt/Al_2O_3+Co/Al_2O_3) despite the fact that Pt was physically separated from Co. The catalysing effect of Pt was attributed to H_2 dissociation and subsequent spillover occurring more competitively than direct H_2 dissociation by the cobalt oxides. The reducibility of Hybrid Pt-Co was less pronounced because the separation of Pt from Co lowered the efficiency of the spillover process. The reduction of $Co_3O_4 \rightarrow Co^0$ occurred via the formation of CoO as a stable intermediate, and it was observed that Pt greatly improved the $CoO \rightarrow Co^0$ reduction, which was severely hindered in the unpromoted sample due to interaction with the support. Although Au improved the reducibility of Au-Co/Al_2O_3, a corresponding effect was not observed with the Hybrid Au-Co sample (Fig. 1). Au surfaces have a lower reactivity towards H_2 (and the subsequent spillover), and it is suggested that separation of Au from Co in Hybrid Au-Co severely diminished the resultant flux of spillover hydrogen compared to Hybrid Pt-Co.

Pt-Co/Al_2O_3 and Au-Co/Al_2O_3 had the highest cobalt-time yields in accordance with their high extents of reduction but also exhibited a synergism in the *apparent* site-time yield compared to the unpromoted sample (Fig. 2). The role of spillover hydrogen was again invoked to explain the synergism during the Fischer-Tropsch reaction, this time providing a ‘cleaning’ effect on the cobalt surface, which allowed for a higher coverage of reactive (versus inert) intermediates. A higher coverage of reactive intermediates explained the higher *apparent* site-time yield, and thus the intrinsic activity of the Co^0 active sites was not necessarily modified by direct interaction with the promoters. Hydrogen spillover was corroborated by the enhanced selectivity towards hydrogenated products when compared at similar levels of CO conversion. Despite the improved reducibility (Fig. 1), the effects of spillover hydrogen under reactive conditions were significantly diminished in Hybrid Pt-Co (Fig. 2). It is suggested that CO adsorption blocked off a large portion of the Pt surface, which in turn diminished the concentration of active sites available for hydrogen adsorption. The negative effect of CO was then compounded by the Pt/Co separation compared to Pt-Co/Al_2O_3 in which Pt and Co were in close proximity.

Contents

Chapter 4. Experimental Techniques 71

Chapter 6. Hydrogen Spillover from Au and Pt Promoters during the Fischer-Tropsch Synthesis 189

Appendices

List of Figures

List of Tables

List of Schemes

Nomenclature

Abbreviations

ASF	Anderson-Schulz-Flory
BTL	Biomass-to-Liquids
CTL	Coal-to-Liquids
DFT	Density Functional Theory
DOR	Degree of Reduction
EXAFS	Extended X-Ray Absorption Fine Structure
FID	Flame Ionization Detector
GC	Gas Chromatography
GHSV	Gas Hourly Space Velocity
GTL	Gas-to-Liquids
HRTEM	High Resolution Transmission Electron Microscopy
HTFT	High Temperature Fischer-Tropsch
ICP-AES	Inductively Coupled Plasma – Atomic Emission Spectroscopy
ID	internal diameter
LTFT	Low Temperature Fischer-Tropsch
MCF	Mesostructured Cellular Foam
MS	Mass Spectrometry
NEXAFS	Near Edge X-Ray Absorption Fine Structure
PetroSA	The Petroleum Oil and Gas Corporation of South Africa (Pty). South Africa's national oil company
Sasol	*Suid Afrikaanse Steenkool, Olie en Gaskorporasie* (South African Coal Oil and Gas Limited)
SMDS	Shell Middle Distillate Synthesis

Abbreviations (cont'd)

SPD	Slurry Phase Distillate
SSITKA	Steady State Isotopic Transient Kinetic Analysis
STY	Site-Time Yield
TCD	Thermal Conductivity Detector
TGA	Thermogravimetric Analysis
TOPAS	Total Pattern Analysis Solutions
TPR	Temperature-Programmed Reduction
TPR-XANES	Temperature-Programmed Reduction combined with X-Ray Absorption Near Edge Structure
WGS	Water-Gas Shift
XANES	X-Ray Absorption Near Edge Structure
XPS	X-ray photoelectron spectroscopy
XRD	X-ray diffraction
XTL	XTL (X = Coal/Gas/Biomass)-to-Liquids

Glossary

Bucket-Brigade	A chain of persons acting to put out a fire by passing buckets of water from hand to hand (Merriam-Webster dictionary).
Catalyst activation	The reduction of catalysts in H_2 to maximise the formation of the metallic cobalt phase prior to the Fischer-Tropsch reaction.
Cobalt-time yield	The number of moles of CO converted in each second per mole of Co present in the catalyst.
Fajans' Rules	A set of rules governing polarisation and covalence. Proposed by Kazimierz Fajans.
Grotthuss Mechanism	A mechanism that governs the unusually high proton mobility in water and other ionic fluids. Proposed by Theodor von Grotthuss.
Hybrid Au-Co	A physical mixture of Au/Al_2O_3 and Co/Al_2O_3.
Hybrid catalyst	A mechanical (physical) mixture of two monometallic catalyst samples
Hybrid Pt-Co	A physical mixture of Pt/Al_2O_3 and Co/Al_2O_3.
Hydrogen activation	The dissociative adsorption of molecular hydrogen.
Hydrogen Spillover	"Spillover involves the transport of active species sorbed or formed on a first surface onto another surface that does not under the same conditions sorb or form the active species" (W.C. Jr Conner & J.L. Falconer).
Interfacial Spillover	The movement of hydrogen from one surface to the next.
Rietveld refinement	A structure refinement technique used to obtain crystal structure from powder x-ray diffraction data by minimising the difference between the measured and calculated profile. Developed by H.M. Rietveld.
Secondary Spillover	Spillover from a surface that does not itself show activity for hydrogen dissociative adsorption.
Site-time yield (STY) or Apparent site-time yield (apparent STY)	The number of moles of CO converted in each second per mole of Co^0 present on the catalyst surface. STY is synonymous with turnover frequency/turnover number.
Steady State Isotopic Transient Kinetic Analysis (SSITKA)	An in situ method used to investigate surface kinetic parameters. It involves the introduction of a step change from an unlabelled to an isotopically labelled reactant after steady state has been achieved.
Co-supported catalysts	Catalysts prepared by *sequential* impregnation of an Al_2O_3 support with cobalt, followed by the reduction promoter.

Chapter 1

Introduction

1.1 The Synthetic Fuels Industry: Past and Present

The International Energy Agency (IEA) reports that economic growth in emerging markets such as Africa, Asia and Latin America will be the principal driver of global energy demand up to 2040 [1]. Growth in the global energy demand is projected at 1-2% per year, and fossil fuels will continue to account for approximately 80% of the energy mix [1]. In the past, the imbalance in the distribution of crude oil reserves meant that oil-producing nations such as those in the Organisation of the Petroleum Exporting Countries (OPEC) were able to dictate the price of this crucial resource, at the expense of oil importers worldwide [2]. In a bid to break their dependence on oil imports, a number of nations continue to look for alternative sources to meet their energy demands, so that today, advances in research and technology mean that new supply options are reorienting the global energy landscape [1, 2]. These new supply options include unconventional resources such as shale gas, coal bed methane (CBM), and oil sands, and renewable resources such as solar, wind, hydro and biofuels, while alternative technology for synthetic transportation fuels includes XTL (X= coal/gas/biomass)-to-liquids.

Germany was the pioneer of the synthetic fuels industry [3-5]. Following the successful commercialisation of the ammonia and methanol synthesis processes, the chemical conglomerate I.G. Farben (now AGFA-Gevaert, BASF, Bayer and Sanofi) went on to develop the industrial production of synthetic hydrocarbons from the Bergius process, while Ruhrchemie established commercial Fischer-Tropsch operations [3-5]. Due to this early innovation, Germany was able to operate 12 Bergius process plants and 9 Fischer-Tropsch plants between 1927 and 1945 [4]. Although less popular nowadays, the Bergius process developed by the chemist Friedrich Bergius in 1913, was the more established of the two, and contributed up to 95% of Germany's aviation fuel during World War II [3,4]. This process was more suitable to gasoline production (primarily for aviation) from the abundant German lignite (brown coal) deposits compared to the Fischer-Tropsch Process, which produced mainly diesel, low-grade gasoline, waxes, and raw materials for the chemical industry [3,4].

Other nations also developed parallel synthetic fuel production programs including Britain, Canada, Japan, South Africa, and the US with varying success [4,5]. In 1935, Britain commercialised a coal liquefaction plant using bituminous coal as a feedstock with a capacity of 1.28 million barrels per year; the plant operated until 1939 when it was modified to convert creosote to aviation fuel [5]. Japan had industrial scale coal-to-liquid plants (Fischer-Tropsch and coal liquefaction) to support its operations during World War II. The US constructed three Fischer-Tropsch plants and one coal liquefaction plant in the post World War II era although none ever reached design capacity. In Africa, Sasol set up its first coal-to-liquids (CTL) facility in Sasolburg with a total capacity of 200 barrels per day in 1955 [6, 7]. However, by the late 1960s, most countries had shut down their synthetic fuel facilities and halted all major research in the field primarily due to the discovery of oil reserves in the Middle East. The sheer magnitude of these reserves eased fears of peak oil, resulting in a drop in crude oil prices that rendered the synthetic fuel industry economically unsound [8]. Although sporadic research continued in various facilities especially during the oil crises of the 1970s by companies such as Gulf Oil (Chevron) and Standard Oil (Exxon), it was South Africa that spearheaded Fischer-Tropsch research and development by setting up two plants in Secunda, namely Sasol II and Sasol III, in 1980 and 1982 respectively [7,9].

The modern history of the synthetic fuel industry cannot be told without acknowledging the pivotal contributions to research and development made by Sasol in South Africa. A number of parallels can be drawn between South Africa and Germany's adoption of the synthetic fuels industry. In the 1950s, the Apartheid Policy enforced by the South African government started to draw great criticism from the rest of the world. Sasol was founded to develop South Africa's synthetic fuels industry in the face of economic isolation caused by sanctions imposed on the state. Like Germany, South Africa had abundant coal resources [9]. The difference between the two nations came in the form of the bituminous (black) coal in South Africa being better suited to fuel production via the Fischer-Tropsch Synthesis, unlike the German lignite (brown) coal, which was younger, and better suited to fuel production via coal liquefaction (Bergius Process) [4]. The South African government granted Sasol the rights to use the Fischer-Tropsch technology previously purchased by Anglovaal (a local mining company) from Ruhrchemie and Lurgi Gesellschaft für Wärmetechnik [10, 11].

Today, South Africa remains a world leader in Fischer-Tropsch technology courtesy of Sasol and PetroSA, which between them operate four Fischer-Tropsch plants in the country, so that

30% of the liquid fuels consumed in the country comes from synthetic fuel. Sasol also operates Fischer-Tropsch plants outside South Africa including Oryx GTL (with Qatar Gas) and Escravos GTL, which is licensed to Chevron and Nigeria National Petroleum Corporation. Another key player in the Fischer-Tropsch industry is Shell, which operates Fischer-Tropsch plants on an industrial scale in Malaysia (Bintulu GTL) and Qatar (Pearl GTL). An upcoming player in the synthetic fuels industry is China, which is rapidly developing CTL technology. Research and development has been spearheaded by Synfuels China, which focuses on slurry-phase and iron-based technology. A number of companies including the Shenhua Group, Shanxi Lu'an and Yitai already have/are setting up commercial CTL operations. Compared to the Fischer-Tropsch process, research on direct coal liquefaction previously carried out by companies such as ExxonMobil, ConocoPhillips, Kohleoel-Anlage Bottrop GmbH and NEDOL (Japan) is only carried out on a limited scale today, with Headwaters Incorporated in the US as a key player. As of 2014, only the Shenhua Group in China operates a direct coal liquefaction (DCL) facility at 20 000 barrels per day based on Headwaters Incorporated Technology [12, 13].

The future of the synthetic fuel industry continues to look lucrative, especially with the trends seen in the price of natural gas, which increases at a slower rate than that of oil and creates an appreciable profit margin for Gas-to-Liquids plants (sasol.com; US Energy Information Administration). Proposed future operations on the South African front include Sasol's two shale-gas-to-liquids plants in North America (Louisiana and Alberta) and an in-land GTL plant in Uzbekistan while PetroSA is in talks with Mozambique to set up the 5th synthetic fuel facility in Southern Africa with a planned capacity of 40 000 barrels per day [14]. The magnitude of investment into gas-to-liquids operations was brought to a high in 2013 with Sasol's \$20 billion investment in Louisiana, which became the largest foreign direct investor-manufacturing project in the history of the US [15].

Biomass is a more recent consideration as a Fischer-Tropsch feedstock and is seen as a potential carbon neutral source of liquid transportation fuels, which cannot be produced from other renewable sources of energy such as wind and solar [16-18]. Biomass for the Fischer-Tropsch process can be derived from sources such as wood and agricultural waste, while some interesting innovative technologies include coal-algae agglomerates from coal fines (waste) such as the Coalgae™ technology developed at the Nelson Mandela Metropolitan University in South Africa. In biomass-to-liquids (BTL) technology, utilisation of waste and plants grown on degraded land helps overcome some criticisms raised by the controversial ‘Food versus Fuel’ debate. Nevertheless, BTL technology faces fierce competition from the already well-established biomass-to-ethanol industry. Commercial BTL projects have been in the pipelines of Rentech Inc and Neste Oil-Stora Enso who plan to scale-up their current demonstration facilities in the US and Finland respectively, while China has proposed demonstration facilities from 2015. Unfortunately, financial setbacks have plagued industrial scale BTL operations, more recently with CHOREN Industries GmbH filing for insolvency just before commissioning a demonstration plant in Freiburg (Germany) in 2011. At full capacity, this plant would have been the world’s largest semi-commercial BTL plant at 18m litres of SunDiesel® per annum and 45 MW of power [16, 17].

1.2 Industrial Set-up of the Fischer-Tropsch Plant

A clear advantage of the Fischer-Tropsch Process is its flexibility with respect to the raw material feedstock, which can include biomass, coal and gas. Natural gas is ideal due to lower NO_x and SO_x emissions and higher energy efficiency, which makes it less costly to operate [8]. Apart from fuel production, XTL operations produce high value chemicals such as olefins, phenolics and alcohols, which in spite of having a comparatively limited market fetch higher prices per tonne. In South Africa, Fischer-Tropsch operations have spawned off other industries such as polymer production by Sasol polymers (previously Polifin Ltd), detergent alcohol production by Sasol Olefins and Surfactants, and ammonia explosives production in collaboration with Dyno Nobel (USA).

The processes on a Fischer-Tropsch plant fall into three distinct categories: syngas generation, syngas conversion, and hydrocarbon processing.

Syngas generation involves either gasification (coal) or reforming (methane/natural gas) and accounts for 60-70% of the capital and operating costs of the Fischer-Tropsch plant [8]. Due to its lower H_2/CO ratio, the production of syngas from coal is less efficient, resulting in 50% loss to CO_2. At the CTL facility in Secunda, syngas is produced in Lurgi dry ash gasifiers in which coal is burned with steam and oxygen.

Methane reforming by both Sasol and PetroSA is carried out catalytically in autothermal reformers while partial oxidation is used at Shell's Bintulu Plant. Following purification, the H_2/CO ratio is adjusted to maximise conversion in the Fischer-Tropsch reactors downstream of the syngas generation processes.

Syngas conversion can be carried out in two modes, namely: the Low Temperature Fischer-Tropsch (LTFT) and the High Temperature Fischer-Tropsch (HTFT) processes. The Low Temperature Process can be carried out at temperatures of up to 275°C and 20 bar and is geared to the production of high molecular weight hydrocarbons (waxes) from which diesel is obtained. Due to the high exothermicity of the reaction, Fischer-Tropsch reactors are designed to maximise heat removal to prevent catalyst deactivation and to control the product distribution [8]. Currently, Shell's Bintulu plant uses a cobalt catalyst packed in multitubular reactors from which the produced wax trickles. The original LTFT reactors employed by Sasol were also multitubular reactors containing an iron catalyst packed in 2050 tubes that were each 12m long. These were subsequently replaced by slurry reactors whose advantages included lower differential pressure drops, lower catalyst consumption, and the possibility to operate isothermally, which allowed for higher operating temperatures and conversions. Both cobalt and iron-based catalysts are used in the low-temperature operation. Despite their higher cost, cobalt-based catalysts are preferred due to their ability to withstand high water partial pressures, which allows for higher per pass conversions.

In contrast, the high temperature process (HTFT) produces low molecular weight hydrocarbons in the gasoline and kerosene range, and is carried out at 300-350°C and 20 bar. Until 1999, SASOL used 22m tall circulating fluidised bed (CFB) reactors similar to those still in use at the PetroSA plant in Mossel Bay before they were phased out in favour of the synthol reactors. Today, Sasol uses Fixed Fluidised Bed (FFB) reactors known as Sasol advanced synthol (SAS) reactors, with annual capacities of 470 000 tonnes (8m ID) or 850 000 tonnes (10.7m ID).

The processes required during **hydrocarbon processing** of products from the Fischer-Tropsch process are governed by a number of factors including the raw material used, type of catalyst and quality of the specific products required. 40% of Sasol's straight run HTFT reactor product is gasoline, which due to its linearity and lack of aromaticity has a low octane number. Upgrading of this gasoline is thus required so that the co-produced olefins undergo oligomerisation (C_3-C_4), hydrogenation (C_5-C_6) and isomerisation (C_7-C_{10}) in order to meet engine specifications. In contrast, linear unbranched olefins from the LTFT process have a high cetane number (C_N) of about 75 (after hydrotreating) and must be downgraded by blending with crude derived diesel to meet engine specifications (C_N=40-55). The straight run product from the low temperature process is composed predominantly of wax and product upgrading involves wax cracking and olefin oligomerisation, which are carried out in varying degrees in to meet market requirements [6]. In spite of the differences between Sasol's SPD (Slurry Phase Distillate) and Shell's SMDS (Shell Middle Distillate Synthesis) technology, the refining concept is similar and results in comparable syncrude properties [19].

1.3 References

[1] International Energy Agency, “World Energy Outlook 2014. Executive Summary”, http://www.iea.org/textbase/npsum/weo2014sum.pdf; “World Energy Outlook 2013 Factsheet. How will global energy markets evolve to 2035?”, https://www.iea.org/media/files/ WEO2013_factsheets.pdf (accessed May 24, 2015).

[2] Andreas Becker, “OPEC’s influence on oil prices waning?”, Deutsche Welle, Nov 2014, http://www.dw.de/ opecs-influence-on-oil-prices-waning/a-18084928 (accessed May 24, 2015).

[3] D. Yergin (Ed.), The Prize: The Epic Quest for Oil, Money & Power, Simon and Schuster, New York, 2008.

[4] A. N. Stranges, in: B.H. Davis, M.L.Ocelli (Eds.), Fischer-Tropsch Synthesis, Catalysts and Catalysis, Studies in Surface Science and Catalysis, Vol. 163, Elsevier, Amsterdam, 2007, 1-27.

[5] G. M. Kimber, A History of UK Coal Liquefaction, Energy Technology Support Unit (ETSU)/Department of Trade & Industry (DTI) Report No.Coal R078, Harwell, Great Britain, 2009.

[6] M. E. Dry, Catal. Today 6 (1990) 183-206.

[7] M. E. Dry, J. Mol. Catal. 17 (1982) 133-144.

[8] M. E. Dry, Catal. Today 71 (2002) 227-241.

[9] J.C. van Dyk, M.J. Keyser, M. Coertzen, Int. J. Coal Geol 65(2006) 243–253.

[10] K. Halstead, “Oryx Gtl – A Case Study”, The Chemical Engineer (tce), Jul 2 2006. 34.

[11] A.P. Steynberg, M.E. Dry (Eds.), Fischer-Tropsch Technology, Studies in Surface Science and Catalysis, Vol. 152, Elsevier, Amsterdam, 2004.

[12] U.S Department of Energy-National Energy Technology Laboratory, “Direct Liquefaction Processes”, http://www.netl.doe.gov/research/coal/energy-systems/gasification/gasifipedia/direct-liquefaction (accessed Nov 4, 2012).

[13] Reuters Home Page, “China Shenhua Coal-To-Liquids Project Profitable –Exec”, http://www.reuters.com/article/2011/09/08/shenhua-oil-coal-idUSL3E7K732020110908 (accessed Nov 11, 2014).

[14] Reuters Home Page, “PetroSA says in talks with Mozambique for GTL Plant”, http://www.reuters.com/article/2012/04/25/ozabs-mozambique-gas-petrosa-idAFJOE83O07B20120425 (accessed May 13, 2014).

[15] L. Steyn, “Sasol Cracks Major US Fracking Deal”, The Mail and Guardian, http://mg.co.za/article/2013-09-20-00-sasol-cracks-major-us-fracking-deal (accessed May 7, 2014).

[16] M. Hogan, “German Biofuel Firm Choren Declares Insolvency”, Reuters, http://af.reuters.com/article/energyOilNews/idAFLDE7670QA20110708 (accessed Nov 11, 2014).

[17] C. Peters, Choren Industries Company Presentation, Purdue University, May 2008. www.purdue.edu/discoverypark/energy/assets/pdfs/cctr/presentations/choren-purdue-may2008.pdf (accessed May 13, 2014).

[18] M.J.A.Tijmensen, A.P.C. Faaij, C.N. Hamelinck, M.R.M. van Hardeveld, Biomass Bioenergy 23 (2002) 29-152.

[19] D. Leckel, Energy Fuels 23 (2009) 2342-2358.

Chapter 2

Literature Review

2.1 The Fischer-Tropsch Reaction

The Fischer-Tropsch reaction may be described as a surface polymerisation of methylene (CH_2) species, which are formed from a reaction between adsorbed carbon monoxide and hydrogen [1]. The dominant compounds in the Fischer-Tropsch hydrocarbon product spectrum are α-olefins and n-paraffins [1]. Equation 2.1-1 is a stoichiometric expression of the formation of olefins and shows hydrogen molecules reacting with carbon monoxide in a ratio of 2:1 to form each methylene surface species, and water as the co-product. Equation 2.1-1 can be adjusted for the formation of paraffins by adjusting the C/H ratio in the product.

$nCO + 2nH_2 \rightarrow n(CH_2) + nH_2O$ **Equation 2.1-1**

Besides the formation of long-chained hydrocarbons, various side reactions occur at varying frequencies depending on the reaction conditions and the catalyst of choice. Common side-reactions include the undesirable methanation reaction (Eq. 2.1-2), the water-gas shift reaction (Eq. 2.1-3), and the Boudouard reaction (Eq. 2.1-4). The Boudouard reaction has been cited as a cause of long-term catalyst deactivation resulting from the formation of carbonaceous deposits that block active sites [2].

$CO + 3H_2 \rightarrow CH_4 + H_2O$ ΔH_{rxn} (170°C) = -212kJ/mol **Equation 2.1-2**
(Methanation reaction)

$CO + H_2O \leftrightarrow CO_2 + H_2$ ΔH_{rxn} (240°C) = -39.7kJ/mol **Equation 2.1-3**
(Water-Gas Shift reaction)

$2CO \rightarrow CO_2 + C$ ΔH_{rxn} (240°C) = -173kJ/mol **Equation 2.1-4**
(Boudouard reaction)

2.1.1 Product distribution in the Fischer-Tropsch reaction

Besides the α-olefins and n-paraffins as the main products, other Fischer-Tropsch products include internal and branched olefins, branched paraffins, and a range of oxygenates such as alcohols, aldehydes, ketones and aromatics [2]. Consequently, the most accurate Fischer-Tropsch mechanism is one that can account for most, if not all of these products. Many of the widely accepted mechanisms for hydrocarbon formation are variations of the 'Carbide' mechanism originally proposed by Franz Fischer [3] with the more recent adaptation being the Alkyl Mechanism [1].

The elementary steps involved in the Alkyl mechanism are presented in Figure 2.1-1. According to this mechanism, chain initiation involves CO and H_2 dissociation (Steps 1&3). Surface carbide species formed from CO dissociation undergo sequential hydrogenation to eventually form CH_2 and CH_3 species, which are referred to as the 'monomer' and 'chain initiator' respectively.

Initiation

1. $CO + * \rightarrow CO*$
2. $CO* + * \rightarrow C* + O*$
3. $H_2 + 2* \rightarrow 2H*$
4. $C* + H* \rightarrow CH* + *$
5. $CH* + H* \rightarrow CH_2* + *$
6. $CH_2* + H* \rightarrow CH_3* + *$

Propagation

7. $R* + CH_2* \rightarrow RCH_2* + *$

Termination and Desorption

8. $RCH_2CH_2* + H* \rightarrow RCH_2CH_3 + 2*$
9. $RCH_2CH_2* \rightarrow RCH_2CH_2 + H*$

Figure 2.1-1: Elementary steps in 'Alkyl' Mechanism (adapted from Claeys & van Steen, 2004). R = alkyl group i.e. C_nH_{2n+1}, with $n \geq 0$

In the alkyl mechanism, chain growth then occurs by insertion of the CH_2 species into an alkyl group – R. This step of the mechanism is one of the most heavily debated in literature, where it has been shown by some to be unfeasible. Nevertheless, termination to form olefins and paraffins eventually takes place by β-hydrogen abstraction and α-hydrogen addition respectively. Although not depicted in Figure 2.1-1, oxygen removal from the catalyst surface is a fundamental aspect of the Fischer-Tropsch mechanism and has been proposed to result in the formation of both CO_2 and H_2O.

Other proposed Fischer-Tropsch mechanisms include the Alkenyl Mechanism [4-6], the Enol Mechanism [7], and the CO-Insertion Mechanism [8-13]. Despite a lack of consensus on the Fischer-Tropsch mechanism, all postulated mechanisms account for three elementary steps that include chain initiation (i.e. formation of a monomer from CO and H_2), chain propagation (i.e. polymerisation), and finally termination, which is characterised by hydrocarbon desorption from the catalyst surface.

The Fischer-Tropsch product spectrum obeys a well-defined molecular distribution similar to that of a real polymerisation reaction. In fact, the Anderson-Schulz-Flory (ASF) kinetics used to describe the Fischer-Tropsch product spectrum are derived from 'Flory-Schulz' kinetics for homogenous polymerisation reactions. Using only a single parameter known as the chain growth probability – α, ASF kinetics constrain the Fischer-Tropsch product distribution to *a single family of products* whose molar content decreases exponentially with carbon number (Eq. 2.1-5).

$$x_N = (1 - \alpha) \cdot \alpha^{(N-1)} \qquad \textbf{Equation 2.1-5}$$

where:

X_N - mole fraction of molecules with N carbon atoms

α - chain growth probability

N - carbon number

Figure 2.1-2: *Left* shows selectivity of C_1, C_2-C_4 and C_5+ as a function of the chain growth probability (α) and Figure 2.1-2: *Right* shows the ideal ASF plots at various chain growth probabilities. The ASF plots are semi-logarithmic plots of the mole fraction as a function of the carbon number, to which straight trend lines may be fitted. The average molecular weight of the product decreases with chain growth probability, eventually constituting only methane at a chain growth probability of zero [1] (Fig. 2.1-2: *Right*).

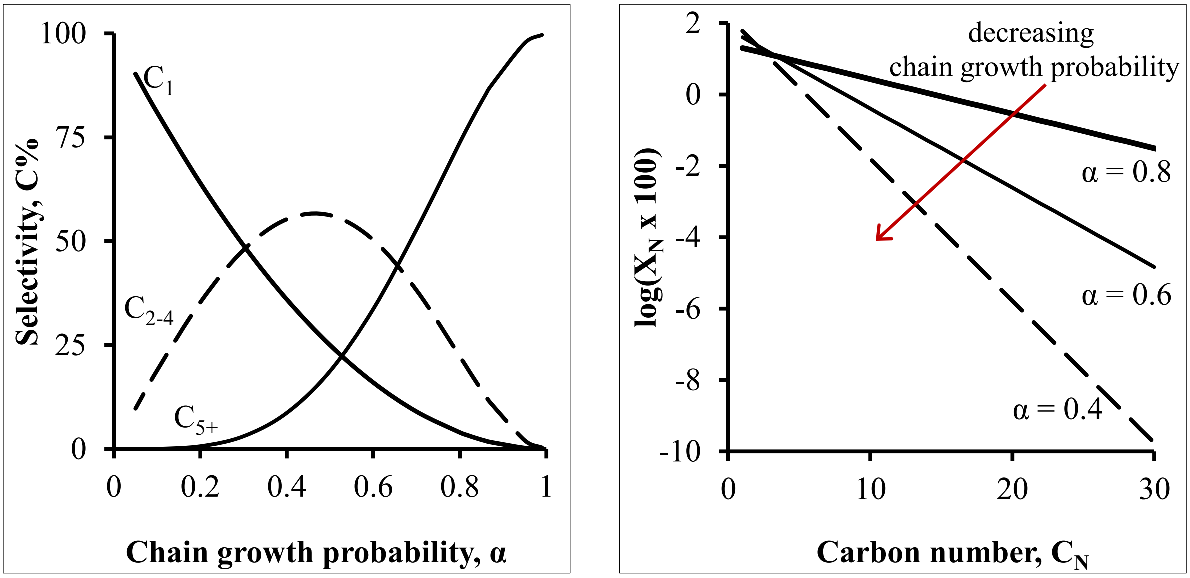

Figure 2.1-2: ***Left:*** Selectivity of C_1, C_{2-4} and C_5+ as a function of α according to ideal ASF kinetics. ***Right:*** Ideal ASF plots of the Fischer-Tropsch product distribution at various chain growth probabilities.

The actual product distribution often deviates from that specified by ideal ASF kinetics. Deviations from the ideal distribution include a range of product families (i.e. olefins, paraffins, alcohols), higher CH_4 content, lower C_2 olefin content, carbon number dependence of α (with fewer olefins reported at high carbon numbers), and different apparent α values for lower and higher molecular weight products [1]. Therefore, the most accurate kinetic models for the Fischer-Tropsch product distribution are those that account for additional reactions including: chain length dependence of solubility, double-bond shift isomerisation, and especially olefin readsorption [14-16]. Since linear α-olefins reportedly constitute the bulk of the primary Fischer-Tropsch reaction products, the final product distribution and chain growth probability at a specific carbon number are directly impacted by the extent and selectivity of the secondary reactions [1]. Secondary reactions occur after the primary Fischer-Tropsch products (particularly olefins) readsorb onto the catalyst surface and undergo further reaction.

2.2 Cobalt-Based Catalysts for the Fischer-Tropsch Reaction

The cobalt-based Fischer-Tropsch catalyst is employed on an industrial scale by Sasol and Shell for the Slurry Phase Distillate (SPD) process and Shell Middle Distillate Synthesis (SMDS) process respectively. The compositions of these catalysts as determined from various literature sources are shown in Table 2.2-1. The new generation Shell catalyst is reportedly Co/TiO_2, while the previous catalyst was Co/SiO_2 with some Zr and possibly other rare earth oxides [17-22]. The Sasol catalyst is said to be Pt-Co/Al_2O_3 with some SiO_2 [23-27].

Table 2.2-1: Composition of commercial cobalt-based Fischer-Tropsch catalysts.

	Shell SMDS [17-22]	**Sasol SPD [23-27]**
active metal	Co	Co
support	TiO_2 (new) SiO_2 (old)	γ-Al_2O_3
reduction promoter	-	Pt Pt:Co molar ratio (<1:100) (added simultaneously with Co)
rare earth oxides	Mn (new) Zr, Ti, Cr(old)	SiO_2
Co loading	10 - 30g per 100g of support	10 - 30g per 100g of support
Preparation	kneading / impregnation	slurry impregnation
Reactor	Multi-tubular packed bed	Slurry

2.2.1 Intrinsic rate of the Fischer-Tropsch reaction on cobalt

The kinetic behaviour of the Fischer-Tropsch reaction may be described using a product distribution model such as the ASF model, or using a rate law expression based on the reactants [29]. Most of the kinetic expressions that describe the intrinsic rate of the Fischer-Tropsch Synthesis on cobalt are derived from regression of a power law of the form $-R_{CO}=aP_{H2}{}^{b}P_{CO}{}^{c}$ [30]. Some kinetic rate expressions from the literature [27, 30-33] are shown below (Eqs. 2.2-1 to 2.2-4).

$$-R_{CO} = \frac{kP_{H_2}P_{CO}}{(1 + K_1P_{CO})^2}$$

Yates & Satterfield [30] **Equation 2.2-1**

$$-R_{CO} = \frac{aP_{H_2}P_{CO}{}^{\frac{1}{2}}}{(1 + bP_{CO}{}^{\frac{1}{2}})^3}$$

Rautavuoma & van der Baan [31] **Equation 2.2-2**

$$-R_{CO} = \frac{aP_{CO}{}^{\frac{1}{2}}P_{H_2}{}^{\frac{1}{2}}}{(1 + bP_{CO}{}^{\frac{1}{2}} + cP_{H_2}{}^{\frac{1}{2}} + dP_{CO})^2}$$

Sarup & Wojciechowski [32] **Equation 2.2-3**

$$r_{C,org} = \frac{k_{C\rightarrow CH}K_H{}^3K_{CO}K_CK_{H_2O}\left({}^{P_{H_2}{}^{\frac{3}{2}}P_{CO}}\big/_{P_{H_2O}}\right)}{(1 + K_H{}^2K_{CO}K_CK_{H_2O}\left(P_{H_2}{}^{P_{CO}}\big/_{P_{H_2O}}\right))^2}$$

van Steen & Schulz [33] **Equation 2.2-4**

The variations in the kinetic expressions may stem from differences in the conversion, reaction conditions, syngas composition, and the type of reactor from which experimental data was obtained to fit a specific expression [30]. Kinetic expressions also differ because some may be derived empirically, while others may incorporate a specific reaction mechanism with assumptions made regarding a slow/rate limiting step [33].

The effect of CO on the Fischer-Tropsch kinetics is complex. Low partial pressures are predicted to have a positive influence on the rate by increasing the availability of surface carbon for incorporation into hydrocarbon chains [33]. On the other hand, the low and/or negative order of CO seen in a number of expressions points to a degree of reaction inhibition. At high partial pressures, CO likely starts to compete with hydrocarbons for active sites, which leads to reaction inhibition [30, 33].

Unlike in the case of Fe where it is generally accepted as an inhibitor, the effect of water on cobalt is considered negligible, although some studies have suggested its role in both enhancement and inhibition of the reaction rate [30, 33-35, 40-42].

Most kinetic expressions show positive order with H_2. An increase in the H_2 partial pressure has generally been observed to correlate positively with the reaction rate within a range of conditions [30-37]. The positive impact of H_2 has been ascribed to its role in increasing the rate of formation of the monomer (CH_x) and in freeing up active sites for carbon surface species by removing O groups as H_2O. The latter case was evident from studies of CO hydrogenation on Co^0 foils in vacuo, which showed that hydrogenation and the removal of O groups from the Co surface was rate limiting instead of CO dissociation [28, 38]. The positive impact of H_2 may also be related to its role in lowering the CO dissociation energy. Ojeda & Mavrikakis [39] showed that hydrogen-assisted CO dissociation is more energetically favourable than direct dissociation to form carbide species on Co(0001). Calculated energy barriers for direct CO dissociation on Co(0001) were found to be high (i.e. 367kJ/mol), which is greater than the reported activation energies on the actual catalysts. Therefore, the considerable energy barrier for direct CO dissociation on Co(0001) means that the hydrogen-assisted route is most likely to be the sole pathway on this surface, although both pathways can compete on iron surfaces [39].

2.2.2 Active sites for the Fischer-Tropsch reaction on cobalt

The Fischer-Tropsch reaction on cobalt is regarded as non-structure sensitive and corresponds well with the number of surface metal sites for metallic crystallites greater than 9nm [43-49]. Exceptions include crystallites smaller than 6-8nm which show much lower site-time yields (turnover frequencies) than expected from their surface areas [50-53]. Differences in the product selectivity that have been reported with crystallites smaller than 8nm include higher CH_4 selectivity, lower C_5+ selectivity and increased selectivity towards olefins [54]. The low activity and poor product selectivity may be a consequence of differences in electronic structure, which results in a variation in the surface coverage of reaction intermediates [55]. Differences in thermodynamic stability due to the high relative surface energy of crystallites smaller than 4.4nm have been shown to increase their susceptibility to oxidation under reaction conditions, despite the same conditions not being favourable to bulk cobalt oxidation [56].

Other factors that may affect the nature of the cobalt active sites besides crystallite size include the nature of the support and the surface interaction with carbon monoxide. The influence of the support is generally regarded as structural because supports do not normally have an influence on the cobalt site-time yield [26, 45] but may affect crystallite size. Studies using SiO_2 and Al_2O_3 supports suggest that the diameter of cobalt oxide (Co_3O_4) increases with the pore diameter because the crystallites are embedded in the pore structure [57-60]. On the other hand, the impact of carbon monoxide on cobalt active sites was demonstrated by Wilson & de Groot [61] who observed an increase in the surface roughness of a Co(0001) surface following exposure to CO, which reportedly results in lower catalyst activity [1, 62].

2.2.3 Deactivation of cobalt-based Fischer-Tropsch catalysts

According to Dry [26], the three key factors that dictate the economic viability of the Fischer-Tropsch process over conventional crude oil are catalyst activity, product distribution, and catalyst life. The average lifespan reported for commercial cobalt catalysts is approximately 5 years [26, 63]. Catalyst activity undergoes a gradual decline with time on stream and although it may be restored with frequent regeneration, irreversible deactivation of the catalyst ultimately prevails and it is no longer economically viable to retain online. Retention of high catalyst activity is a top priority in order to maximise operational profitability because of the high cost of cobalt [64].

The deactivation profiles of two cobalt-based catalysts operated at industrial conditions are shown in Figures 2.2-1 and 2.2-2. The variation in the CH_4 activity with time on stream is also included with the profile in Figure 2.2-2. The evolution of the product selectivity with time on stream has been attributed to the deactivation/decrease in active sites, which decreases the ratio of the Co^0 active phase to the other phases such as oxides that typically arise in a working catalyst [67]. Although not Fischer-Tropsch active, these oxidic cobalt phases may affect the prevalence of side reactions [67].

Two deactivation phases are typically observed, which indicates various sources of deactivation [2, 65]. The first phase of deactivation occurs rapidly and may be reversible while the second more drawn out phase is of greater concern as it is associated with irreversible deactivation phenomena [65]. These two phases are indicated as Phase 1 and Phase 2 in Figures 2.2-1 and 2.2-2. The common causes of the deactivation observed with industrial cobalt catalysts include surface reconstruction and poisoning which are identified as the initial/fast deactivation mechanisms, while deactivation by carbon species, re-oxidation of the active phase (and formation of cobalt-support complexes), leaching of the active phase, and sintering occur over extended periods [2, 65].

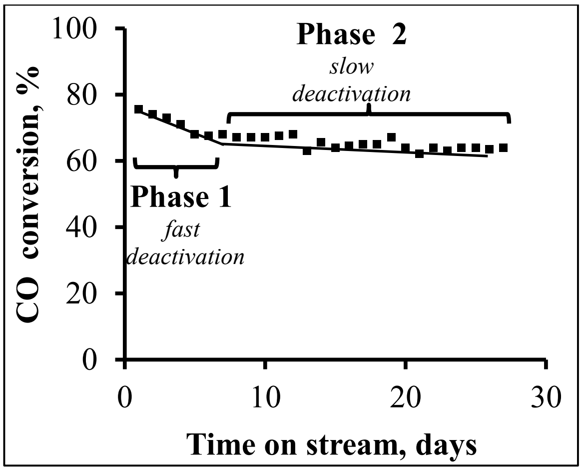

Figure 2.2-1: Deactivation profile of Co/Al_2O_3. Adapted from van Berge & Everson [66].

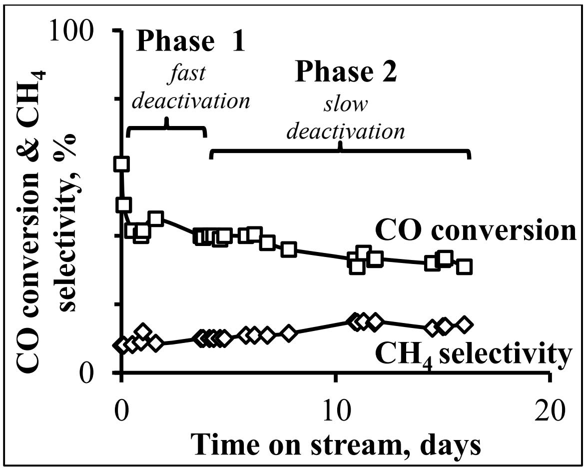

Figure 2.2-2: CO conversion and CH_4 selectivity as a function of time in a slurry reactor. (Co/Al_2O_3; 220°C; 20 bar; H_2/CO = 2.2). Adapted from Khodakov et al. [67].

- **Deactivation due to poisoning**

Poisons for the cobalt-based catalyst may arise from either syngas or may originate from the specific catalyst preparation technique (non-operational poisons). Sulphur is one of the most prevalent and extensively studied cobalt poisons, and rapid losses in activity have been reported at concentrations as low as 0.5ppm [68, 69]. Syngas polishing, which includes sulphur desulphurisation and even the use of ZnO guard beds, is employed in commercial applications to keep sulphur levels below 0.02ppm [2, 70, 71]. Syngas may also contain halides such as chlorine which has been observed to enhance sintering and gas phase transportation of Co and Pt at temperatures in the range of 500-550°C due to the volatility of the corresponding metal chlorides [72, 73]. Chlorine has also been reported to enhance sintering and grain growth of oxidic catalyst supports at high temperatures [72]. Other poisons present in syngas include nitrogen compounds (NO_X, HCN, NH_3) while the non-operational poisons such as alkalis (Na, Li, K) are often found in oxidic supports albeit in small quantities [65, 74, 75]. Alkali metals are reported to increase the selectivity to higher molecular weight hydrocarbons at the expense of the catalyst activity.

- **Surface reconstruction by carbon monoxide (CO)**

The role of CO in surface reconstruction of cobalt was demonstrated by Wilson & de Groot [61] using scanning tunnel microscopy whereby an increase in surface roughness on a Co(0001) surface was reported following exposure to CO. Fischer [62] and Welker [76] observed an immediate drop in activity (TOS<1h) following exposure of Co/Al_2O_3 and Ru/Al_2O_3 to syngas, which was ascribed to reaction inhibition due to surface reconstruction by CO. In both studies, the rapid decrease in activity was not observed when the catalysts were pre-exposed to CO prior to Fischer-Tropsch testing. Surface reconstruction by CO may result from carbon binding to an active cobalt plane and causing it to transform into a less active configuration [2, 54].

- **Re-oxidation of the active phase**

Re-oxidation of the active phase is one of the most commonly inferred causes of deactivation because the cobalt catalyst is exposed to partial pressures of the water co-product, especially at the high conversions required in commercial applications [77-79]. Reoxidation is also regarded as a precursor to both sintering [77] and the formation of irreducible cobalt-support complexes [78]. Although the oxidation of bulk cobalt is not feasible under industrial conditions, thermodynamic calculations were used to determine that the high relative surface energy of small crystallites (<4.4nm) increases their susceptibility to oxidation under reaction conditions [56].

Besides maximising the derived catalyst activity, the use of high metal loadings is reported to aid stabilisation of cobalt-based catalysts against deactivation due to reoxidation [80, 81].

- **Loss of active sites due to sintering**

Sintering results in loss of active metal surface area and has been identified as one of the dominant causes of initial deactivation (<10 days) of the cobalt Fischer-Tropsch catalyst [82, 83]. Crystallite growth is a result of atomic migration (Ostwald Ripening) or crystallite migration (coalescence) and is thermodynamically favourable because it results in a lower surface energy [65].

Mechanistically, migration is analogous to surface diffusion and is thus strongly correlated to the melting point ($T_{melting}$). The corresponding Hüttig temperatures ($0.3T_{melting}$) and Tammann temperatures ($0.5T_{melting}$) provide guidelines for the temperatures at which atoms at defect sites and in the bulk will exhibit mobility respectively [84]. Small cobalt crystallites in particular are susceptible to migration due to their highly uncoordinated surfaces, which result in high surface energy. In addition, the $T_{Hüttig}$ at 253°C is close to the reaction temperature of 220°C, which is reason for concern because the Fischer-Tropsch reaction is highly exothermic (see Eq. 2.1-1).

The susceptibility to sintering has been found to be high for cobalt catalysts with small crystallites [85] and the risk is reportedly pronounced in catalysts containing reduction promoters because they increase the extent of reduction of the very small crystallites, which would have otherwise remained oxidic [65].

o Cobalt deactivation by carbon deposition

Rigorous evidence has been provided for deactivation caused by the unreactive polymeric carbon at industrially relevant Fischer-Tropsch conditions [2, 86]. Carbonaceous species were deduced to adsorb onto both the cobalt active surface and the support, which led to a loss in the catalytically active surface area.

The rate of formation of polymeric carbon with time on stream has been observed to decrease in the presence of noble metal promoters, which is ascribed to an increased rate of removal of carbon species during reaction due to a ‘cleaning’ effect on the Co surface [87].

Another form of deactivation by carbon is pore blockage and blanketing of the active metal surface by heavy wax, which is regarded as a fast form of deactivation [2, 88, 89]. Long-chained hydrocarbons that are present especially during the Low-Temperature Fischer-Tropsch reaction may limit the diffusion of syngas to the active sites, causing a ‘quenching’ effect on the reaction rate [2].

2.2.4 Metal-support interactions (MSIs) and the reduction of cobalt-based catalysts

The reduction behaviour of the cobalt-based catalyst plays a fundamental role in the overall profitability of the process and is one of the most extensively studied aspects of Fischer-Tropsch catalysis. Commercial cobalt-based catalysts require activation in a reducing atmosphere to form metallic cobalt, which is regarded as the active phase for the Fischer-Tropsch reaction [41, 54]. Catalyst regeneration after the inevitable loss in activity with time on stream is also carried out under reducing (and oxidising) atmospheres to regain activity losses caused by poisoning, carbon deposition, and re-oxidation [41, 90]. Complete reduction to metallic cobalt is required to maximise the catalytic mass activity but is seldom achieved, especially when using highly interacting supports such as Al_2O_3. Some factors that have been reported to affect the reducibility of cobalt-based catalysts include metal loading and crystallite size [77, 91-93], the nature of the support [59, 91] calcination temperature [92], and the nature of the cobalt precursor [95-97]. Although numerous, the commonality between these factors is their influence on the strength of the interaction between the support and the nano-sized cobalt crystallites.

Interaction with the support provides the anchorage required to prevent cobalt crystallite migration, sintering, and the associated loss of catalytic activity. The strength of interaction between cobalt and common supports increases as follows: $SiO_2 < TiO_2 < Al_2O_3$ [79, 91, 98, 99]. Unfortunately, strong metal support interactions favour cobalt dispersion at the expense of reducibility, which results in the need for reduction promoters such as Pt in the commercial Al_2O_3 supported catalyst [77, 91, 97, 99-105]. The interaction between an active transition metal and an oxidic support may take on various forms including polarisation of the Co-O bond by Al^{3+} ions [106], an electronic interaction/ligand effect [100, 108], an interfacial surface chemical bond [107], solid-state reaction/ionic diffusion of the metal ions into the structure of the support [100, 103, 107, 109] and spreading/encapsulation/creeping [100]. Besides the detrimental effect on the reducibility, metal support interactions have also been reported to influence the intrinsic activity i.e. reactivity towards CO and H_2 [108, 110].

2.2.4.1 The two-step reduction of Co_3O_4

The consensus is that the reduction of bulk Co_3O_4 in hydrogen occurs via formation of CoO as a stable intermediate according to Equations 2.2-5 and 2.2-6 [111, 112].

$$Co_3O_4 + H_2 \rightarrow 3CoO + H_2O \qquad \textbf{Equation 2.2-5}$$

$$3CoO + 3H_2 \rightarrow 3Co + 3H_2O \qquad \textbf{Equation 2.2-6}$$

Based on the reaction stoichiometry, the temperature-programmed reduction (TPR) profiles of Co_3O_4 would be expected to show two distinct reduction peaks, in a ratio of 1:3 in accordance with the hydrogen consumption. However, the TPR profiles of supported Co_3O_4 tend to deviate from the ideal two-step reduction and exhibit multiple reduction peaks, with a common observation being an additional high temperature reduction peak at temperatures greater than 750°C, which is attributed to the reduction of mixed cobalt-support complexes [91, 93, 97, 106, 109]. As a result, the deviations from the ideal two-step profile have led to alternative peak assignments particularly when using highly interacting supports [106, 113]. These alternative peak assignments usually attempt to account for the reduction of cobalt species in close interaction with the support.

In the more recent literature, technological advancement and increased availability of material and surface science techniques such as X-Ray Absorption Near Edge Structure (XANES), Extended X-Ray Absorption Fine Structure (EXAFS), X-ray Diffraction (XRD) and Magnetometry with in situ capabilities have allowed for better accuracy of the assignments of reducing species in supported cobalt catalysts [60, 67, 93, 94, 114-120]. So far, extensive work carried out by the groups of Jacobs and Khodakov using temperature-programmed reduction combined with XANES (i.e. TPR-XANES) and EXAFS on Al_2O_3 and SiO_2 supports the two-step reduction of $Co_3O_4 \rightarrow CoO \rightarrow Co^0$, with deviations attributed to cobalt species with varying degrees of interaction with the support [60, 67, 93, 114-116, 119].

2.2.4.2 Kinetic models for the reduction of metal oxides

The two kinetic models that are frequently proposed for the reduction of transition metal oxides include the nucleation-growth model (with or without autocatalysis) and the interface-controlled/shrinking core/contracting sphere model [121-127]. There is limited literature on the reduction of Co_3O_4, and more especially on the reduction of supported Co_3O_4 crystallites, so most inferences are based on the literature of other transition metal particles for which a large body of literature exists, including NiO and CuO [121-127]. Even so, Rodriguez et al. [127] caution that the atomic and molecular processes that govern the kinetics of these models are poorly understood even on the most extensively studied oxides.

- **The Interface-Controlled/ shrinking core/ contracting sphere model**

An illustration of the interface-controlled model is shown in Scheme 2.2-1. Included are the typical curves of the degree of reduction (α) as a function of time, and the reduction rate (dα/dt) as a function of α.

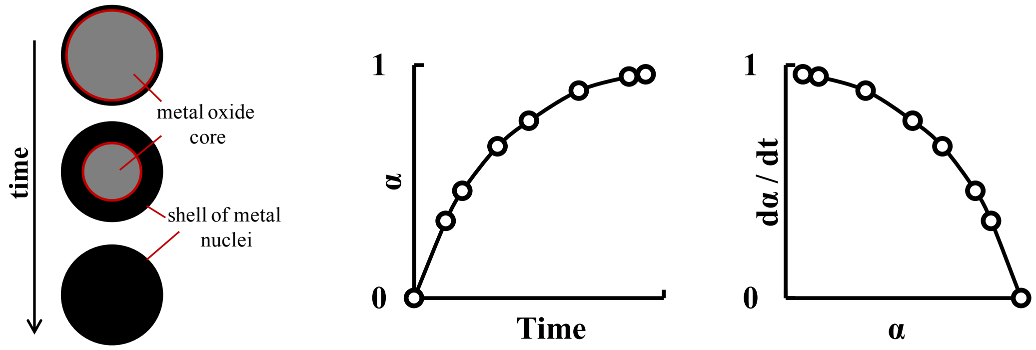

Scheme 2.2-1: ***Left:*** The interface-controlled model, with the interface shown in red. ***Centre:*** Degree of reduction of the metal oxide (α) as a function of time. ***Right:*** The reduction rate (dα/dt) as a function of the degree of reduction [127].

The interface-controlled model is characterised by near instantaneous nucleation of the reduced phase on the outer surface of the metal oxide, and thus does not exhibit an induction period and/or include significant autocatalysis unlike the nucleation model [121, 124]. The nucleus of the new phase proceeds to grow into the core of the metal oxide, which results in a scenario in which the interfacial layer (at which reduction occurs) is greatest at the start of the reduction and gradually decreases until the reduction is complete (interfacial area highlighted in red in Scheme 2.2-1: *Left*). As such, the reduction rate of the interface-controlled model is greatest at the start of the reduction when the interfacial area is highest and declines with the reaction interface, i.e. the reduction rate is proportional to the area of the interface [126, 127]. This behaviour of the reduction rate may be observed in Scheme 2.2-1: *Right*.

In the interface-controlled model, the reduction rate is controlled by diffusion of the gas to the particle surface, diffusion through the reduced phase, and the interfacial reaction and may therefore vary depending on the specific reducing species [127].

- **The Nucleation-Growth model and/or autocatalysis**

An illustration of the nucleation-growth model is shown in Scheme 2.2-2. The reduction of transition metal oxides is described as autocatalytic when it can be catalysed by low valent metal atoms, which are active for hydrogen activation [126, 130]. The reduction rate thus increases as the reaction proceeds because the quantity of low valent metal atoms increases. Included in Scheme 2.2-2 are the typical curves of the degree of reduction (α) as a function of time, and the reduction rate (dα/dt) as a function of α. The curves obtained for the nucleation-growth mechanism are also obtained for autocatalytic reactions [126].

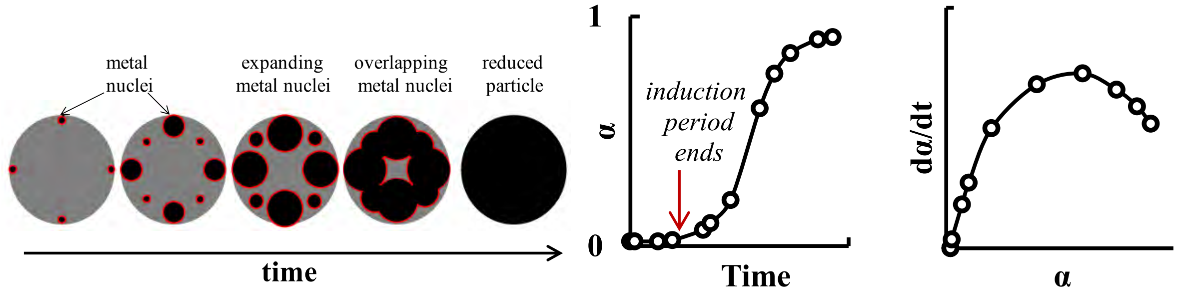

Scheme 2.2-2: ***Left:*** The nucleation-growth model, with the interface shown in red. ***Centre:*** The degree of metal oxide reduction (α) as a function of time. ***Right:*** The reduction rate (dα/dt) as a function of the degree of reduction [127]. The same curves are also obtained during autocatalytic processes [127].

As mentioned previously, a limited and inadequate body of literature exists on the kinetics governing the reduction of supported cobalt nano-crystallites, and most studies simply speculate on the nature of the reduction kinetics. Nevertheless, the reviewed literature sources on cobalt oxide reduction appear deferential towards the nucleation-growth model and/or autocatalysis [59, 98, 115]. The model is characterised by nucleation-growth processes, an induction period during which nucleation sites with a high efficiency for H_2 activation are formed, and the possibility of autocatalysis [127]. During induction, the reduction rate (dα/dt) is low but speeds up rapidly once a critical number of nucleation sites have been generated (see Scheme 2.2-2). The reaction is also said to occur at the interfacial area (highlighted in red in Scheme 2.2-2: *Left*) and so the growth period is characterised by rapid reduction because of the generation of new nuclei and nuclei expansion, which rapidly increases the interfacial area between the two phases. At some point during growth, the nuclei begin to merge/overlap, which results in a decrease in the total interfacial area with time and, consequently, the reaction rate (dα/dt) drops until the old phase has been annihilated [126].

The nucleation-growth model may be described by Avrami-Erofeev kinetics [128], in which it is assumed that the rate-limiting step is the nucleation of the reduced phase [127, 128]. Hydrogen activation is considered critical during reduction of transition metals and is considered rate limiting when activation sites are limited such as during the induction period [129]. Hydrogen activation has also been pinpointed by some as the rate-limiting step of the overall reduction mechanism when the reduction occurs concurrently with autocatalysis [116, 130-132]. Finally, according to Rodriguez et al. [127], removal of O atoms from the bulk of the oxide structure or nucleation to form the metal phase will only become rate limiting after excess hydrogen has been availed for reaction.

Very limited reduction is observed during the induction period (see Scheme 2.2-2: *Centre*), and it is suggested that nucleation sites are generated without formation of a new phase. With time, a sufficiently large quantity of active sites for hydrogen activation is available, and then fast removal of O atoms from the bulk of the oxide proceeds [135]. Induction has been represented as the generation of metal atoms on the outer surface of the oxide [133], and it is suggested that nucleation sites may be surface defects [127, 134, 135] with some studies showing significantly shorter induction periods when highly defective surfaces were used [127, 129]. Increasing the temperature and the hydrogen partial pressure has also been observed to decrease the induction period for oxides of Ni, Cu, Fe, and Rh [125, 127, 135]. On the other hand, the presence of water in the reducing gas has been observed to prolong the induction period, and water is said to destroy the surface defects required for nuclei formation [125, 136]. Although oxide surfaces show very little activity for H_2 activation, Density Functional Theory (DFT) calculations were used to show that defective sites such as adjacent metal atoms with an O vacancy increase the strength of H_2 adsorption and also facilitate its dissociation [127]. The role of defects as nucleation sites was also suggested by a recent study by Ward et al. [112] in which High Resolution Transmission Electron Microscopy (HRTEM) was used to demonstrate that CoO formation was initiated at stepped Co_3O_4 surfaces.

After the induction period, the generated H atoms may penetrate the oxide lattice, from which they later exit with the O atoms as water. Evidence has been shown for migration of hydrogen atoms into the structure of a Cu oxide, which was observed as an initial expansion of the unit cell volume, followed by the expected decrease in the unit cell volume following O removal to form the metal [135]. Kim et al. [135] suggested that the embedding of H atoms in the oxide structure forms a hydrogen bronze ($Cu_{16}O_{16}H_z$, z<1) based on difference electron density maps which showed that H atoms were most likely associated with O atoms to form a hydroxo-group. During the induction period, expansion of the oxide's unit cell volume due to embedding of H into the oxide structure was negligible, but increased with the reduction rate, which indicated that the hydroxo-structures are possible precursors to oxygen removal. It was suggested that formation of these complexes most likely weakened the metal-O bond, to result in oxygen removal as water [135].

Besides penetration of the oxides by hydrogen, diffusion of O^{2-} from the lattice has also been proposed to govern the reduction of transition metal oxides, especially at high temperatures (~330°C) when O vacancies are reportedly mobile [125-127, 137]. According to this model, when an O vacancy is created at the interface/oxide surface by reaction with hydrogen, the nearest O atom from the bulk comes in to take its position [127]. This creates a steady stream of O^{2-} ions to the surface, and nuclei are generated in the regions within the bulk after a sufficient O deficit is achieved. Reduction by O^{2-} migration has been said to occur during the induction period [126, 127]. Reduction via O^{2-} diffusion has also been suggested to govern reduction in the absence of autocatalysis, whereby O^{2-} reacts with *diatomic* H_2 on the surface, with O^{2-} diffusion as the rate-limiting step [129].

2.3 Reduction Promoters in Cobalt-based Fischer-Tropsch Catalysts

2.3.1 Platinum as a reduction promoter

Small quantities of noble metals (ratios of NM:Co = 0.01:100 to 0.3:100) have been observed to significantly improve the reducibility of cobalt-based catalysts and the general trend in the improvement in reducibility is Ru > Rh > Pt > Pd > Re [28, 91, 97-105, 116, 119, 138-142]. The global availability and production of Pt is more than 10 times greater than the other noble metals, which favours its use as the reduction promoter of choice in commercial catalysts.

The active phase of the reduction promoter is said to be metallic and Pt therefore needs to undergo reduction prior to the cobalt oxides in order to aid their reduction [87, 91, 102, 143, 144]. The majority of authors concur that platinum's ability to catalyse the reduction of supported cobalt oxides stems from a high affinity for H_2 activation (and subsequent spillover) and may or may not include electronic effects arising from Pt-Co co-ordination [28, 91, 101, 145-147]. Therefore, the proposed reduction promotion mechanism(s) of Pt are inadvertently linked to its location relative to the cobalt crystallites. Pt must be present on the surface of the catalyst, i.e. exposed to gas phase H_2 in order to activate and spillover hydrogen to the cobalt oxides [144] and on the other hand, Pt must coordinate directly with cobalt in order to induce a ligand/electronic effect. Evidence from EXAFS studies on reduced 0.5%Pt-15%Co/Al_2O_3 (co-impregnated Pt and Co) indicate that Pt-Co coordination occurs up to multiple shells while no Pt-Pt coordination is observed, which indicates that Pt is probably incorporated in the bulk of the cobalt oxide structure or present as single atoms on the cobalt oxide surface [116]. Jermwongratanachai et al. [90] also observed only Pt-Co coordination in a sequentially impregnated 0.5%Pt-25%Co/Al_2O_3 sample. These results concurred with those obtained by Shannon et al. [147] who used aberration-corrected scanning transmission electron microscopy to observe that Pt was present mainly as isolated atoms within the cobalt structure (following reduction and passivation) in a sequentially impregnated 0.3%Pt-20%Co/Al_2O_3 sample.

Besides the improvement in the reducibility, the use of Pt reportedly results in secondary effects on other characteristics of the cobalt catalyst including as dispersion, prevalence of mixed cobalt-support complexes, cobalt deactivation, intrinsic cobalt activity, and the Fischer-Tropsch product selectivity.

- **Effect of Pt on the cobalt dispersion**

A decrease in the average cobalt oxide crystallite size has been reported with Pt and other noble metal promoted Co catalysts especially with weakly interacting supports such as SiO_2 and TiO_2 [97, 98, 103]. Diehl & Khodakov (98) proposed that this effect may be because the noble metal increases the number of crystallisation/nucleation sites for cobalt oxide formation. Diehl & Khodakov (98) also report that modification of the oxide crystallite size occurs to a lesser extent for strongly interacting supports like Al_2O_3 and this is indeed confirmed by other literature [60, 90, 103, 115, 142].

On the other hand, a decrease in the crystallite size after reduction in the presence of noble metal promoters i.e. the cobalt metal crystallite size is often reported regardless of the support and attributed to the fact that these promoters aid the reduction of small Co crystallites and other highly dispersed Co^0 species that would otherwise remain oxidic [67, 91].

- **Effect of Pt on barely reducible cobalt-support complexes**

The TPR profiles of Pt promoted Co/Al_2O_3 do not typically exhibit the high temperature peak (>750°C) that is widely attributed to the formation of mixed cobalt-support complexes [60, 103]. Mixed cobalt-support complexes have been reported to form under various conditions including under high partial pressure of water [77, 78], during preparation [98], high calcination temperatures [92], during reduction [103], and during the Fischer-Tropsch reaction [1, 98].

Cobalt ions are said to be the precursors of mixed cobalt-alumina complexes, which form due to diffusion of Co ions into octahedral or tetrahedral sites of the cation-deficient spinel structure of the Al_2O_3 [107, 121]. This process is facilitated by water and high temperatures such as during calcination [106, 107]. Therefore, Pt and other noble metal promoters prevent the formation of mixed cobalt-support complexes by allowing cobalt ions to reduce at lower temperatures, which in turn lessens their susceptibility to migration into the support structure when exposed to higher reduction/operating temperatures [143].

Other reasons that have been suggested to explain the lower prevalence of cobalt-support compounds in the presence of reduction promoters include reducing the speciation of cobalt to irreducible species during calcination [149] and prevention of reoxidation under reaction conditions [150].

- **Effect of Pt on cobalt deactivation with time on stream**

The deductions from the literature on whether Pt and other noble metal promoters affect catalyst stability with time on stream are mixed. Adverse effects of noble metals on the activity of cobalt with time on stream have been observed for Ru [91, 145], Pt [91, 145, 148], Re [78, 145], and Pd [145, 151, 152]. The effects are probably mixed because many studies do not compare catalysts at the same conversion, which is mandatory because catalyst deactivation is also dependent on the product characteristics such as the water partial pressure, which is a function of the conversion. Furthermore, extended times on stream are required to make definitive conclusions on the deactivation processes which tend to be slow, and yet many laboratory-based studies use comparatively short times on stream than would be required for commercial applications.

- **Effect of Pt on the reactivity of cobalt active sites**

Generally, it follows that the higher amount of the Co^0 active phase after reduction in the presence of noble metal reduction promoters leads to the higher mass-based activity [60, 115]. Numerous literature sources have also reported increases in the site-time yield (STY i.e. turnover frequency/turnover number) in the presence of Pt and other noble metal reduction promoters especially at high promoter-to-cobalt ratios [87, 102, 103, 142].

According to Diehl & Khodakov [98], alloying of the Pt promoter with Co may result in a modified electronic properties and different reactivity towards CO and H_2, which would affect the site-time yield. Xu et al. [153] reported that the Co-H bond was weakened in noble metal promoted samples, which enhanced reactivity with adsorbed CO and resulted in higher activity due to enhanced hydrogenation. Tsubaki et al. [97] also reported modifications in the reactivity of cobalt towards CO due to alloying with Pt and Pd promoters.

In contrast, Schanke et al. [103] used Steady State Isotopic Transient Kinetic Analysis (SSITKA) of methanation experiments to determine that even though the apparent STY (based on CO conversion and Co^0 surface atoms) in 0.4%Pt9.2%Co/Al_2O_3 (and its SiO_2 supported equivalent) was twice as high as that in the unpromoted sample, the true STY of Co^0 remained unaffected. The authors attributed the higher apparent STY in the presence of Pt to an increased coverage of *reactive* intermediates, and obtained a constant true STY of Co^0 after the effects of coverage were decoupled from the apparent STY. The authors suggested that a large portion of the surface of the unpromoted sample was actually covered by unreactive species, with only a portion of the catalyst being available for reaction. Other studies of SSITKA of methanation have also come to the same conclusion as Schanke et al. [103] regarding higher apparent STY but constant true intrinsic Co activity in the presence of noble metal promoters including Kogelbauer et al. [142] on Ru/Co/Al_2O_3 and Vada et al. [102] using Re-Co/Al_2O_3 and Pt-Co/Al_2O_3.

- **Effect of Pt on the Fischer-Tropsch product selectivity**

Generally, Pt has been reported to increase the hydrogenation activity of cobalt-based catalysts. Higher extents of hydrogenation are characterised by higher CH_4 selectivity, and increased paraffin: olefin ratio to the detriment of the C_5+ selectivity and the chain growth probability [98]. Nevertheless, the impact of Pt appears to vary between studies and is probably related to the Pt/Co atomic ratio in the specific catalyst Higher Pt/Co ratios appear to contribute to the increase in the hydrogenation activity [98].

2.3.2 Gold as a reduction promoter

Besides noble metals, coinage (group 11) metals such as Cu, Ag and Au have also been reported to improve the reducibility of cobalt-based catalysts [115, 154-156]. This characteristic of coinage metals is not surprising since they lie in close proximity of noble metals (groups 8-10) in the periodic table.

Until the mid-1980s, the study of Au as a catalyst was all but abandoned owing to its strong noble character, which rendered it unreactive and irrelevant for catalytic chemistry. The turning point in Au catalysis came in the form of two groundbreaking discoveries made by the group of Hutchings [246] and by the group of Haruta [247], when it was discovered that supported nano-sized Au crystallites were active for acetylene hydrochlorination, and low temperature CO oxidation respectively [157]. Since then, the wealth of literature and knowledge of Au catalysis has continued to grow especially with respect to oxidation reactions so that in 1992, the first commercial use of heterogeneous gold catalysts was reported for use as part of an odour-removing component in Japanese restrooms [157]. Unfortunately, the strong focus on Au as an oxidation catalyst has skewed the attention away from its use in other reactions, particularly hydrogenation, for which it has also exhibited appreciable catalytic activity [158].

- **H_2 activation on gold surfaces**

The binding energy of hydrogen atoms is lower, and the energy for H-H bond scission greater on gold surfaces compared to platinum [161, 236]. Furthermore, hydrogen adsorption on gold is limited to low co-ordinated atoms along edges and at corners, which means that only a fraction of the surface of a gold crystallite interacts with hydrogen [161]. Nevertheless, Au has shown activity for H_2 oxidation [162, 163], $CO+CO_2$ hydrogenation to CH_3OH [164, 165] and selective hydrogenation of unsaturated compounds [166, 167]. A particle size dependence as is the case with CO and O_2 chemisorption for which small crystallites (<3nm) are highly active has also been reported for H_2 on Au during H/D exchange on Al_2O_3 [161, 168]. To put this into context, supported Au crystallites in the range of 7nm although active for H/D exchange do not perform much better than the Al_2O_3 support on its own.

Even though gold shows very little activity towards hydrogenation compared to noble metals, it has a distinct advantage of very high selectivities that would otherwise only be obtained on other metals by deliberate active site poisoning [158, 161, 169].

- **Catalysis and reduction promotion by gold under Fischer-Tropsch conditions**

The literature on gold catalysis under Fischer-Tropsch conditions is significantly limited compared to that on Pt and other noble metal promoters. Jacobs et al. [115] carried out a comprehensive study of the performance of Group 11 metals as promoters, which included samples of Au (0.1 to 5.05%) on 15%Co/Al_2O_3. Gold was observed to improve the reducibility and activity of cobalt, but decrease the C_5+ selectivity at loadings greater than 2% (220°C, 20bar & H_2/CO=2). Ahmad et al. [170] using 1.5 to 2.5% Au on 10%Co/Al_2O_3 also reported improvement in the cobalt reducibility. However, in contrast to Jacobs et al. [115], Ahmad et al. [170] found that the C_5+ selectivities even at the highest Au loadings were higher than with the unpromoted sample (220-275°C, 1-5bar & H_2/CO=2).

Jalama et al. [171] found that 0.5 to 5% Au improved the reducibility of 10%Co on Al_2O_3 or SiO_2. However, even the lowest Au loadings were detrimental to CH_4 selectivity, C_5+ selectivity and decreased the olefin/paraffin ratio (220°C, 20bar & H_2/CO=2). In contrast, with 10%Co on TiO_2 promoted with 0.2 to 5%Au, Jalama et al. [172] observed a *decrease* in the reducibility of supported cobalt oxides, although fewer cobalt titanate species were observed. The authors suggested that the Au crystallites used were too large to activate H_2 for the cobalt reduction and indeed XRD diffractograms showed prominent Au^0 peaks. Addition of Au up to a loading of 1% increased the Fischer-Tropsch activity, which was ascribed to fewer cobalt-titanates, but further increases in Au were detrimental and increased the CH_4 production. The decrease in the probability of formation of cobalt titanate species was attributed to the possible deposition of a gold layer between cobalt and TiO_2 support, which was confirmed by the deduction of surface enrichment by cobalt during XPS analyses. Gold's tendency to catalyse the water-gas shift (WGS) reaction was proposed to have resulted in a higher localised hydrogen partial pressure, which increased the hydrogenation activity of cobalt to form more CH_4.

It is unclear why there is such great variation in the behaviour of gold-promoted Co catalysts, but it is hypothesized that the variation in results may arise due variations in experimental conditions and differences in catalyst preparation (e.g gold precursor, selected support, preparation technique, sequential versus co-impregnation with Co).

2.4 Hydrogen Spillover

“Spillover involves the transport of active species sorbed or formed on a first surface onto another surface that does not under the same conditions sorb or form the active species”[173].

Hydrogen spillover is said to be the fastest spillover process, and has been the subject of numerous publications for almost 80 years [173-179]. According to Conner & Falconer [173], the earliest published inference of spillover was made in 1940 by Emmett [180] during studies on the NH_3 synthesis and decomposition, although experimental evidence for surface diffusion of hydrogen came many years later by authors such as Kuriacose [181] and Khoobiar [182]. Kuriacose [181] observed an enhanced rate of H_2 formation from GeH_4 in the presence of Pt wire, which he ascribed to the facilitated recombination of atomic hydrogen on the Pt surface. Khooibar [182] on the other hand, studied the formation of WO_3 bronzes (H_xWO_3) which formed easily at room temperature in the presence of 0.5% Pt/Al_2O_3 and yet temperatures higher than 128°C were required to observe the characteristic blue colour of these bronzes without Pt.

2.4.1 Spectroscopic evidence of hydrogen spillover

Roland et al. [176] identified the inadequacy of spectroscopic techniques in directly observing spillover hydrogen species as one of the greatest hindrances to understanding the hydrogen spillover phenomenon. Furthermore, many of the spectroscopic techniques do not allow for analysis of hydrogen species under actual reaction conditions and as a result, the existence and effect of spillover hydrogen are controversial topics with a number of detractors. Evidenced obtained from some of the spectroscopic techniques is provided below.

- **Resonant photoemission spectroscopy (RPES)**

In a recent publication by Lykhach et al. [183], RPES was used on well-defined $Pt/CeO_2(111)/Cu(111)$ model catalyst to study the surface reduction of the CeO_2 support in order to investigate the existence and propose the chemical nature of spillover hydrogen. At low temperatures (-93°C), atomic hydrogen was deduced to spillover from Pt to CeO_2, resulting in the formation of Ce^{3+} to the detriment of Ce^{4+} features in the valence band photoemission spectra. If however the temperature was raised to >13°C so that desorption of hydrogen from Pt was favoured, back spillover from the CeO_2 to Pt occurred, resulting in reoxidation of the CeO_2 surface and re-emergence of Ce^{4+} ions. The nature of spillover hydrogen in this study was determined as neutral.

○ Proton Nuclear Magnetic Resonance (NMR) spectroscopy

NMR was used by King et al. [184] to study the spillover of hydrogen on various Ru-Cu catalysts supported on SiO_2, with the specific aim to investigate the accuracy of H_2 chemisorption as a method to determine Ru dispersion in these samples. The NMR analyses were carried out at temperatures where only Ru was capable of dissociative hydrogen chemisorption and thus only H/Ru interaction was expected. However, adsorbed hydrogen atoms were observed to experience both a Ru and Cu environment, which was attributed to Ru → Cu spillover of atomic hydrogen. It was concluded that H_2 chemisorption could not be used to accurately titrate Ru surface atoms in a Ru-Cu sample as spillover to Cu would result in the overestimation of Ru dispersion. NMR has also been used to observe spillover hydrogen in other catalyst systems including $Pt \rightarrow Al_2O_3$ [185] and $Pt \rightarrow SiO_2$ [186, 187].

○ Infrared Spectroscopy (IR)

Cavanaugh & Yates [188] proposed a hydrogen spillover mechanism to explain observations made during infrared (IR) analyses of gaseous deuterium (D_2) exchange with OH groups in both Al_2O_3 and Rh/Al_2O_3. At the selected reaction conditions of 0.13 bar and 37°C, H/D exchange was confirmed in Rh/Al_2O_3 but not pure Al_2O_3, indicating that Rh facilitated H/D exchange and effectively $Rh \rightarrow Al_2O_3$ hydrogen spillover. Further confirmation of a spillover mechanism was provided by catalyst pre-treatment in CO after which the rate of formation of the peak corresponding to OD was found to diminish significantly. The preferential adsorption of CO versus D_2 or H_2 is well known on platinum group metals and CO was deduced to inhibit active sites for D_2 and H_2 chemisorption and consequently limit $Rh \rightarrow Al_2O_3$ spillover of hydrogen.

○ Electrical Conductivity

Although not a spectroscopic technique, electrical conductivity has been used to provide direct evidence for hydrogen spillover in Pt/Al_2O_3 [189], Pt/TiO_2 [190], and $Cu\text{-}Co/ZnO_2$ [191]. Roland et al. [190] found that the n-type conductivity of TiO_2 was unaffected by exposure to hydrogen, while it increased in Pt/TiO_2. The increase in n-type conductivity of

Pt/TiO_2 was attributed to the electron donation to the support by spillover hydrogen species from Pt. Spillover hydrogen species were suggested to coexist as H atoms and H^+ ions. An interesting observation was made when a pressed sample composed of halves of Pt/TiO_2 and TiO_2 was exposed to hydrogen. This time, the resistance in the TiO_2 portion decreased albeit at a slower rate than in the Pt/TiO_2 portion, and this was attributed to the time lag as spillover hydrogen species needed to travel longer distances from the Pt/TiO_2 to the TiO_2 component.

2.4.2 Chemical nature of spillover hydrogen species

The important implications of the nature of spillover hydrogen species within reaction mechanisms have meant that their chemical characteristics have not survived the on-going debate surrounding the hydrogen spillover phenomenon. Activated hydrogen species that have been proposed in literature include: H atoms [175], H^+ protons [174, 176, 177], H^- hydrides and H^+-H^- ion pairs [193, 194], H_3^+ species [195] and $H\cdot$ radicals [196]. In a review of the hydrogen spillover phenomenon, Roland et al. [176] concluded that the nature of spillover hydrogen species was dependent on the physico-chemical catalyst properties, and thus could only be understood by the interaction with the surface onto which they were adsorbed. Furthermore, the differences in the deductions made of the chemical nature of spillover hydrogen species were also proposed to arise from the specificity of the reaction mechanism within which spillover occurred, and the type of spectroscopic technique employed for the investigation.

- **Hydrogen atoms**

Spillover hydrogen species have been deduced to be atomic hydrogen based on observations made during infrared spectroscopy, H_2-Temperature-Programmed Desorption (molecular H_2-TPD) and H-Temperature-Programmed Desorption (atomic H-TPD) and the bronze formation in metal organic frameworks. After either H_2 or D_2 adsorption, Infrared spectroscopy on a number of metals show adsorption bands corresponding to M-H or (M-D) but none corresponding to molecular H_2, HD or D_2 adsorption. It thus follows that species that would subsequently spillover from these surfaces would also be atomic rather than molecular [176].

The identity of spillover species as atoms has also been suggested during bronze formation resulting from the diffusion of spillover hydrogen species into metal organic frameworks such as WO_2 and MoO_3 at conditions where only atomic hydrogen could diffuse into these oxides [176].

With respect to H_2-TPD, the high temperature desorption peaks from catalysts composed of noble metals supported on oxides such as Al_2O_3, SiO_2 and zeolites are often assigned to spillover hydrogen. The fact that these peaks are also obtained during *atomic H*-TPD was used to deduce the chemical nature of the spillover hydrogen species as atomic [175].

- **Trihydrogen (H_3^+) species**

In a proposed reaction mechanism for CH_4 formation by demethoxylation of silica aerogel on Pt/Al_2O_3, Bianchi et al. [195] proposed that hydrogen spillover species existed as H_3^+. H_3^+ ions were reportedly formed on Pt by reaction of H atoms with molecular hydrogen, and could migrate from Pt/Al_2O_3 to the silica gel. Although these species were consistent with the proposed reaction kinetics, attempts to confirm their existence using infrared spectroscopy were unsuccessful. Spectroscopic evidence for H_3^+ ions as spillover species has not been found in any of the analysed literature although a triatomic hydrogen species has been postulated as an intermediate in other reaction mechanisms [197, 198].

However, it is worth noting that the existence of triatomic hydrogen ions is widely accepted in astrochemical studies [199].

- **Protons**

The accelerating effect of water on the rate of hydrogen spillover has been used to infer that hydrogen species may spill over as solvated protons [176, 200-202]. Similar deductions have been made in studies where the extent of spillover was found to be dependent on surface acidity and the surface iso-electric point. Baeza et al. [177] suggested that the migrating hydrogen species were probably protonic because the rate of surface diffusion of hydrogen over various surfaces increased with the corresponding iso-electric points. Baeza et al. [177] also suggested that the movement of the proton was likely counterbalanced by transfer of an oppositely charged species such as a hydride ion (H^-) within the bulk of the solid. However, Levy & Boudart [174] suggested an alternative explanation for the dependence of spillover with surface acidity where by protons were transferred, but the electrons remained on the donating metal surface.

Additional support of spillover species as protons comes from electrical conductivity and electrochemical analyses [176, 190, 203]. Keren & Sofer [203] suggested that spillover was analogous to a liquid electrolyte system whereby hydrogen present on metal surfaces dissociated into protons and electrons, which simultaneously spilled over to other surfaces.

- **H^+-H^- ion pairs**

According to the 'Hydrogen Spillover Mechanism' of hydroconversion with bi-functional catalysts, heterocatalytic dissociation of molecular hydrogen on metal surfaces forms an H^+-H^- or H^+-H ion pair [204, 205]. The proton (H^+) acts as the acid by abstracting a hydride ion (H^-) from the hydrocarbon molecule to form a carbenium ion, which is then stabilised by H^- after skeletal rearrangement [204].

As discussed previously, there appears to be a dependence of the chemical nature deduced for spillover hydrogen species on the spectroscopic technique utilised, and the surface with which the spillover species interact. It is also possible that spillover hydrogen species exist in various forms and consequently show varying activity towards different hydrogenation reactions [173, 206, 207]. Baumgarten et al. [206] investigated this concept by testing the action of spillover hydrogen from the same Pt/Al_2O_3 source in separate reactions including H/D exchange, WO_3 bronze formation, and reaction with unsaturated carboxylic acids. Although bronze formation and H/D exchange were observed, the same hydrogen spillover species were unable to hydrogenate the carboxylic acids even at *thermodynamically* favourable conditions. The authors concluded that spillover species were not universally active and needed to be in the *correct chemical state* required for the specific reaction. Nevertheless, it must be kept in mind that both kinetics and thermodynamics must be considered in order for a specific reaction to proceed. Deductions such as those made by Baumgarten et al. [206] are not conclusive because hydrogenation of the more complex hydrocarbon molecules may have indeed occurred, albeit with much slower kinetics compared to the other less complex reactions.

2.4.3 Hydrogen spillover in cobalt-based Fischer-Tropsch catalysts

2.4.3.1 Spillover species during reduction

Inferences of hydrogen spillover in the literature of promoted cobalt-based catalysts are widely based on analogies from comparable catalyst systems such as in bi-functional hydrotreating catalysts for which extensive evidence of spillover has been obtained. There is limited research that rigorously investigates the occurrence and effects of hydrogen spillover under actual operating conditions of Fischer-Tropsch catalysts. The most comprehensive study found so far is that by Hilmen et al. [143] during a Temperature-Programmed Reduction (TPR) study of the Re-Co catalyst system. A more recent study by Beaumont et al. [28] also reports a hydrogen spillover effect during reduction, albeit on a model catalyst system composed of Pt and Co nanoparticles supported on SiO_2.

Hilmen et al. [143] demonstrated that direct Co-Re contact was not required in order to observe the improvement in reducibility compared to the unpromoted Co/Al_2O_3. The authors used model catalysts composed of physical mixtures on $Re/Al_2O_3+Co/Al_2O_3$ for their TPR analyses but did not report on the catalyst behaviour under Fischer-Tropsch conditions. Furthermore, a gap still exists with respect to the behaviour of other noble metal reduction promoters such as Pt due to the different chemical nature. An example of this is that Re oxides reduce at ca. 425°C. Due to the two-step reduction of Co_3O_4, Re oxide reduction generally occurs after that of $Co_3O_4 \rightarrow CoO$, and so Re only catalyses the $CoO \rightarrow Co^0$ reduction step [91, 103, 143, 144].

The consensus is that noble metals reduce at low temperatures and can consequently dissociate H_2, which is then used to reduce cobalt species. When direct promoter-cobalt contact is proposed to be unnecessary for reduction to proceed, chemisorbed hydrogen species from the promoter are said to travel along the support to the unreduced cobalt species via a surface diffusion mechanism [143]. On the other hand, EXAFS studies of Pt, Ru, Pd and Re promoters have shown that direct promoter-Co contact exists, and that in fact these promoter atoms are incorporated within the larger cobalt crystallites or preferentially deposit on the cobalt surface [116, 208]. There exists a form of intimate mixing of Co with noble metal promoters, which could have non-trivial impact on the reducibility, reaction, deactivation, and regeneration processes [59].

2.4.3.2 Spillover hydrogen as a reacting species during hydrogenation and hydrocarbon synthesis

Hydrogen spillover is not limited to promoter effects during reduction but has also been proposed as the underlying cause of other effects including the higher selectivity towards CH_4, stabilisation of cobalt against deactivation with time on stream and modification of the activity of cobalt active sites under Fischer-Tropsch conditions [97, 151, 152]. In an extensive review of spillover, Conner & Falconer [173] proposed that although current reaction mechanisms do not account for spillover species, it is likely that their effect is already incorporated in the proposed reaction kinetics so that spillover can be harnessed during future catalyst design.

Unfortunately, no literature on a systematic investigation of the effects of spillover hydrogen species under commercially relevant Fischer-Tropsch conditions has so far been found although it has been hypothesized in some studies (Yan et al. Catal. Today 160 (2011); Ma et al., synthetic liquids production and refining , 1084 (2011) 127-153). Therefore, this section provides a summary of select literature in which a hydrogen spillover mechanism has been deduced during hydrogenation and hydrocarbon synthesis reactions in an attempt to portray the phenomenon as it could occur under Fischer-Tropsch conditions. The literature on hydrogen spillover provided in this section includes studies in which synergistic effects attributed to hydrogen spillover have been reported under reactive conditions, and in the presence of the common constituents of the cobalt-based Fischer-Tropsch catalyst including cobalt, Al_2O_3, SiO_2, and noble metal promoters. The reactions have also been selected for their relevance/analogy to the Fischer-Tropsch synthesis including CO/CO_2 hydrogenation to CH_4 or CH_3OH and various hydroconversion reactions.

- **Hydrogen spillover during $CO + CO_2$ hydrogenation to methanol**

A mechanism involving spillover hydrogen has been suggested for the $CO+CO_2$ hydrogenation to CH_3OH reaction on Cu/ZnO and Cu/ZrO_2 catalysts [173, 202, 209]. Using a physically mixed $Cu/SiO_2+ZnO/SiO_2$ hybrid catalyst that allowed for physical separation of the two active components, Burch et al. [209] observed a synergistic effect that was independent of direct Cu-ZnO contact. Cu was suggested to have partially reduced the ZnO surface, which under reactive conditions provided extra sites for H_2 activation. Therefore, the synergy arose because the 'CO_x' intermediate species that were adsorbed on the Cu surface were able to react with hydrogen species from two sources instead of one, i.e. H from direct adsorption on Cu *and* spillover H from the reduced ZnO surface.

An analogous synergistic effect may be imagined between reduction promoters and cobalt surfaces under Fischer-Tropsch conditions, where the promoter surface provides additional sites for H_2 activation, followed by spillover to the cobalt surface for reaction. A number of studies have indeed suggested a synergistic effect during the Fischer-Tropsch reaction using Pt-Co catalysts to explain the higher cobalt site-time yield and higher selectivity towards CH_4 compared to the unpromoted sample [90, 95, 97,144].

○ **Hydrogen spillover during hydrodesulphurisation (HDS)**

A synergy attributed to hydrogen spillover has been reported for the Cobalt-Molybdenum and Nickel-Molybdenum sulphided catalyst systems (Co-MoS/Al_2O_3 and Ni-MoS/Al_2O_3). The group of Gil-Llambías and Ojeda [177, 210-212] studied this system at ca. 350°C and 30 bar in a micro-reactor containing beds of monometallic components of Co/Al_2O_3 and Mo/Al_2O_3, which were separated by various inert powders including: SiC, γ-Al_2O_3, carbon, SiO_2, $MgSiO_3$ and zeolites. An illustration of their set-up is provided in Figure 2.4-1: *Left*. The observed synergism decreased with increasing length of the separator bed and correlated strictly with the acidity/iso-electric point (IEP) of the separator, i.e. γ-Al_2O_3 > UCL001 > C > UCL002 > SiO_2 > $MgSiO_3$. From this, it was deduced that hydroxyl groups on the acidic surfaces helped stabilise spillover hydrogen species during their migration from Co → Mo.

Increasing the length of the separator bed between the active surfaces increased the probability of hydrogen recombination and desorption into the gas phase because hydrogen travelled longer distances along the separator, and as a result the flux of spillover hydrogen from the Co to the Mo component was reduced. Although both the Co-Mo and Ni-Mo systems exhibited a synergy attributed to spillover hydrogen during hydrodesulphurisation, it is worth noting that the synergism due to Ni was less pronounced than that of Co, which was attributed to nickel's lower affinity for hydrogen dissociation [177, 211].

An interesting observation was made using γ-Al_2O_3 monoliths, which were extrudates of ca. 40mm, whose extreme ends were impregnated by Co and Mo with varying lengths of separation. An illustration of a monolith is shown in Figure 2.4-1: *Right*. It was observed that almost double the conversion was obtained for the same distance of separation along the γ-Al_2O_3 monolithic bed compared to when the γ-Al_2O_3 separator bed composed of powder alumina particles was used. This observation was attributed to an improved efficiency in the transportation of spillover hydrogen species along the monoliths, because hydrogen did not have to 'jump' between the particles of the powder when it migrated from the Co to the Mo phase for reaction.

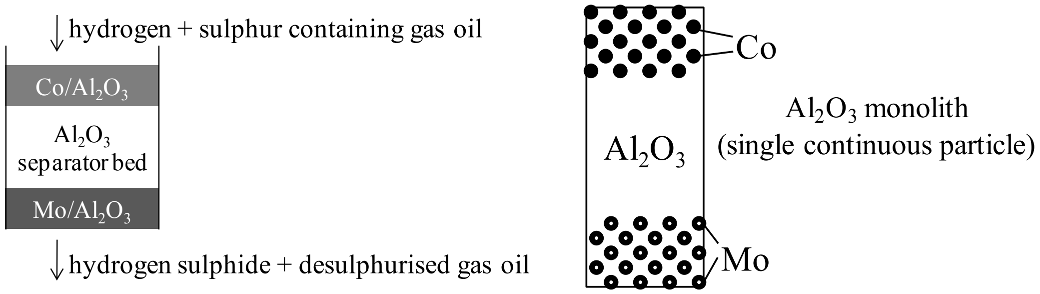

Figure 2.4-1: ***Left:*** Illustration of the set up used to investigate hydrogen spillover during hydrodesulphurisation (HDS) using separate catalyst beds. ***Right:*** A continuous monolithic Al_2O_3 particle with Co and Mo impregnated at extreme ends. Adapted from Baeza et al. [177].

These studies demonstrated a reaction synergy because of spillover hydrogen, which could be observed in spite of extensive separator beds of up to 10mm. Spillover hydrogen species successfully negotiated these long distances between the hydrogen donor (Co or Ni) and the hydrogen acceptor (Mo) surfaces. The lower activity observed with Ni-Mo compared to Co-Mo indicated that the synergy could be manipulated by using metals with different affinities for hydrogen activation. This is relevant to the assertion that the H_2 activation by reduction promoters such as Pt results in the higher degree of methanation compared to the unpromoted Co catalyst [95, 97, 145, 213]. If spillover from reduction promoters indeed occurs under reaction conditions, then it follows than its effects may be manipulated by using promoters with varying activity towards hydrogen activation such as Au.

- **Hydrogen spillover during hydroconversion on bifunctional catalysts**

Some of the most dramatic evidence of the fundamental role played by spillover hydrogen in a reaction mechanism has been obtained during hydroconversion on bi-functional catalysts [205, 214-218]. The classical mechanism during these reactions was that the hydrogenation and dehydrogenation functions were provided by the metal component while skeletal rearrangement of the hydrocarbon occurred at the acid sites. As a result, this mechanism necessitated gas phase diffusion of hydrocarbon intermediates between the two sites [219, 220]. The classical mechanism was subsequently disputed by contradictory experimental evidence that showed that the acidic component provided the active sites for both the skeletal restructuring *and* hydrogenation/dehydrogenation [205]. The noble metal component only served to provide activated hydrogen species via hydrogen spillover and surface diffusion [205].

Besides the fundamental involvement of spillover hydrogen in the hydroconversion mechanism, spillover hydrogen in bifunctional catalysts has been shown to prevent coking and as a result help maintain a high catalytic activity of the acidic component [173]. Parera et al. [221] observed that Pt helped to regenerate a heavily coked Al_2O_3 sample that had been physically mixed with the Pt/Al_2O_3 naphtha reforming catalyst. In the presence of Pt, coke removal under reducing and oxidising conditions occurred at significantly lower temperatures and the authors deduced that hydrogen and oxygen activation and subsequent spillover from the Pt surface played a fundamental role in the regeneration.

These observations from bifunctional catalysis are particularly relevant to the Fischer-Tropsch catalysis in which coke formation and the accumulation of unreactive carbonaceous species has been identified to block cobalt active site and as a result cause of long-term deactivation (see Sec. 2.2.3). The presence of a reduction promoter such as Pt may prevent the build-up of these carbonaceous species and as such help maintain high catalyst activity over extended periods.

- **Hydrogen spillover during CO_2 methanation**

The deduction that noble metals may provide a ‘cleaning’ effect on cobalt is supported by a recent study by the group of Somorjai who used the CO_2 methanation reaction ($H_2/CO_2 = 3$, 200°C, 1&6 bar) as a probe reaction to study the mechanistic role of Pt during the cobalt-catalysed Fischer-Tropsch reaction [28, 192]. The site-time yield in the presence of Pt was found to be 6 times that of the unpromoted Co, which was attributed to the ‘cleaning’ of the cobalt surface by Pt (which itself was not active for the reaction).

The results from this study are shown in Figure 2.4-2. The structure of the model catalysts used was confirmed by HRTEM, in situ Near Edge X-Ray Absorption Fine Structure (NEXAFS) spectroscopy and Inductively Coupled Plasma – Atomic Emission Spectroscopy (ICP-AES) as discrete monometallic Pt (12nm) and/or Co (10nm) nano-particles supported on Mesostructured Cellular Foam (MCF)-17 mesoporous SiO_2 (catalyst structure included in Fig. 2.4-2). The catalyst with the highest activity was that with adjacent (but physically separated) Pt and Co nanoparticles that were present in a mass ratio of Co/Pt=20, followed by the monometallic Co sample. Hardly any reaction was observed in a Pt-Co bimetallic sample (Pt/Co=1) because Pt segregated to the surface of the nanoparticles (bimetallic also shown in Fig. 2.4-2). The mechanistic role of Pt was suggested as two fold, the first involved H_2 activation followed by spillover along the SiO_2 support to the Co nanoparticles to aid their reduction during activation in H_2. The second Pt effect involved a similar spillover action under reactive conditions, which provided a 'cleaning' action via removal of near surface or even subsurface oxygen/oxides that accumulate on the cobalt surface following C-O bond breaking. A relevance/applicability to the Fischer-Tropsch reaction was claimed due to the similar reaction mechanism, reaction conditions, reactants, and products (which included CO and short-chained hydrocarbons).

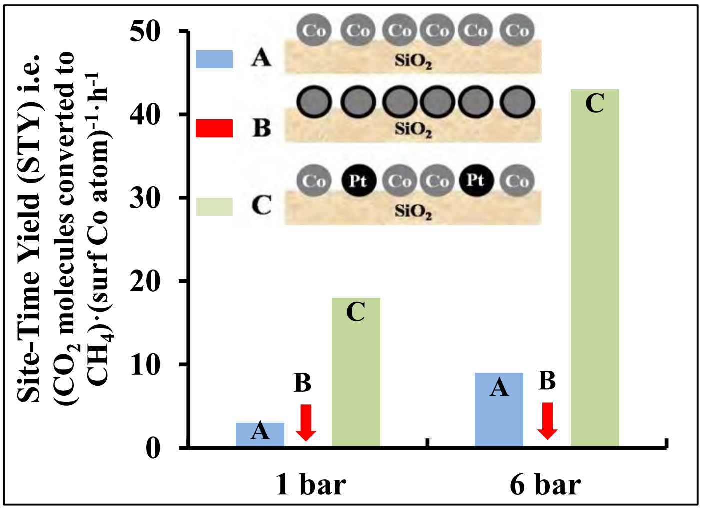

Figure 2.4-2: Site-time yield (STY) during the CO_2 methanation reaction (H_2/CO_2=3, 200°C, 1&6 bar) for the 3 model catalysts (A, B, C) supported on MCF-17 mesoporous SiO_2
A: 10 nm Co nano-particles; **B:** 11 nm Co−Pt bimetallic nano-particles with preferential surface enrichment of Pt (red arrows show only trace conversion to CH_4); **C**: 10 nm Co and 12 nm Pt nano-particles mixed in solution and subsequently deposited on support [28].

2.4.4 Intrinsic steps involved in the spillover and surface migration of hydrogen

Scheme 2.4-1 illustrates the intrinsic steps that may occur during the reduction of a metal oxide in the presence of a noble metal promoter according to a hydrogen spillover mechanism. The process is initiated by dissociative adsorption of H_2 on the promoter surface (Step 1). This is followed by the spillover step during which hydrogen atoms cross the promoter-oxide interface (Step 2). Reduction may then occur when the spillover hydrogen atoms react with oxygen in the structure of the metal oxide to form water, leaving the metallic phase behind (Step 3). Alternatively, spillover can occur from an isolated promoter crystallite to the surface of the support (Step II). During this process, a strong hydrogen-metal bond is broken in favour of a bond/interaction with the receiving support surface. Surface migration of hydrogen atoms may then occur via the surface hydroxyl (OH) groups of the oxidic support (Step III). Finally, spillover from the support to the metal oxide may occur (Step IV), followed by reduction (Step 3). Reduction via spillover competes with direct H_2 adsorption at active sites of the cobalt oxides which are depicted as two adjacent metal atoms with an O vacancy (i.e. a defect) between them (Step A).

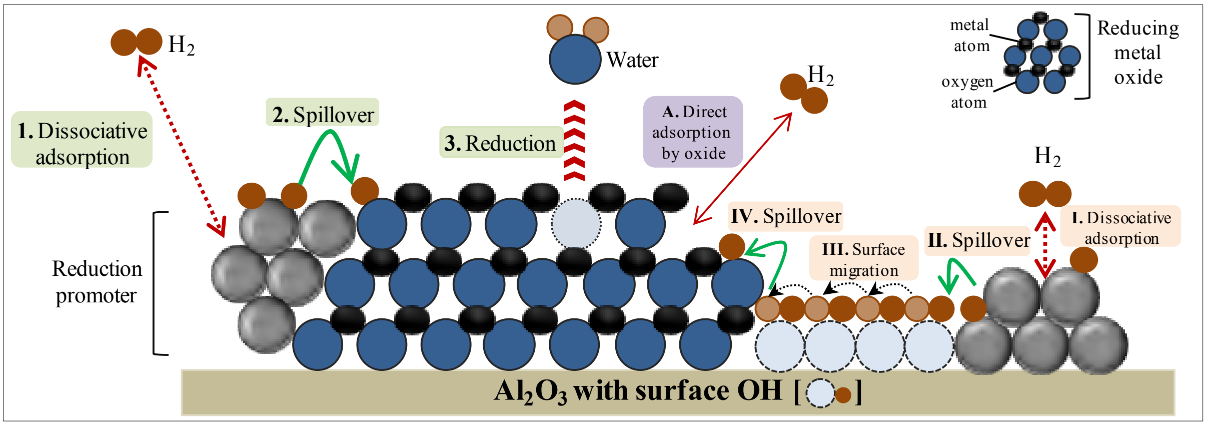

Scheme 2.4-1: Intrinsic stepsof spillover hydrogen during the promoter-aided reduction of a metal oxide. Adapted from Conner & Falconer [173] and Luo & Epling [222].

Besides reacting with reducible oxides, the spillover species may react with adsorbed molecules on the oxidic support such as coke in naphtha reforming catalysts [221] or with adsorbed species on the active metal such as CO_x intermediates during CH_3OH synthesis [209].

2.4.5 The 'Bucket-Brigade' model for surface migration of hydrogen on oxidic surfaces

The transfer of spillover hydrogen across the donor metal/support interface requires formation of different bonds. This is because the metal-H bond must break to allow spillover hydrogen to bond to other atoms such as O, Al, Si and Ti on the surface of the support. On the other hand, surface migration on oxidic surfaces that separate the hydrogen donor from the acceptor may occur via exchange of equivalent bonds in adjacent hydrogen-bonded hydroxyl groups (see Scheme 2.4-1). Migration distances for spillover hydrogen have been reported in the range of a few nanometres to several centimetres [178, 205, 210-212, 214, 223]. The mode of hydrogen movement across metals, oxidic surfaces, and even carbon surfaces is likely to differ due to chemically different surface atoms, which interact differently with the migrating hydrogen. The nature of this interaction, and the quantity of sites with which hydrogen can interact during migration is also expected to vary the speed of hydrogen transfer. The nature of the interaction between spillover hydrogen and various surfaces has been proposed to include van der Waals interactions [173], hydroxyl groups [28, 177, 178], and electronic interactions [176].

Surface diffusion of spillover hydrogen species reportedly involves interaction with surface oxygen atoms or hydroxyl groups on oxidic surfaces such as Al_2O_3, SiO_2, TiO_2, and zeolites. In fact, it has been suggested that hydrogen migrates by continuously forming and breaking adjacent OH bonds but this is unlikely because the energy barrier for this process would be too high [222]. A viable alternative explanation is the 'bucket-brigade' mechanism where surface OH groups do not migrate, but rather act as a bucket brigade by passing along spillover hydrogen species. The interactions with hydrogen are proposed to be weak H---OH bonds, which enable a process that has a much lower energy barrier and results in the fast rates of surface diffusion. The bucket-brigade model has been directly referred to, or inferred in a number of studies [173, 222, 224].

The bucket-brigade model of hydrogen transfer is shown in Scheme 2.4-2. The movement of hydrogen is analogous to the Grotthuss mechanism, which was first proposed by Theodor von Grotthuss [225] in a publication in 1806. The Grotthuss mechanism governs the unusually high proton mobility in water via a network of hydrogen bonds [226]. Spillover hydrogen (H_α) from the dissociating metal Me^I migrates to a secondary surface Me^{II} for reaction via a hydrogen-bonded network of OH groups on the surface of an oxidic support. On Al_2O_3, spillover hydrogen is transferred within a hydrogen-bonded network of surface OH groups. When H_α transfers from the dissociating metal surface Me^I onto an O atom in its vicinity, it is received and then passed in an on-going exchange of covalent and hydrogen bonds between neighbouring OH groups (OH_θ/ OH_ε/ OH_σ /OH_Ω) [173]. The spillover H_α does not physically migrate along the oxidic support to a secondary surface (Me^{II}) but rather triggers a knock-on effect, which causes the net displacement of hydrogen along the hydrogen-bonded chain of surface OH groups. When H_α crosses the metal-support interface to the closest surface OH group, the effect is that H_Ω, which is at the extreme end of the chain, is 'pushed' out of the network towards Me^{II}.

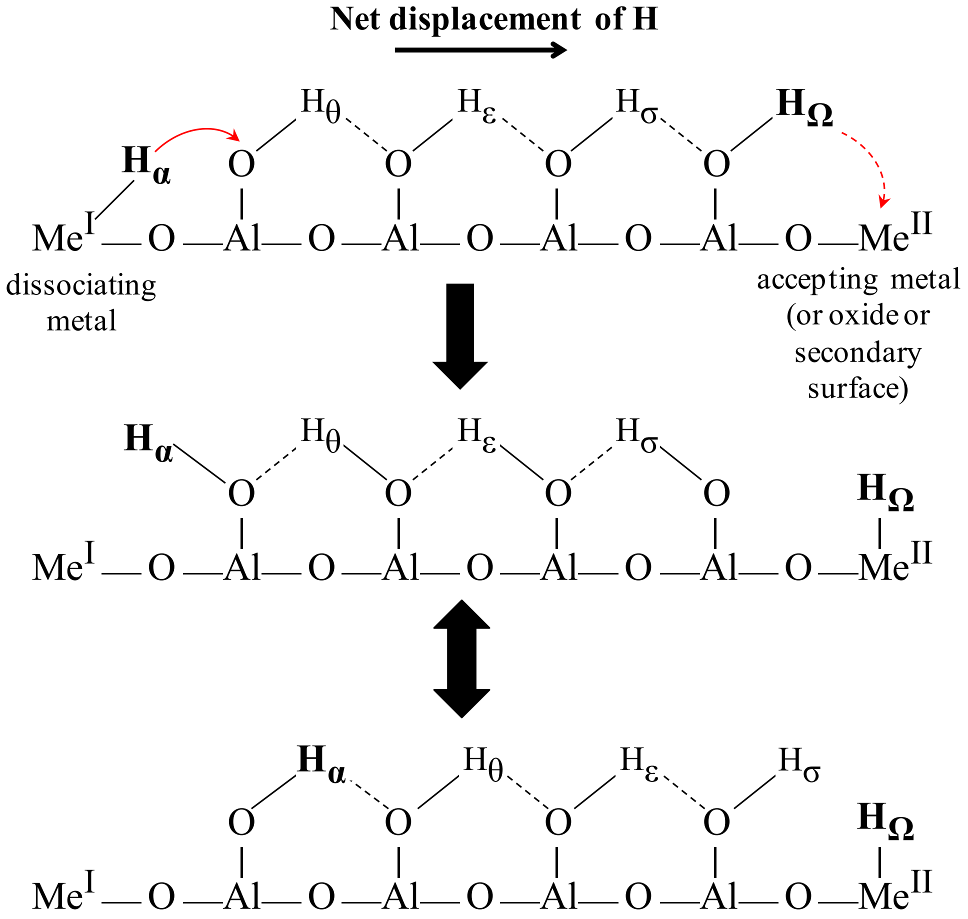

Scheme 2.4-2: Illustration of the surface migration of hydrogen according to the bucket-brigade model/Grotthuss-type mechanism. (—) = covalent bonds and other interactions; (- - -) = hydrogen bonding. Adapted from Carley et al. [224].

Mobility in this manner is high because it is the charge of H_α that is transferred, rather than its mass. Infrared analysis on oxidic surfaces has been used to observe hydrogen-bonded OH groups, which typically constitute just a fraction of the total surface hydroxyl groups [223, 227]. The work by Cevallos-Candau & Conner [223] indicates that these hydrogen-bonded OH groups are the primary pathways for spillover hydrogen. Therefore, it is plausible that only a small fraction of the total surface OH groups are used for spillover and that the surface of an oxidic support need not be saturated with OH groups to facilitate the migration of spillover hydrogen species.

Based on the bucket-brigade model, it is not surprising that water has been observed to accelerate the rate at which hydrogen species are transferred during a range of reactions including Co_3O_4 reduction in the Re-Co/Al_2O_3 system [143], NO_x reduction, WO_3 bronze formation and H_2-TPD [174, 176, 200-202, 222, 228]. It is likely that water participates in a dynamic equilibrium with surface OH groups, which causes them to remain on the oxidic surface in order to facilitate the transfer of spillover hydrogen. Movement via surface OH groups is supported by Baeza et al. [177] who found that the extent of spillover increased with the surface acidity (i.e. level of hydroxylation) and the surface iso-electric point (see Sec. 2.4.3.2 & Fig. 2.4-1). Baeza et al. proposed that OH groups stabilised the migrating hydrogen. During H_2-TPD experiments, Miller et al. [230] noted a parallel between surface OH groups on the various supports and the size of the desorption peak assigned to spillover hydrogen. Using catalysts composed of supported Pt on various oxides, they found that this peak diminished when consecutive TPD experiments were carried out and when the temperature of the reductive pre-treatment was increased. This was attributed to the irreversible loss of surface OH groups, which are required for stabilisation of spillover hydrogen species. Furthermore, the importance of surface OH groups was emphasized by the greater quantities of spillover hydrogen on acidic (i.e. more hydroxylated) versus non-acidic supports during HDS experiments [177, 211].

In contrast, during a H_2-TPD study on Pt/Al_2O_3, Kramer & Andre [175] concluded that hydroxyl groups were unimportant for the spillover of hydrogen, and suggested that surface defects, vacancies, or even surface Al atoms were required instead. This contradictory conclusion stemmed from the argument that if hydroxyl groups were responsible for spillover, then their absolute quantity would be expected to correlate with that of spilt over hydrogen. The authors determined a spilt over atomic hydrogen capacity of ca. $10^{12}cm^{-2}$, which was significantly lower than the typical number of hydroxyl groups on γ-Al_2O_3 ($10^{15}cm^{-2}$). It is not difficult to imagine that the number of hydroxyl groups on a surface would somewhat correlate with the quantity of spillover hydrogen it can transfer or hold. However, it may have been presumptuous for Kramer & Andre [175] to dismiss the role of hydroxyl groups on this basis based on the observations made by Cevallos-Candau & Conner [223]. Cevallos-Candau & Conner [223] found that only associated surface hydroxyls actively facilitated the surface migration of spillover hydrogen. These associated hydroxyls constitute a minor fraction of the total hydroxyl groups (1-10% on SiO_2) and are a better indication of the quantity of sites available to hydrogen.

2.4.6 Interfacial transfer of spillover hydrogen species

The bucket-brigade model provides an account of the migration of hydrogen over oxidic surfaces such as catalyst supports. However, before this transportation can occur, a very strong H-Metal bond must be broken to allow hydrogen species to spillover from the dissociating metal onto the oxidic support.

Due to the large binding energy between H and metal atoms, this interfacial transfer is energetically hindered and herein lays one of the root causes of scepticism associated with hydrogen spillover. Levy and Boudart [174] argued that since the adsorption energy between an H atom and metal is at least half that of gaseous H_2 dissociation, temperatures higher than 527°C would be required to remove atomic H from a metal such as Pt. Since the temperatures observed for hydrogen spillover are much lower, these authors stated that an alternative path must exist in which new bonds with the accepting surface are formed as the H-M bond is broken. The process suggested was formation of a *solvated proton* (on the metal) when a co-catalyst with a high proton affinity such as water abstracted the adsorbed hydrogen atom from the dissociating metal surface. This proton could then be easily transferred via a molecularly adsorbed co-catalyst monolayer to the site where it was required. Formation of the proton was determined to be exothermic and compensated for the energy required to break the H-M bond. Levy & Boudart [174] derived their deductions from a study involving the formation of H_xWO_3 bronzes in Pt/WO_3 catalysts in the presence of various co-catalysts whose proton affinities decreased as follows: H_2O>CH_3OH> C_2H_5OH>n-C_3H_7OH> n-C_4H_9OH>t-C_4H_9OH. The rate of bronze formation was found to increase with proton affinity, indicating a faster rate of abstraction of hydrogen from metal surfaces and thus their subsequent spillover.

The postulated importance of a co-catalyst is well illustrated by the difficulty in observing the effects of hydrogen spillover when experiments are carried out under conditions of very low water-partial pressure such as at temperatures > 500°C or at ultra-high vacuum. According to Benson et al. [200], the fast rates of WO_3 bronze formation when Pt/Al_2O_3 is present at room temperature, such as those reported by Khoobiar [182] and Kohn & Boudart [229] were only possible because the catalyst samples used were insufficiently dry or because water was (deliberately) added prior to the reaction. When samples were dried for long periods under Ultra High Vacuum (UHV), the effects of spillover during WO_3 bronze formation could not be reproduced. The latter case was attributed to loss of physisorbed water from the Al_2O_3 support surface, which resulted in severe inhibition of the migration of spillover hydrogen [200]. Benson et al. [200] reported that fast rates of WO_3 bronze formation required a monolayer of adsorbed H_2O and proposed that the rapid transportation of hydrogen occurred via transfer of an H atom between adjacent H_2O molecules to form H_3O or a similar hydrated species. It is suggested that water plays at least two roles during the spillover process, the first is stabilising surface OH groups via a dynamic equilibrium to facilitate movement along the support according to the bucket brigade model, and the second is acting as a co-catalyst to facilitate movement across the metal oxide interface.

Recently, Conradie et al. [178] used DFT calculations to determine that the driving force for hydrogen spillover was the difference in the energetic stability between adsorbed hydrogen on Rh(111) and the adsorbed hydrogen at low coverages on the TiO_2 support (rutile (001)) on which H had a higher adsorption energy. It must be noted that in this study, H was assumed to bond directly to an O atom coordinated to two Ti atoms instead of associating with an already existing OH group as implied by the bucket-brigade model (Scheme 2.4-2). The adsorption energy of H (relative to H_2 in the gas) on rutile (001) and coverages of 0.25ML to 1ML was determined in the range of -2.03 to -0.35eV, compared to -0.54 to -0.51eV on Rh(111). Based on the latter ranges, at high H coverages, the adsorption energy on (rutile (001) decreased below that of the metal, which then caused the driving force to reverse, and result in reverse spillover and recombination of H_2 on Rh.

Alternative pathways that might lead to interfacial spillover of hydrogen include: transfer of only weakly chemisorbed hydrogen atoms [231], 'jumpover' of activated hydrogen atoms via the gas phase [232] and 'bridges' at the metal-support interface [196, 230, 233, 234]. With regard to interfacial bridges, introduction of a layer of carbon (to form a carbon bridge) in the interstices of metal crystallites and the support has been shown to enhance the rate of hydrogen spillover to carbon supports and into metal-organic frameworks [196, 234]. Bridges may also be specific types of hydroxyl groups that are only present at the interface between metal crystallites and oxidic supports [201, 230, 233]. During H/D Temperature Programmed Exchange on SiO_2 and Ni/SiO_2, Cece & Gonzales [233] observed a type of OH group with a low O-H bond energy that was only present when SiO_2 was impregnated with Ni. The quantity of these OH groups increased with Ni dispersion (and therefore interstitial area) and they were theorised to correspond to OH groups that had been modified by interaction with Ni. These interfacial OH groups reportedly interacted with the Ni surface and the activation energy for their H/D exchange was only a third that of the bulk OH groups. These modified OH groups were postulated to be proton acceptors that could provide a low energy transfer of hydrogen from the Ni surface by abstracting protons and thus acting as a 'bridge' at the interface between Ni and the surface OH groups of the SiO_2 support.

2.4.7 The kinetics of hydrogen spillover

Both interfacial spillover and surface diffusion along the receiving oxidic surface have been proposed as the rate-limiting step for hydrogen transportation via surface migration. Diffusion along the donor metal surface itself is hardly ever considered rate limiting because of the high diffusion coefficients of hydrogen on metal surfaces in the range of 10^{-7} to $10^{-6}cm^2s^{-1}$, and the corresponding low activation energies in the range of 16kJ/mol to 25kJ/mol [173, 235, 236].

- **Surface diffusion as the slow step**

Consider the surface diffusion coefficients of atomic hydrogen on various oxidic supports in Table 2.4-1. The coefficients were obtained during studies of spillover from Pt to oxidic support surfaces in the context of various reactions. The coefficients in Table 2.4-1 are significantly low in contrast to the fast surface diffusion on metal surfaces and it is thus not surprising that Kramer & Andre [175] considered surface diffusion on the oxidic support to be rate limiting.

Table 2.4-1: Surface diffusion coefficients determined for hydrogen migration along various oxidic surfaces. Adapted from Conner & Falconer [173].

Reference	**Reaction**	**Pathway/surface**	**Temperature, °C**	**Surface diffusion coefficient, $cm^2 \cdot s^{-1}$**
Kramer & Andre [175]	H_2-TPD	Pt or Ni → **Al_2O_3**	400	10^{-15} (Ea = 120kJ·mol^{-1})
Fleisch & Abermann [245]	Reduction of Ag_2S	Pt → **SiO_2**, Pt → **C**	100-200	10^{-14} to 10^{-11} (Ea = 65kJ·mol^{-1})
Dmitriev et al. [239]	H/D exchange	Pt → **Y-zeolites**	200	10^{-6}
Carley et al. [224]	H/D exchange	Pt/Al_2O_3 → **SiO_2**	205	10^{-5}-10^{-4}
Neikam & Vannice [196]	H_2 adsorption	Pt → **Ce-Y zeolite**	140	10^{-10}

- **Interfacial spillover as the slow step**

Proponents of interfacial spillover as the slow step argue that breaking a strong M-H bond in favour of a weaker bond with a support is unlikely to be exothermic but rather a highly activated endothermic or energetically neutral process [173, 240]. In support of a slow interfacial spillover step across the donor metal periphery and not surface diffusion on the receiving oxidic surface, Cevallos-Candau & Conner [223] developed a technique illustrated in Figure 2.4-3. The novelty of the technique was that it allowed a decoupling of the interfacial spillover step from the surface diffusion on a SiO_2 surface, which had not been done in other studies in which kinetic parameters were determined such as those in Table 2.4-1.

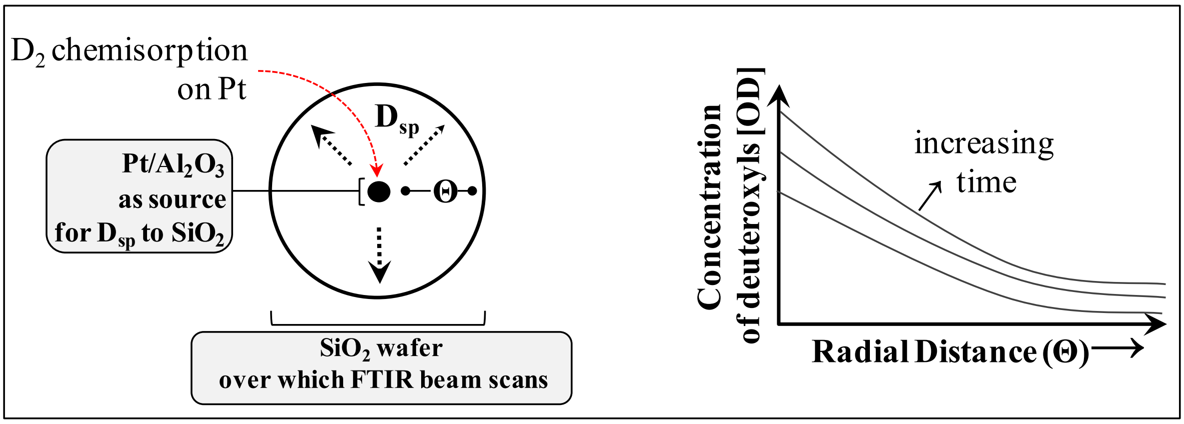

Figure 2.4-3: Schematic of experiment showing <1mm 'spot' of Pt/Al_2O_3 in centre of a 25.4mm SiO_2 wafer over which FTIR beam was scanned. On the right is the increase in concentration of OD as measured by IR over time and position. D_{sp} = spillover deuterium [223].

Infrared spectroscopy was used to monitor deuterium movement from an isolated 1mm point source of Pt/Al_2O_3 in the centre of a 25.4mm circular SiO_2 wafer during H/D exchange. Infrared spectra could be collected at various radial distances from the Pt/Al_2O_3 source, but strictly along the SiO_2 wafer, which was the receiving surface for deuterium spillover species (Fig. 2.4-3).

From the IR analysis, two kinds of OH and OD groups were identified on the SiO_2 surface at $3755cm^{-1}$ and $2755cm^{-1}$ respectively. The sharp portion of the peaks at each frequency was attributed to isolated OH and OD groups, while the shoulder at slightly lower frequencies was assigned to associated (hydrogen-bonded) OH or OD groups. During H/D exchange, substitution of the isolated OH groups with deuterium increased slowly, but proportionally with time and never reached saturation. On the other hand, deuterium substitution of the associated OH not only proceeded at a faster rate but also quickly reached saturation coverage and began to slow down. The authors explained that only the associated OH groups, which made up only 1-10% of the total OH groups on SiO_2, were actually readily available for the transport of spillover hydrogen species. Only when these co-ordinated OH groups approached saturation did they slowly begin to exchange deuterium with their free/non-associated OH neighbours as an effect of dilution.

In the described manner, Candau-Cevallos & Conner [223] determined surface diffusion coefficients on the oxide support that were actually 10^9 higher than other studies (values from other studies shown in Table 2.4-1). Even though the coefficients in the studies in Table 2.4-1 were obtained during spillover from Pt to oxidic supports, the kinetics of the interfacial spillover step were not decoupled from those of surface migration across the oxidic surface, which according to Candau-Cevallos & Conner [223] negatively affected the overall surface diffusion coefficients.

With regard to the rate-limiting step, it is important to consider the conditions under which kinetic parameters were determined in order to gauge their accuracy, especially in light of the broad range of surface diffusion coefficients reported for the same surfaces in Table 2.4-1. For example, Candau-Cevallos & Conner [223] noted that the H/D exchange proceeded so fast when the catalyst samples were not dry such that a concentration gradient with increasing distance from the spillover source could not be measured as depicted in Figure 2.4-3. To obtain kinetic parameters, the samples were dried to drop the water partial pressure to $<10^{-5}$ Torr. 10^{-5} Torr had been determined as the threshold value below which atmospheric water had no effect as a co-catalyst for spillover as asserted by Levy & Boudart [174] (refer to co-catalysts in Sec. 2.4.6). Another example of the effect of the reaction conditions on kinetic parameters is that by Kramer and Andre [175] who used H_2-TPD analyses on different Pt/Al_2O_3 catalysts to study spillover. Kramer and Andre [175] determined a very small surface diffusion coefficient of $10^{-15} cm^2 \cdot s^{-1}$ on Al_2O_3 and thus deduced surface diffusion as the slow step. However, in that study, catalyst pretreatment prior to the TPD was carried out at 550°C, which would have led to substantial dehydroxylation of the Al_2O_3 support surface [227, 238]. This was likely to have hindered the surface migration on Al_2O_3 as specified by the bucket-brigade model in Section 2.4.5. It is therefore plausible that the authors could have obtained kinetic parameters that were more favourable to surface diffusion if pre-treatment had been carried out at a lower temperature since the Al_2O_3 surface would have been more hydroxylated.

Finally, it must be cautioned that some studies, including those in Table 2.4-1, have determined spillover parameters in the context of more complex reactions such as the reduction of oxides/sulphides. For studies other than those involving H/D exchange (a simple reaction), other possible rate limiting steps such as desorption of products like H_2O and H_2S during reduction must be eliminated to get more representative kinetic parameters [223]. Even parameters determined during H/D exchange are not strictly independent as they may vary with the donor metal's affinity for hydrogen activation. An example is Pt on which Hydrogen dissociation is a fast compared to less active metals like Ni with which the rate of

H/D exchange has been observed to vary with dispersion and metal loading [233]. Ultimately, the measured kinetics of hydrogen spillover may also include the donor metal's affinity for H_2 activation.

2.4.8 Some counter arguments to hydrogen spillover in catalytic reactions

In spite of the extensive evidence in support of surface mobility of reactive species such as hydrogen, some caution must be exercised before inferring spillover because the majority of deductions are based on experimental results rather than direct spectroscopic observation of the migrating species (see Sec. 2.4.1).

- **Metal atom migration**

The observations attributed to the actions of spillover hydrogen during analyses that involve the use of physically mixed 'hybrid' catalysts in order to separate the catalytically active components have also been attributed to physical migration of the metal containing components especially if present as a carbonyl, nitrate, chloride or oxide [222, 241].

During the reduction of iron oxide in physical mixtures of Fe_2O_3+noble metals supported on zeolites, Lebedeva et al. [241] reported that the enhancement in Fe_2O_3 reduction was not due to the migration of spillover hydrogen species but rather to migration of the unreduced form of the noble metal. Enhancement in the reduction of Fe_2O_3 was only observed after thorough grinding and high temperature calcination (>500°C) of the hybrid catalysts, and was consequently attributed to the direct contact with the migrated noble metal clusters. Using TEM and EDX, RhO and PtO_2 clusters were shown to migrate out of the zeolite structure onto the Fe_2O_3, thereby enhancing metallic iron formation. The observations of Lebedeva et al. [241] demand for a more thorough examination of previous studies on hybrid catalysts in which spillover was deduced at high temperatures due to the probability of migration of active components.

- **The H/D Exchange reaction via other pathways**

A strong argument against spillover is specific to the numerous H/D exchange experiments in which it is deduced that H/D exchange only occurs due to deuterium spillover from the metal, followed by migration along an oxidic support [223, 233, 239, 242]. Consequently, the appearance of OD groups to the detriment of OH groups is used to deduce the occurrence of surface migration of hydrogen. Apparently, this is not strictly the case as H/D exchange can also occur by proton exchange between neighbouring M-H/M-D, OH and OD groups without the net transport of hydrogen [242]. Following chemisorption of deuterium, protonic exchange between M-D and a periphery OH group of a support can occur to form M-H and a periphery OD group in a manner akin to dilution, which does not result in net proton transfer from the metal surface [242]. This alternative pathway for H/D exchange however does not necessarily disprove spillover but rather provides an alternative explanation for the appearance of OD groups on oxidic surfaces to the detriment of OH groups.

2.5 Consolidation

Despite the aforementioned counter arguments, the wealth of experimental and spectroscopic literature that exists even beyond the select studies covered in this literature review strongly indicates that spillover hydrogen may play an important role in Fischer-Tropsch catalysis. Hydrogen spillover has already been invoked as the mechanism by which reduction promoters such as Pt and Au improve the reducibility of cobalt-based Fischer-Tropsch catalysts, and some studies have suggested that action of spillover hydrogen species may result in synergistic effects on the catalyst activity and increase the extent of hydrogenation in the product distribution. However, a gap in the literature exists because no rigorous study of the contribution of spillover hydrogen during reduction and under commercial Fischer-Tropsch conditions has so far been found. The promoted Fischer-Tropsch catalyst is a complex, multi-component system involving cobalt, noble metal promoters, and oxidic supports, and this literature review suggests that understanding the interaction of spillover hydrogen with the chemically different catalyst constituents may aid future catalyst design.

2.6 References

[1] M. Claeys, E. van Steen, Stud. Surf. Sci. Catal 152 (2004) 601-680.

[2] D.J. Moodley, “On the Deactivation of Cobalt-based Fischer-Tropsch Synthesis Catalysts”, PhD Thesis, Eindhoven University of Technology, The Netherlands, 2008.

[3] F. Fischer, H. Tropsch, Brennstoff-Chem. 7 (1926) 97-104.

[4] P.M. Maitlis, Pure Appl. Chem. 61 (1989) 1747-1754.

[5] P.M. Maitlis, H. Long, R. Quyoum, M. Turner, Z.-Q. Whang, J. Chem. Soc. Chem. Comm. 1 (1996) 1-8.

[6] P.M. Maitlis, R. Quyoum, H. Long, M. Turner, Appl. Catal. A: Gen. 186 (1999) 363-374.

[7] H. Storch, N. Golumbic, R. Anderson (Eds.), The Fischer-Tropsch and Related Synthesis, John Wiley and Sons, New York, 1951.

[8] K.G. Anderson, J.G Ekerdt, J. Catal. 95 (1985) 602-604.

[9] M.E. Dry, Catal. Today 6 (1990) 183-206.

[10] J. Hindermann, G. Hutchings, A. Kiennemann, Cat. Rev. Sci. Eng. 35 (1993)1-127.

[11] A. Sternberg, J. Wender, in: Proc. Intern. Conf. Coord. Chem. London, The Chemical Society, 1959.

[12] S. Roginski, in: Proceedings of 3rd Congr. on Catal.: Amsterdam, 1965, 939-943.

[13] H. Pichler, H. Schulz, Chem.-Ing. Techn. 42 (1970) 1162-1174.

[14] H. Schulz, M.Claeys, Appl. Catal. A: Gen. 186 (1999) 91-107.

[15] R.J. Madon, S.C. Reyes, E. Iglesia, J. Phys. Chem. 95 (1991) 7795-7804.

[16] E. Iglesia, S.C. Reyes, R.J. Madon, J. Catal., 129 (1991) 238-256.

[17] R.J. Dogterom, R.M. van Hardeveld, M.J. Reynhout, B.A. van de Werff, Shell Internationale Research Maatschappij B.V., US Patent 11/793,671 (2005).

[18] R.J. Dogterom, M. Reynhout, Shell Internationale Research Maatschappij B.V., U.S. Pat. Appl. 10/573,795 (2004).

[19] McEwan, Senden. "The Shell Middle Distillate Synthesis (SMDS) Experience." In 16th World Petroleum Congress. World Petroleum Congress, 2000.

[20] E.J. Creyghton, C.M.A.M. Mesters, M.J. Reynhout, G.L.M.M. Verbist, Shell Internationale Research Maatschappij B.V., U.S. Pat. Appl. 11/954,346 (2007).

[21] M.F.M. Post, S.T. Sie, European Pat. Appl., 0 167 215 A2 (1986).

[22] H. Heetveld, S.A. Posthuma, H.M.H Wechem, U.S. Patent 5 486 542 (1996).

[23] R. Oukaci, A.H. Singleton, J.G. Goodwin Jr. Appl. Catal. A: Gen. 186 (1999) 129-144.

[24] J.L. Visagie, H.M. Veltman, Sasol Technology (Proprietary) Limited, Pat. Appl. PCT/IB2005/054375 (2005).

[25] P.J. van Berge, J. van de Loosdrecht, J.L. Visagie, Sasol Technology (Proprietary) Limited, US Pat. Appl. US 10/159,970 (2002).

[26] M.E. Dry, Catal. Today 71 (2002) 227-241.

[27] F.G. Botes, B. van Dyk, C. McGregor, Ind. Eng. Chem. Res., 48 (2009) 10439-10447.

[28] S.K. Beaumont, S. Alayoglu, C. Specht, W.D. Michalak, V.V. Pushkarev, J. Guo, N. Kruse, G.A. Somorjai, J. Am. Chem. Soc. 136 (2014) 9898-9901.

[29] C.G. Visconti, E. Tronconi, L. Lietti, R. Zennaro, P. Forzatti, Chem. Eng. Sci. 62 (2007) 5338-5343.

[30] I.C. Yates, C.N. Satterfield, Energy Fuels 5(1991)168-173.

[31] A.I.O. Rautavuow, H.S. van der Baan, Appl. Cat. A: Gen 1(1981) 247-272.

[32] B. Sarup, B.W. Wojciechowski, Can. J. Chem. Eng. 67 (1989) 62-74.

[33] E. van Steen, H. Schulz, Appl. Catal. A: Gen. 186 (1999) 309-320.

[34] M.A. Vannice, Catalysis Reviews—Science and Engineering, 14 (1976) 153-191.

[35] G.A. Jr Huff, C.N. Satterfield, Ind. Eng. Chem., Process Des. Dev. 23 (1984) 696-705.

[36] R. Zennaro, M. Tagliabue, C. H. Bartholomew, Catal. Today 58 (2000) 309–319.

[37] R.B. Anderson, in: P.H. Emmett (Ed.), Catalysis, Vol. 4, Reinhold, New York, 1956, 257-283.

[38] J. Lahtinen, T. Anraku, G.A. Somorjai, Catal. Lett. 25 (1994) 241-255.

[39] M. Ojeda, R. Nabar, A.U. Nilekar, A. Ishikawa, M. Mavrikakis, E. Iglesia, J. Catal. 272 (2010) 287-297.

[40] H. Schulz, M. Claeys, S. Harms, Stud. Surf. Sci. Catal. 107 (1997) 193-200.

[41] A.M. Saib, D.J. Moodley, I.M. Ciobîca, M.M. Hauman, B.H. Sigwebela, C.J. Weststrate, J.W. Niemantsverdriet, J. van de Loosdrecht, Catal. Today 154 (2010) 271-282.

[42] Z.-J. Wang, S. Skiles, F. Yang, Z. Yan, D.W. Goodman, Catal. Today 181(2012)75-81.

[43] S.L. Soled, E. Iglesia, R.A. Fiato, J. E. Baumgartner, H. Vroman, S.Miseo, Top. Catal. 26 (2003) 101-109.

[44] E. Iglesia, S. Reyes, R. Madon, S. Soled, Adv. Catal. 39 (1993) 221-302.

[45] E. Iglesia, Appl. Catal. A: Gen. 161 (1997) 59-78.

[46] G. Haddad, B. Chen, J.G. Goodwin, J. Catal. 161 (1996) 274-281.

[47] M. Rothaemel, K.F. Hanssen, E.A. Blekkan, D. Schanke, A. Holmen, Catal. Today 38 (1997) 79-84.

[48] F. Rohr, O.A. Lindvag, A. Holmen, E.A. Blekkan, Catal. Today 58 (2000) 247-254.

[49] J. P. den Breejen, P. B. Radstake, G. L. Bezemer, J. H. Bitter, V. Frøseth, A. Holmen, K.P. de Jong, J. Am. Chem. Soc. 131 (2009) 7197–7203.

[50] R.C. Reuel, C.H.Bartholomew, J. Catal. 85 (1984) 78-88.

[51] A.S. Lermontov, J.-S. Girardon, A. Griboval-Constant, S. Pietrzyk, A.Y. Khodakov, Catal. Lett. 101 (2005) 117-126.

[52] G.L. Bezemer, U. Falke, A.J. van Dillen, K.P. de Jong, Chem. Commun. 6 (2005) 731-733.

[53] A.S. Lisitsyn, A.V. Golovin, V.L. Kuznetsov, Y.I. Yermakov, J. Catal. 95 (1985) 527-538.

[54] G. L. Bezemer, J.H. Bitter, H.P. Kuipers, H. Oosterbeek, J.E. Holewijn, X. Xu, , F. Kapteijn, A. J. van Dillen, K.P. de Jong, J. Am. Chem. Soc. 128 (2006) 3956-3964.

[55] P.B. Radstake, J.P. den Breejen, G.L. Bezemer, J.H. Bitter, K.P. de Jong, V. Frøseth, A. Holmen, Stud. Surf. Sci. Catal. 167 (2007) 85-90.

[56] E. van Steen, M. Claeys, M. E. Dry, J. van de Loosdrecht, E.L. Viljoen, J. L.Visagie,. J. Phys. Chem. B 109 (2005) 3575-3577.

[57] A.Y. Khodakov, Catal. Today 144 (2009) 251-257.

[58] Ø. Borg, S. Eri, E. A. Blekkan, S. Storsæter, H.Wigum, E. Rytter, A. Holmen, J. Catal. 248 (2007) 89-100.

[59] G. Jacobs, Y. Ji, B.H. Davis, D. Cronauer, A.J. Kropf, C.L. Marshall, Appl. Catal. A: Gen. 333 (2007) 177-191.

[60] W. Chu, P. A. Chernavskii, L. Gengembre, G. A. Pankina, P. Fongarland, A. Y. Khodakov, J. Catal. 252 (2007) 215-230.

[61] J. Wilson, C. de Groot, J. Phys. Chem. 99 (1995) 7860-7866.

[62] N. Fischer, "Preparation of nano and Angstrom sized cobalt ensembles and their performance in the Fischer-Tropsch synthesis", PhD Thesis, University of Cape Town, South Africa, 2011.

[63] H. Schulz, Appl. Catal. A: Gen. 186 (1999) 3-12.

[64] J. van de Loosdrecht, B. Balzhinimaev, J.A. Dalmon, J.W. Niemantsverdriet, S.V. Tsybulya, A.M. Saib, P.J. van Berge, J.L. Visagie, Catal. Today 123 (2007) 293-302.

[65] N.E. Tsakoumis, M. Rønning, Ø. Borg, E. Rytter, A. Holmen, Catal. Today 154 (2010) 162-182.

[66] P.J. van Berge, R.C. Everson, Stud. Surf. Sci. Catal. 107 (1997) 207-212.

[67] A.Y. Khodakov, W. Chu, P. Fongarland, Chem. Rev. 107 (2007) 1692-1744.

[68] C. H. Bartholomew, R. M. Bowman, Appl. Catal. 15 (1985) 59-67.

[69] A. L. Chaffee, I. Campbell, N. Valentine, Appl. Catal. 47 (1989) 253-276.

[70] M.J. van der Burgt, J. van Klinken, S.T. Sie, in: Proc. Synfuels Worldwide Symp., Washington, DC, 11-13 November, 1985.

[71] M.E. Dry, in: J.R. Anderson, M. Boudart (Eds.), Catalysis - Science and Technology, Springer, Berlin, 1, 1981, 159-255.

[72] C.H. Bartholomew, Appl. Catal. A: Gen. 212 (2001)17-60.

[73] M.J. Jr D'Aniello, D.R. Monroe, C.J. Carr, M.H. Krueger, J. Catal. 109 (1988) 407-422.

[74] S. Eri, J.G. Jr Goodwin, G. Marcelin, T. Riis, U.S. Patent, 4,880,763 (1989).

[75] J. Gaube, H.F. Klein, Appl. Catal: A Gen. 350 (2008) 126-132.

[76] C.A. Welker, “Ruthenium based Fischer-Tropsch Synthesis on Crystallites and Clusters of Different Sizes”, PhD Thesis, University of Cape Town, South Africa, 2007.

[77] G. Jacobs, P.M. Patterson, T.K. Das, M. Luo, B.H. Davis, Appl. Catal. A: Gen. 270 (2004) 65-76.

[78] A.M. Hilmen, D. Schanke, K.F. Hanssen, A. Holmen, Appl. Catal. A: Gen. 186 (1999) 169-188.

[79] S. Storsæter, Ø. Borg, E.A. Blekkan, A. Holmen, J.Catal. 231 (2005) 405-419.

[80] P.J. van Berge, J. van de Loosdrecht, J. Barradas, A. M. van der Kraan, Catal. Today 58 (2000) 321-34.

[81] P.J. van Berge, J. van de Loosdrecht, E. Caricato, S. Barradas, B.H. Sigwebela, United States Patent 6,455,462 (2002).

[82] M.J. Overett, B. Breedt, E. du Plessis, W. Erasmus, J. van de Loosdrecht, Prep. Pap. Am. Chem. Soc., Div. Petrol. Chem. 53 (2008) 126 -128.

[83] H. Karaca, J. Hong, P. Fongarland, P. Roussel, A. Griboval-Constant, M. Lacroix, K. Hortmann, O. V. Safonova, A. Y. Khodakov, Chem. Commun. 46 (2010) 788-790.

[84] J.A. Moulijn, A.E. van Diepen, F. Kapteijn. Appl. Catal. A: Gen. 212 (2001) 3-16.

[85] G.Z. Bian, N. Fujishita, T. Mochizuki, W. S. Ning, M. Yamada, Appl. Catal. A: Gen. 252 (2003) 251-260.

[86] D.J. Moodley, J. van de Loosdrecht, A.M. Saib, M.J. Overett, A.K. Datye, J. W. Niemantsverdriet, Appl. Catal. A: Gen. 354 (2009) 102-110.

[87] E. Iglesia, S.L. Soled, R.A. Fiato, G.H. Via, J. Catal. 143 (1993) 345-368.

[88] M.K. Niemela, A.O.I. Krause, Catal. Lett. 42 (1996) 161-166.

[89] H.W. Pennline, S.S. Pollack, Ind. Eng. Chem. Prod. Res. Dev. 25 (1986) 11-14.

[90] T. Jermwongratanachai, G. Jacobs, W.D. Shafer, V. R. R. Pendyala, W. Ma, M. K. Gnanamani, S. Hopps, G. A. Thomas, B. Kitiyanan, S. Khalid, B. H. Davis, Catal. Today 228 (2014) 15-21.

[91] G. Jacobs, T.K. Das, Y. Zhang, J. Li, G. Racoillet, B. H. Davis, Appl. Catal. A: Gen. 233 (2002) 263-281.

[92] A.Y. Khodakov, A. Griboval-Constant, R. Bechara, F. Villain, J. Phys. Chem. B 105 (2001) 9805-9811.

[93] A.Y. Khodakov, J. Lynch, D. Bazin, B. Rebours, N. Zanier, B. Moisson, P. Chaumette. J. Catal. 168 (1997) 16-25.

[94] Y. Zhang, D. Wei, S. Hammache, J. G. Jr Goodwin, J. Catal. 188 (1999) 281-290.

[95] S. Sun, K. Fujimoto, Y. Yoneyama, N. Tsubaki, Fuel 81 (2002) 1583-1591.

[96] M. P. Rosynek, C. A. Polansky, Appl. Catal. 73 (1991) 97-112.

[97] N. Tsubaki, S. Sun, K. Fujimoto, J. Catal. 199 (2001) 236-246.

[98] F. Diehl, A. Y. Khodakov, Oil Gas Sci. Technol.- Rev. IFP 64 (2009) 11-24.

[99] W. Ma, G. Jacobs, D.E. Sparks, M. K. Gnanamani, V. R. R. Pendyala, C. H. Yen, J.L.S. Klettlinger, T.M. Tomsik, B.H. Davis, Fuel 90 (2011) 756-765.

[100] F. Morales, B.M. Weckhuysen, Catalysis 19 (2006) 1-40.

[101] G. Jacobs, P.M. Patterson, Y. Zhang, T. Das, J. Li, B.H. Davis, Appl. Catal. A: Gen. 233 (2002) 215-226.

[102] S. Vada, A. Hoff, E. Ådnanes, D. Schanke, A. Holmen. Top. Catal. 2 (1995) 155-162.

[103] D. Schanke, S. Vada, E. A. Blekkan, A. M. Hilmen, A. Hoff, A. Holmen. J. Catal. 156 (1995) 85-95.

[104] S. Sun, N. Tsubaki, K. Fujimoto, Chem. Lett. 2 (2000) 176-177.

[105] G. Jacobs, T.K. Das, P.M. Patterson, J. Li, L. Sanchez, B.H. Davis, Appl. Catal. A: Gen. 247 (2003) 335-343.

[106] P. Arnoldy, J. A. Moulijn, J. Catal. 9 (1985) 38-54.

[107] R. L. Chin, D.M. Hercules, J. Phys. Chem. 86 (1982) 360-367.

[108] C.H. Bartholomew, R.C. Reuel, Ind. Eng. Chem. Prod. Res. Dev. 24 (1985) 56-61.

[109] W.-J. Wang, Y.-W. Chen. Appl. Catal. 77 (1991) 223-233.

[110] L. Ji, J. Lin, H. C. Zeng, J. Phys. Chem. B 104 (2000) 1783-1790.

[111] D. Potoczna-Petru, L. Kepinski. Catal. Lett. 73 (2001) 41-46.

[112] R.Ward, E. D Boyes, P. L. Gai, J. Phys.: Conf. Ser. 522 (2014) 012009.

[113] A. Lapidus, A. Krylova, V. Kazanskii, V. Borovkov, A. Zaitsev, J. Rathousky, A. Zukal, M. Jancalkova, Appl. Catal. 73 (1991) 65-81.

[114] H. Karaca , O.V. Safonova, S. Chambre, P. Fongarland, P. Roussel, A. Griboval-Constant, M. Lacroix, A.Y. Khodakov, J. Catal. 277 (2011) 14-26.

[115] G. Jacobs, M. C. Ribeiro, W. Ma, Y. Ji, S. Khalid, P. T. Sumodjo, B. H. Davis, Appl. Catal. A: Gen. 361 (2009) 137-151.

[116] G. Jacobs, J.A. Chaney, P. M. Patterson, T. K. Das, J. C. Maillot, B.H. Davis, J. Synchrotron Rad. 11 (2004) 414-422.

[117] B. Ernst, A. Bensaddik, L. Hilaire, P. Chaumette, A. Kiennemann, Catal. Today 39 (1998) 329-341.

[118] A.M. Saib, A. Borgna, J. van de Loosdrecht, P.J van Berge, J.W. Niemantsverdriet, Appl. Catal. A: Gen. 312 (2006) 12-19.

[119] J. S. Girardon, A. Constant-Griboval, L. Gengembre, P.A. Chernavskii, A.Y. Khodakov, Catal. Today 106 (2005) 161-165.

[120] B. Clapham, "The Development of an In-Situ X-Ray Diffraction Cell for Fischer-Tropsch Catalyst Characterisation", Masters' Thesis, University of Cape Town, South Africa, 2012.

[121] J.T. Richardson, L.W. Vernon, J. Phys. Chem. 62 (1958) 1153-1157.

[122] J.A. Rodriguez, J.Y. Kim, J.C. Hanson, M. Perez, A.I. Frenkel, Catal. Lett. 8 (2003) 247-254.

[123] B. Jankovic. J. Phys. Chem. Solids 68 (2007) 2233-2246

[124] R.P. Furstenau, G. McDougall, M.A. Langell, Surf. Sci. 150 (1985) 55-79;

[125] B. Delmon, in: G. Ertl, H. Knozinger and J.Weitkamp (Eds.), Handbook of Heterogeneous Catalysis, VCH-Wiley, New York, 1997, 264.

[126] J. Wimmers, P. Arnoldy, J.A. Moulijn. J. Phys. Chem. 90 (1986) 1331-1337.

[127] A. Auroux (Ed.), Calorimetry and Thermal Methods in Catalysis, Vol. 154 of Springer Series in Materials Science, Springer-Verlag Berlin, Heidelberg, 2013.

[128] J.A. Rodriguez, J.C. Hanson, A.I. Frenkel, J.Y. Kim, M. Pérez, J. Am. Chem. Soc. 124 (2002) 346-354.

[129] T. Ressler, R.E. Jentoft, J.Wienold, M.M.Günter, O. Timpe, J. Phys. Chem. B, 104 (2000) 6360-6370.

[130] P. Arnoldy, J.C.M. de Jonge, J.A. Moulijn, J. Phys. Chem. 89 (1985) 4517-4526.

[131] J. Sloczynski, J. Solid State Chem. 118 (1995) 84-92.

[132] J. Sloczynski, W.J. Bobinski, J. Solid State Chem. 92 (1991)420-435.

[133] Y. Koga, L.G. Harrison, in: C.H. Bamford, C.F.H. Tipper, R.G. Compton (Eds.), Comprehensive Chemical Kinetics, Vol. 21, Elsevier, Amsterdam, 1984, 120.

[134] C.T. Williams, E.K.-Y. Chen, C.G. Takoudis, M.J. Weaver. J. Phys. Chem. B, 102 (1998) 4785-4794.

[135] J.Y. Kim, J.A. Rodriguez, J.C. Hanson, A.I.Frenkel, P. L. Lee. J. Am. Chem. Soc. 125 (2003) 10684-10692.

[136] J.T. Richardson, R. Scates, M.V. Twigg, Appl. Catal. A: Gen. 246 (2003) 137-150.

[137] T.J. Ressler, Phys. Chem. B 106 (2002) 7719-7720.

[138] G. E. Batley, A. Ekstrom, D.A. Johnson, J. Catal. 34 (1974) 368-375.

[139] K. Takeuchi, T. Matsuzaki, H. Arakawa, T. Hanaoka, Y. Sugi, Appl. Catal. 48 (1989) 149-157.

[140] M. Reinikainen, M.K. Niemelä, N. Kakuta, S. Suhonen, Appl. Catal. A: Gen. 174 (1998) 61-75.

[141] D. Bazin, L. Borko, Z. Koppány, I. Kovacs, G. Stefler, L.I. Sajo, Z. Schay, L. Guczi, Catal. Lett. 84 (2002) 169-182.

[142] A. Kogelbauer, J.G. Jr Goodwin, R.Oukaci, J.Catal. 160 (1996) 125-133.

[143] A.M. Hilmen, D. Schanke, A. Holmen, Catal. Lett. 38 (1996) 143-147.

[144] G. Jacobs , J. A. Chaney, P. M. Patterson,T.K. Das, B. H. Davis, Appl. Catal. A: Gen. 264 (2004) 203-212.

[145] W. Ma, G. Jacobs, R. Keogh, D.B. Bukur, B. H. Davis. Appl. Catal. A: Gen. 437 (2012) 1-9.

[146] L.Guczi, D. Bazin, I. Kovacs, L. Borko, Z. Schay, J. Lynch, P.Parent, C. Lafon, G. Stefler, Z. Koppany, I. Sajo, Top. Catal. 20 (2002) 129-139.

[147] M.D. Shannon, C.M. Lok, J.L. Casci, J. Catal. 249 (2007) 41-51.

[148] T.K. Das, G. Jacobs, B.H. Davis, Catal. Lett. 101 (2005) 187-190.

[149] J. Hong, P.A.Chernavskii, A.Y. Khodakov, W. Chu, Catal. Today, 140 (2009) 135-141.

[150] B. Jongsomjit, J. Panpranot, J.G. Jr Goodwin, J. Catal. 204 (2001) 98-109.

[151] L. Guczi, L. Borkó, Z. Schay, D. Bazin, F. Mizukami Catal. Today 65 (2001) 51-57.

[152] L. Guczi, Z. Schay, G. Stefler, F. Mizukami J. Mol. Catal. A-Chem. 141 (1999) 177-185.

[153] D. Xu, W. Li, H. Duan, Q. Ge, H. Xu, Catal. Lett. 102 (2005) 229-235.

[154] G. S. van Wyk, "The Effect of Copper as a Chemical Promoter on the Performance of a Cobalt-based Fischer-Tropsch Synthesis Catalyst", Masters' Thesis, University of Cape Town, South Africa, 2000.

[155] H. Wang, H. Zhu, Z. Qin, G. Wang, F. Liang, J. Wang: Catal. Commun. 9 (2008) 1487-1492.

[156] L. Leite, V. Stonkus, L. Ilieva, L. Plyasova, T. Tabakova, D. Andreeva, E. Lukevics. Catal. Commun. 3 (2002) 341-347.

[157] G.J. Hutchings, M. Haruta, Appl. Catal. A: Gen. 291 (2005) 2-5.

[158] P. Claus, Appl. Catal. A: Gen. 291 (2005) 222-229.

[159] L. Stobinski, R. Dus, Czech J. Phys. 43 (1993) 1035-1040.

[160] L. Stobinski, R. Dus, Vacuum 45 (1994) 299-301.

[161] G. Bond, C. Louis, D.T. Thompson (Eds.), Catalysis by Gold, Catalytic Science Series-Vol. 6. Imperial College Press, London, 2006.

[162] P. Landon, P. J. Collier, A.J. Papworth, C.J. Kiely, G.J. Hutchings, Chem. Commun. 18 (2002) 2058-2059.

[163] T. Ishihara, Y. Ohura, S. Yoshida, Y. Hata, H. Nishiguchi, Y. Takita, Appl. Catal. A: Gen. 291 (2005) 215-221.

[164] P.J.A. Tijmb, F.J. Waller, D.M. Brown, Appl. Catal. A: Gen. 221 (2001) 275-282.

[165] H. Sakurai, M. Haruta, Appl. Catal. A: Gen. 127 (1995) 93-105.

[166] A. Hugon, L. Delannoy, C. Louis, Gold Bull. 41 (2008) 127-138.

[167] O. Mitsutaka, T. Akita, M. Haruta, Catal. Today, 74 (2002) 265-269.

[168] A. C. Gluhoi, H.S.Vreeburg, J.W. Bakker, B.E. Nieuwenhuys, Appl. Catal. A: Gen. 291 (2005) 145-150.

[169] J. Jia, K. Haraki, J. N. Kondo, K. Domen, K. Tamaru, J. Phys. Chem. B 104 (2000) 11153-11156.

[170] N. Ahmad, S.T. Hussain, B. Muhammad, J. A. Anderson, N. Ali, S. M. Abbas, in: Proceedings of 2013 10th International Bhurban Conference on Applied Sciences & Technology (IBCAST) Islamabad, Pakistan, 15- 19 January, 2013.

[171] K. Jalama, N.J. Coville, H. Xiong, D. Hildebrandt, D. Glasser, S. Taylor, A. Carley, J. A. Anderson, G.J. Hutchings, Appl. Catal. A: Gen. 395 (2011) 1-9.

[172] K. Jalama, N.J. Coville, D. Hildebrandt, D. Glasser, L. L. Jewell, Top. Catal. 44 (2007) 129-136.

[173] W.C. Jr Conner, J.L. Falconer, Chem. Rev. 95 (1995) 759-788.

[174] R.B. Levy, M. Boudart, J. Catal. 32 (1974) 304-314.

[175] R. Kramer, M. Andre, J. Catal. 58 (1979) 287-295.

[176] U. Roland, T. Braunschweig, F. Roessner, J. Mol. Catal. A: Chem. 127(1997) 61-84.

[177] P. Baeza, M. Villarroel, P. Avila, A. L. Agudo, B. Delmon, F.J. Gil-Llambías, Appl. Catal. A: Gen. 304 (2006) 109-115.

[178] J. Conradie, J. Garcia, J. W. Niemantsverdriet. J. Phys. Chem. C. 116 (2012) 25362-25367.

[179] G. M. Pajonk, Appl. Catal. A: Gen. 202 (2000) 157-169.

[180] P.H. Emmett, in: 12th Report of the Committee on Catalysis, Wiley, New York, 1940, 64.

[181] J. Kuriacose, Ind. J. Chem. 5(1957) 646.

[182] S. Khoobiar, J. Phys. Chem. 68 (1964) 411-412.

[183] Y. Lykhach, T. Staudt, M. Vorokhta, T. Skála, V. Johánek, K. C. Prince, V. Matolín, J. Libuda, J. Catal. 285 (2012) 6-9.

[184] T. S. King, X.Wu, B.C. Gerstein, J. Am. Chem. Soc. 108 (1986) 6056-6058.

[185] D.H. Lenz, W.C. Jr Conner, J.P. Fraissard, J. Catal. 117 (1989) 281-289.

[186] T. C. Sheng, I. D. Gay, J. Catal. 77 (1982) 53-56.

[187] P. Chiaranussati, L.F. Gladden, R.W. Griffiths, S.D. Jackson, G. Webb, Chem. Eng. Res. Des. 71 (1993) 267-272.

[188] R. R. Cavanagh, J. T. Jr Yates, J. Catal. 68 (1981) 22-26.

[189] M. Stoica, M. Caldararu, F. Rusu, N.I. Ionescu, Appl. Catal. A: Gen. 183 (1999) 287-293.

[190] U. Roland, R. Salzer, T. Braunschweig, F. Roessner, H. Winkler, J. Chem. Soc., Faraday Trans. 91 (1995) 1091-1095.

[191] E.P.S. Barrett, A.J. Blackburn, M.A. Yates, Y. Wang, P.A. Sermon. Stud. Surf. Sci. Catal. 7 (1993) 207-212.

[192] S.K. Beaumont, S. Alayoglu, C. Specht, N. Kruse, G.A. Somorjai, Nano Lett. 14 (2014) 4792-4796.

[193] E. Kikuchi, T. Matsuda, Stud. Surf. Sci. Catal. 77 (1993) 53-60.

[194] K. Fujimoto, K. Maeda, K. Aimoto, Appl. Catal. A: Gen. 91 (1992) 81-86.

[195] D. Bianchi, M. Lacroix, G. M. Pajonk, S. J. Teichner, J. Catal. 68 (1981) 411-418.

[196] W.C. Neikam, M.A. Vannice, J. Catalysis 27 (1972) 207-214.

[197] S. Tsuchiya, Y. Amenomiya, R.J. Cvetanovic, J. Catal. 20 (1971) 1-9.

[198] W. C. Jr Conner, R.J. Kokes, J. Catal. 36 (1975) 199-210.

[199] H. Kragh, Astron. Geophys. 51 (2010) 6-25.

[200] J.E. Benson, H.W. Kohn, M. Boudart, J. Catal. 5 (1966) 307-313.

[201] P.A. Sermon, G.C. Bond, J. Chem. Soc. Faraday Trans. 176 (1980) 889-900.

[202] K.-D Jung, A.T. Bell, J. Catal. 193 (2000) 207-223.

[203] E. Keren, A. Soffer, J. Catal. 50 (1977) 43-55.

[204] T. Kusakari, K. Tomishige, K. Fujimoto, Appl. Catal. A: Gen. 2241 (2002) 219-228.

[205] F. Roessner, U. Roland. J. Mol. Catal. A: Chem. 112 (1996) 401-412.

[206] E. Baumgarten, R. Wagner, C. Lentes-Wagner, J. Catal. 104 (1987) 307-311.

[207] W.C. Jr Conner, G.M. Pajonk, S.J. Teichner. Adv. Catal. 34 (1986) 1-79.

[208] L.E.S. Rygh, C.J. Nielsen, J. Catal. 194 (2000) 401-409.

[209] R. Burch, S.E. Golunski, M.S. Spencer, J. Chem. Soc. Faraday Trans. 86 (1990) 2683-2691.

[210] J. Ojeda, N. Escalona, P. Baeza, M. Escudey, F.J. Gil-Llambias, Chem. Commun. 13 (2003) 1608-1609.

[211] P. Baeza, M.S. Ureta-Zañartu, N. Escalona, J. Ojeda, F. J. Gil-Llambías, B. Delmon. Appl. Catal. A: Gen. 274 (2004) 303-309.

[212] N. Escalona, R. García, G. Lagos, C. Navarrete, P. Baeza, F.J. Gil-Llambías, Catal. Commun. 7 (2006) 1053-1056.

[213] T. Jermwongratanachai, G. Jacobs, W. Ma, W.D. Shafer, M.K. Gnanamani, P. Gao, B. Kitiyanan, B.H. Davis, J.L.S. Klettlinger, H. Y. Chia, D.C. Cronauer, A.J. Kropf, C.L. Marshall, Appl. Catal. A: Gen. 464 (2013) 165-180.

[214] K.-H. Steinberg, U. Mroczek, F. Roessner, Stud. Surf. Sci. Catal. 46 (1988) 81-90.

[215] T. Chow, S.H. Park, W.M.H. Sachtler, Appl. Catal. 19 (1985) 349-364.

[216] U. Mroczek, “Zur Rolle des Spillover bei der Kohlenwasserstoffumwandlung an Zeolithen”, PhD Thesis, Universiteit Leipzig, The Netherlands, 1987.

[217] A. El-Tanany, G.M. Pajonk, K.-H. Steinberg, S.J. Teichner, Appl. Catal. 39 (1988) 89-106.

[218] K. Aimoto, K. Fujimoto, K. Maeda, Stud. Surf. Sci. Catal. 77 (1993) 165-169.

[219] P.B. Weisz, E.W. Swegler, Science 126 (1957) 31-32.

[220] G.A. Mills, H. Heinemann, T.A. Milliken, A.G. Oblad, Ind. Eng. Chem 45 (1953) 134-137.

[221] J.M. Parrera, E.M. Traffano, J.C. Musso, C.L. Pieck, Stud. Surf. Sci. Catal. 17 (1983) 101-108.

[222] J.-Y. Luo, W. S. Epling, Appl. Catal. B: Environ. 97 (2010) 236-247.

[223] J. F. Cevallos-Candau, W.C. Jr Conner, J. Catal. 106 (1987) 378-385.

[224] A.F. Carley, H.A. Edwards, B. Mile, M.W. Roberts, C.C. Rowlands, J. Chem. Soc. Faraday Trans. 90 (1994) 3341-3346.

[225] C.J.D. von Grotthuss, Ann. Chim. 58 (1806) 54-74.

[226] N. Agmon, Chem. Phys. Lett. 244 (1995) 456-462.

[227] J.B. Peri, J. Phys. Chem. 69 (1966) 211-219.

[228] L. Lietti, I. Nova, P. Forzatti, J. Catal. 257 (2008) 270-282.

[229] H.W. Kohn, M. Boudart. Science 145 (1964) 149-150.

[230] J.T. Miller, B.L. Meyers, F.S. Modica, G.S. Lane, M. Vaarkamp, D. C. Koningsberger J. Catal. 143 (1993) 395-408.

[231] K. Gadgil, R.D. Gonzalez, J. Catal. 40 (1975) 190-196.

[232] G.A. Badun, B.F. Johnson, N.E. Shchepina, Mendeleev Commun. 19 (2009) 235-236.

[233] J.M. Cece, R.D. Gonzalez, J. Catal. 28 (1973) 254-259.

[234] Y. Li, R.T. Yang, J. Am. Chem. Soc. 128 (2006) 8136-8137.

[235] C.H. Mak, J.L. Brand, A. A. Deckert, S.M.J. George, J. Chem. Phys. 85 (1986) 1676-1680.

[236] K.J. Sladek, E.R. Gilliland, R.F. Baddour, Ind. Eng. Chem. Fund. 13 (1974) 100-105.

[237] J. Greeley, M. Mavrikakis, J. Phys. Chem. B 109 (2005) 3460-3471.

[238] G. Kennedy, L.R. Baker, G.A. Somorjai, Angew. Chem. 126 (2014) 3473-3476.

[239] R.V. Dmitriev, A.N. Detjuk, C.N. Minachev, K.H. Steinberg, in: G.M. Pajonk, S.J. Teichner, J.E. Germain (Eds.), Proceedings of the first international symposium on the spillover of adsorbed species, Elsevier, Amsterdam, 1983.

[240] R. Prins, V. K. Palfi, M. Reiher, J. Phys. Chem. C 116 (2012) 14274−14283.

[241] O.E. Lebedeva, W.-A. Chiou, W.M.H. Sachtler, J. Catal. 188 (1999) 365-374.

[242] R. Prins, Chem. Rev. 112 (2012) 2714−2738.

[243] J.H. Sinfelt, P.J. Lucchesi, J. Am. Chem. Soc. 85 (1963) 3365-3367.

[244] J.C. Schlatter, M.J. Boudart, J. Catal. 24 (1972) 482-492.

[245] T. Fleisch, R. Abermann, J. Catal. 50 (1977) 268-278.

[246] G.J. Hutchings, J. Catal. 96 (1985) 292.

[247] M. Haruta, N. Yamada, T. Kobayashi, S. Iijima, J. Catal. 115 (2) (1989) 301.

Chapter 3

Scope and Novelty of this Work

3.1 Objectives

The perspective on the operation of the Pt promoter is polarised between 'Hydrogen Spillover', which is a so-called remote-control effect that would otherwise occur in the absence of Pt-Co coordination, and 'ligand/electronic effects' that demand direct Pt-Co coordination. Therefore, the objective of this study is to explicate the operation of Pt and Au as promoters of the Co/Al_2O_3 catalyst by decoupling hydrogen spillover from effects that require direct promoter-cobalt coordination. The analysis is segmented into two core sections with the first investigatingthe role of hydrogen spillover during the reduction of cobalt oxides (Chapter 5) while the second section covered the effect of hydrogen spillover during the Fischer-Tropsch reaction at commercial conditions (Chapter 6).

3.1.1 Use of model 'hybrid' catalysts to isolate the effects of hydrogen spillover

The employment of model 'hybrid' catalysts, which are mechanical mixtures of monometallic constituents of the promoted catalyst, presents a novel way to investigate the role of hydrogen spillover in the Pt-Co and Au-Co catalyst systems. Thus far, no systematic investigation of the hydrogen spillover phenomenon using hybrid catalyst systems during both reduction and under commercially relevant conditions has been encountered in the published literature.

The purpose of hybrid catalysts was to isolate hydrogen spillover as a remote-control promoter effect, from the ligand/electronic effects that require coordination of the promoter to the active cobalt component (Sec. 2.3.1). Hydrogen spillover is often invoked to explain the facilitation of the reduction of cobalt oxides (Sec. 2.4.3.1). However, the effect is less frequently invoked under Fischer-Tropsch conditions even though evidence of a synergy due to spillover hydrogen has been provided for a number of comparable reactions involving CO and CO_2 hydrogenation (Sec. 2.3.1, Sec. 2.4.3.2). The effects of spillover under Fischer-Tropsch conditions are conceivable because most kinetic expressions show positive order with H_2 and an increase in H_2 partial pressure has generally been observed to correlate positively with the reaction rate. Hydrogen lowers the activation energy for CO dissociation, increases the rate of formation of the monomer (CH_x), and is said to free up active sites by removing oxygen and carbon species (Sec. 2.2.1, Sec. 2.4.3.2) that have been cited as causes of deactivation (Sec. 2.2.3). It is therefore likely that the effects of spillover hydrogen species may already be incorporated in the Fischer-Tropsch reaction mechanism and account for the changes that are typically reported in promoted catalysts including the higher cobalt site-time yield and greater selectivity towards hydrogenated products.

3.1.2 Gold as a reduction promoter for the cobalt-based catalyst

The operation of a reduction promoter is widely attributed to its activity for H_2 dissociative adsorption. The kinetics of spillover have also been reported to depend on a number of factors including the dissociating metal's affinity for hydrogen (Sec. 2.4.3.2) and so the differences in the reactivity towards H_2 and CO between platinum and gold (Sec. 2.3) may provide insights into the role of spillover hydrogen during cobalt reduction and under LTFT reaction conditions. Unfortunately, the strong focus on Au as an oxidation catalyst has biased the attention away from its use in other reactions, particularly hydrogenation for which it has also exhibited some catalytic activity (Sec. 2.3.2). This study sought to contribute to the currently limited body of literature on gold as a hydrogenation catalyst, promoter and substitute of platinum under Fischer-Tropsch conditions.

3.1.3 Catalyst characterisation using in situ techniques

In recent years, the use of in situ techniques to study the behaviour of catalyst systems has grown exponentially because they provide real time structural information during catalytic processes (Sec. 2.2.4.1). In situ techniques including XPS, TGA and XRD in an in-house novel capillary reactor set-up was used to elucidate the behaviour of the cobalt-based catalyst during both reduction and under Fischer-Tropsch conditions.

3.2 Real World Context

Although the Fischer-Tropsch process has been shown to be economically viable on an industrial scale, various arenas still need to be explored to lower the capital and production costs. These arenas include elimination of the costly Air Separation Units (from which oxygen for reforming/gasification is obtained) in favour of air, development of more compact high-volume reactors, process integration to maximise heat recovery, minimisation of water consumption, and innovation in the Fischer-Tropsch catalyst design. In the latter case, a key area of concern is the high cost of cobalt-based LTFT catalyst. Per unit mass, cobalt is significantly more expensive than the iron catalyst, which necessitates maximization of catalyst performance with respect to catalyst life and product selectivity. As a result, there has been a decades-long drive to discover alternative catalyst constituents that are cheaper, more selective, more active, and longer lasting.

Numerous gaps in the understanding of Fischer-Tropsch catalysis still prevail, with the problem compounded by multiple and complex catalyst constituents, and the use of varying reaction conditions (pressure, temperature, and H_2/CO ratio) to infer certain catalytic behaviours that may not necessarily hold true at real industrial conditions. Therefore, optimisation of the performance of the cobalt-based catalyst requires a rigorous analysis and understanding of the behaviour of the cobalt-based catalyst at near commercial conditions as used in this work.

With regard to the use of Pt and Au promoters in this study, South Africa has some of the greatest global reserves of these metals, both of which continue to play pivotal roles in the country's economic outlook. There is thus a constant drive to find viable beneficiation outlets for these resources such as the Platinum Development Initiative (PDI), which was established in 1997 by Mintek (the national mineral research organisation) to increase the industrial use of Pt and is a joint venture with big platinum mining companies including Anglo Platinum, Impala Platinum and Lonmin. Today, South Africa accounts for up to 16% of the total global production of catalytic converters (with PGM catalysts). In 2000, Mintek set up 'Project AuTEK' to research and develop new applications for gold in catalysis. Project AuTEK is a joint venture with the three biggest South African mining houses including Anglogold Ashanti, Gold Fields and Harmony Gold.

Chapter 4

Experimental Techniques

4.1 Catalyst Preparation

This work comprised the Platinum-Cobalt catalyst system and the Gold-Cobalt catalyst system (Fig. 4.1-1). The Platinum-Cobalt catalyst system was prepared using slurry impregnation and comprised four characteristic catalysts including 20%Co/Al_2O_3, 0.5% Pt/Al2O3, Hybrid Pt-Co, and 0.5%Pt-20%Co/Al_2O_3. The hybrid catalyst was a loose mechanical mixture of equal mass portions of Pt/Al_2O_3 and Co/Al_2O_3 and was so prepared to maintain the same Pt/Co ratio of 1:40 in Pt-Co/Al_2O_3. The same batch of Co/Al_2O_3 was used for the preparation of a corresponding Gold-Cobalt catalyst system, although gold addition was carried out via anionic exchange.

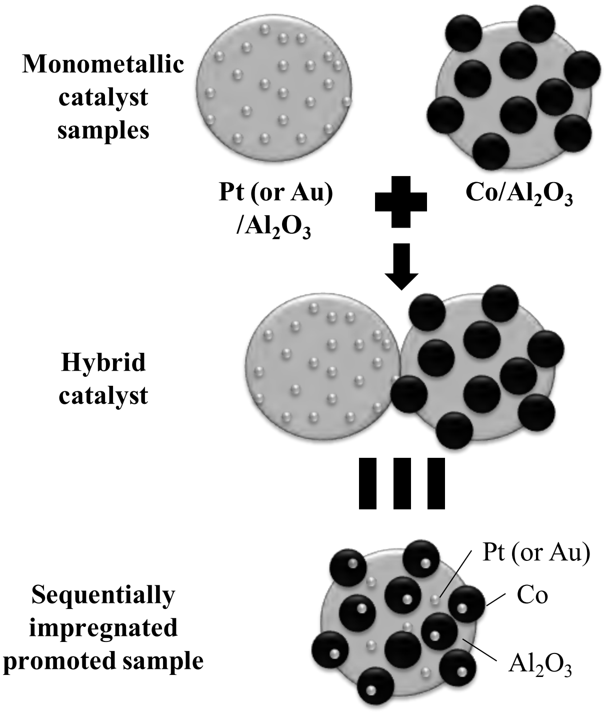

Figure 4.1-1: An illustration of a catalyst system showing the characteristic catalyst samples including two monometallic samples, a hybrid sample, and a sequentially impregnated promoted sample.

4.1.1 Catalyst preparation via slurry impregnation

The γ-Al_2O_3 support (Puralox SCCa 5-150; Sasol Germany) was characterized using BET to yield the following characteristics: surface area=162m^2/g), pore volume=0.5 cm^3/g and pore diameter=10.1 nm. The reported possible impurities in Puralox SSCa include SiO_2 (150ppm), Fe_2O_3 (125 ppm) and Na_2O (25ppm) [1].

4.1.1.1 Milling the alumina support

Prior to impregnation, the support was milled to a fine powder in a bench top McCrone Micronising Mill®. The milling procedure involved mixing 4ml of the support particles with approximately 7ml of ethanol. The alumina-ethanol suspension was then poured into a grinding jar containing cylindrical agate grinding elements where it was milled for 2.5 minutes. The resulting suspension was then dried in an oven at 60°C to evaporate the ethanol, and recover the dry alumina powder, now with an approximate particle size distribution of D_{90}=15.5μm. Milled alumina was used in the preparation of all samples used in this study.

4.1.1.2 Preparation of 20%Co/Al_2O_3 in two sequential impregnation steps

Slurry impregnation was selected for preparation of 20%Co/Al_2O_3 as it has been shown to improve the homogeneity of cobalt compared to the widely used incipient wetness technique [2].

To obtain the slurry, the milled support was added to an aqueous solution of $Co(NO_3)_2 \cdot 6H_2O$ (Sigma Aldrich - 98%) prepared using a volume of deionised water equal to 3 times the pore volume. Due to the limitation of the maximum salt solubility of 1.34g/ml in water, two sequential impregnations using aqueous solutions of the cobalt precursor with concentrations of 1.27M and 1.58M respectively were required to attain the cobalt loading of 20%. Following the first impregnation step, the sample was transferred to a flask that could be attached to a BUCHI® rotary evaporator. The liquid portion of the slurry was then evaporated by the rotation of the flask in an 85°C oil bath and under vacuum of 50-100mbar for 30-45 minutes. The moist sample recovered from the rotary evaporator then underwent further drying in an oven for 12 hours at 120°C. Thereafter, dry sample was calcined at 350°C in a fluidised bed reactor. This was carried out under a continuous airflow of $50 ml \cdot min^{-1} \cdot gAl_2O_3^{-1}$ for 6 hours to allow the supported nitrate species to decompose to oxidic cobalt i.e.

$Co(NO_3)_2$ → Co_3O_4. The calcined sample was subsequently used to prepare the slurry for the 2nd impregnation and the same sequence of steps repeated to obtain a calcined 20%Co/Al_2O_3.

The calcined Co/Al_2O_3 sample was separated into five five batches. Two batches were used for the subsequent doping with Au or Pt, and another two batches were physically mixed with the monometallic Pt or Au samples to make Hybrid Pt-Co and Hybrid Au-Co.

4.1.1.3 Preparation of 0.5%Pt-20%Co/Al_2O_3 and 0.5%Pt/Al_2O_3

The Pt-Co/Al_2O_3 was prepared by slurry impregnation of a portion of calcined 20%Co/Al_2O_3 with an aqueous solution of 0.0171M $Pt[(NH_3)_4]Cl_2.H_2O$. Pt/Al_2O_3 was prepared at the same precursor concentration but in a slurry of Al_2O_3 instead. Tetraammine Platinum (II) chloride monohydrate- $Pt[(NH_3)_4]Cl_2.H_2O$ with a purity of 99% was available from Strem Chemicals.

The sequence of drying steps carried out for the cobalt impregnation was followed to obtain calcined 0.5%Pt-20%Co/Al_2O_3 and 0.5%Pt/Al_2O_3. In order to obtain Hybrid Pt-Co, equal mass portions of calcined Pt/Al_2O_3 and Co/Al_2O_3 were manually mixed to attain a visibly homogenous sample with a Co/Pt mass ratio of 40. No further catalyst treatment was carried out on the mechanical mixture.

4.1.2 Preparation of gold catalysts via anion exchange

The anion exchange method developed by Case [3] was used to prepare Au/Al_2O_3 and Au-Co/Al_2O_3. This method was selected over the slurry impregnation technique used for Co and Pt because it was shown to produce small (<10nm), well-distributed gold crystallites that were active for hydrogenation reactions [3, 4].

The theory behind the anion exchange method is that when γ-Al_2O_3 is added to an acidic solution of the $HAuCl_4$ precursor, surface OH groups are protonated and depart as water, leaving behind the vacant Lewis acid sites. These Lewis acid sites are then rapidly taken up by gold-chloro-hydroxy complexes, resulting in an overall ion exchange on the Al_2O_3 surface. Figure 4.1-2 shows the various gold-chloro complexes that may be present at a given pH, while Figure 4.1-3 shows the Zeta potential measurement for γ-Al_2O_3 and the corresponding iso-elctric point. At pH values below the iso-electric point, the Al_2O_3 surface is positively charged, which allows for a higher uptake of gold due to electrostatic interaction with the anionic gold species in the precursor solution shown in Figure 4.1-2.

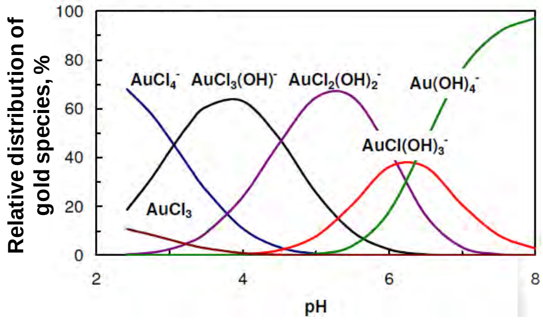

Figure 4.1-2: Speciation of gold as a function of pH in a 500ml solution of 2.54mmol/L of $HAuCl_4$. pH changed by addition of NaOH [8].

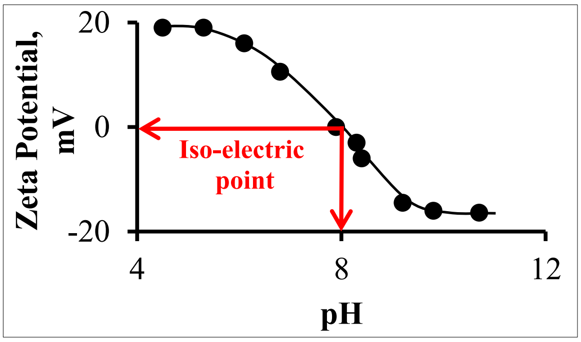

Figure 4.1-3: Zeta potential measurement for γ-Al_2O_3 showing iso-electric point [9].

The same method was used to prepare Au/Al_2O_3 and Au-Co/Al_2O_3 even though the technique was based on deductions made only on Au/Al_2O_3 catalysts [3]. It was hypothesized that the interaction of the anionic gold complexes with calcined Co/Al_2O_3, i.e. Co_3O_4/Al_2O_3, would not deviate greatly from the behaviour with pure Al_2O_3. Co_3O_4 has an iso-electric point of 7.5, which is comparable to the iso-electric point of Al_2O_3 [6, 7, 9] (see Fig. 4.1-3). It was expected that the surface of Co_3O_4/Al_2O_3 would be positively charged at the same pH as pure Al_2O_3 and consequently allow for electrostatic interaction with the gold anions. The presence of the Co_3O_4 crystallites on the Al_2O_3 surface was thus not expected to adversely affect the loading efficiency of the gold in this method.

Using a basis of 10g of milled Al_2O_3, preparation of 0.5%Au/Al_2O_3 was initiated by addition of 0.35ml of 250gAu/l $HAuCl_4$ to deionised water to make up a 1L solution. Excess gold precursor was used in this step to account for the 55% loading of efficiency of gold reported for this method [3]. 2M NaOH solution was added drop-wise to adjust the pH of the solution to between 4 and 5 prior to addition of the Al_2O_3 support. Addition of Al_2O_3 causes a slight increase in pH as protons are removed from solution although the pH remains in the range of 4 and 5. From Figure 4.1-2, the dominant gold chloro-hydroxy complexes in this pH range are $AuCl_2(OH)_2^-$, which according to Ivanova et al. [5] are most ideal for anion exchange catalyst due to bidentate adsorption to the Al_2O_3 surface.

Anionic exchange involves a stoichiometric substitution of the hydroxyl groups on the Al_2O_3 surface with the gold-chloro-hydroxy complexes, but a weaker electrostatic attraction may occur between the Al_2O_3 support and the gold complexes, especially with the unhydrolysed $AuCl_4^-$ ion (see Fig. 4.1-2). An ammonia-washing step was incorporated after the technique to allow for substitution of Cl^- ions with hydroxyl groups and facilitate the removal of weakly bound gold complexes from the Al_2O_3 surface. Otherwise, the highly mobile, weakly bound gold complexes would result in very large crystallites due to sintering during the calcination process, while Cl^- ions are a well-known cause of deactivation and have been observed to facilitate sintering of gold crystallites [5].

4.2 Catalyst Characterisation

4.2.1 Inductively Coupled Plasma Optical Emission Spectroscopy (ICP-OES)

A Varian Vista-Pro analyser was used to determine the elemental composition of all the prepared catalyst samples in this study. Sample preparation involved dissolution of 0.1-0.2 g of sample in *aqua regia* and then microwaving the obtained solution for 30 minutes in order to complete the digestion process.

4.2.2 Transmission Electron Microscopy (TEM)

Transmission Electron Microscopy (TEM) was used to determine the size distributions of Al_2O_3 supported crystallites of Co, Pt, and Au. TEM analyses were carried out on the calcined and reduced samples.

A Zeiss LEO 912-Omega Transmission Electron Microscope and a FEI Tecnai^{TM} F20 Field Emission TEM coupled with EDS (Energy-dispersive X-ray spectroscopy) were employed for this study.

Sample preparation involved the ‘resin embedding’ and the ‘sonication’ methods. In the resin embedding method, micrograms of a catalyst sample were placed in a 1.5ml microcentrifuge tube to which a few drops of plastic resin were added and the mixture stirred to eliminate trapped air. The filled microcentrifuge tube was placed in an oven at 80^{o}C for 12-16 hours (overnight) to allow the resin to set. Thereafter, glass knives were used to section the solidified resin into thin slices of <90nm which were placed on a carbon-coated copper grid for analysis.

For the sonication method, a few micrograms of a catalyst sample were added to a microcentrifuge tube, which was then filled with ethanol, sealed and placed in an ultrasonic bath to allow the catalyst particles to fragment into sufficiently thin samples. A few drops of the slurry of the fragmented sample were subsequently added to carbon-coated copper grids for analysis.

Image processing of the obtained micrographs involved the use of ImageJ^{TM} software (open source) to measure approximately 100 crystallites in order to obtain the crystallite size distributions.

4.2.3 Hydrogen temperature-programmed reduction coupled with a thermal conductivity detector (H_2 TPR-TCD)

H_2 TPR-TCD was used to study the effect of the Au and Pt promoters on the reduction behaviour of Al_2O_3-supported Co_3O_4.

AutoChem 2950 HP and AutoChem 2910 Chemisorption Analyzers from Micromeritics were used for the H_2 TPR-TCD analyses. These automated table-top systems include a quartz U-tube reactor and allow for temperatures of up to 1100°C. The basic set-up of the AutoChem 2910 is shown in Figure 4.2-1. All H_2 TPR-TCD experiments were carried out at atmospheric pressure using 5%H_2-Ar. A typically experiment involved a catalyst bed of approximately 0.1g through which the reducing gas was flowed at a GHSV (NTP) of $2500ml\cdot(min\cdot gCo)^{-1}$. The sample temperature was ramped at 10°C/min from 60 or 100°C to a maximum temperature of 950°C, at which point the temperature was maintained for 2 hours. All samples were dried at 120°C in Ar for 60 minutes prior to every analysis.

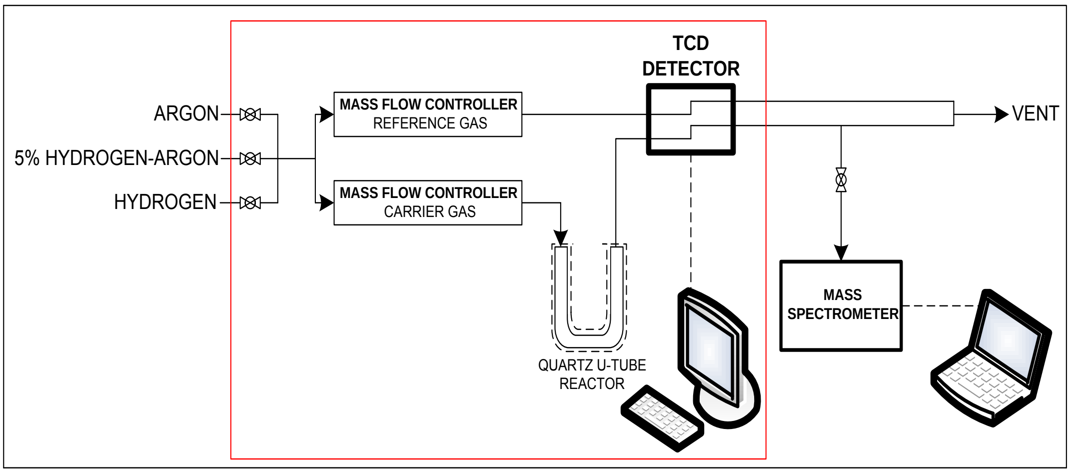

Figure 4.2-1: Simplified schematic of the AutoChem 2910 Chemisorption Analyzer showing connection to the TCD and a mass spectrometer connected in series. The red outline marks the components within the analyzer.

Variations in this basic experiment included using the AutoChem 2910 to co-feed water vapour or couple with a Mass Spectrometer. The AutoChem 2910 is equipped with a vapour generator that comprises a 50ml flask and a heating mantle for analyses that require vapourised liquids. For water co-feeding, the reducing gas was sparged through the water-filled flask at room temperature and atmospheric pressure prior to being fed to the U-tube reactor.

The TCD incorporated in the analyzers was used to quantify the differences in thermal conductivity between the products from the U-tube reactor and the corresponding reference flow rate (see Fig. 4.2-1) and thus did not provide a qualitative analysis. For qualitative analyses, a bleed from the reactor exhaust line was sent to a Pfeiffer Omnistar GSD 300 Mass Spectrometer (see Fig. 4.2-1).

4.2.4 Isothermal thermogravimetric analysis (TGA)

Isothermal thermogravimetric analyses were carried out to determine the effect of the reduction promoters on the degree of reduction (DOR) and the rate of reduction of Al_2O_3-supported Co_3O_4. The results from the TGA were also used to postulate a kinetic model for the reduction of supported Co_3O_4 nano-crystallites.

A Mettler-Toledo TGA/SDTA 851^e was used for the thermogravimetric analyses. Alumina crucibles of 70µl were used as sample holders, which allowed for catalyst masses of ca. 50mg. All analyses were carried out at the activation conditions of 350°C in pure H_2 ($1000ml\cdot min^{-1}\cdot g_{Co}^{-1}$), 1 bar, for 12 hours. An analysis commenced with a drying step in N_2 ($1000ml\cdot min^{-1}\cdot g_{Co}^{-1}$), which involved a $10^oC\cdot min^{-1}$ ramp from 60°C to 350°C, held for an hour, at which point H_2 was introduced. The 12-hour reduction was followed by a re-oxidation step in synthetic air ($1000ml\cdot min^{-1}\cdot g_{Co}^{-1}$) for an hour, after which the temperature returned to ambient and the analysis terminated.

The temperature profile for a typical TGA analysis is shown in Figure 4.2-2. The degree of reduction (DOR) could be determined from both the reduction and re-oxidation steps according to the simplified overall stoichiometric equations shown inset. The mass loss during the drying step corresponded to the loss of physisorbed water and possibly surface OH groups. The mass loss during reduction, and gain during oxidation was assumed to correspond to removal or incorporation of O into the cobalt structure.

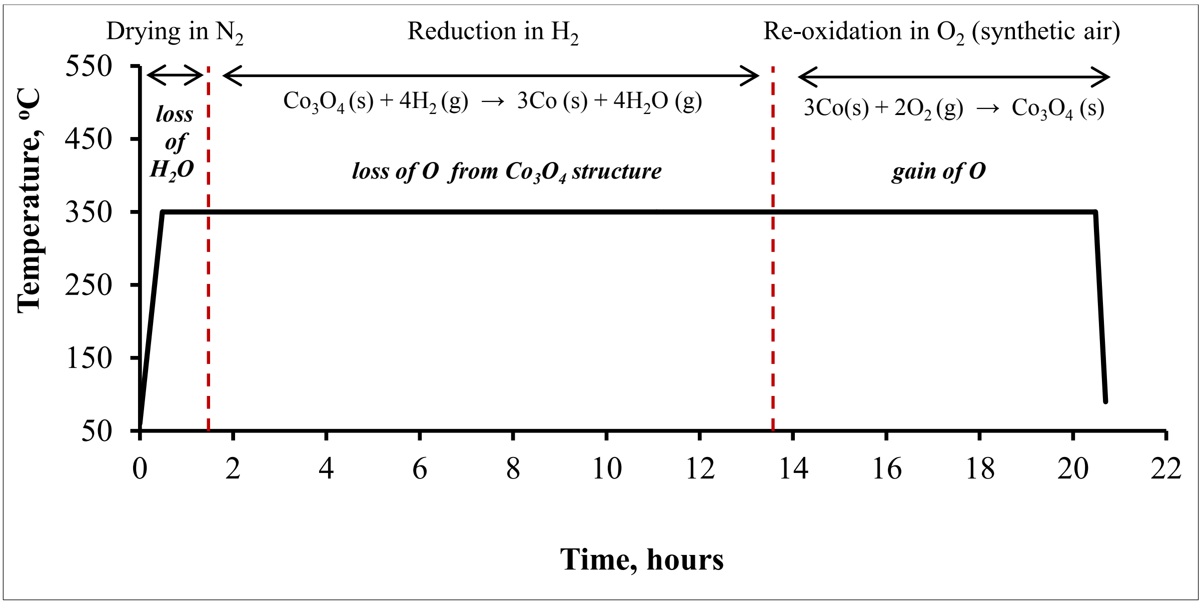

Figure 4.2-2: Temperature profile during a typical thermogravimetric analysis. The reduction and re-oxidation steps according to the simplified overall stoichiometric equations are shown inset.

4.2.5 X-Ray Diffraction (XRD)

X-ray diffraction was used to identify the crystalline phases and determine Co crystallite sizes in the calcined and reduced samples. The results from the in situ XRD analyses during activation of the various catalysts in hydrogen were used to determine the effect of Au and Pt on the evolution of the Co_3O_4, CoO, and Co^0 phases with time. The in situ XRD data was thus complementary to the data obtained during the isothermal thermogravimetric analyses (see Sec. 4.2.4).

A Bruker D8 Advance Diffractometer with a Co-Kα radiation source (λ = 1.78897Å) was used for the XRD analyses. Powder diffractograms of all the prepared (calcined) samples were collected over a 2θ range of 15°-130° at a scan rate of 2θ=0.006°/step and a scan time of 0.3s/step. The International Centre for Diffraction Data PDF-2 database was used to identify all the peaks/phases in the diffractograms.

Rietveld refinement using TOPAS 4.2® software was used to determine crystallite sizes and composition of the cobalt phase. Rietveld refinement is a structure refinement technique used to obtain crystal structure from the x-ray diffraction data by minimising the difference between the measured and calculated profile. Unfortunately, the Puralox SCCa 5-150 support is a mixture of γ-Al_2O_3 and a smaller amount of δ-Al_2O_3 whose crystal structure remains unknown [10]. As a result, there was no crystal structure file (*cif* file) available that could accurately define the Al_2O_3 phase as required for the refinement. Therefore, a 'peaks phase' group model was defined to fit the Al_2O_3 peaks (i.e. the peaks that did not correspond to Co, Pt, or Au). The drawback of this technique was that the catalyst composition, i.e. cobalt versus alumina loading could not be determined. Only the relative contribution within the cobalt phase can be calculated using this method, i.e. $Co^0+CoO+Co_3O_4 = 100\%$.

4.2.5.1 In situ X-ray diffraction during isothermal reduction at 350°C

In situ XRD experiments were carried out for all cobalt-containing samples during the selected catalyst activation conditions (350°C, pure H_2 at $1440 ml\cdot min^{-1}\cdot gCo^{-1}$, 1 bar, 12 hours). These analyses were carried out in an Anton-Paar XRK-900 reaction chamber attached to the Bruker D8 Advance Diffractometer. Powder diffractograms were collected over a 2θ range of 40-98.9° at a scan rate of $2\theta=0.0123°$/step and a scan time of 0.2s/step. The duration of each scan was 16 minutes, to which a 13.4-minute delay was added, so that 26 diffractograms could be collected during a single in situ reduction experiment.

4.2.5.2 In situ X-ray diffraction during temperature-programmed reduction at 350°C (including co-feeding of water vapour)

In situ XRD experiments during temperature-programmed reduction were carried out for all cobalt-containing samples in a patented in-house in situ X-ray diffraction cell [13] that could be mounted to the BrukerD8 Advance Diffractometer. The schematic of the cell is shown in Figure 4.2-3: *Left* and a detailed image of the position of the reactor and the heaters is shown on the right.

The reactors were borosilicate capillaries (L=75mm, OD=1mm, wall thickness=0.01mm) into which 20-30mg of catalyst was packed, and the ends plugged with silane treated gas wool. The temperature in the reaction zone was maintained by two Elstein MSH infrared heaters, and a K-type thermocouple could be inserted directly into the capillary reactor with its tip at the centre of the catalyst bed.

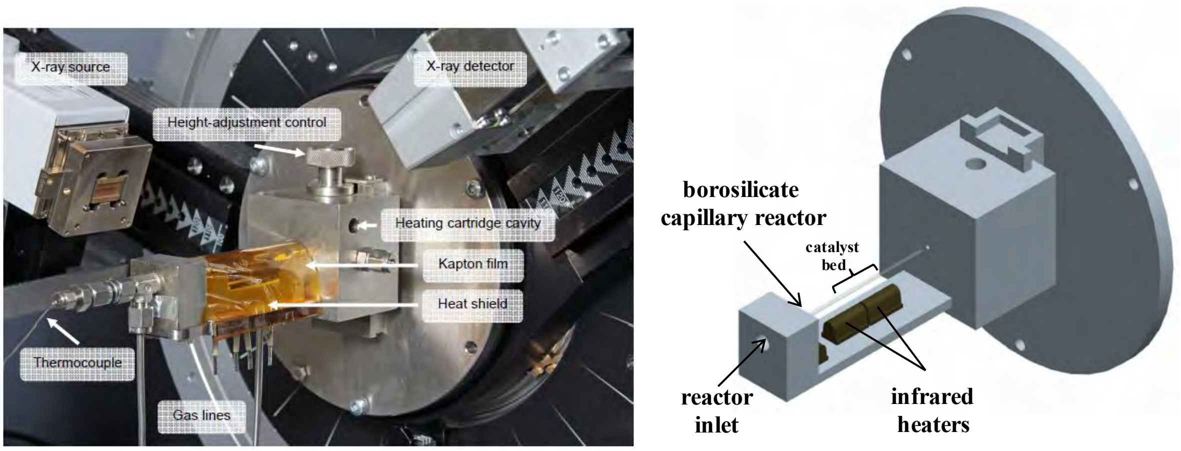

Figure 4.2-3: ***Left:*** Patented in-house in situ XRD cell [13] fitted to a Bruker D8 Advance Diffractometer. The borosilicate capillary reactor is present underneath the Kapton film heat shield. ***Right:*** A detailed image of the positioning of the borosilicate capillary reactor and catalyst bed relative to the infrared heaters [11, 13].

Powder diffractograms were collected over a 2θ range of 40-95° at a scan rate of $2\theta=0.0123°$/step, and a scan time of 0.41s/step. The analyses were carried out in pure H_2, a temperature range of up to 425°C, and a heating ramp rate of 1°C/min. Note that these conditions were in contrast to the H_2 TPR-TCD analyses in Section 4.2.3 carried out in 5%H_2-Ar, a temperature range of up to 950°C, and a ramp rate of 10°C/min. The XRD analyses were limited by the maximum operating temperature of the cell (~500°C).

A long scan time of approximately 30 minutes necessitated that the slow temperature ramp of 1°C/min was employed because it limited the temperature difference within the same diffractogram. The high temperatures required for the TPR analyses necessitated the use of borosilicate capillaries, which unfortunately have low linear absorption coefficients of ca. 71.0cm^{-1} [11, 12]. The use of borosilicate capillaries therefore resulted in a loss of signal intensity, which negatively affected the accuracy of the Rietveld refinement.

The temperature-programmed reduction analyses during which water vapour was co-fed involved saturation of the reducing H_2 gas by flowing it through a packed vessel of water saturated Chromosorb P (acid-washed, 60-80 Mesh) from Sigma-Aldrich. Saturation of the gas was carried out at room temperature and pressure.

4.2.6 X-Ray Photoelectron Spectroscopy (XPS)

XPS was used to obtain the elemental composition in the calcined and reduced catalyst samples and to identify the oxidation states of Co, Pt, and Au.

A VG Escalab 200 MKII Spectrometer with an Al Kα radiation source (Al Kα = 1486.3eV) was used for the XPS analyses. Analysis of each sample involved taking wide scans from 0-1200eV followed by multiple narrower scans in the region of characteristics peaks of Co, Pt, and Au to obtain a high signal to noise ratio. CasaXPS® Software was used to analyse the various spectra obtained and tabulated values of the electron binding energies of various elements were available from the 'Handbook of X-ray Photoelectron Spectroscopy' [14].

XPS utilises the Photoelectric Effect and involves irradiating a sample with photons of certain energy - $h\nu$. When the atoms within the sample adsorb these photons, they release electrons with a certain kinetic energy E_k. The binding energy (E_b) of these electrons can then be calculated using the Equation 4.2-1, in which φ is a work function characteristic to the spectrometer [15]. Since the electrons can only travel between 1-10 inter-atomic distances, the probing depth of XPS is less than 6nm, making it a surface sensitive technique. E_b of an electron depends on the attraction it feels from the nuclei within its environment and is thus element specific. With XPS, core shell electrons are normally used in elemental analysis but can also been used to determine the oxidation state of an element because different oxidation states result in shifts from the main elemental photoelectron line because the electrons experience a different strength of attraction to the atomic nuclei. Changes in the oxidation state of an element result in shifts of 0-3eV. Normally, the higher the oxidation state, the higher the binding energy [15].

$$E_b = h\nu - E_k - \varphi \qquad \textbf{Equation 4.2-1}$$

Most samples were prepared by pressing a thin layer of each catalyst sample evenly over sticky carbon tape. The carbon tape was advantageous because it helped prevent sample charging, although the spectra of the samples presented large background C 1s peaks (285eV), which were in close proximity to the Au 4d (335eV and 353eV) and Pt 4d (317.5 and 334eV) peaks. Consequently, samples were also analysed in metallic sample holders to enable better identification of the peaks adjacent to C 1s. In this case, sample charging was prevented by bombardment with low energy electrons and all spectra normalised relative to the adventitious C 1s peak.

4.2.6.1 Quasi - in situ X-ray photoelectron spectroscopy analyses of reduced samples

Quasi-in situ XPS analyses were used to determine the effect of reduction promoters on the Co phases formed following reduction. Due to its surface sensitivity, the results from XPS were complementary to the bulk phase data obtained from the in situ XRD analyses (see Sec. 4.2.5.1) and the TGA (see Sec. 4.2.4).

In situ XPS analyses of the reduced catalyst samples were carried out in the Kratos AXIS Ultra Spectrometer equipped with a monochromatic Al Kα radiation source (Al Kα = 1486.6eV). The catalysts were activated at the selected standard reduction conditions of 350°C for 12 hours, after which the inlet and outlet of the tubular quartz reactor were sealed in pressurised hydrogen. The reactor was transferred to an Argon-flushed glove box to enable sample preparation without the risk of reoxidation. Sample preparation was carried out by pressing the reduced catalysts into sticky carbon tape, after which the samples were transferred under an inert atmosphere from the glove box to an isolated chamber that could be inserted in the spectrometer for analysis.

4.2.7 Hydrogen chemisorption

Hydrogen Chemisorption analyses were used to calculate the metal surface area and dispersion in the activated catalysts.

Measurements were performed in a Micromeritics ASAP 2020 Analyzer using the static volumetric high vacuum technique. 0.1-0.2g of catalyst was loaded into a U-tube quartz reactor, which was then dried overnight at 90°C. Catalyst activation was carried out in situ according to the selected pre-treatment reduction conditions of 350°C in pure H_2 for 12 hours after which the system was evacuated for the chemisorption analyses.

The H_2 adsorption isotherms were measured at 125°C, isotherms were collected between 0 and 500 mmHg, and strongly versus weakly adsorbed species were distinguished by measuring a second isotherm after the system had been evacuated for 60 minutes.

4.3 Low Temperature Fischer-Tropsch Reaction in the Laboratory-Scale Test Unit

The **reactor loading** was adjusted so that 0.1g of cobalt was present, while the metal loading was maintained at 0.05g for the Pt/Al_2O_3 and Au/Al_2O_3 samples. All catalysts were mechanically mixed with silicon carbide (SiC) in a ratio of 1:5 in order to increase the heat removal capacity of the catalyst bed.

The selected catalyst **activation treatment** was a reduction in pure H_2 at 350^oC and atmospheric pressure. The Gas Hourly Space Velocity (GHSV) of H_2 was set to a high value of $720ml\cdot(min\cdot gCo)^{-1}$(NTP) to minimise the generation of high water partial pressures, which have been reported to facilitate sintering and the formation of strong metal support interactions [16, 17]. A 12-hour reduction period was selected to allow for overnight completion of the pre-treatment.

The **reaction conditions** selected for the LTFT reaction were 20 barg, 220^oC, $H_2/CO=2$, and a $GHSV_{syngas}$ of 2400 $ml\cdot(min\cdot gCo)^{-1}$. On completion of the reduction, the reactor was allowed to cool to 150^oC and flushed with Ar. The rig was then pressurised, and the required flow rate of syngas set while on ‘reactor bypass mode’ to allow for verification of the syngas concentration using the online GC-TCD. Thereafter, the syngas flow was set to ‘reactor mode’ and the reactor temperature ramped to 220^oC at a rate of $1^oC/min$.

The slow temperature ramp was selected to avoid sudden temperature runaways because of the high exothermicity of the reaction. High temperatures could result in sintering especially at the high conversions typically attained at start-up. The slow temperature ramp also allowed the liquid hydrocarbon product to slowly build-up around the catalyst, which helped prevent temperature runaways because the liquid increased the aggregated heat capacity of the catalyst bed compared to pure syngas.

The temperature ramp at start-up meant that reaction conditions were only realised after approximately 1.5 hours on stream, at which point **on-line analysis** of the permanent gases including H_2, CO, CH_4, and CO_2 began. The GC-TCD used was a Varian 3300 equipped with a 10ft X 1/8” stainless steel carbosieve column (SUPELCO) with Ar as the carrier gas. The ampoule technique [18-21] was used for **off-line** sampling of the gaseous hydrocarbon product, which commenced as soon as steady-state conversions were observed with the GC-TCD. The gaseous hydrocarbon product in the collected ampoules was analysed using a

Varian 3900 GC-FID. The reference gases for the TCD and FID analyses were N_2 and cyclohexane (C_6H_{12}) respectively. For this purpose, **reference gas cylinder** composed of 10ppm C_6H_{12}-in-N_2 was periodically made-up onsite.

The duration of each Fischer-Tropsch run (including reduction) was approximately 3 days, after which the reactor was allowed to cool to room temperature under an Ar flush, and the test-unit was depressurised to 1 barg. A **passivation** treatment in pure CO_2 was subsequently carried out to allow for spent catalyst recovery. The conditions used were GHSV of 400ml/min·gCo, 1 barg, 25°C, for 1 hour.

4.3.1 Operation of the laboratory test unit

The Piping and Instrumentation Diagram (P&ID) of the laboratory test unit and an illustration of the reactor are shown in Figure 4.3-1 and Figure 4.3-2 respectively. LabVIEW® software was used as a graphical interface to control the heaters and mass flow controllers while the reactor pressure was manually controlled.

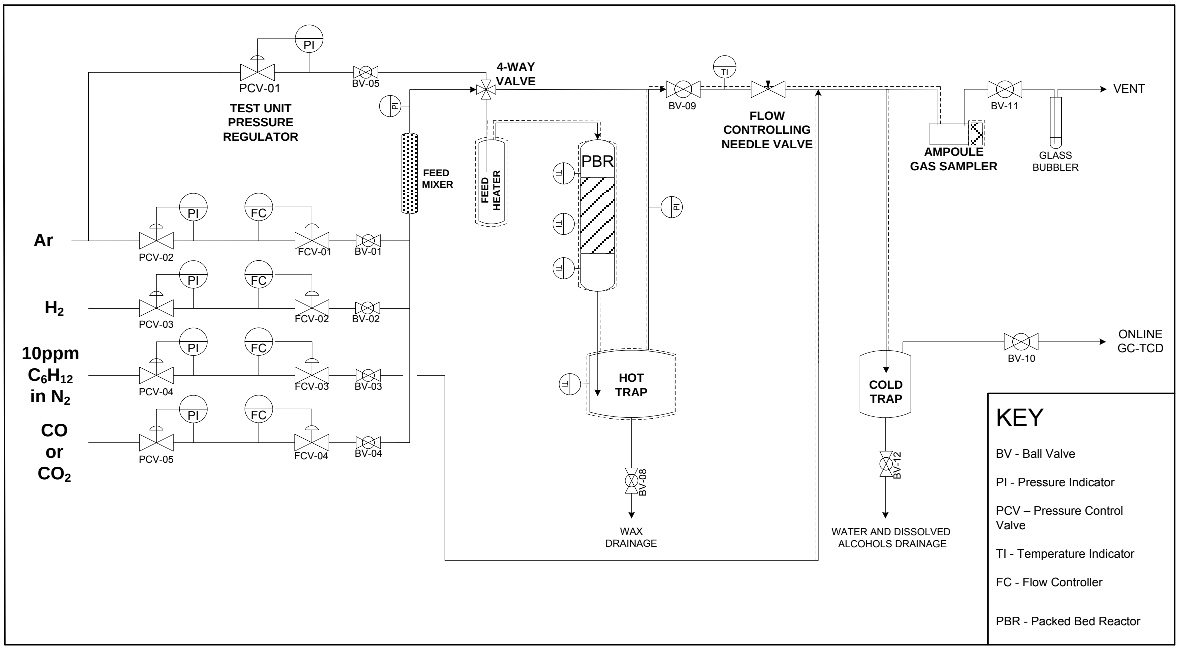

Figure 4.3-1: Piping and Instrumentation Diagram (P&ID) of the laboratory test-unit.

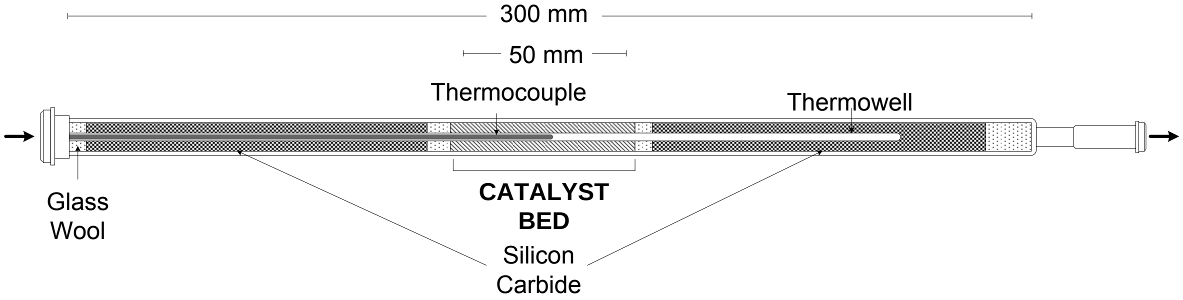

Figure 4.3-2: Illustration of the Stainless Steel Packed Bed Reactor (PBR) used for the Fischer-Tropsch reactions (to scale). L=325 mm, OD = ½”, and ID = 10mm.

In order to ensure homogeneity prior to being fed to the reactor the reactor, the fresh gases were blended in Feed Mixer, which was a stainless steel tube packed with glass beads. The packing resulted in a labyrinth of narrow channels through which the product gases were forced, mixing turbulently in the process. The mixed feed was then pre-heated to 150°C in the Feed Heater, which was a ½” wide stainless steel tubing packed with SiC into which the gases were fed via a dip-tube. The heated syngas was then fed to the reactor via a **4-Way Valve** that operated in two modes, namely ‘reactor flow’ mode and ‘reactor bypass’ mode. During the ‘reactor flow’ mode, the syngas flowed through the reactor with high-pressure Ar in the bypass line and vice versa during ‘reactor by-pass’ mode.

The high pressure Ar was used in combination with the Flow Controlling **Needle valve** to control the reactor pressure, which was set as follows: the 4-Way Valve was first set to ‘reactor bypass’ mode and the Ar pressure set to the required value of 20 bar via the Test-unit Pressure Regulator. The Flow Controlling Needle valve was then adjusted so that it allowed for an outlet flow-rate equal to F_{syngas} + 20ml/min (of Ar). The syngas flow rate was then set via the corresponding mass flow controllers. The Fischer-Tropsch reaction started when the 4-Way Valve was switched to ‘reactor flow’ mode after which no further adjustment of the Flow Controlling Needle valve was required.

Temperature control in the reactor was carried out by manipulating the temperatures of the three coil heaters placed along the length of the reactor tube in order to attain an isothermal region of approximately 100 mm in which the catalyst was loaded (see Fig. 4.3-2). Fischer-Tropsch products that were liquid at above 180°C and 20 bar condensed in the Hot Trap, while the more volatile products remained in the gaseous product, which was subsequently mixed with the 10 ppm C_6H_{12}-in-N_2 **reference gas** mixture. Thereafter online product analysis was carried out using the GC-FID or off-line samples were collected using glass ampoules at the **Ampoule Gas Sampler**.

4.3.2 Ampoule sampling technique

The ampoule sampling technique used for offline analysis using the GC-FID was developed by the group of Schulz [18-21].

Figure 4.3-3 includes an image of an ampoule sampling point and the ampoules before and after sample collection. The temperature of the sampling point was maintained at 200°C to prevent condensation of the less volatile products and obtain a representative product distribution in the FID chromatograms. Making of the ampoules involved using a butane torch to remould commercially available glass Pasteur pipettes '**A**' into a form that was suitable for ampoule sampling point after which the pipettes were evacuated and sealed. To collect a sample, the evacuated ampoule '**B**' was inserted (capillary end first) through a gas tight septum within the ampoule sampling port. The extreme end of the capillary was then broken off by turning the breaking fork, at which point the gas product was rapidly sucked into the evacuated ampoule. The base of the capillary end was subsequently sealed using a hand held brulée torch to the form '**C'**, which could be placed in an ampoule-breaking set-up configured to the Varian 3900 GC-FID.

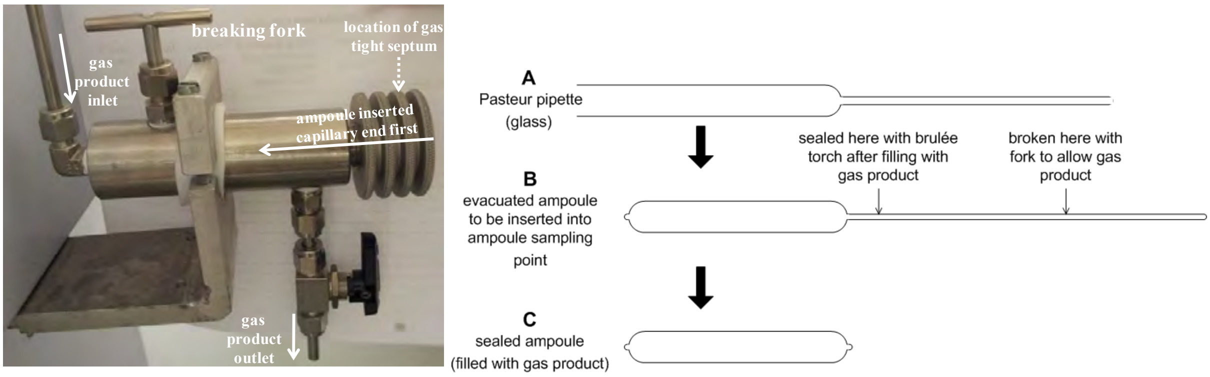

Figure 4.3-3: ***Left:*** Image of an ampoule sampling point. ***Right:*** Illustration of the glass Pasteur pipettes before and after ampoule samples are collected

4.3.3 10ppm cyclohexane in N_2 reference gas cylinder

The reference gases for the TCD and FID analyses were N_2 and cyclohexane (C_6H_{12}) respectively, and thus a 35 bar **reference gas cylinder** composed of 10ppm C_6H_{12}-in-N_2 was periodically made-up on-site and connected downstream of the hot trap (see Fig. 4.3-1).

Figure 4.3-4 includes the schematic of how the reference gas cylinder was prepared. The process involved filling a U-shaped ¼” stainless steel tubing with approximately 9ml of liquid cyclohexane. The U-shaped pipe was then attached upstream of an empty cylinder (with a two-way flow valve in the cylinder head), and upstream of a full pure N_2 cylinder. Thereafter, the N_2 cylinder was opened, which allowed the gas to push the cyclohexane into the empty reference gas cylinder. The reference gas cylinder was allowed to fill to a maximum pressure of 35bar to maintain the cyclohexane in the gas phase. Thereafter, the filled 10-ppm cyclohexane (C_6H_{12})-in-N_2 reference gas cylinder was calibrated using a GC-FID and a standard calibration gas from a cylinder with a known composition.

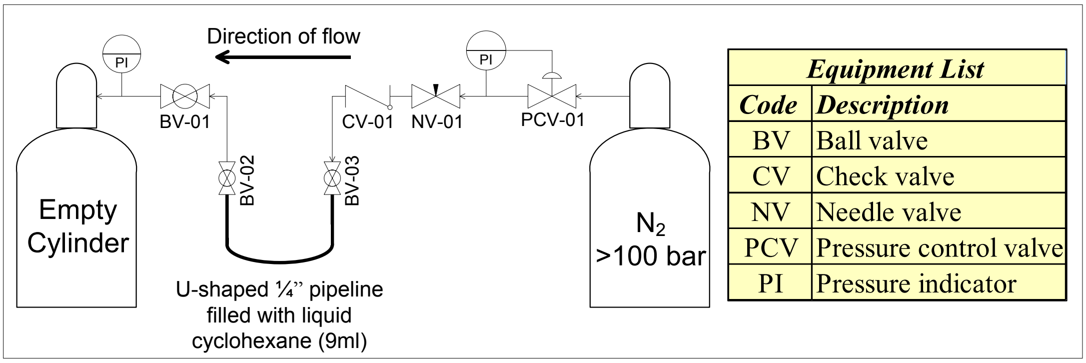

Equipment List

Code	***Description***
BV	Ball valve
CV	Check valve
NV	Needle valve
PCV	Pressure control valve
PI	Pressure indicator

Figure 4.3-4: Schematic of the set-up used to prepare the 10-ppm cyclohexane (C_6H_{12}) in N_2 reference gas cylinder.

4.4 References

[1] Sasol Technology Technical Data Sheets, “PURALOX®/CATALOX® High purity activated aluminas”, http://www.sasoltechdata.com/tds/PURALOX_CATALOX.pdf (accessed Oct 9, 2014).

[2] G. Jacobs, P.M. Patterson, Y. Zhang, T. Das, J. Li, B.H. Davis, Appl. Catal. A: Gen. 233 (2002) 215-226.

[3] J. Case, “Gold catalysts prepared by ion exchange for use in ethylene glycol oxidation: An exploratory study”, Masters’ Thesis, University of Cape Town, South Africa, 2008.

[4] T. van Heerden, “Characterization of Au catalysts for CO hydrogenation”, Masters’ Thesis, University of Cape Town, South Africa, 2012.

[5] S. Ivanova, C. Petit, V. Pitchon, Appl. Catal. A: Gen. 267 (2004) 191-201.

[6] C. Pirovano, S. Trasatti, J. Electroanal. Chem. Interfacial Electrochem. 180 (1984)171-184.

[7] S. Ardizzone, G. Spinolo, S. Trasatti, Electrochim. Acta 40 (1995) 2683-2686.

[8] E. van Steen, Unpublished data, University of Cape Town, South Africa, 2009.

[9] S. Zwane, Unpublished data, University of Cape Town, South Africa, 2003.

[10] W. Gao (Ed.), Developments in High Temperature Corrosion and Protection of Materials, Woodhead Publishing Ltd, Cambridge, 2008.

[11] B. Clapham, “The Development of an In-Situ X-Ray Diffraction Cell for Fischer-Tropsch Catalyst Characterisation”, Masters’ Thesis, University of Cape Town, South Africa, 2012.

[12] Capillary Tube Supplies Ltd., “Glass Specification” http://www.capillarytubes.co.uk/acatalog/Glass_Specification.html (accessed Oct 13 2014).

[13] M.C.M. Claeys, N.F. Fischer. United States Patent 8 597 598.

Image courtesy of M. Wüst, “Unpublished data”, University of Cape Town, South Africa, 2011.

[14] W.F. Stickle, P.E. Sobol, K. D. Bomben (Eds.), Handbook of X-ray Photoelectron Spectroscopy, Vol. 40, Perkin Elmer, Eden Prairie – Minnesota, 1992.

[15] J.W. Niemantsverdriet, Spectroscopy in Catalysis, 3rd ed., Wiley-VCH, Weinheim, 2007.

[16] C.H. Bartholomew “History of Cobalt Catalyst Design for Fischer-Tropsch Synthesis” Presentation at AIChE 2003, New Orleans, LA (www.fischertropsch.org).

[17] J. van de Loosdrecht, B. Balzhinimaev, J.A. Dalmon, J.W. Niemantsverdriet, S.V. Tsybulya, A.M. Saib, P.J. van Berge, J.L. Visagie, Catal. Today 123 (2007) 293-302.

[18] H. Schulz, H. Gökcebay, in: J.R. Kosak (Ed.), Catalysis of Organic Reactions, Marcel Dekker, New York, 1984.

[19] H. Schulz, S. Nehren, Erdol and Kohle Erdgas, Petrochem. 39 (1986) 93-94.

[20] H. Schulz, Appl. Catal. A: Gen. 186 (1999) 3–12.
[21] H. Schulz, M. Claeys, Appl. Catal. A: Gen. 186 (1999) 71-90.

Chapter 5

Hydrogen Spillover during the Reduction of Pt and Au Promoted Co/Al_2O_3 Catalysts

5.1 Analysis of Prepared Catalyst Samples

5.1.1 Metal loading and catalyst composition

Table 5.1-1 shows the metal loading in the *calcined* catalyst samples according to ICP-OES. The deviations in the cobalt loading were small, i.e. just 8-16% of the target and were probably associated with the characterisation technique and the weighing of the precursor during preparation. With cobalt nitrate, the error associated with weighing is often elevated due to variation in the extent of hydration that is typically observed with the salt [1].

Table 5.1-1: Metal loading of Co, Pt and Au in *calcined* samples according to ICP-OES.

	Metal loading, wt.%*		
	Co	**Promoter**	
		Pt	**Au**
Co_3O_4/Al_2O_3	20.0 ± 0.18	-	-
Pt/Al_2O_3	-	0.57± 0.05	-
$Pt-Co_3O_4/Al_2O_3$	20.1 ± 0.25	0.63± 0.02	-
Au/Al_2O_3	-	-	0.33 ± 0.00
$Au-Co_3O_4/Al_2O_3$	21.7± 0.12	-	0.30

*Prepared loadings were 0.5%Promoter and 20%Co in reduced catalyst OR 0.5%Promoter and 18.6%Co in calcined catalyst.

The gold loading was much lower than the target loading of 0.5% despite using 55% excess gold precursor ($HAuCl_4$) during the catalyst preparation (Sec. 4.1.2). Besides arising from possible errors in the ICP-OES analysis, deviations in the final loading likely stemmed from the anion exchange technique, in which the metal loading efficiency varies with a number of factors including the support type and the pH, which determines the dominant gold-chloro-hydroxy complex in solution (Sec. 4.1.2). Even though the anion exchange technique results in small crystallites with a relatively narrow size distribution, gold reportedly has a low affinity for oxidic supports, which results in low loading efficiencies even at the ideal pH values [2]. The ammonia washing step, which was incorporated to exclude Cl^- ions, was also expected to exacerbate the final Au loading because washing reportedly results in loss of approximately 30% of the Au [2].

5.1.1.1 X-ray Diffraction (XRD)

Figure 5.1-1 shows the X-ray diffractograms of the Al_2O_3 support and the calcined samples in the Pt-Co and Au-Co catalyst systems. The subsequent Table 5.1-2 includes the characteristic peak positions of γ-Al_2O_3, Co_3O_4, CoO, Pt, and Au obtained from the International Centre for Diffraction Data PDF-2 database. The structure of the Puralox SCCa 5-150 support contained a mixture of γ-Al_2O_3 and δ-Al_2O_3 (Fig. 5.1-1). As discussed in Sec. 4.2.5, the crystal structure of δ-Al_2O_3 is unknown and was not available in the International Centre for Diffraction Data PDF-2 database. Rietveld refinement to obtain the provided Co_3O_4 crystallite sizes was therefore carried out by defining a 'Peaks Phase' for the Al_2O_3 support as described in Sec. 4.2.5. The predominant state of cobalt in all samples was Co_3O_4 and a crystallite size of 12.7nm was determined for Co/Al_2O_3 (Fig. 5.1-1).

Pt-Co Catalyst System: The 14.2% increase in the Co_3O_4 crystallite size of Pt-Co/Al_2O_3 compared to Co/Al_2O_3 suggested a degree of sintering, which may have arisen from the extra calcination step following impregnation of Co/Al_2O_3 with Pt (Sec. 4.1.1.3). Despite detection via ICP (Table 5.1-1), no peaks corresponding to a Pt phase were observed in the diffractograms of Pt/Al_2O_3 and Pt-Co/Al_2O_3 (Fig. 5.1-1). Pt peaks may have overlapped with those of other catalyst constituents but were also less likely to be observed due to the low metal loading, and the resultant small Pt crystallite sizes. The lower threshold for detection using X-ray diffraction is approximately 30Å.

Au-Co Catalyst System: Despite detection via ICP, no peaks corresponding to gold (or its oxides) were visible in Au/Al_2O_3, although a very small gold peak was visible with Au-Co/Al_2O_3 at $2\theta = 44.5^\circ$ (Fig. 5.1-1). Most Au peaks included in Table 5.1-2 were not observed due to overlap with either Co_3O_4 or Al_2O_3 peaks. Like in the Pt-Co catalyst system, the promoter crystallites were less likely to be observed due to the low metal loadings, and the consequent small crystallite sizes.

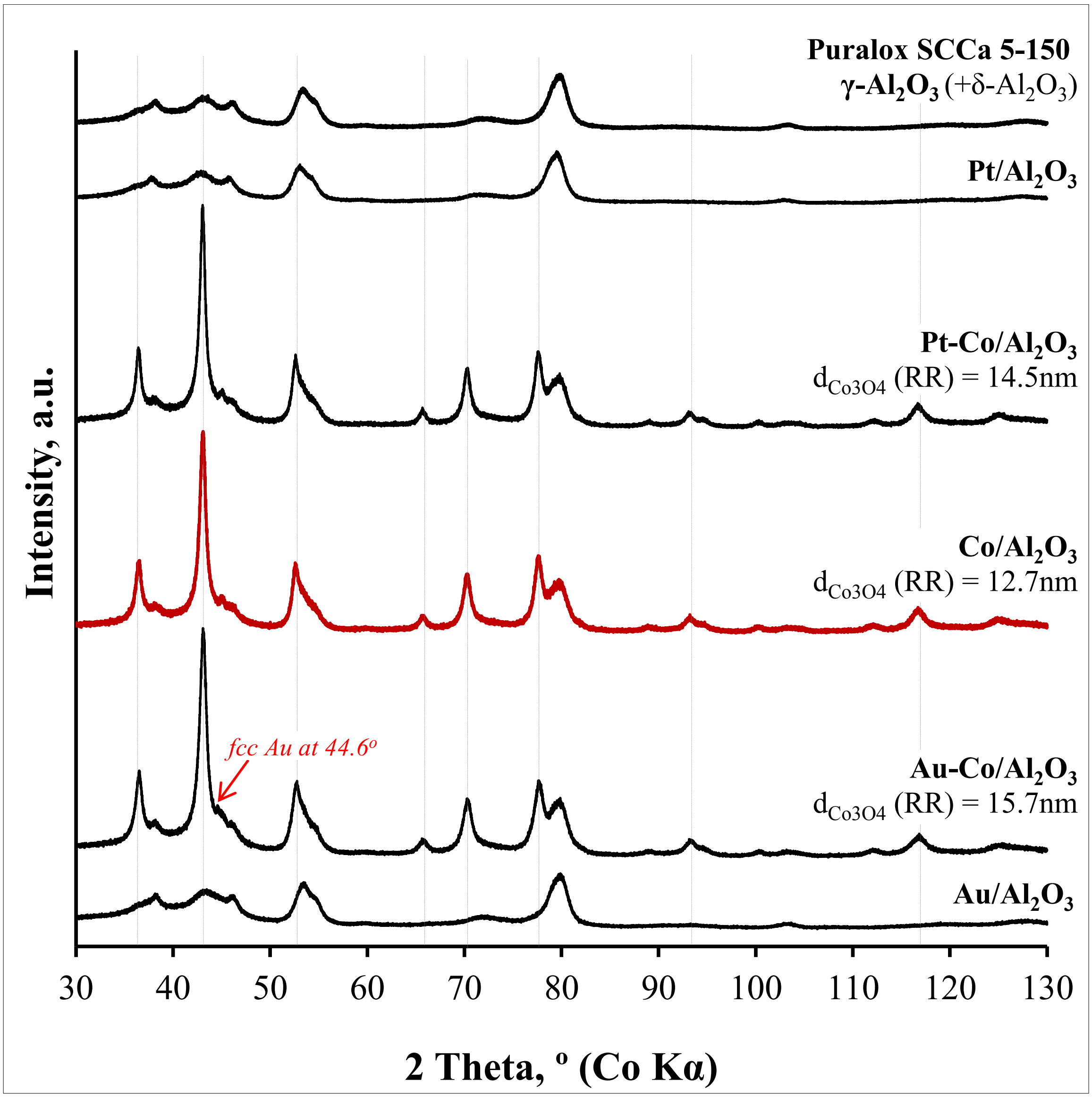

Figure 5.1-1: X-ray Diffractograms of the γ-Al_2O_3 support and calcined samples. The Co_3O_4 crystallite sizes were determined using Rietveld refinement (RR). Grey vertical lines indicated the main Co_3O_4 peak positions.

Table 5.1-2: Characteristic peak positions of γ-Al_2O_3, Co_3O_4 , CoO, $CoAl_2O_4$, fcc Pt and fcc Au according to the International Centre for Diffraction Data PDF-2 database.

Structure	**Peak positions (2θ, °)**									
γ-Al_2O_3	43	46.1	53.4	54.8	60	71.8	79.7			
Co_3O_4	43	45	52.6	57.7	65.6	70.3	77.6	81.8	88.8	116.5
CoO	42.6	49.7	72.9	88.2	77.6	88.7				
$CoAl_2O_4$	42.9	52.5	65.6	70.1						
fcc Pt	46.5	52.2	80.3	98.2	104.3					
fcc Au	44.6	52.0	76.7	93.3						

5.1.1.2 X-ray photoelectron spectroscopy (XPS)

Figure 5.1-2 includes the broad XPS scans of the all samples used in this study.

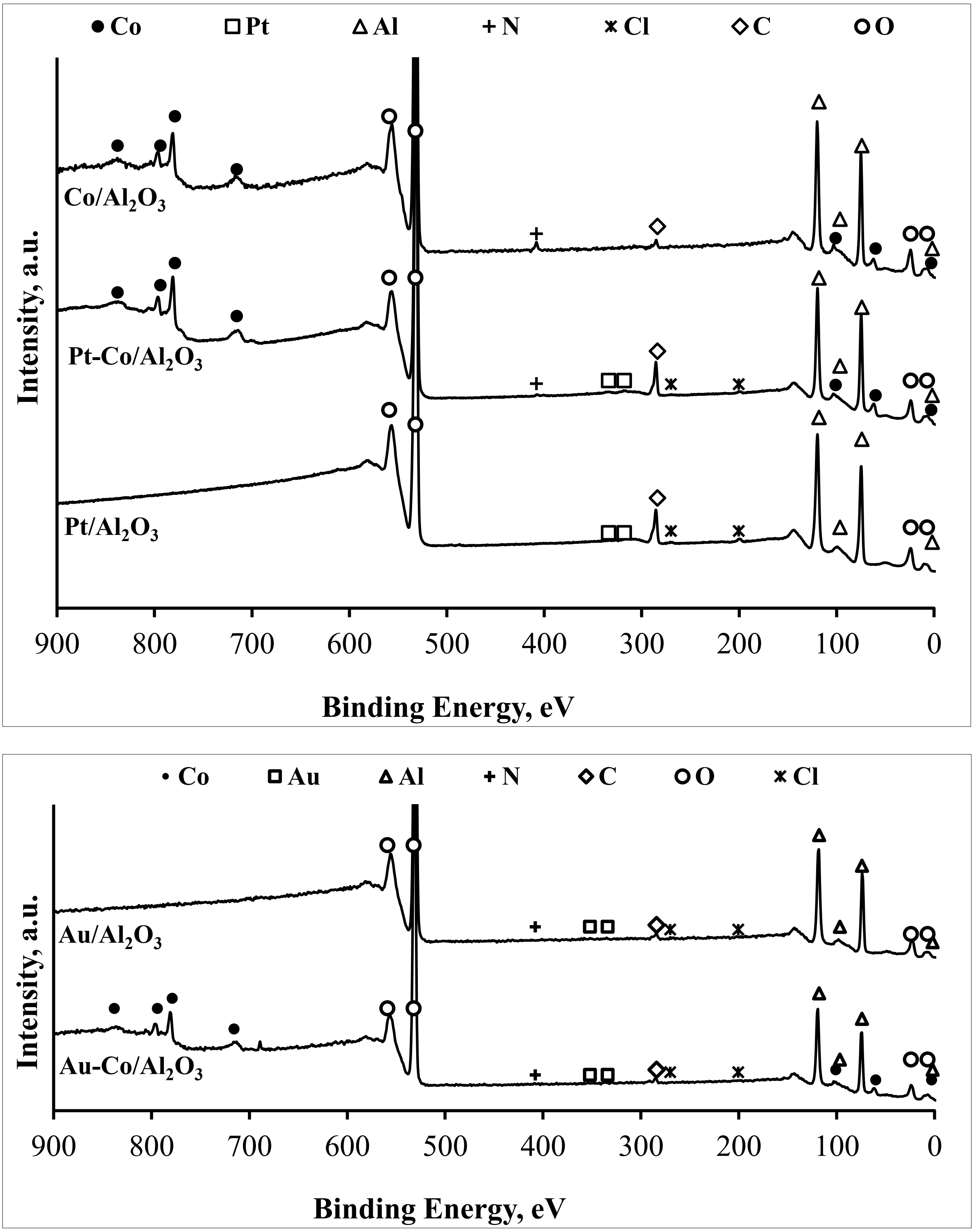

Figure 5.1-2: Broad X-ray Photoelectron Spectroscopy (XPS) scans showing all identified elements. ***Top:*** Pt-Co Catalyst System. ***Bottom:*** Au-Co Catalyst System.

XPS provided an elemental surface analysis and was used to shed light on the environment of the cobalt phase. Peaks corresponding to Au, Pt, O, Al and Co were observed in the relevant samples as expected from the catalyst preparation and X-ray diffraction. For all samples, the characteristic peak of ubiquitous atmospheric carbon was also observed at 284.5eV (C 1s). Except in the case of the spent samples following the Fischer Tropsch reaction (Appendix F1), it was unlikely that the catalyst samples contributed any integral carbon to this peak.

Peaks corresponding to Co, O and Al were present in the broad scan of Co/Al_2O_3. However, besides the C 1s peak, peaks consistent with nitrogen at 408eV (N 1s) were also observed and attributed to leftover nitrates from the use of the $Co(NO_3)_2 \cdot 6H_2O$ precursor during catalyst preparation. The N 1s peak at 408eV was also observed in $Pt\text{-}Co/Al_2O_3$. In addition, very small chlorine peaks at 271eV and 200.5eV, corresponding to Cl 2s and Cl 2p respectively were observed in the scans of the calcined $Pt\text{-}Co/Al_2O_3$ and Pt/Al_2O_3 samples. These peaks were attributed to the use of the Tetrammine Platinum (II) Chloride precursor during catalyst preparation. Peaks corresponding to nitrogen/nitrates at 408eV (N 1s) were absent on the surface of $Au\text{-}Co/Al_2O_3$. Leftover nitrates from the $Co(NO_3)_4$ precursor were most likely removed during the ion exchange preparation technique used for Au, which was added *sequentially* to the already prepared and calcined Co/Al_2O_3 sample (Sec. 4.1.2). Leftover nitrates may have dissolved into solution during the extended aging times that included stirring the sample in water for 24 hours. Leftover nitrates may have also been eliminated during the subsequent washing steps with both water and ammonia. Very low intensity chlorine peaks at the Cl 2s photoelectron line, which were also present with the Pt-Co System, were visible in the broad scans of the gold samples. These small peaks were remnants of the gold precursor ($HAuCl_4$) and persisted despite the ammonia washing step following the anion exchange technique.

The Co 2p regions of the Co/Al$_2$O$_3$, Pt-Co/Al$_2$O$_3$ and Au-Co/Al$_2$O$_3$ samples are shown in Figure 5.1-3: *Left*, while the Co 2p region of the bulk Co$_3$O$_4$ reference compound is included in Figure 5.1-3: *Right*. The Co 2p peaks were similar to those of the bulk Co$_3$O$_4$ reference compound, and thus the XPS analyses concurred with the results from XRD (Fig. 5.1-1) where Co$_3$O$_4$ was found to be the dominant cobalt phase.

The characteristic Co 2p doublet (Co 2p$_{3/2}$ and Co 2p$_{1/2}$), which arises due to spin-orbit splitting [3] was observed for all samples. In elemental Co, the main photoelectron lines are present at 793eV (Co 2p$_{1/2}$) and 778eV (Co 2p$_{3/2}$). However, Co is in a higher oxidation in Co$_3$O$_4$, which causes the main photoelectron lines to shift by +3eV. The binding energy of the relevant Co species increases as follows: Co^0 < Co^{2+} < Co^{3+}. Therefore the Co 2p peaks were asymmetric because both Co^{3+} and Co^{2+} ions occur in Co$_3$O$_4$. The Co 2p peaks of Co^{3+} and Co^{2+} were also accompanied by shoulders at higher binding energies known as 'shake-up satellites'. Shake-up occurs when an emitted photoelectron collides with another electron within the atom and loses some of its kinetic energy, which causes it to appear at a higher binding energy. Shake-up could also be leveraged to ascertain oxidation states because the satellites are greater for Co^{2+} compared to Co^{3+}, and are not present with Co^0. It can be observed that the shake-up peaks in the various samples in Figure 5.1-3 were broad, which was because the shake-up peaks of Co^{2+} were present at +5eV while those of Co^{3+} were present at +10eV from the main elemental photoelectron lines.

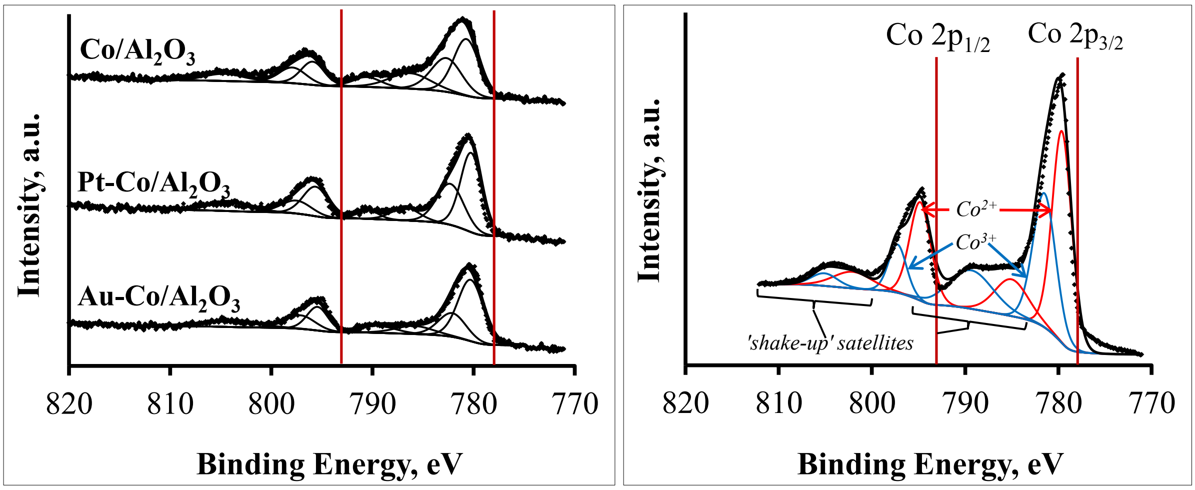

Figure 5.1-3: XPS Scans in the Co 2p region of calcined samples. Vertical lines indicate the main photoelectron lines of elemental Co at 793eV (Co 2p$_{1/2}$) and 778eV (Co 2p$_{3/2}$). ***Left:*** Co/Al$_2$O$_3$, Pt-Co/Al$_2$O$_3$, and Au-Co/Al$_2$O$_3$. ***Right:*** bulk Co$_3$O$_4$ reference compound.

The contribution of two oxidation states is more clear with the peak deconvolution of the Co_3O_4 reference sample due to the high peak intensity (Figure 5.1-3: *Right*). A pair of Gaussian peaks was fitted at each Co 2p photoelectron line to represent the contribution of Co^{3+} and Co^{2+}, followed by a second pair of peaks under each shake-up satellite. The ideal area ratio of each pair of Gaussian peaks was 2:1 in line with the stoichiometry of Co_3O_4, i.e. $2Co^{3+}$: $1Co^{2+}$: $1O_4^{2-}$ but this was not strictly adhered to for the best-fit curves.

Figure 5.1-4 shows the Pt 4d region of the Pt containing samples, while Figure 5.1-5 shows the Au 4d region of the Au containing samples. The peaks corresponding to both promoters had much lower signal to noise ratios than the cobalt peaks in Figure 5.1-3 because the low promoter loadings were used. Unfortunately, the low peak intensities inhibited precise deductions concerning the oxidation state of both promoters.

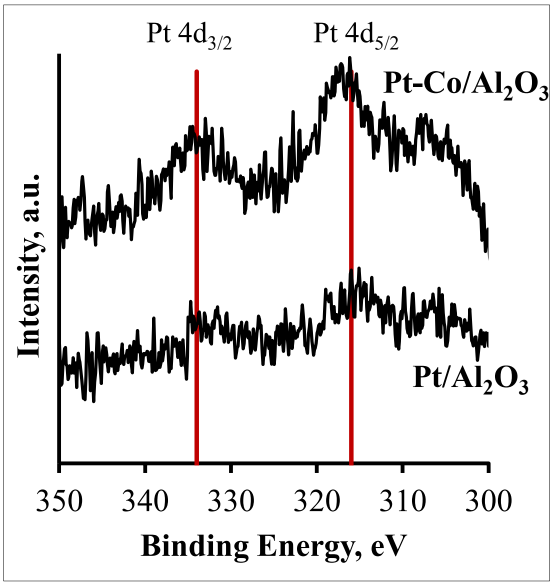

Figure 5.1-4: XPS Scans in the Pt 4d region of calcined Pt-Co/Al_2O_3 and Pt/Al_2O_3. The red lines at 315 and 332eV represent the main elemental photoelectron lines.

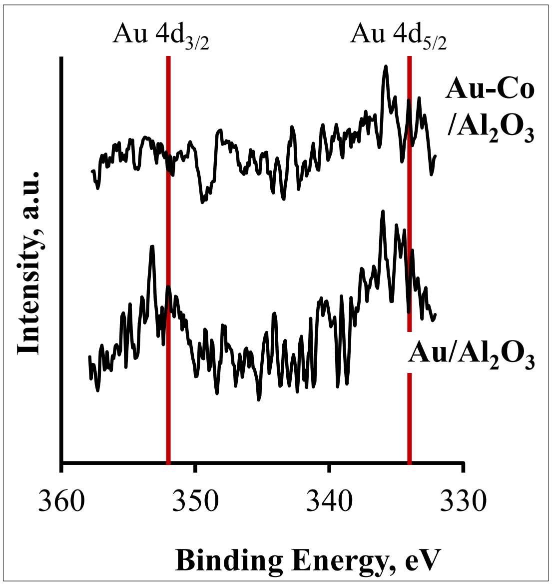

Figure 5.1-5: XPS Scans in the Au 4d region of calcined Au-Co/Al_2O_3 and Au/Al_2O_3. The red lines at 353 and 335eV represent the main elemental photoelectron lines.

The Pt 4d peaks in Pt-Co/Al_2O_3 (at 317.5 and 334eV) were shifted to higher binding energies relative to the main photoelectron lines of elemental Pt, which appear at 315 and 332eV. Shifts to higher binding energies are indicative of higher oxidation states (i.e. fewer electrons per atom) [3]. Therefore, Pt may have been oxidic following calcination, which was unexpected due to its strong noble character.

The Au 4d peaks appeared at slightly higher binding energies (~+1.4eV) relative to the main elemental photoelectron lines at 335eV and 353eV. This too suggested that Au was in a higher oxidation state and not present as metallic Au^0. As with the Pt-Co catalyst system, the low peak intensities inhibited accurate determination of the Au oxidation state. It was noted that the perceived shift in the binding energy of the Au 4d peaks may have arisen from interference with the tail of the C 1s peak at 285eV (due to ubiquitous atmospheric carbon; refer to broad scan in Fig. 5.1-2). Determination of the oxidation state of the Au crystallites was thus inconclusive due to the low peak intensities, and the potential interference from the C 1s peak.

5.1.2 Size distributions of Co, Pt and Au particles

5.1.2.1 Size distributions of particles in the Pt-Co catalyst system

Co/Al_2O_3: The results from Transmission Electron Microscopy (TEM) analyses of the Co/Al_2O_3 sample are shown in Figures 5.1-6 and 5.1-7. The TEM micrographs of calcined Co/Al_2O_3 (Fig. 5.1-6: *Left* & *Centre*) were taken following sample preparation using the resin embedding method, and clearly showed the cobalt clusters and the structure of the Al_2O_3 support. The TEM micrographs of reduced Co/Al_2O_3 (Fig. 5.1-6: *Right* and Fig. 5.1-7) were taken following sample preparation using the sonification method.

With supported catalysts, TEM imaging is dependent on the differences in density between the active metal and the support because this provides the contrast required to differentiate between the components. However, the electron density of metallic oxides is lower than that of the corresponding metals, and closer to that of the Al_2O_3 support, which caused difficulties in distinguishing Co_3O_4 particles from the support. With calcined Co/Al_2O_3, only the *clusters* of cobalt particles in the range of 150-250 nm were clearly visible (Fig. 5.1-6: *Left*) but the individual cobalt particles were difficult to make-out (Fig. 5.1-6: *Centre*). A cobalt cluster arises during the calcination process when large $Co(NO_3)_2$ droplets segregate into smaller ones as they decompose [4], which causes the Co particles to concentrate in circular areas of up to a few hundred nanometres in diameter. The size of a cluster is thus roughly equivalent to that of the corresponding $Co(NO_3)_2$ droplet from which it formed [4]. Due to the low contrast between the Al_2O_3 and Co_3O_4, and it was not possible to obtain particle size distributions in the *calcined* sample for comparison with those in the *reduced* samples.

Reducing the catalyst samples prior to TEM analysis introduced the contrast required to accurately identify the cobalt particles (Fig. 5.1-6: *Right* & Fig. 5.1-7: *Left*). The corresponding cumulative lognormal distribution of a sample size of 100+ cobalt particles is shown in Figure 5.1-7: *Right* from which it is observed that all the cobalt particles were smaller than 17nm. The average cobalt particle size and standard deviation are included inset and were determined to be 10.0nm and 6.3nm respectively from the best-fit curve fitted to the lognormal distribution. The particle size distributions were measured using ImageJ® software.

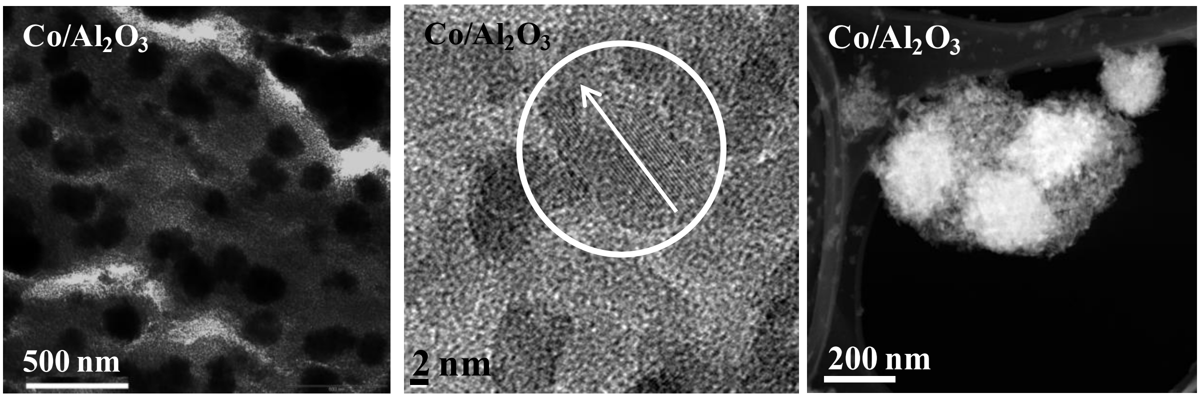

Figure 5.1-6: ***Left:*** TEM micrograph of calcined Co/Al$_2$O$_3$ showing 150-200nm Co$_3$O$_4$ clusters on the Al$_2$O$_3$ support. ***Centre***: A Co$_3$O$_4$ particle with visible lattice spacing in calcined Co/Al$_2$O$_3$ is circled. The arrow shows the direction and length of the lattice planes. ***Right:*** STEM micrograph showing illuminated Co clusters in reduced Co/Al$_2$O$_3$.

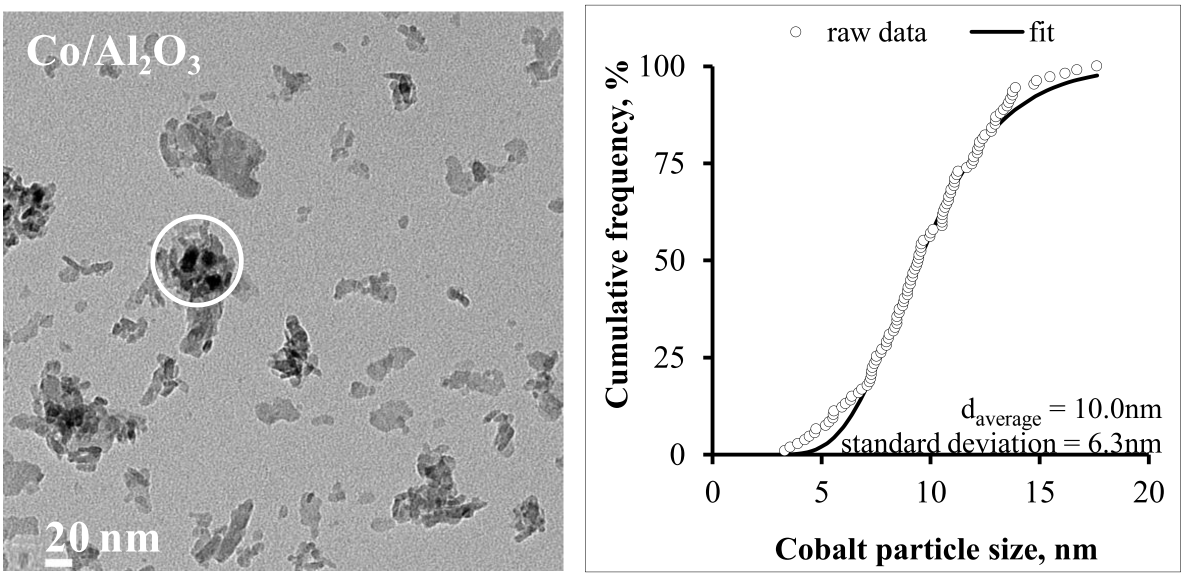

Figure 5.1-7: ***Left:*** TEM micrograph of reduced Co/Al$_2$O$_3$ with some Co particles enclosed in a circle. ***Right:*** Best fit cumulative lognormal distribution to a sample size of 100+ cobalt particles in reduced Co/Al$_2$O$_3$. Note that reduction was carried out at 400°C.

Pt/Al_2O_3: The results from TEM analyses of Pt/Al_2O_3 are shown in Figures 5.1-8 and 5.1-9. The contrast between Pt and the support in the calcined samples was poor so both Pt/Al_2O_3 and Pt-Co/Al_2O_3 were reduced at 400ºC for 4 hours (and then passivated), after which sample preparation was carried out using the sonication method. The Pt particles were denser, and clearly visible in the reduced sample, which suggested that they were probably present as oxides in calcined Pt/Al_2O_3. This observation concurred with the XPS analysis of the Pt 4d region of calcined PtAl_2O_3 in Figure 5.1-4, which was consistent with non-metallic Pt species due to the shift of the peaks to higher binding energies relative to the elemental photoelectron lines.

The cumulative lognormal distribution of 130+ Pt particles is shown in Figure 5.1-8: *Right* from which the average Pt particle size was determined as 1.3nm and the standard deviation as 0.85nm. The small Pt particles were in accordance with expectations from the XRD diffractogram in Figure 5.1-1 in which Pt peaks were not observed. It was not surprising that a Pt phase was not detected because the threshold for detection using X-ray diffraction is approximately 30Å, and yet Figure 5.1-8: *Right* showed that 90% of the Pt particles had diameters smaller than 2nm.

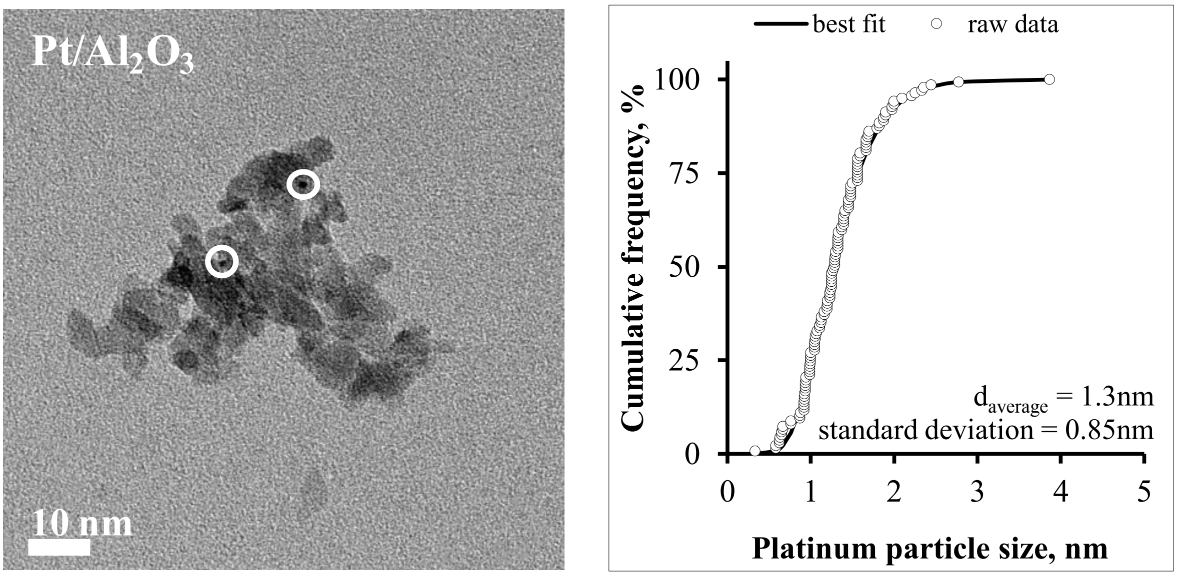

Figure 5.1-8: ***Left:*** TEM micrograph of reduced Pt/Al_2O_3 with some Pt particles identified by circles. ***Right:*** Best fit cumulative lognormal distribution to a sample size of 130+ Pt particles in reduced Pt/Al_2O_3. Note that reduction was carried out at 400ºC.

TEM coupled with Energy-dispersive X-ray spectroscopy (EDS) was used to obtain a localised chemical composition and the results from a single-point analysis on a Pt particle in reduced Pt/Al_2O_3 are shown in Figure 5.1-9. The detected elements included Pt, Al, and O, while the C and the Cu were from the carbon coated copper grid.

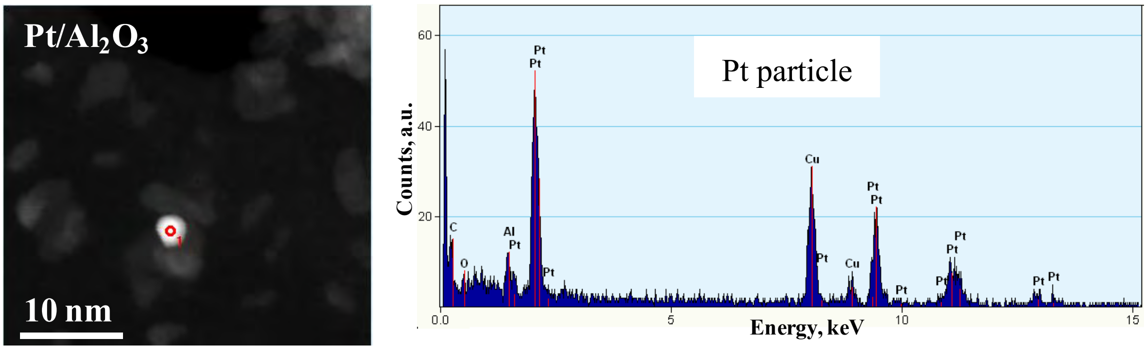

Figure 5.1-9: ***Left:*** STEM micrograph of <u>reduced</u> Pt/Al_2O_3 with an illuminated Pt particle used to obtain an EDS single-point elemental analysis. ***Right:*** Results of the EDS single point analysis showed the presence of Pt, Al, O and Cu from the copper grid.

Pt-Co/Al_2O_3: The results from TEM analyses of Pt-Co/Al_2O_3 are shown in Figures 5.1-10 and 5.1-11. The catalyst was also reduced at 400°C for 4 hours and then passivated, after which sample preparation was carried out using the sonication method. Pt particles were clearly visible in the micrographs of reduced Pt-Co/Al_2O_3 (Fig. 5.1-10: *Left*). EDS point analyses were used to confirm the assignment of Pt and Co particles as shown in Fig. 5.1-10: *Right*. A single point elemental analysis at the centre of the observed Pt particle confirmed the presence of Pt and Al, while Cu and C were from the carbon-coated copper grid.

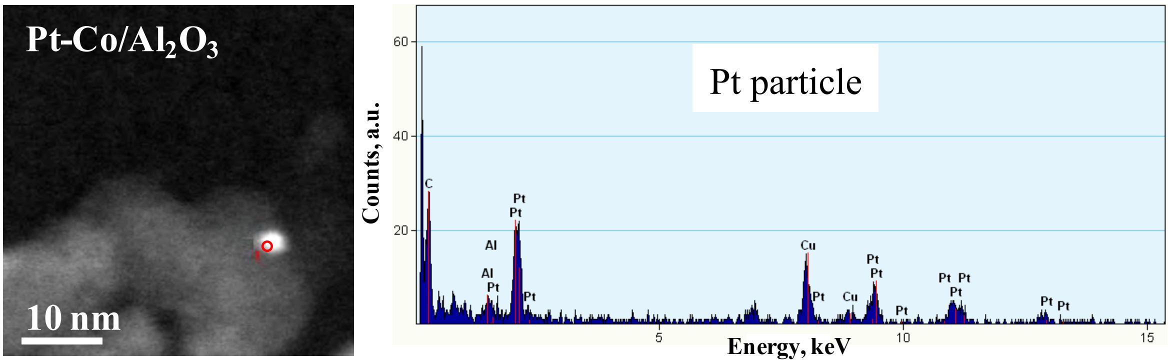

Figure 5.1-10: ***Left:*** STEM micrograph of reduced Pt-Co/Al_2O_3 showing a Pt particle (illuminated) and the circle marking the position of a single point EDS analysis. ***Right:*** Results of the EDS single point elemental analysis showing the presence of Pt, Al, C, and Cu. C and Cu were from the carbon coated copper grid.

The reduced sample was characterised by Co particles in a cluster, while Pt particles appeared to be evenly dispersed over the Al_2O_3 support surface (Fig. 5.1-11: *Left*). Some coordination between Pt particles and/or atoms and Co particles was expected because an EXAFS study of a sequentially impregnated and reduced 0.5%Pt-25%Co/Al_2O_3 sample prepared in a similar manner [5] showed that direct Pt-Co contact occurred to a great extent, and that Pt atoms had a high preference for co-ordination to Co. Unfortunately, the contrast between Pt and Co particles in the TEM micrographs of reduced Pt-Co/Al_2O_3 was poor due to comparable densities, which made it impossible to detect any bimetallic particles and/or Pt-Co co-ordination.

The best-fit cumulative lognormal distribution curve to a sample size of 80+ cobalt particles in reduced Pt-Co/Al_2O_3 is shown in Figure 5.1-10: *Right*, from which the average cobalt particle size and standard deviation were determined as 10.3 nm and 6.4 nm respectively, and all the cobalt particles were less than 16 nm.

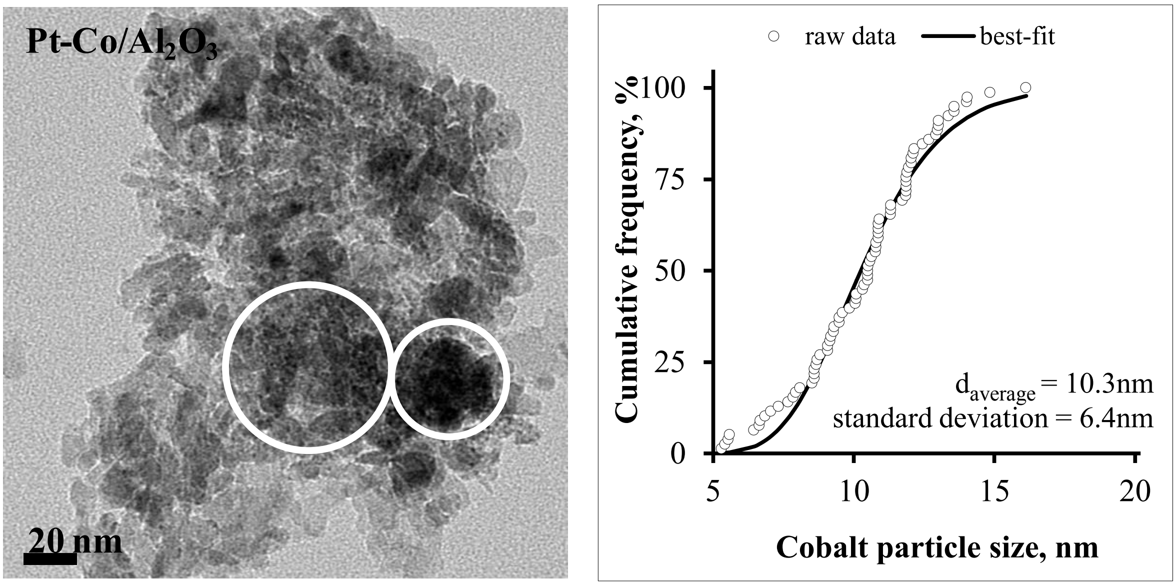

Figure 5.1-11: ***Left:*** TEM micrograph of reduced (and then passivated) Pt-Co/Al_2O_3. Small, highly dispersed Pt particles are highlighted by the larger circle while a cluster of Co particles is enclosed in the smaller circle. ***Right:*** Best fit cumulative lognormal distribution to a sample size of 80+ cobalt particles in reduced Pt-Co/Al_2O_3. Note that reduction was carried out at 400°C.

5.1.2.2 Size distributions of particles in the Au-Co catalyst system

The TEM micrographs and graphs of the cumulative lognormal distribution of the Au particles in Au/Al_2O_3 and Au-Co/Al_2O_3 are shown in Figures 5.1-12 to 5.1-14, while the micrographs and graphs of the cumulative lognormal distribution of the Co particles in reduced Au-Co/Al_2O_3 are shown in Figure 5.1-15. The sonification method was used to obtain sufficiently thin samples for all the micrographs, and the particle size distributions were also measured using ImageJ® software. Au particles were clearly visible in the both the calcined samples and the reduced samples as regions of high density, unlike the case of Pt, which was only easy to identify after reduction. The sharp contrast between the Au particles and the Al_2O_3 support suggested that Au was in a metallic state following calcination. Note that the XPS scans in the Au 4d region suggested that Au species were oxidic because the main photoelectron lines were shifted to higher binding energies. However, the assignment of an oxidation state was inconclusive because of the low peak intensities (Fig. 5.1-5).

The particle size distribution of Au was of particularly interest because a particle size dependence for H_2 and CO activation has been reported for supported Au nanoparticles (Sec. 2.3.2). Au in both Au/Al_2O_3 and Au-Co/Al_2O_3 appeared as small, well-dispersed particles. The size distribution of Au particles was narrow and the average particle size was 2.3nm (Au/Al_2O_3), 3.2nm (Au-Co/Al_2O_3) and 3.6nm (reduced Au-Co/Al_2O_3), which attested to the success of the anion exchange technique in producing relatively small particles. The gold particle sizes were in agreement with the XRD data where a gold phase was not observed in Au/Al_2O_3, which was used to deduce that the particle sizes were too small and below the 30Å threshold required for detection using XRD. However, a small Au diffraction peak was observed with calcined Au-Co/Al_2O_3, which was consistent with the particle size distribution shown in Figure 5.1-13 where 70% of the Au particles were larger than 3nm.

Even though cobalt particles were not discernible in the calcined sample, clusters of 30+ cobalt particles were clearly visible following reduction of Au-Co/Al_2O_3 (Fig. 5.1-15: *Left*). The average particle size of Co in reduced (and passivated) Au-Co/Al_2O_3 was determined from the cumulative lognormal distribution as 11.1nm (Fig. 5.1-15: *Right*), which was in a similar range as the reduced Co/Al_2O_3 (10.0nm) and reduced Pt-Co/Al_2O_3 (10.3nm).

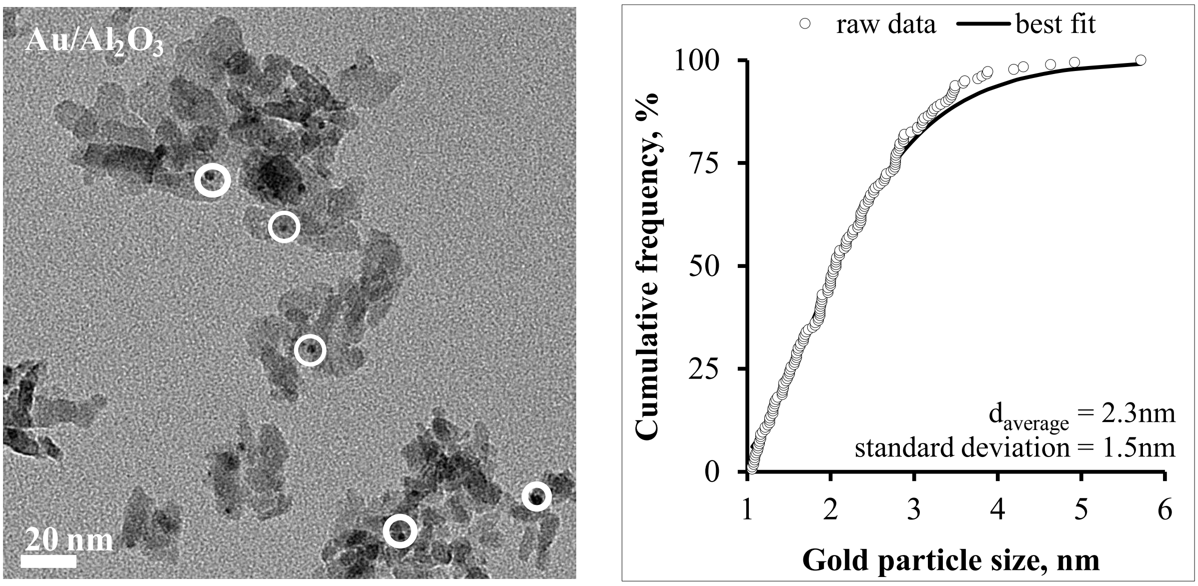

Figure 5.1-12: ***Left:*** TEM micrograph of <u>calcined</u> Au/Al_2O_3 with some Au particles identified by circles. ***Right:*** Best fit cumulative lognormal distribution to a sample size of 177 Au particles in <u>calcined</u> Au/Al_2O_3.

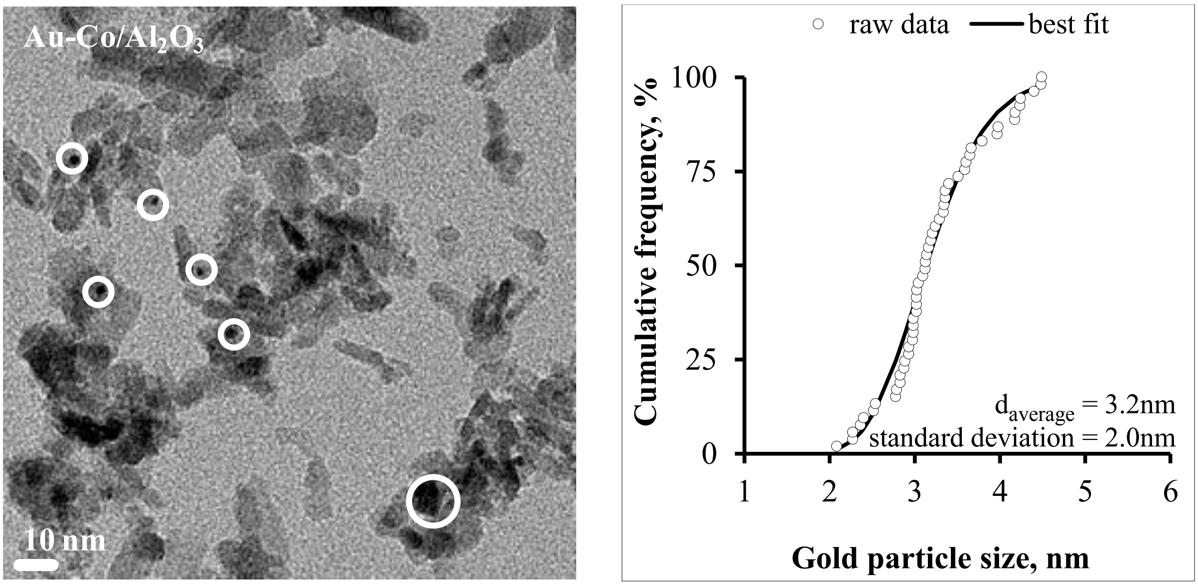

Figure 5.1-13: ***Left:*** TEM micrograph of <u>calcined</u> Au-Co/Al_2O_3 showing well dispersed Au particles. ***Right:*** Best fit cumulative lognormal distribution to a sample size of 53 Au particles in <u>calcined</u> Au-Co/Al_2O_3.

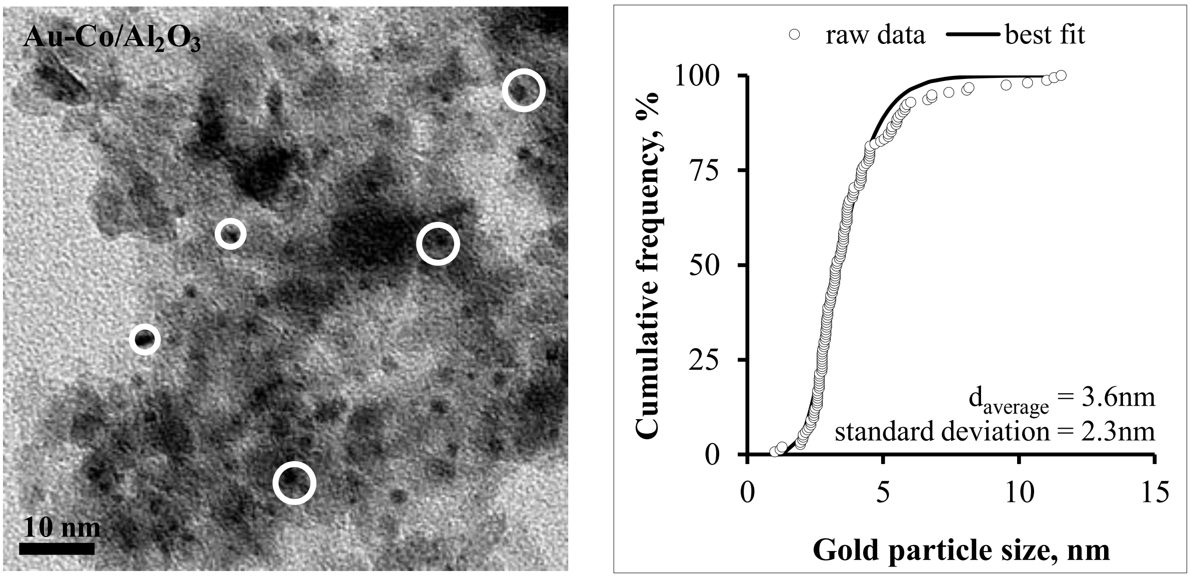

Figure 5.1-14: ***Left:*** TEM micrograph of reduced and passivated Au-Co/Al_2O_3 showing well dispersed Au particles. ***Right:*** Best fit cumulative lognormal distribution to a sample size of 155 Au particles in reduced (and passivated) Au-Co/Al_2O_3. Note that reduction was carried out at 400°C.

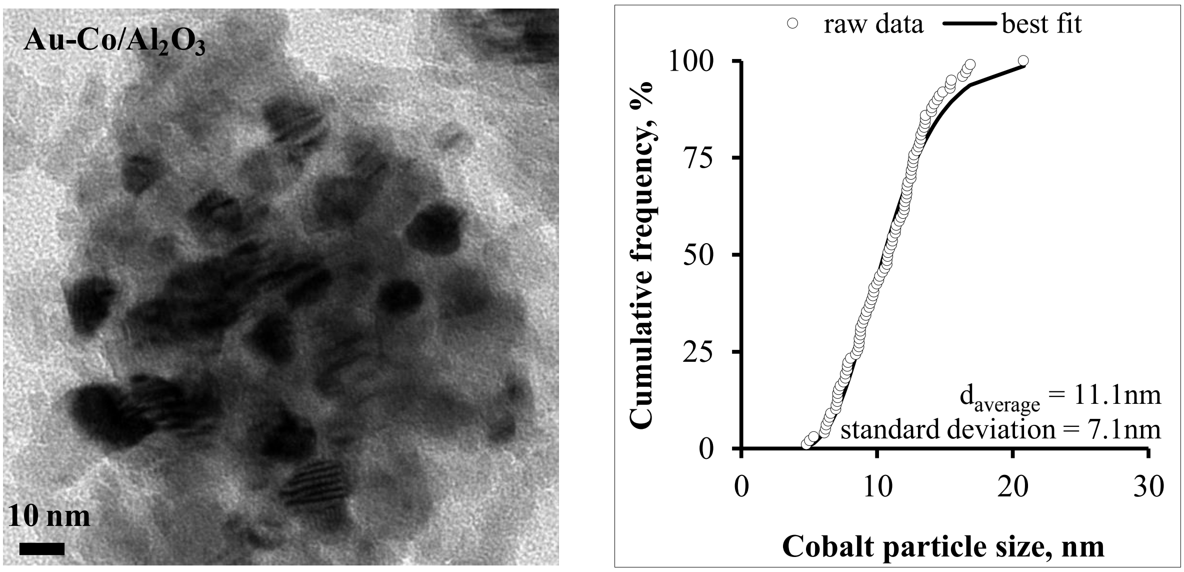

Figure 5.1-15: ***Left:*** TEM micrograph of reduced and passivated Au-Co/Al_2O_3 showing well dispersed Co particles in a cluster. ***Right:*** Best fit cumulative lognormal distribution to a sample size of 99 Au particles in reduced (and passivated) Au-Co/Al_2O_3. Note that reduction was carried out at 400°C.

It is worth noting that the calculated sizes of the reduced Co^0 crystallites in the range of ca. 10nm for Co/Al_2O_3, Pt-Co/Al_2O_3 and Au-Co/Al_2O_3 were consistent with a contraction in the particles size after the reduction of Co_3O_4 crystallites, whose sizes had been determined in the range of 12.7 to 15.7 nm using Rietveld refinement of the XRD data.

5.2 Species Identification in the TPR Profile of Calcined Co/Al_2O_3

The TPR profile of calcined Co/Al_2O_3 is shown in Figure 5.2-1: *Top*. Temperature-programmed reduction (TPR) was carried out in 5%H_2-Ar from 60 to 950ºC, using a heating rate of 10ºC/min. A Thermal Conductivity Detector (TCD) was used to monitor differences between the inlet and product streams from which the hydrogen consumption could be determined. Five distinct reduction peaks were identified in the profile, which has been deconvoluted using Gaussian peaks to indicate the suggested peak positions. The Gaussian peaks were only used to qualitatively fit the profile, and so their peak sizes do not necessarily correspond to the quantity of hydrogen consumed in the specific reduction reaction.

The corresponding MS profile of the reduction of calcined Co/Al_2O_3 is included in Figure 5.2-1: *Bottom*. A mass spectrometer (GC-MS) was connected in series with the TCD to identify the reduction products. The monitored ions in the MS profile included those with m/z of 2 (H_2), 18 (H_2O), 30 (NO) and 46 (NO_2), but the ion with m/z = 46 (NO_2) was not detected during the analysis. The TCD and MS analyses were set to start simultaneously on exposure of the catalyst sample to the reduction gas, but a 15-minute lag was required for the TCD signal to stabilise prior to recording. In Figure 5.2-1, the time axis of the MS profile was thus been adjusted to correspond with that of the TPR profile. The region highlighted in grey was thus only detected by the mass spectrometer since it occurred before the TCD signal had stabilised.

The MS profile of H_2 (m/z = 2) showed some consistency with the TCD signal, which was indicative of H_2 consumption. The mass spectrometer detected the evolution of physisorbed water immediately following exposure of the catalyst to the reducing gas as could be deduced from the great increase in the intensity of the ion with m/z = 18 (highlighted in the grey region). The evolution of this large quantity of physisorbed water (bottom) appeared to have been responsible for the initial *negative* peak in TCD signal (*top*) that often appeared from 0 to 10 minutes. After the initial large peak, the profile of H_2O (m/z = 18) mirrored that of H_2 (m/z = 2) with a very brief time lag, and closely followed that of the TCD signal, which indicated that water was a product of the reduction processes of the five distinct reduction peaks in the TPR profile.

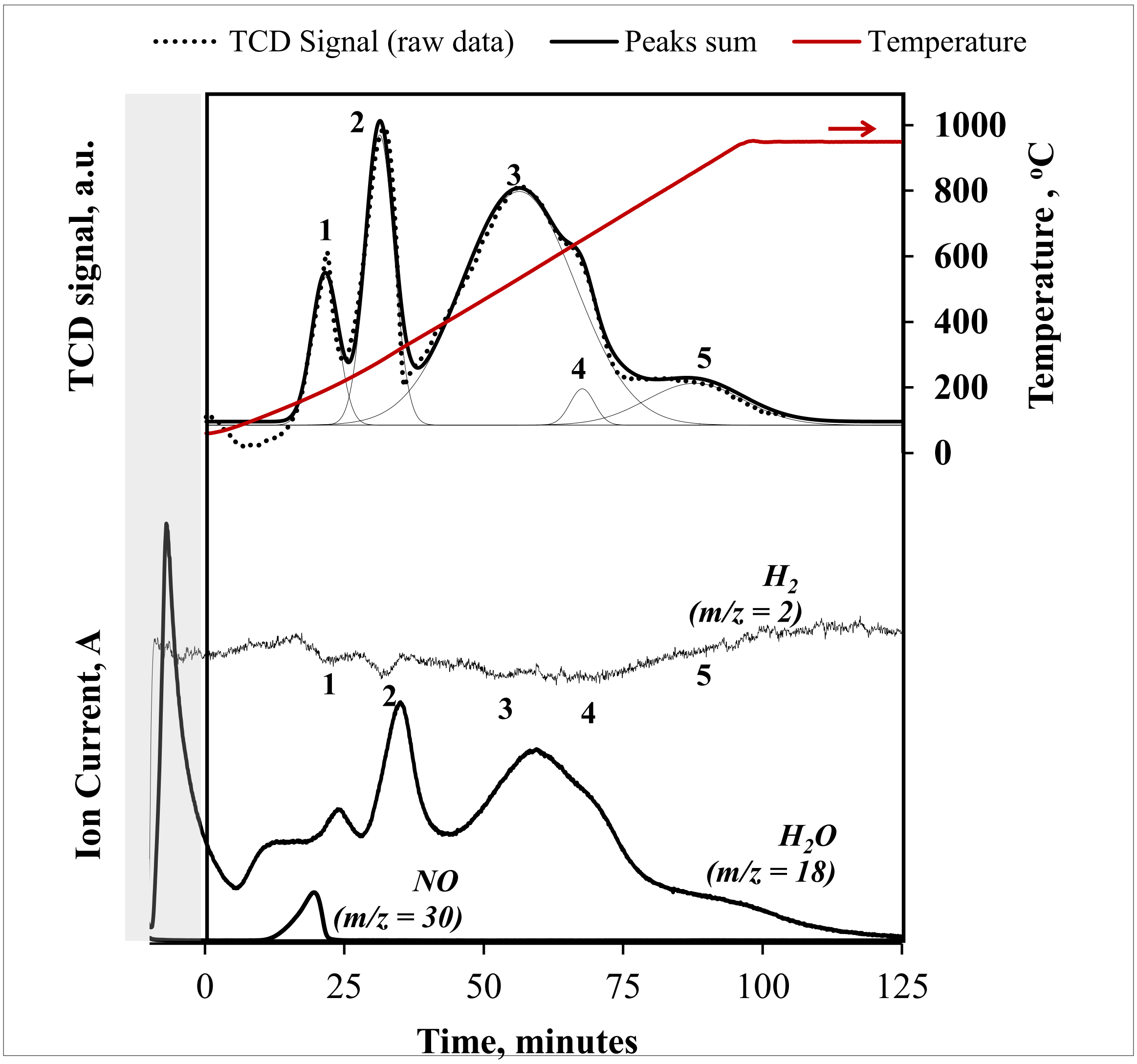

Figure 5.2-1: ***Top:*** H_2 TPR-TCD profile with time of calcined Co/Al_2O_3 (prepared on **milled** Al_2O_3) with Gaussian peaks used to highlight the various reduction peaks. ***Bottom:*** The corresponding MS profile during the reduction of calcined Co/Al_2O_3.

Following the TPR – MS analysis, in situ TPR-XRD and a series of H_2 TPR-TCD analyses of various reference samples were employed to aid the identification of the species associated with the five reduction peaks. The analyses and criteria used to determine the peak identities are discussed subsequently.

- ***Peak 1 at 192°C***

The first peak in the TPR profile coincided with evolution of NO (m/z=30) in the MS profile, and was therefore deduced to involve the reduction of nitrate species.

Nitrates were remnants of the $Co(NO_3)_2$ precursor, and were also observed as low-intensity nitrogen peaks in the broad XPS scan of calcined Co/Al_2O_3 (Fig. 5.1-2). The binding energy of the small N 1s peak at 408eV corresponded with the expected binding energy of nitrate species [6] and its low intensity indicated that any leftover nitrates were present in low quantities.

Nitrates may have persisted as $Co(NO_3)_2$ or as ions adsorbed on the catalyst surface without necessarily forming a crystalline phase with cobalt. Although $Co(NO_3)_2$ peaks were not observed with XRD (Fig. 5.1-1), the low quantities indicated by the N 1s peak would have been difficult to detect as they were likely present as small, finely dispersed and/or amorphous particles that lacked long-range ordering [7].

The persistence of $Co(NO_3)_2$ even after calcination at 350°C was peculiar because bulk $Co(NO_3)_2$ reportedly decomposes to Co_3O_4 at temperatures above 240°C [8]. Stabilisation by the Al_2O_3 support was thought to have made $Co(NO_3)_2$ decomposition more difficult. Indeed, it is generally observed that under the same conditions, $Co(NO_3)_2$ is more persistent with Al_2O_3 compared to SiO_2 supports, which is an indication of the stronger interaction and stabilising nature of Al_2O_3 [7]. The presence of residual $Co(NO_3)_2$ in calcined cobalt-based catalysts is frequently reported in the literature, and is highly dependent on the calcination temperature [7-11].

Further investigation into the identity of Peak 1 included H_2 TPR-TCD analyses on selected reference materials including bulk Co_3O_4, $Co(NO_2)_3/Al_2O_3$ and Co/Al_2O_3_500°C. Bulk Co_3O_4 was available from Merck (99.8%), $Co(NO_2)_3/Al_2O_3$ was a portion of the uncalcined Co/Al_2O_3 following a single impregnation with the $Co(NO_2)_3{\cdot}6H_2O$ precursor, while Co/Al_2O_3_500°C was a portion of the calcined Co/Al_2O_3 that had undergone an additional 6-hour calcination step at 500°C. The TPR profiles of these reference compounds are shown in Figure 5.2-2. The first reduction peak in **bulk Co_3O_4** only started to materialise at 140°C and had a maximum at 230°C. This was in contrast to Peak 1, which started to appear at temperatures below 100°C and thus suggested that the corresponding reducing species were unlikely to have been purely due to an oxidic form of cobalt. Recalcination of Co/Al_2O_3 at

500°C appeared to have eliminated Peak 1 based on the TPR profile of the **Co/Al_2O_3_500°C**. This was in line with the literature where the persistence of Al_2O_3 supported cobalt nitrates was found to be dependent on the calcination temperature, which had to be at least 380°C for cobalt nitrates to completely disappear [8, 9]. Finally, the first reduction peak of **$Co(NO_3)_2/Al_2O_3$** appeared at 194°C, which compared well with Peak 1 at 192°C.

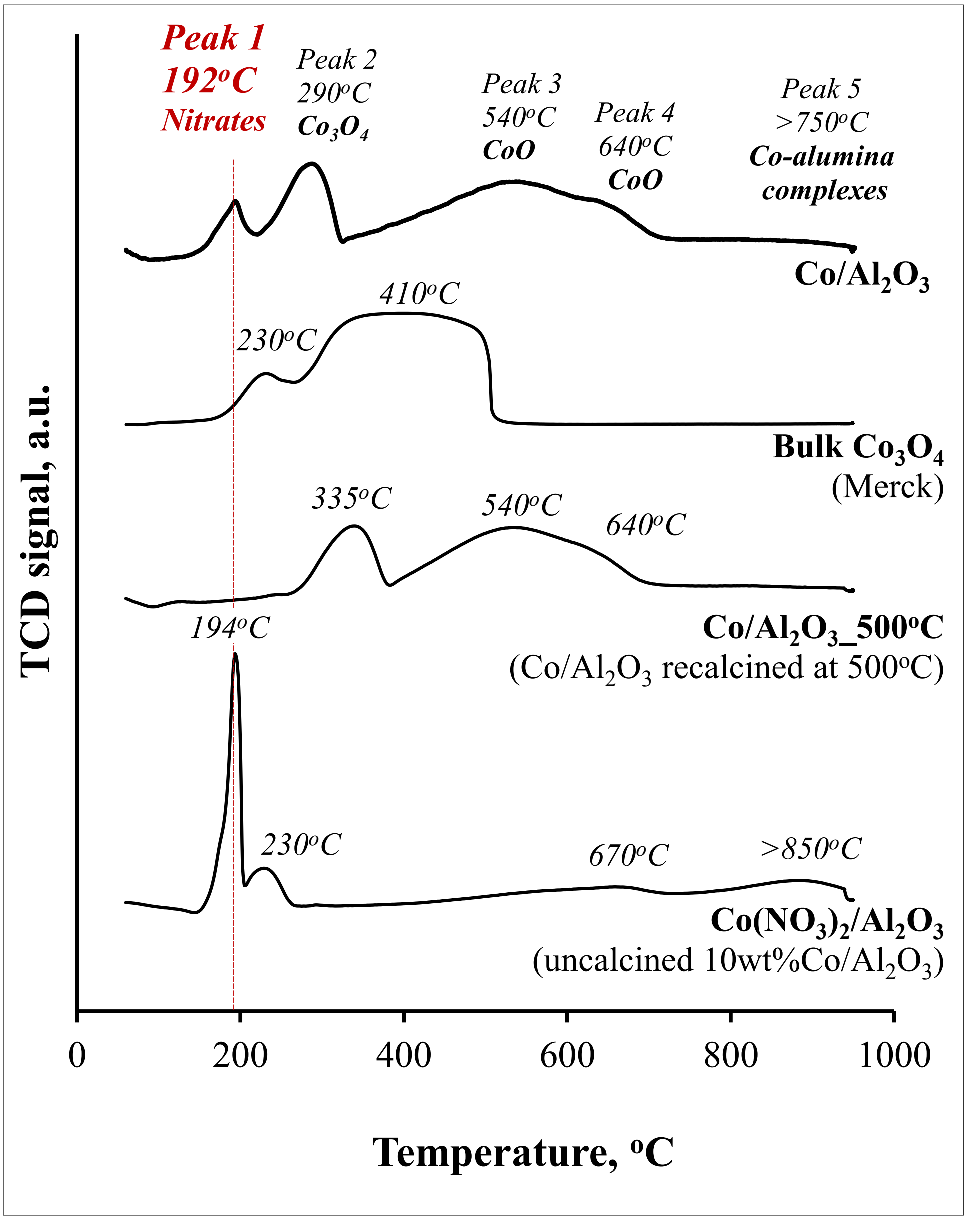

Figure 5.2-2: TPR profiles of selected reference samples used to aid the identification of Peak 1.

The simultaneous evolution of NO (m/z = 30) and H_2O (m/z = 18) with Peak 1 suggested that they were the reduction products of the nitrate decomposition (Fig. 5.2-1). Various NO_x

groups have been reported as products of $Co(NO_3)_2$ decomposition (in air and H_2) [10, 12, 13], but only NO and NO_2 were measured during the TPR-MS analysis, and only NO was detected.

Using mass spectrometry, Polansky et al. [14] also found that the reduction of $Co(NO_3)_2$ occurred via formation of nitric oxide (NO) and proposed that $Co(NO_3)_2$ reduced by formation of CoO as an intermediate. Stoichiometrically, the hydrogen-assisted decomposition of $Co(NO_3)_2$ to H_2O and NO should result in a corresponding increase in the quantity of oxidic cobalt (CoO or Co_3O_4); direct $Co(NO_3)_2 \rightarrow Co^0$ decomposition/reduction was not expected due to the strong oxidising nature of the expected NO_x products.

Reduction of leftover nitrates via formation of oxidic cobalt was supported by the TPR profile of $Co(NO_3)_2/Al_2O_3$ in Figure 5.2-2, which showed that reduction occurred in 4 peaks, with the 2nd peak appearing at a temperature comparable to that of Co_3O_4 in the profile of Co/Al_2O_3. Therefore, the hydrogen-assisted decomposition of Al_2O_3 supported $Co(NO_3)_2$ was suggested to proceed according to Scheme 5.2-1.

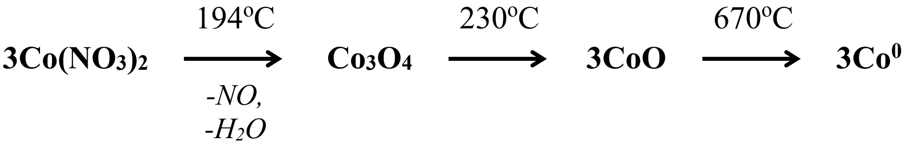

$$\mathbf{3Co(NO_3)_2} \xrightarrow[-NO,\ -H_2O]{194^{\circ}C} \mathbf{Co_3O_4} \xrightarrow{230^{\circ}C} \mathbf{3CoO} \xrightarrow{670^{\circ}C} \mathbf{3Co^0}$$

Scheme 5.2-1: Proposed sequence of the hydrogen-assisted decomposition of Al_2O_3 supported $Co(NO_3)_2$ via formation of Co_3O_4.

Peak 1 occupied 9% of the area under the TPR profile of Co/Al_2O_3 in Figure 5.2-1. It was thus determined that if Peak 1 was *solely* due to hydrogen-assisted cobalt nitrate decomposition, then only ca. 4.6% of the cobalt in calcined Co/Al_2O_3 would have been present as $Co(NO_3)_2$. This small quantity of nitrates was consistent with the small size of the N 1 s peaks in the XPS spectrum.

Besides cobalt nitrates, other cobalt species also reportedly reduce at temperatures in the range of Peak 1, i.e. ~ 192°C. From the TPR profile of Co/Al_2O_3 in Figure 5.2-1, it may be observed that the adjacent Peak 2 (assigned to Co_3O_4 reduction) appears to have a low-temperature front, which suggested that some Co_3O_4 might have contributed to Peak 1. From the literature, van de Loosdrecht et al. [15] reported that CoO(OH) was the preferred phase of oxidic cobalt when H_2O and NO_x concentrations are kept low during the calcination of

$Co(NO_3)_2$. The reduction of CoO(OH) → Co^0 occurred at 100-200°C via formation of Co_3O_4 and CoO as intermediates [15]. In the current study, CoO(OH) was not detected by either XRD (Fig. 5.1-1) or XPS (Fig. 5.1-2), and the use of GC-MS (Fig. 5.2-1) could not provide further insights because the reduction products of CoO(OH) were indistinguishable from those of other oxidic cobalt species.

- ***Peak 2 at 290°C and Peak 3 at 540°C***

Peaks 2 and 3 were attributed to the reduction of Co_3O_4 and CoO respectively according to Equations 5.2-1 and 5.2-2.

Peak 2: $Co_3O_4 + H_2 \rightarrow 3CoO + H_2O$ **Equation 5.2-1**

Peak 3: $3CoO + 3H_2 \rightarrow 3Co + 3H_2O$ **Equation 5.2-2**

Peaks 3 and 2 occupied 60.6% and 19.0% of the total area under the Co/Al_2O_3 TPR profile and were therefore present in a ratio of 3.2:1. The ideal stoichiometric ratio of 3:1 is rarely exhibited by supported cobalt catalysts in the reviewed literature [9, 16, 17].

Further investigation into the identities of Peak 2 and 3 included an in situ XRD analysis of Co/Al_2O_3 during temperature-programmed reduction in the Anton-Paar XRK-900 reaction chamber described in Section 4.2.5. The diffractograms collected in the course of the analysis are shown in Figure 5.2-3: *Left* while Figure 5.2-3: *Right* shows the intensities of the characteristic peaks of Co_3O_4, CoO, and Co^0 as a function of temperature. Figure 5.2-3 indicated that supported Co_3O_4 reduced to Co^0 via formation of CoO as an intermediate in agreement with Equations 5.2-1 and 5.2-2.

The Co_3O_4 intensity started to decrease at 225°C, which coincided with the increase in intensity of CoO ($2\theta=49.7^\circ$). After reaching a maximum at approximately 330°C, the intensity of CoO declined gradually until the analysis was terminated. The intensity at $2\theta=51.7^\circ$, which was where the peak of fcc Co was expected increased in a manner that mirrored the decrease of the CoO intensity.

Peak 2 (290°C) was therefore attributed to Co_3O_4 → CoO reduction which according to in situ XRD occurred from 225-300°C while Peak 3 (540°C) was attributed to CoO→fcc Co reduction, which according to the in situ XRD analysis started to occur at 330°C.

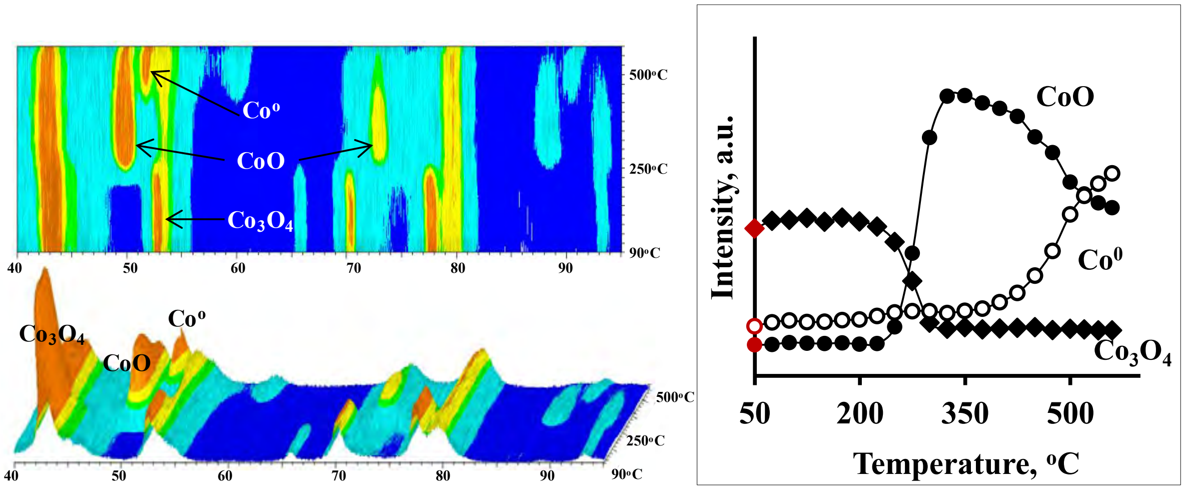

Figure 5.2-3: ***Left***: XRD scans taken during in situ temperature-programmed reduction of calcined Co/Al_2O_3 at a heating rate of 1°C/min. ***Right***: Changes in peak intensities of CoO (49.7°), Co_3O_4 (70.3°), and fcc Co (51.7°) as a function of temperature.

○ *Peak 4 at 640°C and Peak 5 at >750°C*

Peaks 4 and 5 were assigned to the reduction of cobalt species that were in close interaction with the support.

In the TPR profile in Figure 5.2-1, Peak 4 was the small shoulder of the broad reduction peak that also encompassed Peak 3, which was assigned to CoO→Co^0 reduction. Therefore, Peak 4 was also attributed to the reduction of Co^{2+}, and specifically to Co^{2+} ions that were in close interaction with the Al_2O_3 support, which may have included small crystallites, individual atoms, or atoms at the interface between the support and the cobalt crystallites. The width of the CoO reduction peak in supported cobalt-based catalysts has been reported to depend on the type of support and crystallite size. The CoO reduction peak is often narrower in less stabilising supports such as SiO_2 [17-19]. Due to the increased likelihood of strong metal-support interactions, small crystallite sizes (<6nm) reportedly result in wider CoO peaks compared to 20-70nm crystallites [17-19].

In Figure 5.2-2, which shows the reduction profiles of various reference catalysts, it can be observed that profile of Co/Al_2O_3 was shifted to higher temperatures compared to bulk Co_3O_4. According to Arnoldy & Moulijn [9], Al^{3+} ions in the support can polarise the Co-O bond, which strengthens the charge on Co and increases the lattice energy, resulting in the need for higher reduction temperatures for supported cobalt species.

Peak 5 (>750°C) was assigned to the reduction of non-stoichiometric cobalt aluminate complexes because it appeared in the same temperature range typically observed for the reduction of bulk $CoAl_2O_4$ [9, 20]. According to Chin et al. [21], under normal calcinations conditions, the formation of mixed cobalt aluminate complexes is limited to the cobalt-alumina interface/first few outer layers of the Al_2O_3 support. The complexes arise from the migration of Co ions into octahedral and tetrahedral sites of the Al_2O_3 because the Al_2O_3 crystal structure is a spinel deficient of cations [22, 23]. Apparently, cations in octahedral sites are reducible while those in tetrahedral sites are not [21]. The assignment of Peak 5 is supported by Jacobs et al. [17], who used EXAFS to determine that the high temperature reduction peak was a mixed cobalt and alumina compound with a structure similar to that of crystalline $CoAl_2O_4$.

Table 5.2-1 summarises the temperatures, peaks areas and the proposed reducing species of the five distinct reduction peaks in the TPR profile of Co/Al_2O_3 based on the various analyses discussed thus far. The assignments were in agreement with the deductions made in other studies on the reduction of Co/Al_2O_3 catalysts [7-20].

Table 5.2-1: Properties and proposed identities of the five distinct reduction peaks in the H_2 TPR-TCD profile of Co/Al_2O_3.

	Temperature,°C	**Area, %**	**Proposed reducing species**
Peak 1	192	9.0	$Co(NO_3)_2$, NO_3^-, CoO(OH), Co_3O_4
Peak 2	290	19.0	Co_3O_4
Peak 3	540	60.6	CoO
Peak 4	640	2.0	CoO, CoO in close interaction with Al_2O_3
Peak 5	>750	9.3	Non-stoichiometric cobalt aluminate complexes, $CoAl_2O_4$

5.3 Development of the Model Catalyst Systems using H_2 Temperature-Programmed Reduction (H_2 TPR-TCD)

Exploratory TPR analyses were used to aid the development of the catalyst systems used in this study. The results from these analyses were fundamental because they provided evidence that reduction promotion in the presence of a promoter was dependent on *successful* surface migration of hydrogen species from the promoter to Co and in turn supported the theory that reduction most likely involved a hydrogen spillover mechanism. The results from these preliminary analyses are hereby discussed as a prelude to the H_2 TPR-TCD analyses in Section 5.4.

5.3.1 H_2 TPR-TCD analyses of preliminary samples prepared on unmilled (unmodified) Puralox SCCa 5-150

The exploratory H_2 TPR-TCD analyses were carried out with preliminary catalyst samples that were prepared using the unmodified (i.e. not milled) Al_2O_3 support particles (d_{Al2O3}=120µm). The results are shown in Figure 5.3-1 and include the reduction profiles of Co/Al_2O_3, Pt/Al_2O_3, Hybrid Pt-Co and Pt-Co/Al_2O_3. Pt/Al_2O_3 did not exhibit any reduction peaks, while the reduction peaks of Hybrid Pt-Co appeared at near identical temperatures to those of unpromoted Co/Al_2O_3, which implied that the reduction had followed a similar process. On the other hand, the reduction profile of Pt-Co/Al_2O_3 shifted to lower temperatures, signifying an improvement in cobalt reducibility compared to Co/Al_2O_3.

Because Pt did not impact the reducibility of Hybrid Pt-Co but improved the reducibility of the cobalt oxides in the Pt-Co/Al_2O_3, i.e. when both active metals were on the same support and/or in direct physical contact, it was deduced that either:

- spillover hydrogen from Pt was indeed present but for yet undetermined reasons could only impact Co reducibility in Pt-Co/Al_2O_3 and not in Hybrid Pt-Co
- or direct Pt-Co physical contact played an essential role in the promoting effect that Pt had on the reduction of supported Co oxides, and therefore reduction promotion could involve an alternative mechanism to spillover.

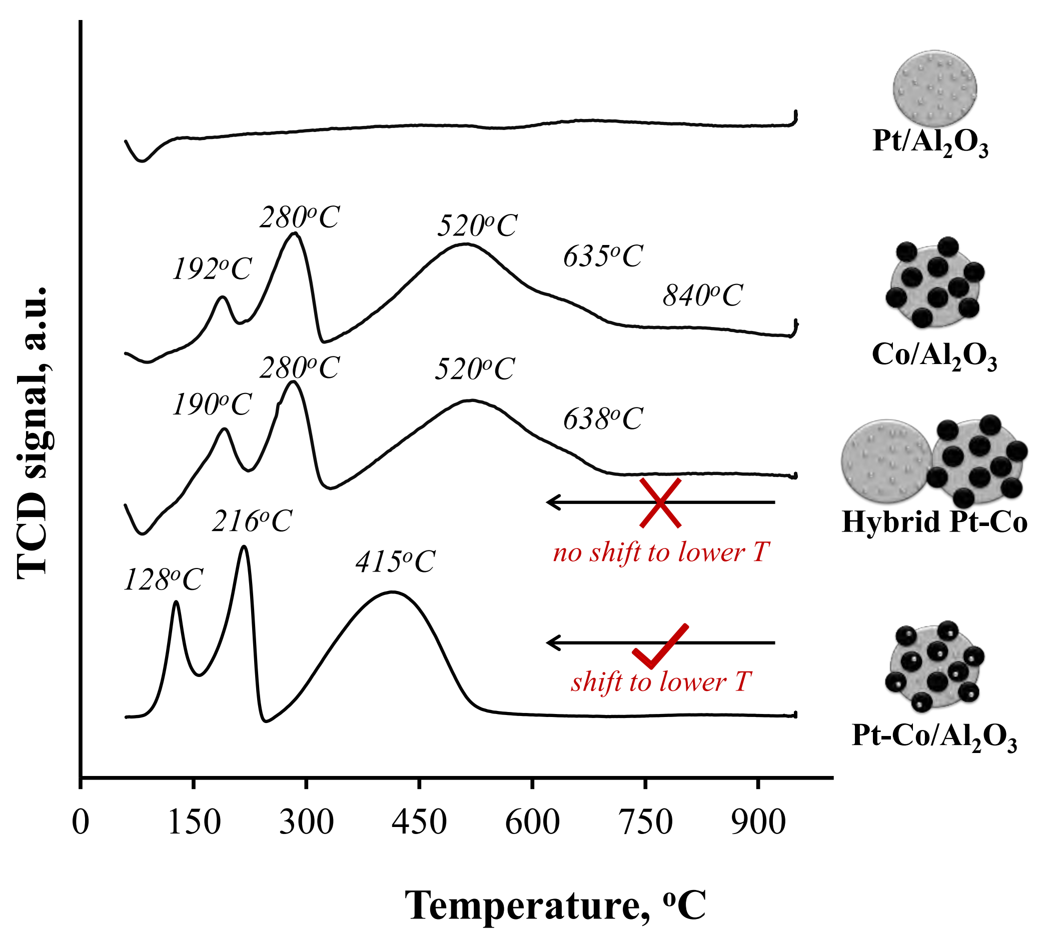

Figure 5.3-1: Exploratory TPR profiles of the preliminary catalyst samples. Preliminary samples were prepared without milling the support i.e. using unmodified Al_2O_3 (Puralox SCCa 5-150).

The unaltered TPR profile of Hybrid Pt-Co was contrary to expectations of a reduction mechanism facilitated by spillover hydrogen as has been frequently invoked in the literature [17, 18, 24-30]. In addition, H_2 activation has been reported to be the rate-limiting step during the reduction of cobalt and other transition metal oxides (Sec. 2.2.4.2), and so Pt, as a highly active surface for H_2 activation compared to cobalt oxides was expected to have enhanced the reducibility in Hybrid Pt-Co as seen with Pt-Co/Al_2O_3. Consequently, it was hypothesized that the reasons for the poor reducibility of Hybrid Pt-Co, in spite of its Pt constituent, lay in the physicochemical dissimilarities between the two promoted samples.

The proposed pathways (I, II, III) of spillover hydrogen species during reduction are illustrated in Scheme 5.3-1. Three main pathways of spillover hydrogen were proposed for co-supported Pt-Co/Al_2O_3 and Hybrid Pt-Co. In Pt-Co/Al_2O_3, spillover hydrogen had the most direct pathway (Pathway I) i.e. Pt → Co, unless the active components were not in direct physical contact, in which case the Pt → Al_2O_3 → Co pathway (Pathway II) involving migration over the Al_2O_3 support would have been available. The pathway in Hybrid Pt-Co was similar to Pathway II because it involved migration over the support, except that hydrogen needed to negotiate at least one inter-alumina interface as follows: Pt → Al_2O_3 ⇒ Al_2O_3 → Co (Pathway III in Scheme 5.3-1: *Right*).

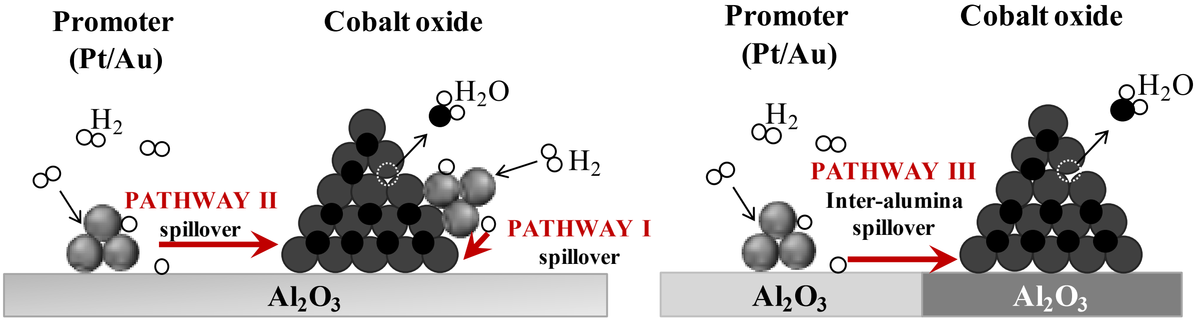

Scheme 5.3-1: Proposed pathway of spillover H. ***Left:*** Pt-Co/Al_2O_3. ***Right:*** Hybrid Pt-Co.
Pathway I: Pt → Co
Pathway II: Pt → Al_2O_3→ Co
Pathway III: Pt → Al_2O_3 ⇒ Al_2O_3 → Co

The hydrogen pathway in Hybrid Pt-Co became highly discontinuous at the inter-alumina interface, and it was hypothesized that herein laid the major physical difference between the promoted samples. Hydrogen transfer via spillover involves a surface migration and will only occur if the surfaces of the hydrogen donor (i.e. Pt) and acceptor (i.e. Co) are in direct physical contact or in *indirect* physical contact by having interconnected surfaces between them. Surface continuity between the donor and acceptor is mandatory for successful surface migration, and it was conceivable that the discontinuity introduced by use of separate supports resulted in a very low Pt → Co spillover transfer efficiency across the inter-alumina interface compared to Pt-Co/Al_2O_3 in which direct Pt → Co spillover could occur.

The importance of surface continuity to the successful migration of spillover hydrogen has also been reported in the literature (Sec. 2.4.3.2). Studies by Hilmen et al. [16] and Baeza et al. [31] on Al_2O_3 supported hybrid samples highlighted the importance of intimate contact in enabling the smooth transition of spillover hydrogen between the support particles. In a study of CoMo catalysed hydrogen desulphurisation (HDS), Baeza et al. [31] demonstrated that *monolithic* support particles were highly conducive for spillover compared to samples where Co and Mo were on separate supports (Sec. 2.4.3.2). Spillover was enhanced when using Al_2O_3 monoliths, which were cylindrical extrudates with Co and Mo crystallites at each extremity (refer to image of monolithic support in Fig. 2.4-1). As a single continuous support particle, the monolith was deduced to behave as a very fine powder with a very high surface area and thus multiple contact points between particles to allow for surface migration [31].

In light of these deductions, it was hypothesised that the surface continuity could be enhanced by crushing the support to a finer powder in order to mimic a monolithic support particle.

5.3.2 H_2 TPR-TCD analyses of crushed and milled catalyst samples with improved surface continuity

Table 5.3-1 includes the particle size distribution and 'Al_2O_3 outer surface area: volume ratio' following crushing and milling of the preliminary catalyst samples. A portion of the catalysts was crushed using an agate mortar and pestle, while a second portion was milled to a much finer powder using a bench top McCrone Micronising Mill®. It was thought that the increase in the Al_2O_3 outer surface area: volume ratio would improve the inter-alumina contact and result in a more continuous surface. The D_{90} of Puralox SCCA 5-150 decreased only slightly from 128 to 121µm after crushing in the agate mortar, compared to 15.5µm after milling. The high mechanical strength of Al_2O_3 probably rendered manual crushing inefficient compared to the mechanised process in the McCrone Mill, which reportedly allows for size reduction to <5µm; the mill also allows for 'wet grinding' in ethanol, which is reportedly more effective [32, 33]. The obtained D_{90} of 15.5µm after milling was responsible for the significantly higher Al_2O_3 SA:volume ratio, and was expected to significantly improve the surface continuity.

Table 5.3-1: Particle Size Distributions (PSD) and outer surface area to volume ratios of selected unmodified, crushed and milled catalyst samples used for the exploratory analyses.

Sample	**PSD,µm**		**Al_2O_3 outer SA:volume, µm^{-1*}**
	D_{50}	***D_{90}***	
Puralox SCCa 5-150 (unmodified)	83.5	128	α (= 0.03)
Crushed Hybrid Pt-Co (agate mortar & pestle)	71.9	121	1.1α (= 0.033)
Milled Hybrid Pt-Co (McCrone Mill)	5.57	15.5	8.3α (= 0.25)

* Calculations based on a support diameter equal to the D_{90}.

The TPR profiles of the preliminary samples before and after milling/crushing are shown in Figure 5.3-2. The profile of *crushed* Hybrid Pt-Co remained relatively unaltered, while the reduction of the *milled* sample was complete by 600°C, which was indicative of improved reducibility. It was unsurprising that the TPR profile of the crushed Hybrid Pt-Co remained unaltered considering the inadequacy of manual crushing as evidenced by the negligible decrease in the D_{90} (Table 5.3-1). On the other hand, the continuity of the *milled* sample was expected to have been much improved, which facilitated a higher Pt → Co spillover transfer efficiency.

To isolate alterations in the reduction behaviour that may have arisen from milling, a portion of (unpromoted) Co/Al_2O_3 was also milled and analysed using TPR. The TPR profile of this sample is also included in Figure 5.3-2 from which it was evident that the shape of the reduction peaks was altered *even in the absence of Pt*. Milling may have altered the pore diffusivity of the products since the particle sizes and thus the length of the pores were significantly reduced. Alternatively, the multiplicity seen in the third peak of milled Co/Al_2O_3, which had local maxima at 390°C, 500°C and 625°C, may have arisen from changes in the nature of the cobalt species. During milling, there was a chance that some crystallites would be dislodged from the support, especially if located at points along which the support particles would subsequently fracture. Loose cobalt oxide crystallites would have been free of metal-support interactions (MSI) and as a result experienced a more facile reduction as suggested by the low temperature shoulder at approximately 390°C in the profile of milled Co/Al_2O_3.

The milling technique was incorporated into the preparation of all subsequent catalysts following the favourable results obtained in the exploratory TPR analyses. However, **only the support particles were milled** (prior to catalyst preparation) to limit the likelihood of crystallite (Pt or Co) dislodgement/repositioning during the milling process.

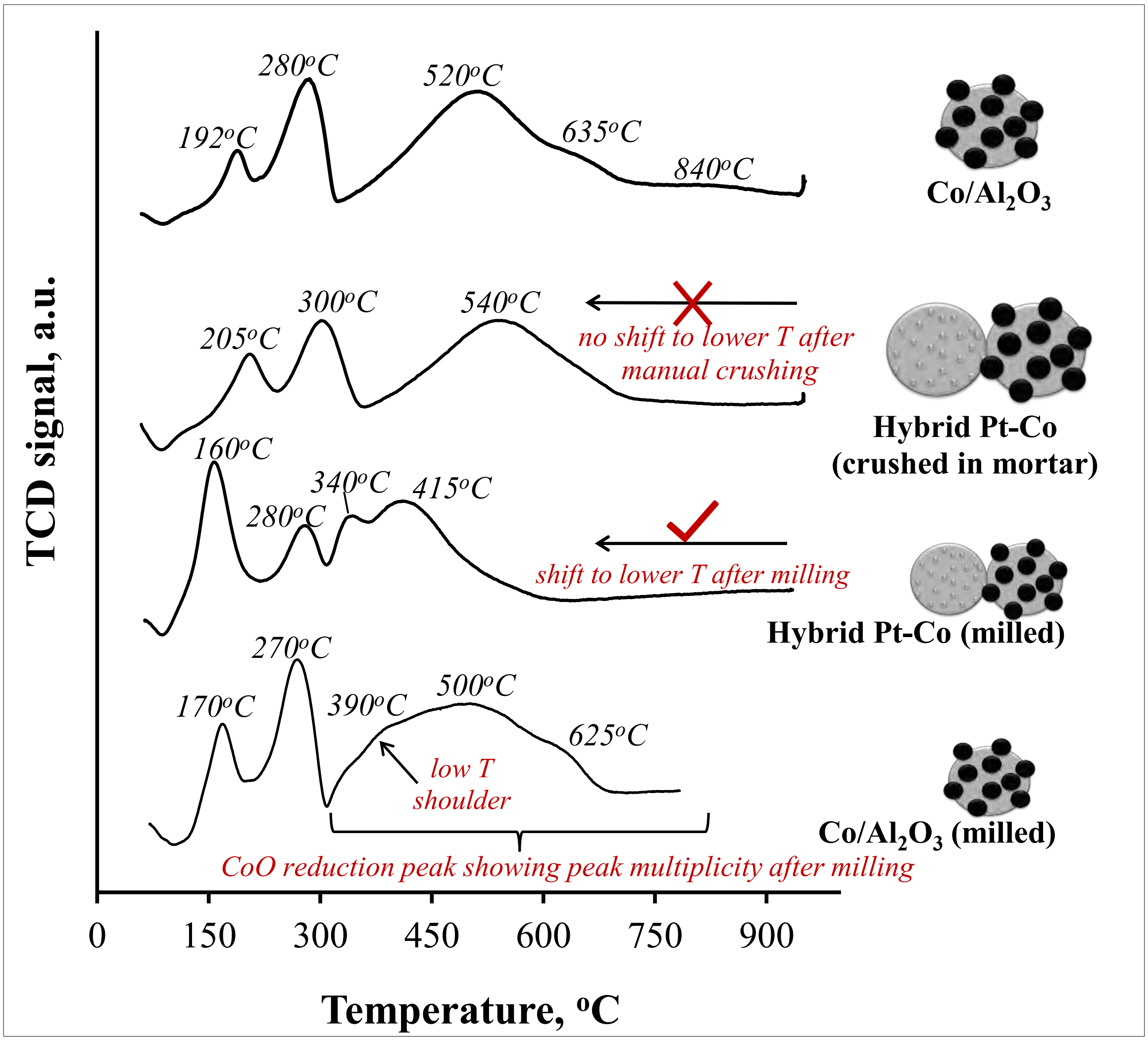

Figure 5.3-2: Exploratory TPR profiles of the preliminary Co/Al_2O_3 and Hybrid Pt-Co catalyst samples after crushing in an agate mortar and milling in a McCrone micronising mill.

Indeed, the reduction peaks of Hybrid Pt-Co and Co/Al_2O_3 prepared on milled Al_2O_3 were no longer broad and flattened (Sec. 5.4), and it was thought that minimising the risk of dislodged crystallites may have contributed to this. Dislodged crystallites were particularly undesirable in Hybrid Pt-Co because they increased the odds that direct physical contact would be established between loose Pt and Co crystallites, and consequently cast doubt on any improved reducibility arising *solely* from a hydrogen spillover mechanism; re-establishment of donor-acceptor coordination is one of the common counter-arguments against spillover discussed in Section 2.4.8.

5.4 Characterisation of the Reduction Behaviour of Pt and Au Promoted Co/Al_2O_3 using H_2 Temperature-Programmed Reduction

5.4.1 Temperature-programmed reduction under dry conditions

- ***Pt-Co Catalyst System***

The profiles obtained during the TPR analysis of the Platinum-Cobalt catalyst system supported on milled Al_2O_3 (< 20µm) are shown in Figure 5.4-1. The reducibility of the samples was deduced to have increased as follows: Co/Al_2O_3 < Hybrid Pt-Co < Pt-Co/Al_2O_3. Figure 5.4-1 demonstrated that direct Pt/Co co-ordination was not actually required to obtain a higher degree of reduction in Pt promoted Co-based Fischer-Tropsch catalysts.

The reduction profile of the hybrid sample reflected the improved reducibility introduced by milling the Al_2O_3 support to enhance surface continuity as indicated by the exploratory TPR analyses in the preceding section. The enhanced reduction despite the great promoter/Co separation suggested that reduction promotion could occur via a remotely controlled mechanism such as spillover in which direct promoter/Co co-ordination was not mandatory. Nonetheless, even though spillover did not require direct promoter/Co contact, a continuous surface between the two components was mandatory to allow successful migration of hydrogen species over adjacent Al_2O_3 support particles. Therefore, no effects of spillover were observed when a high degree of surface discontinuity existed as in the case of the large, unmilled Al_2O_3 particles because the discontinuity obstructed inter-Al_2O_3 spillover. Milling increased the inter-Al_2O_3 contact area, which enhanced surface continuity and allowed for greater hydrogen transfer across adjacent support particles. Therefore, the results in Figure 5.4-1 provided evidence of hydrogen transportation via surface migration because transportation by other means such as gas phase diffusion would not have depended on the surface continuity and as such been affected by milling.

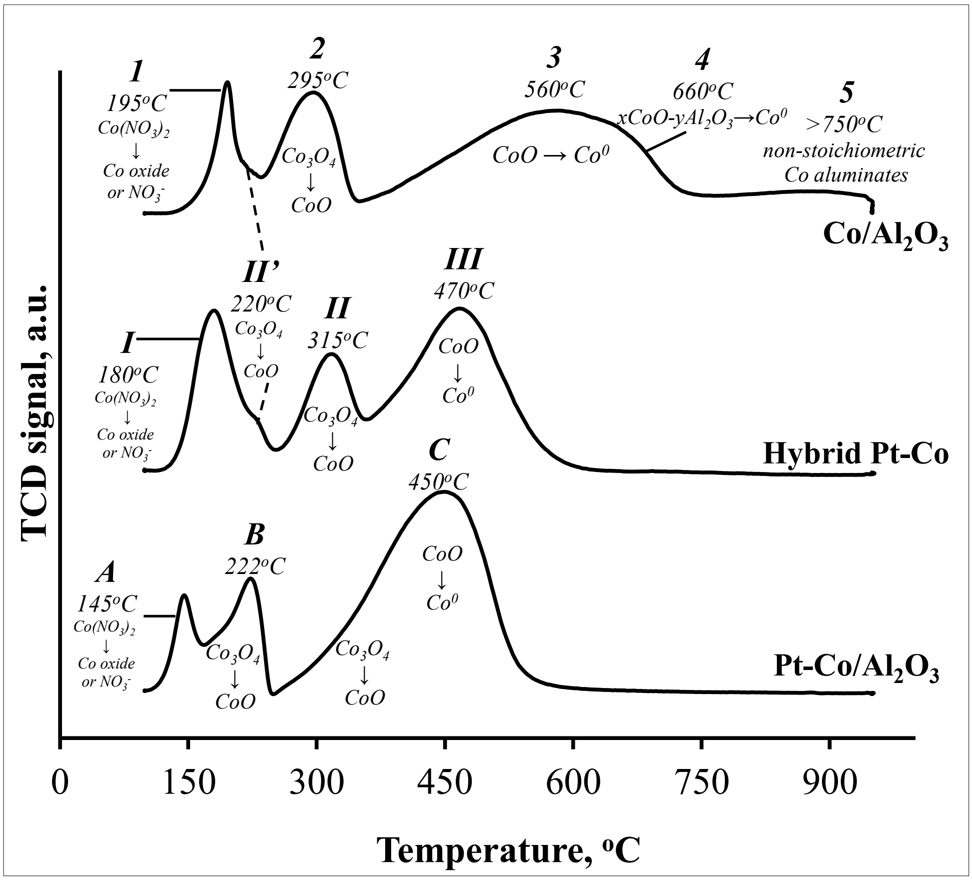

Figure 5.4-1: TPR profiles of Co/Al_2O_3, Hybrid Pt-Co and $Pt\text{-}Co/Al_2O_3$ prepared on milled Al_2O_3. The proposed reducing species contributing to each peak are included.

In the literature, the importance of surface continuity was also stressed by Hilmen et al. [16] using Hybrid Re-Co catalysts. The reduction promotion by Re was **only** observed after the hybrid sample with support particles of 38-53μm was 'gently' ground, and then pressed into composites of 425-850μm. It is worth mentioning that compression of the hybrid samples to particles of 500μm+ was attempted as part of the exploratory analyses detailed in the preceding section, but did not result in any improvement in the reducibility. It is suggested that the grinding carried out prior to the preparation of the large composites by Hilmen et al. perhaps played a role in the observed improved reducibility or that the higher Re loading they used may have been advantageous.

Hybrid Pt-Co: With respect to the reduction profiles in Figure 5.4-1, **Co/Al_2O_3** exhibited the five characteristic peaks detailed in Section 5.2. With Hybrid Pt-Co, the reduction peaks of Co/Al_2O_3 not only shifted to lower temperatures but also changed shape. The peak assigned to nitrate decomposition (Peak I) appeared 15°C lower and was broader due to a more prominent high temperature shoulder at 225°C (Peak II'). Peak II' was attributed to easily reducible Co_3O_4 species because its appearance coincided with a decrease in the size of the main Co_3O_4 reduction peak (Peak II). Peak II' might have also been present in the Co/Al_2O_3 sample as a high temperature tail of the first peak, and was simply enhanced by the Pt promoter in the hybrid samples. It was evident that reduction of CoO underwent the greater change in the presence of Pt because it shifted by 110°C, compared to the Co_3O_4 peak that did not shift at all. In addition, the CoO peak did not include the high temperature shoulder (more difficult to reduce) attributed to the reduction of CoO in close interaction with the support.

A noteworthy observation was the fact that the high temperature peak assigned to the reduction of *non-stoichiometric cobalt aluminates completely disappeared*. Non-stoichiometric cobalt aluminates reportedly form more easily when Co ions are exposed to high concentrations of water and high temperatures such as during calcination [34, 35]. In the literature, it has been proposed that promoters may prevent the formation of mixed support oxides by intimate interaction (physical and/or chemical) with the cobalt or by preferentially depositing as a layer between cobalt crystallites and the support [29, 36]. However, since the peaks corresponding to non-stoichiometric cobalt aluminates disappeared, it is suggested that direct Pt/Co contact was not actually required to prevent the formation of mixed oxides. Pt facilitated the reduction of cobalt species via a remote-control mechanism, which allowed Co ions to reduce at sufficiently low temperatures and concurrently prevented the formation of mixed cobalt-alumina complexes. The latter deduction is particular significant, because it suggested that the mixed cobalt-alumina complexes often observed in the reduction profile of Co/Al_2O_3 do not actually form during calcination, but rather during the TPR analyses. Otherwise, the reduction peaks corresponding to cobalt-alumina complexes would have also been observed in the reduction profile of Hybrid Pt-Co, which contained the same batch of Co/Al_2O_3. A similar conclusion was reached by Hilmen et al. [16] using Hybrid Re-Co hybrid samples.

Pt-Co/Al_2O_3: Like Hybrid Pt-Co, the reduction profile of Pt-Co/Al_2O_3 exhibited only three predominant reduction peaks. The first reduction peak was assigned to nitrates in accordance with the XPS data in Figure 5.1-2. However, the N 1s peak in the broad XPS scan of Pt-Co/Al_2O_3 was significantly smaller than in Co/Al_2O_3, which concurred with the observation that the nitrate decomposition peak in the TPR profile was smaller. Pt-Co/Al_2O_3 probably had fewer leftover nitrates because the extra calcination step following impregnation with the Pt precursor facilitated further nitrate decomposition. Moreover, impregnation with Pt involved continuous stirring of the already calcined Co/Al_2O_3 in an aqueous solution of the Pt precursor, which could have caused dissolution and redispersion of leftover nitrates, resulting in the observed differences seen in the profile of Pt-Co/Al_2O_3.

With regard to the main cobalt oxide reduction peaks, both Co_3O_4 (222°C) and CoO (450°C) reduction peaks shifted significantly compared to Co/Al_2O_3. In addition, like with Hybrid Pt-Co, no peaks assigned to the reduction of cobalt in close interaction with the Al_2O_3 support were present.

From the TPR analysis, it was apparent that Pt in Hybrid Pt-Co caused the reduction behaviour of supported cobalt oxides to mimic that in Pt-Co/Al_2O_3, but the hybrid sample was at a disadvantage because separation of Pt from Co most likely lowered the efficiency of spillover. The improvement in reducibility with physically mixed hybrid catalysts has been observed by Hilmen et al. [16] with the Re-Co-Alumina catalyst system and with the Pt-Co-Titania system tested during the preparatory experiments for the current study. The results from the Pt-Co Titania System are provided in Appendix E1.

- ***Au-Co Catalyst System***

The profiles obtained during the TPR analysis of the Gold-Cobalt catalyst system are shown in Figure 5.4-2 from which the reducibility of the samples was deduced to increase as follows: (Co/Al_2O_3 ≈ Hybrid Au-Co) < Au-Co/Al_2O_3. The peculiar characteristic of the Au-Co System was that despite improving the reducibility of Au-Co/Al_2O_3, Au did not have a corresponding impact on the reducibility of the Hybrid Au-Co sample.

Hybrid Au-Co: The five major reduction peaks in the TPR profile of Co/Al_2O_3 were observed with Hybrid Au-Co, with unremarkable variation in their reduction temperatures. The ratio of the peaks assigned to CoO and Co_3O_4 reduction remained at an approximate value 2.8:1, indicating a two-step reduction of $Co_3O_4 \rightarrow 3CoO \rightarrow 3Co^0$ in a manner similar to that observed with Co/Al_2O_3. Despite some subtle differences in peak morphology such as a slightly prominent low-temperature shoulder - Peak 3' (indicative of slightly improved reduction) at the CoO reduction peak, it was apparent that the reducibilities of Hybrid Au-Co and unpromoted Co/Al_2O_3 were not statistically different.

Au-Co/Al_2O_3: The reducibility of Au-Co/Al_2O_3 was much improved compared to the hybrid sample, and occurred in just two major reduction peaks. Unlike the other cobalt containing samples, no peak was assigned to nitrate decomposition because broad XPS scans did not reveal a N 1s peak at 408eV (see Fig. 5.1-2). As discussed previously, any leftover nitrates were probably removed during the series of washing steps that followed the anion exchange technique.

Therefore, the principal reduction peaks were assigned to Co_3O_4 (Peak A), while Peak B most likely involved a combination of Co_3O_4 and CoO reduction. This assignment was based on the peak areas, which were present in a ratio of 1:4, and as such deviated from the ideal area/hydrogen consumption ratio of 1:3.

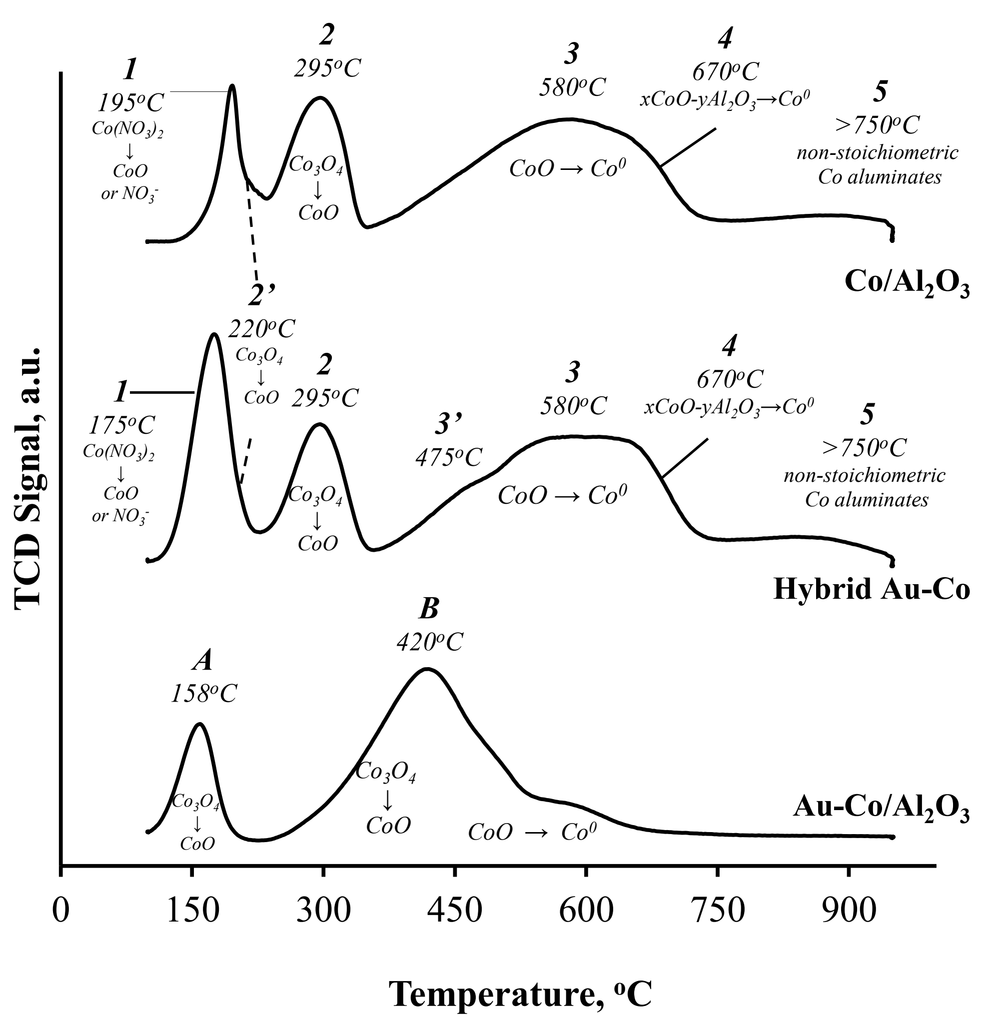

Figure 5.4-2: TPR profiles of Co/Al_2O_3, Hybrid Au-Co and $Au-Co/Al_2O_3$ prepared on milled Al_2O_3. The proposed reducing species contributing to each peak are included.

The TPR profile of the Au-Co/Al_2O_3 was compared to those obtained in the limited literature on gold as a promoter for the Co/Al_2O_3 catalyst; the profile concurred with Ahmad et al. [37] using (1.5-2.5%)Au-10%Co/Al_2O_3, and Jacobs et al. [38] using 1.51%Au-15%Co/Al_2O_3 but differed greatly from Jalama et al. [39] using (0.5-5%)Au-10%Co/Al_2O_3, where prominent peaks corresponding to mixed cobalt alumina complexes were observed. The discrepancy with Jalama et al. [39] could have arisen from multiple causes including use of the **co-precipitation** preparation technique (versus **sequential** impregnation) and the higher calcination temperature of 400°C. It is suggested that the deposition order of Co and Au may affect the reduction behaviour based on a recent publication by the group of Bartholomew [40], which showed that co-deposited (noble) metal promoted Co/Al_2O_3 catalysts reduced more easily than sequentially impregnated samples.

5.4.1.1 The catalysing effect of Au and Pt promoters on the reduction of cobalt oxides via hydrogen spillover

H_2 activation has been proposed as the rate-limiting step during the reduction of cobalt and other transition metal oxides (Sec. 2.2.4.2). Oxidic surfaces show very little activity for H_2 activation. In fact, according to the nucleation-growth kinetic model, sites that are active for H_2 activation (nucleation centres) must be generated during an induction period before reduction can proceed (Sec. 2.2.4.2). Nucleation centres have been proposed to be defects such as metal atoms with an oxygen vacancy between them, since two adjacent metal atoms would be required to dissociate H_2 (Sec. 2.2.4.2). When a reduction promoter is present, H_2 activation need not occur at nucleation centres/defects (which is very slow) but may occur on the promoter surface.

Scheme 5.4-1 shows the two competing routes (i.e. direct activation –Route 1 by the cobalt oxide versus spillover from the promoter –Route 2) for H_2 activation during the reduction. In the schematic, the sites on the cobalt oxides on which hydrogen may adsorb prior to the reduction are denoted S_1. Activated hydrogen is denoted $H{\cdot}S_1$ and is a form of atomic hydrogen chemisorbed at these S_1 sites. $H{\cdot}S_1$ is in a form that is readily available for reaction with the lattice oxygen in the bulk of the oxide crystallites to form water. $H{\cdot}S_1$ may be formed via Route 1, which involves direct dissociative adsorption of H_2 from the gas phase by the cobalt oxide surface, or via Route 2, which involves spillover from the promoter surface. In order for the promoters to catalyse the reduction of cobalt oxides, the rate of H_2 activation (i.e. $H{\cdot}S_1$ formation) according to Route 2 must be greater than that via Route 1.

Therefore, the improved reducibility of Hybrid Pt-Co, Pt-Co/Al_2O_3, and Au-Co/Al_2O_3 in Figures 5.4-1 and 5.4-2 suggested that the promoters catalysed the reduction of the cobalt oxides by facilitating the formation of active H species via hydrogen spillover (Route 2), and thus lowering the overall activation energy for the reduction as reported in the literature [28].

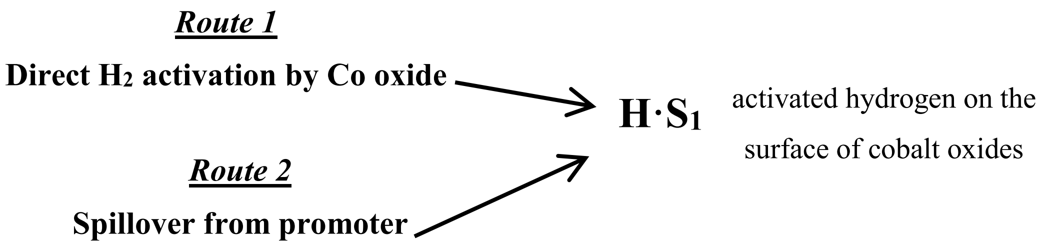

Scheme 5.4-1: Competing routes of hydrogen activation during the reduction of cobalt oxides. S_1 denotes hydrogen adsorption sites on the cobalt oxide surface, and $H{\cdot}S_1$ is an adsorbed intermediate form of hydrogen for the reduction.

- ***Au versus Pt: H_2 activation and spillover***

The TPR profiles of the Au-Co system are overlaid with the Pt-Co system in Figure 5.4-3, which clearly illustrates the stronger catalysing effect of Pt on the reduction of cobalt oxides.

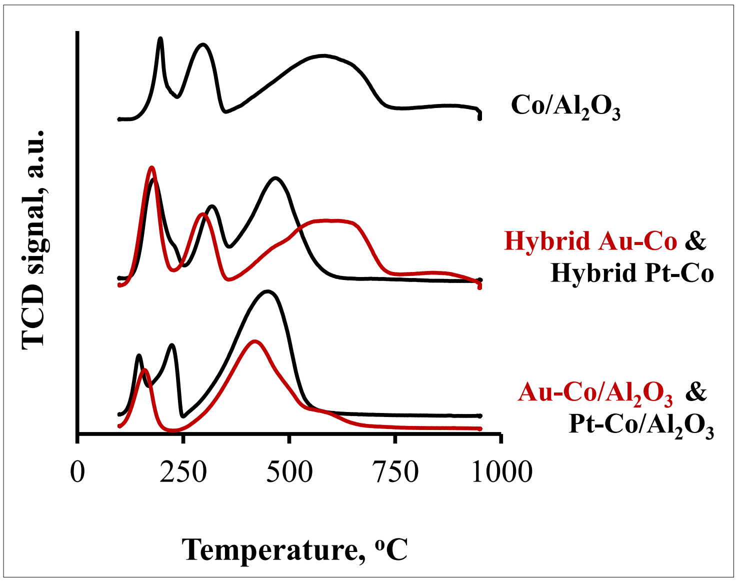

Figure 5.4-3: TPR profiles of the Au-Co Catalyst System overlaid with those of the Pt-Co Catalyst System.

The reduction of Pt-Co/Al_2O_3 appears more facile than that of Au-Co/Al_2O_3 because its profile is complete by 580°C, compared to about 850°C with Au-Co/Al_2O_3. Furthermore, the reduction of the Hybrid Pt-Co sample improved, while that of Hybrid Au-Co was comparable to the unpromoted sample.

The differences between the two catalyst systems highlighted the dependence of the reducibility of supported cobalt oxides on a promoter's reactivity towards hydrogen. The ideal surface for H_2 activation dissociates H_2 easily and has a moderate-to-strong binding energy of atomic hydrogen, both of which are properties of most transition and platinum group metals [41]. However, H binding is weaker and dissociation is highly activated on coinage metals such as gold, silver, and copper [41]. Table 5.4-1 includes the binding energy of hydrogen on Au, Pt and Co surfaces from Greeley & Mavrikakis [41]. Regardless of the surface (fcc, hcp or top), the binding energy of hydrogen is lower on Au than it is on Pt and even Co. Based on the lower hydrogen binding energy and greater barrier for H-H scission on coinage metals, it is hypothesized that the rate at which H_2 was activated and spilled over to the cobalt oxides was lower on Au versus Pt. Nonetheless, the reduction of Au-Co/Al_2O_3 was still much improved compared to the unpromoted sample, which indicated that Au → Co spillover was still competitive.

Table 5.4-1: Binding energy and perpendicular distance of hydrogen to the plane of nearest-neighbour surface metal atoms, and estimated surface diffusion barriers for surface hydrogen on Au, Pt and Co surfaces [41].

		Binding Energy, eV*
Au	fcc	-2.22
	hcp	-2.17
Pt	fcc	-2.72
	hcp	-2.68
	top	-2.66
Co	fcc	-2.89
	hcp	-2.86

*reference state is gas-phase atomic H and the clean metal slab at infinite separation from each other [41]

- ***Hybrid versus co-supported catalysts: the impact of physicochemical dissimilarities on hydrogen spillover***

The dissimilarities between the TPR profiles of the hybrid samples and the co-supported samples highlighted the influence that their physicochemical differences had on the hydrogen spillover process and the resultant improvement in cobalt reducibility.

Consider Figure 5.3-2 in the preceding section, which included illustrations of how the reduction of cobalt oxides was envisaged to occur via a spillover hydrogen mechanism in either a co-supported sample or a hybrid sample. Hydrogen migration from the promoter was thought to be most efficient when the promoter was present of the same support as the cobalt oxides because the direct promoter → Co spillover pathway was available. In contrast, hydrogen in a hybrid sample needed to negotiate a minimum of 3 interfaces i.e. 3 spillover steps to reach the cobalt oxides including promoter → Al_2O_3 spillover, Al_2O_3 → Al_2O_3 spillover across adjacent support particles, and eventually Al_2O_3 → Co spillover.

In addition to negotiating multiple interfaces, hydrogen needed to migrate long distances across the Al_2O_3 support to reach the cobalt oxides, both of which were likely to have lowered the efficiency of spillover. It was theorised that navigation across multiple interfaces was more kinetically hindered and more detrimental to the efficiency of spillover compared to surface diffusion over the Al_2O_3 support surfaces. The deduction that interfacial spillover was the slow step is supported by the work by Cevallos-Candau & Conner [42], who determined a hydrogen surface diffusion coefficient on oxidic surfaces that was up to 10^9 times greater when the influence of **interfacial spillover** was decoupled from **surface diffusion** (see in Sec. 2.4.6). It was also apparent that the $Al_2O_3 \rightarrow Al_2O_3$ spillover step across adjacent support particles was most detrimental because of the **surface discontinuity** introduced by use of separate support particles. Therefore, the necessity of spillover across numerous interfaces, but especially at the inter-alumina interface was hypothesized to have resulted in the lower reducibility of the hybrid samples compared to the co-supported samples.

Despite these shortcomings, the improved reduction in **Hybrid Pt-Co** suggested that H_2 activation and spillover was more competitive than direct adsorption by cobalt (Fig. 5.4-1).

On the other hand, the '$Au \rightarrow Al_2O_3 \rightarrow Al_2O_3 \rightarrow Co$' spillover pathway in **Hybrid Au-Co** was probably uncompetitive, which allowed reduction to proceed without assistance from the Au promoter. It was hypothesized that poorer H_2 activation by Au and the detrimental surface discontinuity introduced by use of separate supports coincided to result in the poor reducibility of Hybrid Au-Co.

5.4.2 The effect of water vapour on the reduction behaviour of Pt and Au promoted Co/Al_2O_3

The hypothesis behind co-feeding water with the reducing gas during H_2-TPR analyses was based on the bucket-brigade model for surface migration of hydrogen via surface hydroxyl groups on Al_2O_3, and the role of water as a co-catalyst for interfacial spillover.

According to the bucket-brigade model, spillover hydrogen species on Al_2O_3 are mobilised by hydroxyl groups. In particular, the surface diffusion of hydrogen along oxidic surfaces reportedly requires hydrogen-bonded hydroxyl groups (versus isolated hydroxyl groups). Therefore, according to the bucket-brigade model, hydrogen is transferred by associating with the hydrogen-bonded network of hydroxyl groups via a Grotthuss-type mechanism as was illustrated in Scheme 2.4-2. The presence of hydrogen-bonded hydroxyl groups would have been especially relevant to the hybrid samples, where the only available hydrogen pathway included extensive migration along at least two adjacent support particles. Hydrogen-bonded hydroxyl groups exchange hydrogen/deuterium more rapidly than the isolated groups (HD exchange proposed to occur via spillover) but account for just 1-10% of the total OH groups on oxidic surfaces [42-44].

However, evidence of water loss was observed during the H_2-TPR-MS analysis of Co/Al_2O_3 described in Section 5.2, when a large peak corresponding to water (m/z=18) was seen to appear at < 100°C (Fig. 5.2-1). This peak occurred prior to the reduction of any cobalt species. The peak was expected to have included mainly physisorbed water, but it was likely that water formed from the condensation of surface hydroxyl groups was also lost. The detrimental condensation of surface hydroxyl groups to eliminate water probably persisted in the course of the H_2-TPR analyses because the catalysts were exposed to extreme temperatures of up to 950°C for extended periods.

Thermogravimetric studies during H_2 activation and H_2-TPR experiments using the pure Al_2O_3 support and samples from both catalyst systems showed that Al_2O_3 lost 0.03-0.06gH_2O/gAl_2O_3 when exposed to temperatures of up to 350°C. Figure 5.4-4 shows one of the dehydration isotherms obtain with calcined γ-Al_2O_3. The isotherm was similar to those typically observed in the literature [43]. The dehydration is characterised by initial rapid weight loss of physisorbed water. This is followed by slow, gradual weight loss, which also includes surface hydroxyl groups (both isolated and H-bonded) as higher temperatures were attained.

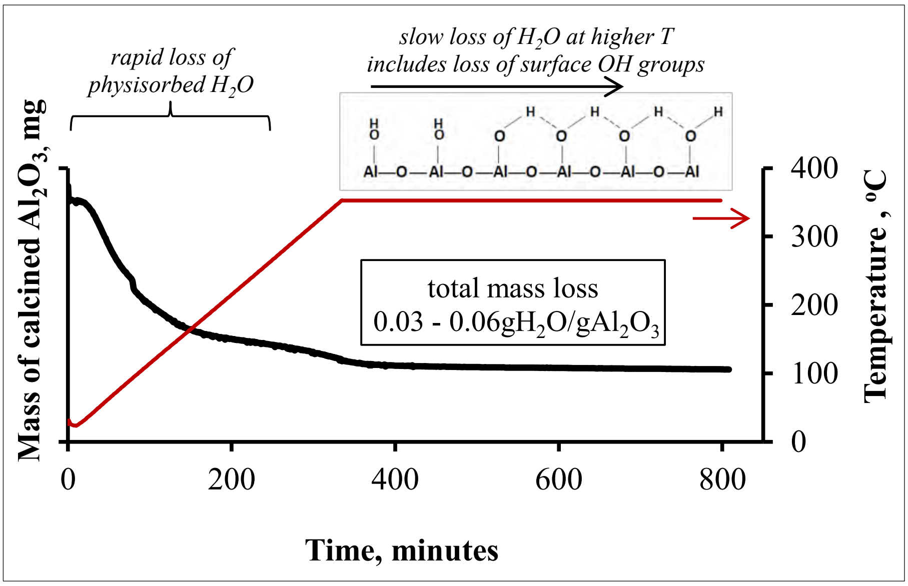

Figure 5.4-4: Thermogravimetric analysis of calcined γ-Al_2O_3 during a H_2-TPR analysis under 4%H_2 -Ar. Temperature ramped at 1°C/min, mass losses attributed to water. γ-Al_2O_3 calcined at 360°C for 6 hours prior to analysis.

A typical Al_2O_3 surface has the capacity for 2 x 10^{15} hydroxyl groups per cm^2 [45]. Therefore based on the surface area of the Puralox SCCA 5-150 support of $162m^2/g$, the support had a mass-based hydroxyl group capacity of approximately $9x10^{-5}$g/gAl_2O_3. This was significantly lower than the 0.03 - 0.06gH_2O/gAl_2O_3 mass loss from the Al_2O_3 according to the gravimetric studies, which demonstrated that the largest portion of the mass loss was due to physisorbed water. According to Peri [43, 44], considerable quantities of physisorbed water are held by γ-Al_2O_3 surfaces at temperatures below 100°C, but all physisorbed water molecules are removed by 400°C. On the other hand, infrared analyses show that the intensities of absorption bands assigned to OH groups decrease with temperature, and only disappear at temperatures above 850°C.

5.4.2.1 *The effect of water vapour on the reduction of cobalt oxides during H_2 TPR-TCD*

From the literature, the movement of hydrogen is not just dependent on the extent of hydroxylation/surface acidity of oxidic surface but also on the presence of molecular water i.e. physisorbed water (Sec. 2.4.5 & 2.4.6). OH groups act as vehicles on the surface of oxides, while water and even other molecules with a high proton affinity such as alcohols can act as co-catalysts for interfacial spillover. Apparently, water molecules in a monolayer can abstract an adsorbed H atom from the surface of the dissociating metal to form a proton. This proton could then be easily transferred through the monolayer to an oxide surface, i.e. across the metal oxide interface (Sec. 2.4.6). This mechanism reportedly helps compensate for the energy required to break the H-M bond in favour of a much weaker bond to the receiving oxide surface.

Figure 5.4-5 shows the results from H_2-TPR-TCD analyses during which the reducing gas was saturated with water at nominal temperature and pressure prior to reduction. The composition of the reducing gas was therefore 3.1% H_2O - 4.8% H_2 - 90.9% Ar, and thus had $H_2O:H_2$ ratio of 0.64:1. Exposure to a water saturated gaseous atmosphere has been shown to induce rehydroxylation of dry Al_2O_3 even at temperatures higher than 600^{o}C [43] and so a higher extent of hydroxylation was expected to have occurred despite the extreme temperatures reached during H_2 TPR analyses. Due to the presence of water, the TCD signal during the water co-feeding experiments was noisy, and did not improve even after a water trap was introduced upstream of the TCD. From Figure 5.4-5, it is clear that the presence of water vapour caused the TPR profiles of all samples to shift to higher temperatures, which was consistent with a more difficult reduction.

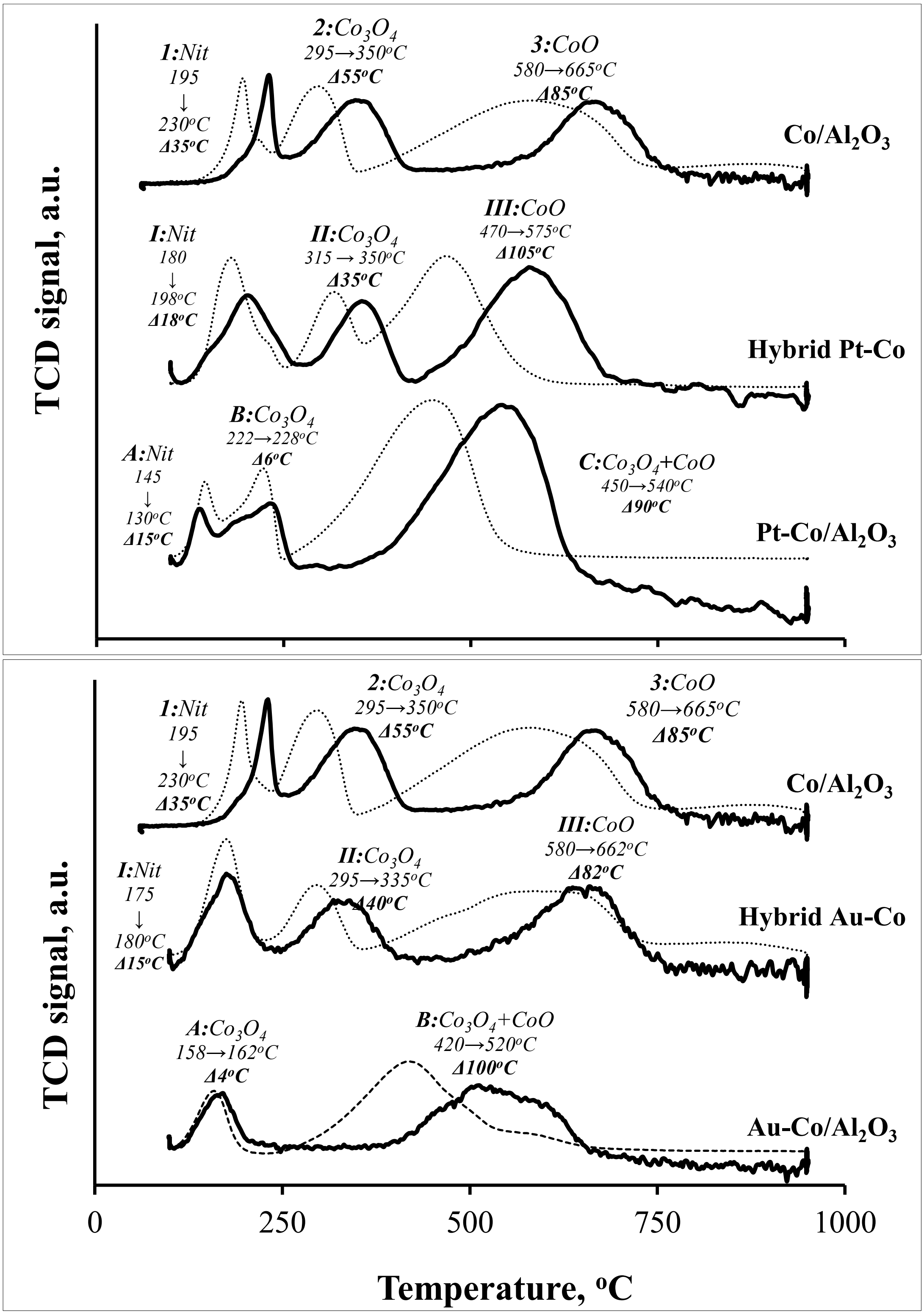

Figure 5.4-5: H_2 TPR-TCD profiles of obtained with a reducing gas composed of 3.1% H_2O - 4.8% H_2 - 90.9% Ar, i.e. H_2O:H_2 ratio of 0.64:1. The profiles (dark bold curves) are overlayed with those from the dry H_2-TPR analysis (pale curves). ***Top:*** Pt-Co Catalyst System. ***Bottom:*** Au-Co Catalyst System.

Co/Al$_2$O$_3$: The peaks in the reduction profile of Co/Al$_2$O$_3$ shifted by Δ35°C (nitrates), Δ55°C (Co$_3$O$_4$) and Δ85°C (CoO). Although the shapes of the nitrate and Co$_3$O$_4$ reduction peaks remained relatively unaltered, that of CoO changed significantly. Besides shifting by the greatest extent, the area of the CoO peak was approximately half that under dry conditions, which indicated that the quantity of reducible species in this temperature range had decreased. The position of the peak was also at the same temperature as the high temperature shoulder assigned to the CoO species in close interaction with the support in Section 5.2. This suggested that water vapour increased the extent to which CoO interacted with the support, which in turn hindered the reducibility. Therefore, it was deduced that the high H$_2$O:H$_2$ ratio of 0.64:1 most likely facilitated the mobility of hydrated cobalt oxides/cobalt ions into the structure of the support, resulting in the formation of difficult to reduce cobalt-alumina complexes and increasing the level of metal support interactions. The total area/hydrogen consumption under the profile of Co/Al$_2$O$_3$ decreased due to the smaller CoO reduction peak. This demonstrated that a lower quantity of cobalt reduced in the TPR analysis temperature range of 100-950°C, and thus some cobalt species remained unreduced despite the extreme reduction temperatures. The formation of irreducible Co was supported by the fact that the peak assigned to the reduction of mixed cobalt alumina complexes had completely disappeared, which indicated that perhaps even higher reduction temperatures were required for reduction. Evidence of formation of cobalt-alumina complexes was observed in the spent catalyst recovered on the completion of the TPR analysis, which had turned from the typical dark-grey/black following dry reduction, to the characteristic blue colour of CoAl$_2$O$_4$.

Hybrid Pt-Co: Compared to the dry H$_2$-TPR profile, the peaks shifted to higher reduction temperatures as follows: Δ18°C (nitrates), Δ35°C (Co$_3$O$_4$) and Δ105°C (CoO). Like with the Co/Al$_2$O$_3$ sample, the CoO reduction peak shifted to the greatest extent but unlike the Co/Al$_2$O$_3$, the shape of this peak was not as greatly altered. Nonetheless, the CoO peak did separate more from the preceding Co$_3$O$_4$ peak, and showed some tailing at low temperatures, which was consistent with less facile reduction. The total area under the TPR profile was relatively unchanged unlike the case of Co/Al$_2$O$_3$, which indicated that all the Co was reducible by the end of the analysis at 950°C. This observation suggested that the presence of Pt helped counter the water-induced effect of formation of Co species that were completely irreducible in the temperature range of the TPR.

Pt-Co/Al$_2$O$_3$: On average, the peaks in this sample shifted the least compared to the dry H$_2$-TPR profile within the Pt-Co Catalyst System. The nitrate peak only shifted by Δ15°C, the Co$_3$O$_4$ peak by just Δ6°C and the third peak (C) shifted by Δ90°C. Even though the third peak showed some initial tailing (indicative of slower kinetics/delayed nucleation), the total area under the TPR profile seemed unchanged in the presence of water. Like with Hybrid Pt-Co, this suggested an enhancing effect of Pt in partially countering the detrimental effect that water had on the formation of irreducible Co species.

Hybrid Au-Co: The reduction profile was similar to that of the unpromoted Co/Al$_2$O$_3$ sample. Even in the presence of water, Au in the hybrid catalyst did not improve the reducibility of cobalt oxides.

Au-Co/Al$_2$O$_3$: It was interesting that the first peak of the profile of Au-Co/Al$_2$O$_3$ was almost unaltered in shape and location, and thus unaffected by the presence of water. Only the maximum of the second reduction peak (B) shifted greatly, by Δ100°C. The onset of the peak appeared to tail, which indicated that water vapour slowed the rate at which nucleation occurred compared to dry H$_2$-TPR analyses. The high temperature shoulder of Peak B was also pronounced, which indicated that the presence of water vapour increased the quantity of difficult to reduce cobalt species.

5.4.2.2 The effect of water vapour on the reduction of cobalt oxides during in situ XRD

In situ XRD analyses during H$_2$ TPR with water co-feeding were also carried out in a borosilicate capillary reactor as described in Section 4.2.5.2. XRD allowed for the analysis of the cobalt phases and was complementary to the H$_2$-TPR-TCD analyses in which the assignment of reducing species is often a subject of contention, and becomes even more complex in the presence of water.

The in situ XRD-TPR results are shown in Figures 5.4-6 to 5.4-10 and include the complete XRD diffractograms collected in the course of the reduction as a function of temperature, and graphs of peak intensities of the peaks corresponding to CoO (49.7°), Co$_3$O$_4$ (70.3°) and Co^0 (51.7°) as a function of temperature to better illustrate the trends in the reduction with and without water. It must be noted that the long scan time of approximately 30 minutes necessitated that a slow temperature ramp (1°C/min) was employed because it limited the temperature difference within the same diffractogram. Furthermore, water co-feeding in this case included saturation of pure H_2 (rather than 5%H_2-Ar) with water at room temperature, which resulted in a lower H_2O:H_2 partial pressure of 0.03:1 compared to 0.64:1 during the H_2-TPR TCD analyses. All the details regarding the methodology of these analyses are explained in Section 4.2.5.2.

Under dry conditions, the intensity of the peak corresponding to Co_3O_4 ($2\theta=70.3^o$) in **Co/Al_2O_3** decreased rapidly from 160°C, and had completely disappeared by 220°C (Figure 5.4-6). This reduction was much slower in the presence of water, where the peak intensity declined more slowly from about the same initial temperature, but only disappeared after 290°C. The reduction of CoO was even more hindered. Under dry conditions, the CoO peak decreased steadily and had completely disappeared by about 400°C. However, when water was present, the maximum intensity of the CoO peak was shifted by ca. 50°C and the rate of decline of the CoO intensity was much slower, so that some CoO persisted even at the end of the reduction at 425°C. The negative effect of water on Co^0 formation was quite pronounced, the evolution of the Co^0 phase shifted from about 175°C under dry conditions to 400°C in the presence of water.

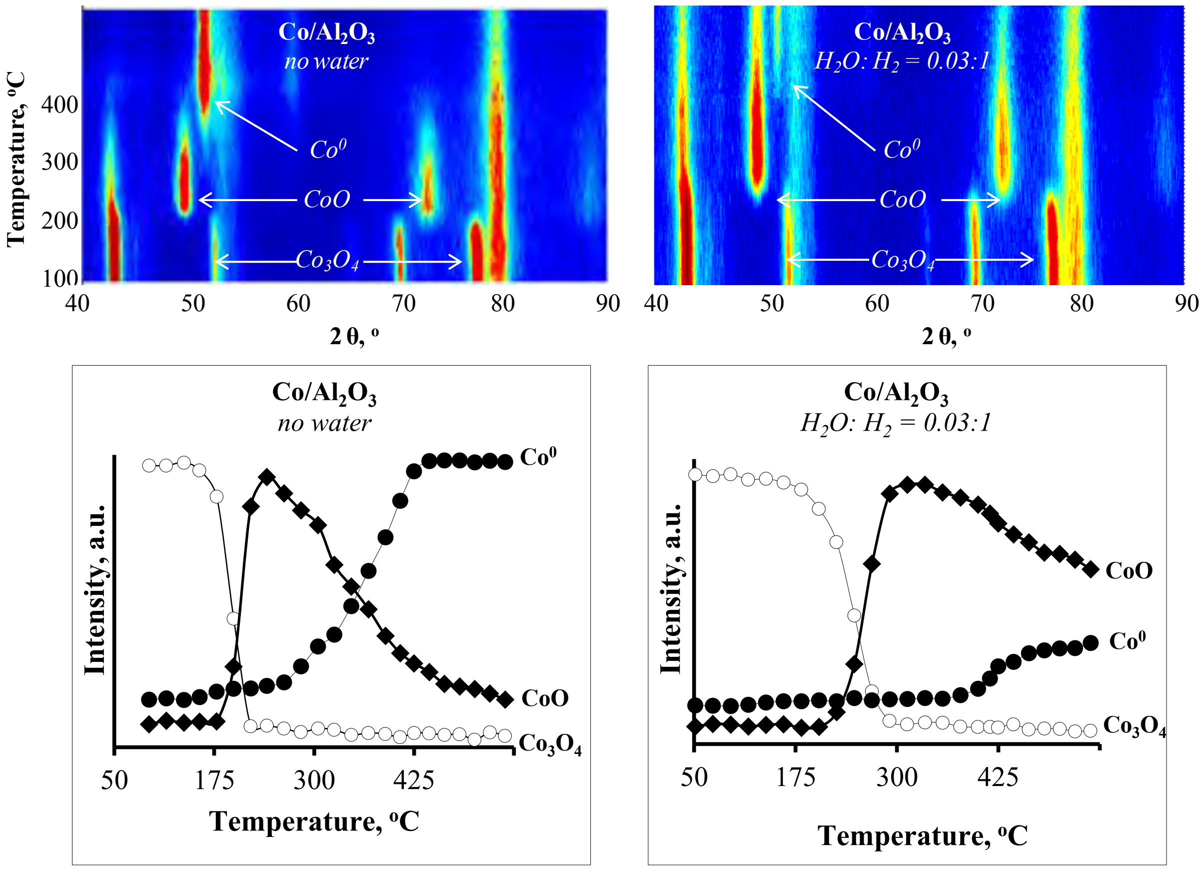

Figure 5.4-6: XRD scans taken during in situ XRD-TPR of Co/Al_2O_3.

The reduction of **Hybrid Au-Co** followed a similar pattern as that of Co/Al_2O_3.What was interesting with regard to the **Hybrid Pt-Co**, **Pt-Co/Al_2O_3** and **Au-Co/Al_2O_3** samples was that their reduction did not seem to have been greatly affected by the presence of water. The curves of the peak intensities of Co_3O_4, followed the same trends and occurred at the same temperatures with or without water. Only the rate at which the intensity of the CoO peak declined in favour of the Co^0 seemed to have been slightly slower. This was evidence that the presence of Au and Pt promoters helped counteract the negative effects of water.

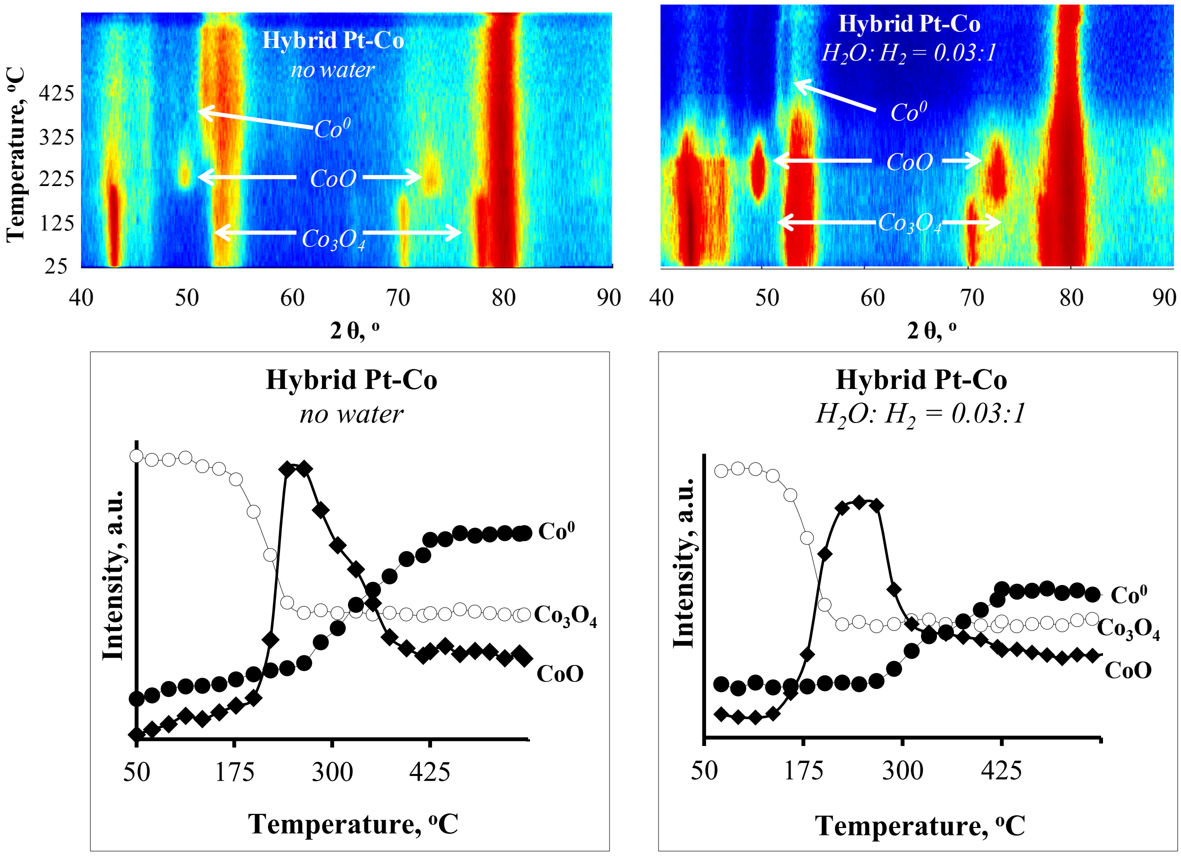

Figure 5.4-7: XRD scans taken during the in situ XRD-TPR of Hybrid Pt-Co.

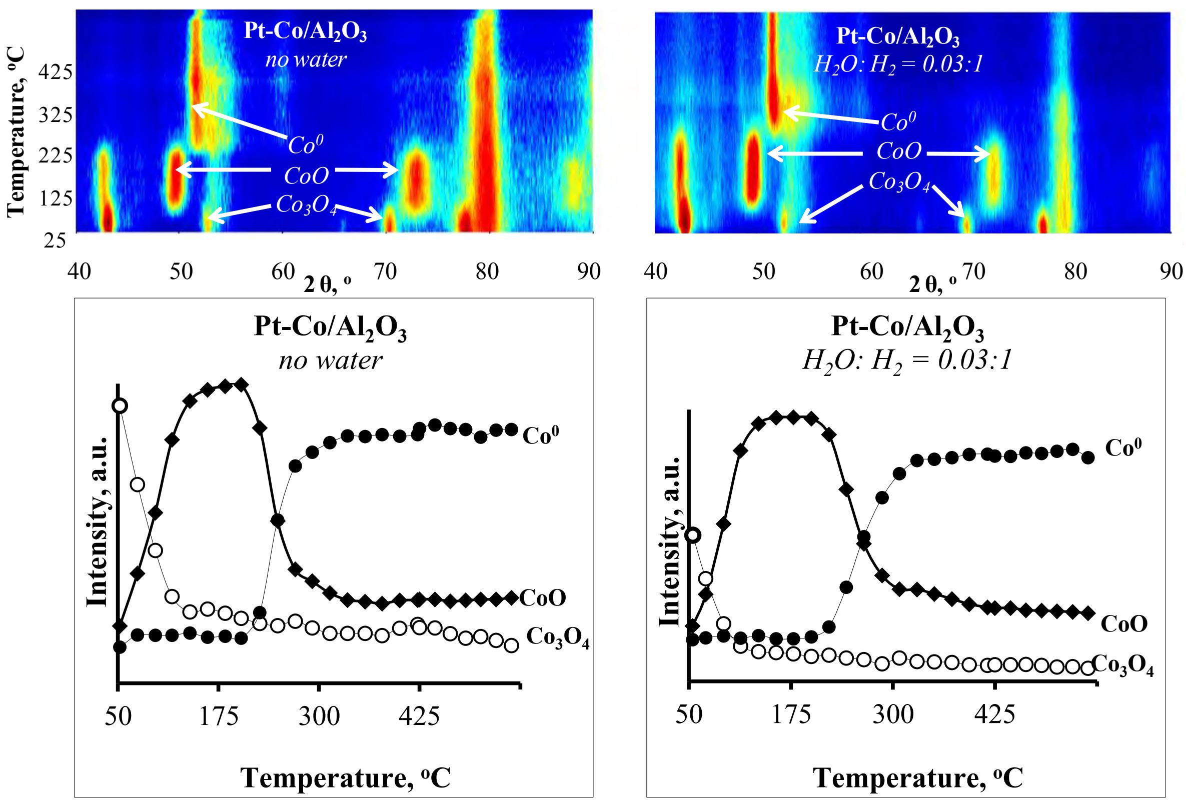

Figure 5.4-8: XRD scans taken during the in situ XRD-TPR of Pt-Co/Al₂O₃.

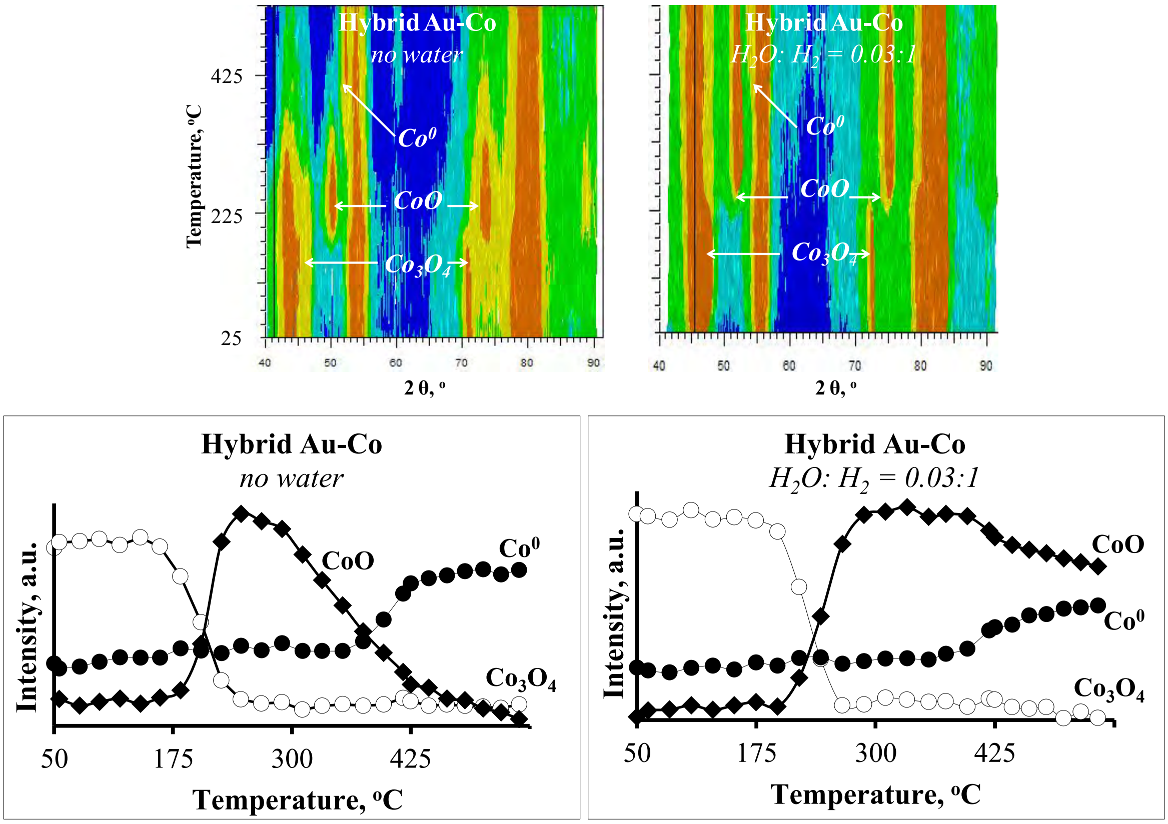

Figure 5.4-9: XRD scans taken during the in situ XRD-TPR of Hybrid Au-Co.

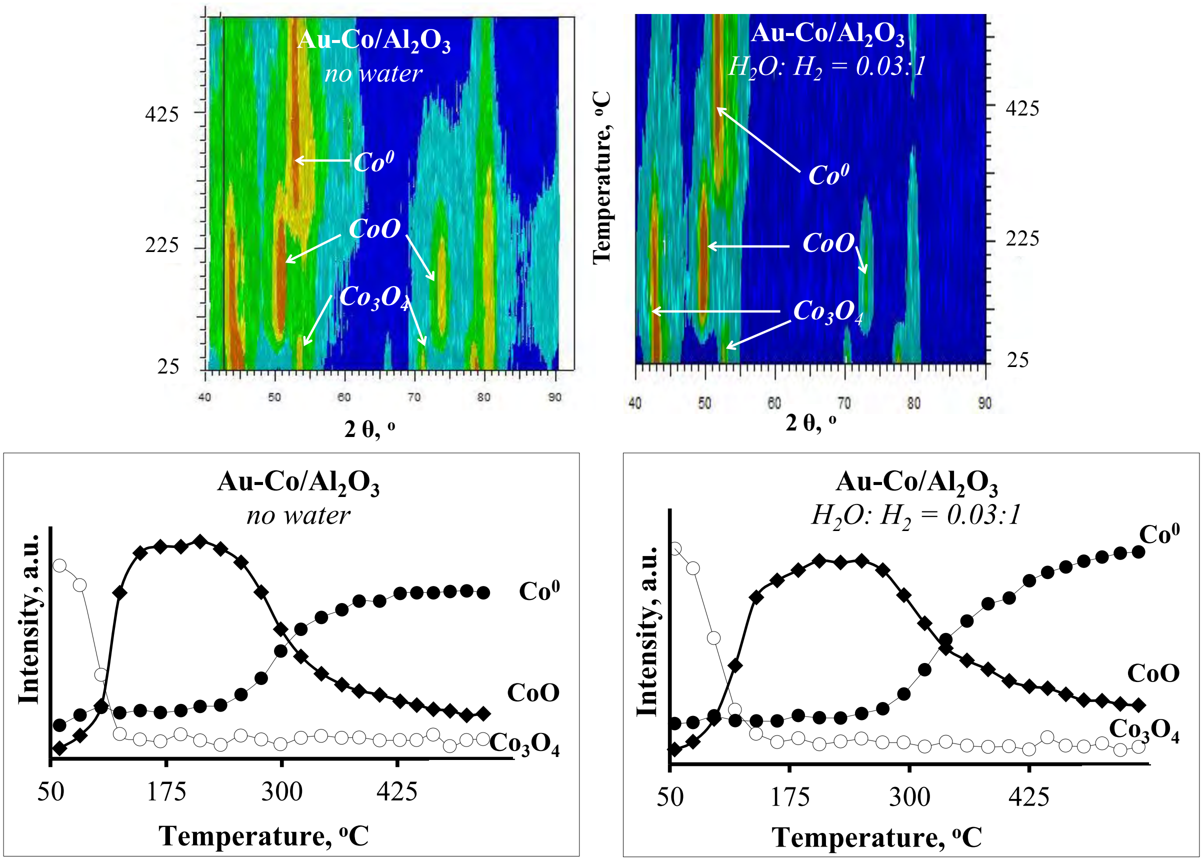

Figure 5.4-10:XRD scans taken during the in situ XRD-TPR of Au-Co/Al_2O_3.

○ *Consolidation*

The negative effect of water during the reduction and under Fischer-Tropsch conditions has been attributed to the ability of water to hydrate cobalt oxides and the support, which enhances the movement of ions into the cation-deficient spinel structure of Al_2O_3 [21-23, 34, 46-49]. As discussed during the peak assignment of the TPR profile in Section 5.2, Co ions can migrate into both octahedral and tetrahedral sites of γ-Al_2O_3, where by the Co in octahedral sites is reducible, while that in tetrahedral sites is not [21, 23]. This was specifically relevant for Co/Al_2O_3 and Hybrid Au-Co because the total reducible Co in the TPR profile up to 950°C decreased. The total decrease was evident from the smaller area under the CoO peak and the disappearance of the high temperature reduction peak assigned to non-stoichiometric cobalt alumina complexes. It may therefore be deduced that water facilitates the particularly detrimental migration into tetrahedral sites [23].

These deductions are supported by the work of Goodwin et al. [23] during an extensive study that involved H_2-TPR in water vapour concentrations of 0.6-20% on Ru-Co/Al_2O_3. These authors also observed that the shift of the Co_3O_4 peak was minimal and that the CoO peak position shifted to higher temperatures as the water vapour content increased. Water reportedly had no effect on the reducibility of Co_3O_4, and the small shifts to higher temperatures were attributed to slight variations in the partial pressure of hydrogen following water addition. On the other hand, the great change in the CoO peak was attributed to changes induced by water vapour [23].

In any case, the TPR profiles (Fig. 5.4-5) further demonstrated that promoters catalysed the reduction of Co oxides, and even helped to partially alleviate the negative effects of water. This was especially relevant with the reduction of CoO. In Co/Al_2O_3, the CoO peak was not just smaller, but the onset of the peak tailed significantly, indicating slow kinetics and slow nucleation of Co^0 [23]. However, the extent of tailing was much lower in the presence of promoters particularly with $Pt\text{-}Co/Al_2O_3$ but also Hybrid Pt-Co, which showed that the presence of Pt helped speed up the nucleation by a remote-control mechanism. It is well known that water prolongs the induction step and thus the initial rate of nucleation during the reduction of metal oxides. Nucleation sites, which are said to be defects, are formed during the induction step (Sec. 2.2.4.2). According to Arnoldy & Moulijn [50] water *destroys* the surface defects required for nuclei formation. Interestingly, Arnoldy & Moulijn deduced that the role of water, even during the reduction of unsupported iron oxide particles was complex. Even though water retarded the nucleation step during the reduction of the oxide particles, it could enhance the reduction rate by accelerating hydrogen spillover between Fe^0 nuclei and the oxide, i.e. water enhanced autocatalysis but retarded induction.

In summary, the positive effects of water during the reduction of supported cobalt oxides may include enhancing the extent of hydroxylation for movement via the bucket-brigade model, facilitating a physisorbed monolayer in which water can act as a co-catalyst for interfacial spillover, and facilitating autocatalysis. On the other hand, the negative effects of water include facilitating the movement of Co ions into both octahedral and irreducible tetrahedral sites, and delaying the nucleation/prolonging the induction period.

The lower $H_2O:H_2$ ratio during the in situ XRD analyses helped prevent the detrimental formation of cobalt aluminates, which were not observed in any of the XRD diffractograms (Figs. 5.4-6 to 5.4-10). This was evidenced by the fact that the samples remained dark grey/black following reduction in water, unlike after the H_2 TPR-TCD when some samples contained a blue hue that is characteristic of $CoAl_2O_4$. It was also possible that some non-stoichiometric mixed cobalt alumina complexes had indeed formed during the reduction but did not have sufficient three-dimensional, long-range order for detection with XRD [23].

Therefore, the negative effects of water clearly countered the benefits that had been hypothesized based on its positive effect on spillover. However, it must be kept in mind that from the literature, the experiments in which the enhancing role of water on spillover is reported include processes like HD exchange or H-bronze formation (Sec. 2.4.4). These processes do not necessarily include mechanisms in which H_2O would have contradictory effects. Therefore, the fact that reduction did not improve in the hybrid samples was not actually evidence that water did not have a positive effect on spillover. Based on these results, it is suggested that even though the presence of water may facilitate hydrogen spillover, the positive effects are more likely to be observed during reactions in which water does not play an additional detrimental effect. Enhanced spillover in the presence of water is thus more likely to be observed during reactions such as H/D exchange and temperature programmed desorption (TPD) as described in Section 2.4.

Attempts to lower the saturation temperature in order to decrease the P_{H2O} and thus control the undesirable formation of strong metal support interactions failed due to limitations associated with the analysis equipment. New experiments to pre-treat the catalysts with a flow of H_2O-Ar (i.e. Ar saturated with H_2O) prior to dry H_2 TPR-TCD analyses also failed because the obtained reduction profiles were identical to those carried out under just dry H_2-TPR conditions. These particular experiments were attempted because they had proved successful during the TPR study by Hilmen et al. [16] using Hybrid Re-Co catalysts. The fact that Hilmen et al. [16] observed an improvement in the reducibility of the Re-Co-Al_2O_3 catalyst system in the presence of water highlighted the chemical differences between the Pt and Re promoters for the cobalt-based catalyst. For example, Re oxides form more easily in water and are volatile at high temperatures, which could have caused them to migrate and establish direct coordination with the Co oxides. This was not the only discrepancy with the Re-Co system studied by Hilmen et al. [16]. The other difference was the fact that an improvement in the reduction was observed when Hybrid Re-Co was pressed into composites of 425-850μm. As discussion in Section 5.4.1, compression of Hybrid Pt-Co into particles of 500μm+ did not result in a similar improvement in reducibility.

5.5 The Effect of Pt and Au promoters on the reduction of Cobalt Oxides during Isothermal Catalyst Activation

Three complementary characterisation techniques, including Thermogravimetric Analysis (Sec. 5.5.1), in situ XRD-TPR (Sec. 5.5.2) and quasi-in situ XPS (Sec. 5.5.3) were utilised as part of a multifaceted approach to study the effects of the Pt and Au reduction promoters during catalyst activation (12 hours in pure H_2, 350°C, and 1 bar). Thermogravimetric Analyses were used to quantify the improvement in the extent of reduction, while the in situ XRD analyses and the quasi-in situ XPS analyses were used to examine the effects of the promoters on the bulk and surface composition of the activated catalysts respectively. A comprehensive picture of the catalysing effect of Pt and Au during the activation step was fundamental to this work because this pre-treatment generates the active sites for the Fischer-Tropsch reaction.

5.5.1 Effect of Pt and Au promoters during the isothermal activation process studied by TGA

Figure 5.5-1 includes the results from the thermogravimetric analyses carried out at the selected standard catalyst activation conditions for the Fischer-Tropsch reaction.

The procedure followed for each analysis is detailed in Section 4.2.4. At the start of the analysis, the catalyst was dried in N_2 to prevent erroneous assignment of the loss of physisorbed water to a reducing species. The loss of physisorbed water ranged from 0.13-0.40 g_{H2O}/g_{Co}, with the greatest loss associated with the hybrid samples. The TGA of the pure Al_2O_3 support (Appendix E2) was used to determine that physisorbed water was present in ratio of $0.063 g_{H2O}/g_{Al2O3}$, and hence most of it (> 75%) was associated with the Al_2O_3 support. Therefore, the hybrid samples experienced the greatest mass loss during drying because they were mechanical mixtures of two supported monometallic samples, with twice the amount of Al_2O_3 in the other samples.

Mass loss during the H_2 Stage and mass gain during the O_2 Stage in Figure 5.5-1 were indicative of a sample's degree of reduction. In the **Pt-Co Catalyst System**, the mass loss was greatest in Pt-Co/Al_2O_3, followed by in Hybrid Pt-Co, which supported the promoting effect of Pt on the reducibility of supported cobalt oxides. In the **Au-Co Catalyst System**, the mass loss was greatest in Au-Co/Al_2O_3, but was nearly indistinguishable between Hybrid Au-

Co and Co/Al_2O_3. The latter observation confirmed the TPR and in situ XRD results in Sec. 5.4 as to the little difference between the two catalysts' reduction.

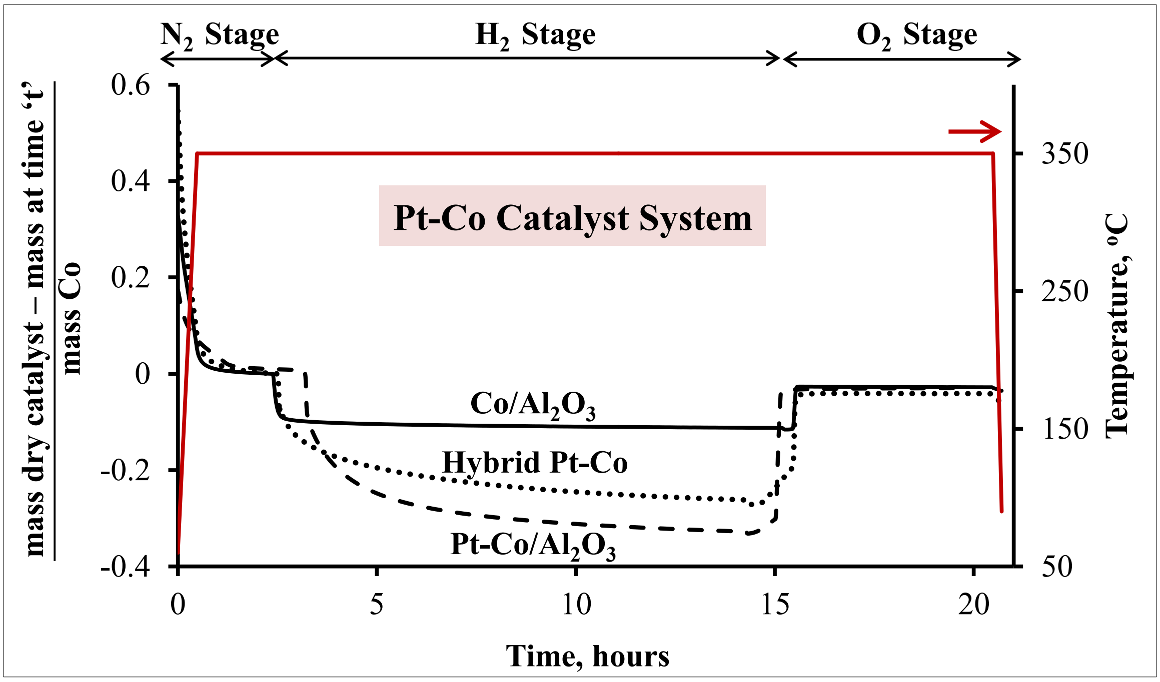

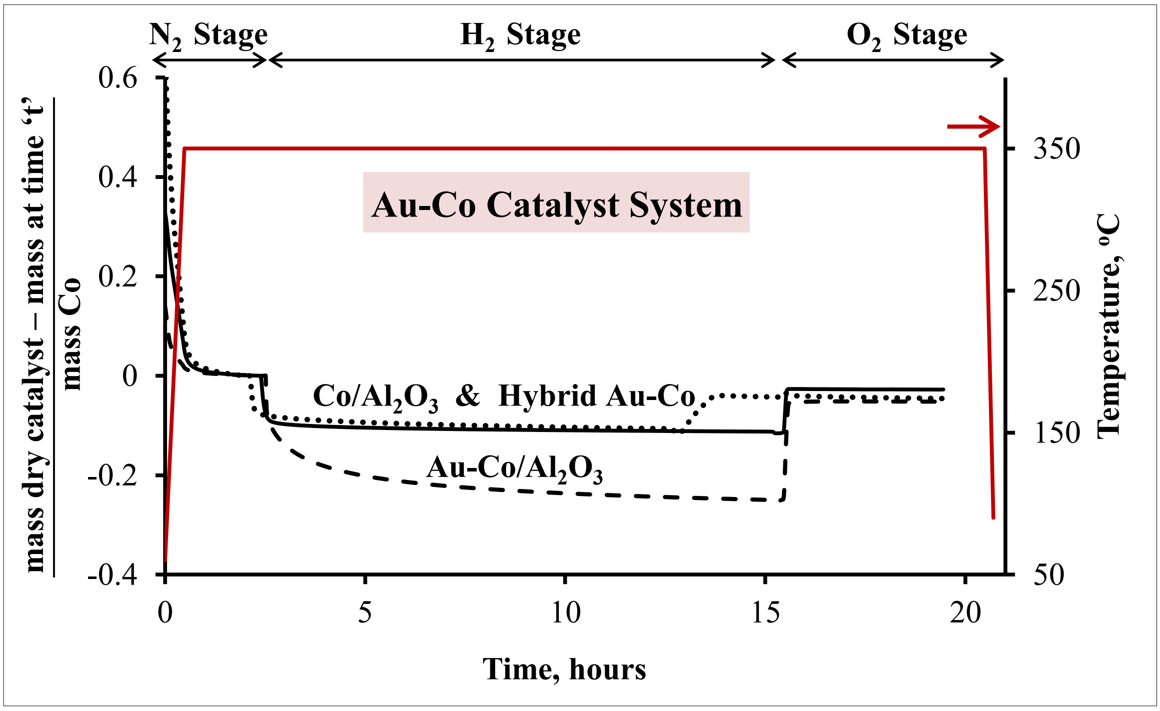

Figure 5.5-1: Thermogravimetric Analysis (TGA) profiles during the isothermal activation at 350°C.
Sample drying carried out in pure N_2, reduction/activation carried out in pure H_2, and re-oxidation step carried out in synthetic air. All flow rates maintained at $1000 ml \cdot min^{-1} \cdot g_{Co}^{-1}$ and temperature ramped at 10°C/min.

5.5.1.1 The effect of promoters on the degree of reduction (DOR)

The degrees of reduction were calculated according to Equations 5.5-1 and 5.5-2, in which it was assumed that oxygen (O) was lost from the supported Co_3O_4 during the H_2 Stage, and gained during the O_2 Stage as indicated in Figure 5.5-1. Therefore, the degrees of reduction were analogous to an *oxygen conversion* because they took the direct $Co_3O_4 \rightarrow Co^0$ reduction and vice versa into account, without the formation of CoO as an intermediate.

$$Degree\ of\ reduction\ (DOR) = \frac{\Delta\ mass\ during\ reduction}{mass\ of\ O\ in\ Co_3O_4\ loaded} \times 100 \qquad \textbf{Equation 5.5-1}$$

$$Degree\ of\ reduction\ (DOR)_{ox} = \frac{\Delta\ mass\ during\ oxidation}{mass\ of\ O\ in\ Co_3O_4\ loaded} \times 100 \qquad \textbf{Equation 5.5-2}$$

Table 5.5-1 shows the calculated degrees of reduction based on the reduction and the oxidation stages of the thermogravimetric analyses. Ideally, the degrees of reduction according to Equations 5.5-1 (DOR) and 5.5-2 (DOR_{ox}) should be equal, but the values determined from the O_2 Stage (DOR_{ox}) were lower for all samples. The discrepancy may have arisen from a number of reasons including: non-oxidisable species, incomplete drying in N_2, and the presence of impurities and other cobalt species in the calcined samples. If drying in N_2 had been incomplete, then a portion of the mass lost in the H_2 Stage would have been due to water loss, and a corresponding gain would not have been observed in the O_2 Stage. The presence of nitrates in the calcined samples (as $Co(NO_3)_2$ or ions adsorbed on the catalyst surface) would have also resulted in a greater mass loss during the H_2 Stage and led to a higher perceived degree of reduction based on the H_2 stage. Due to the presence of nitrates, it was hypothesized that the calculated DOR during the H_2 stage was less accurate.

In any case, the overall trend in the degree of reduction calculated using either equation was similar and increased as follows: (Co/Al_2O_3 ≈ Hybrid Au-Co) < $Au\text{-}Co/Al_2O_3$ < Hybrid Pt-Co < $Pt\text{-}Co/Al_2O_3$.

Table 5.5-1: Degree of reduction (DOR) following isothermal reduction and oxidation at 350°C.

	Degree of reduction (DOR), %	
	H_2 Stage (DOR)	***O_2 Stage (DOR_{ox})***
Co/Al_2O_3	30.9	23.2
Hybrid Pt-Co	71.8	60.5
$Pt\text{-}Co/Al_2O_3$	89.8	81.6
Hybrid Au-Co	31.3	18.0
$Au\text{-}Co/Al_2O_3$	67.5	53.9

The enhanced reduction in spite of the great Pt-Co separation in Hybrid Pt-Co suggested promotion via a remote-control promotion mechanism in agreement with the observations made during the TPR analyses. The lower reducibility of Hybrid Pt-Co compared to $Pt\text{-}Co/Al_2O_3$ also concurred with the TPR analyses in which the diminished efficacy of reduction via a spillover mechanism was attributed to the multiple interfacial spillover steps required of hydrogen in the hybrid samples.

The trend in the degree of reduction was consistent with the less effective reduction promotion effect of Au compared to Pt. $Au\text{-}Co/Al_2O_3$ only increased the DOR by a factor of 2.2 (compared to a factor of 3.0 with $Pt\text{-}Co/Al_2O_3$) and the promotion effect of Au on the reduction of Hybrid Au-Co was not statistically relevant. As discussed in the preceding section, Au surfaces are less active for H_2 activation and so the formation of the hydrogen species required for the reduction of cobalt oxides is less competitive with Au versus Pt promoters. The lower reactivity of Au probably contributed to the poor overall kinetics of spillover across multiple interfaces in Hybrid Au-Co, which resulted in the unremarkable improvement in the DOR.

As a matter of interest, the calculated DOR of **Hybrid Pt-Co** was comparable to that of **$Au\text{-}Co/Al_2O_3$** despite a much greater promoter-cobalt separation (Table 5.5-1). Analogous behaviour was seen in the TPR analyses in Figure 5.4-3, where the profiles of these two samples were also observed to terminate at similar temperatures.

5.5.1.2 *Evidence of a 'threshold' degree of reduction (DOR) due to cobalt-alumina interaction*

Since metallic cobalt is the active phase for the Fischer-Tropsch reaction, it is more useful to determine its content in the reduced samples, rather than the DOR as reported in Table 5.5-1. The values in Table 5.5-1 were calculated based on the assumption that Co_3O_4 reduced directly to Co^0 when in fact, in situ XRD-TPR analyses in Section 5.2 showed that Co_3O_4 reduction occurred via formation of a stable CoO intermediate. Therefore, not all the mass lost during the H_2 Stage resulted in the formation of Co^0 since some O would have been consumed in the formation of the CoO intermediate. Scheme 5.5-1 is an illustration of the reduction sequence of a Co_3O_4 crystallite and the corresponding loss of O from the Co_3O_4 structure.

$$\mathbf{Co_3O_4} \xrightarrow{-25\%\ O_{total}} \mathbf{CoO} \xrightarrow{-75\%\ O_{total}} \mathbf{Co^0}$$

Scheme 5.5-1: Reduction sequence of an ideal Co_3O_4 crystallite assuming a two-step reduction with CoO as an intermediate.

Based on an ideal 2-step reduction, nucleation of a pure CoO phase would occur after removal of 25% of the O from the structure of Co_3O_4. In this ideal scenario, Co_3O_4 and Co^0 can not co-exist. Therefore, ideally, formation of Co^0 would require that a minimum threshold DOR of 25% was exceeded. According to Scheme 5.5-1, a reduced ideal/perfect cobalt crystallite with a DOR of 25-100% contains a mixture of CoO and Co^0. On the other hand, a reduced crystallite with DOR < 25% would not contain any metallic Co^0, but rather a mixture of unreduced Co_3O_4 and CoO. However, it must be cautioned that the calculated values of the DOR shown in Table 5.5-1 were cumulative over an entire sample i.e. over multiple crystallites, and were not necessarily representative of each individual cobalt crystallite as implied by the ideal reduction sequence in Scheme 5.5-1. A catalyst sample contains multiple crystallites of varying sizes and varying degrees of interaction with the support and/or promoter. Due to the different physicochemical environment of the crystallites, it is unfeasible that the *same* value of the degree of reduction can be attained *simultaneously* by all the disparate crystallites. For example, the DOR of 30.9% calculated for Co/Al_2O_3 could be identical for each crystallite, but could also be the *cumulative* value over the entire sample if 20% of the crystallites are fully reduced and the rest have a DOR of 13.6% (i.e. 0.2 x 100% + 0.8 x 13.6% = 30.9%).

Figure 5.5-2 shows the reduction curves determined from the TGA results i.e. the degree of reduction (DOR) as a function of time. Also included is a line along the threshold DOR, which corresponds to a loss of 25% of the total O from the Co_3O_4 and curves of bulk Co_3O_4, from Batley et al. [51]. Among the supported samples, the curve of Pt-Co/Al_2O_3 increased fastest with time. That of Au-Co/Al_2O_3 closely followed Hybrid Pt-Co in accordance with the comparable values of DOR in these samples. The effect of the promoters was evidenced by the fact that the curves of Hybrid Pt-Co, Pt-Co/Al_2O_3 and Au-Co/Al_2O_3 increased far above that of unpromoted Co/Al_2O_3.

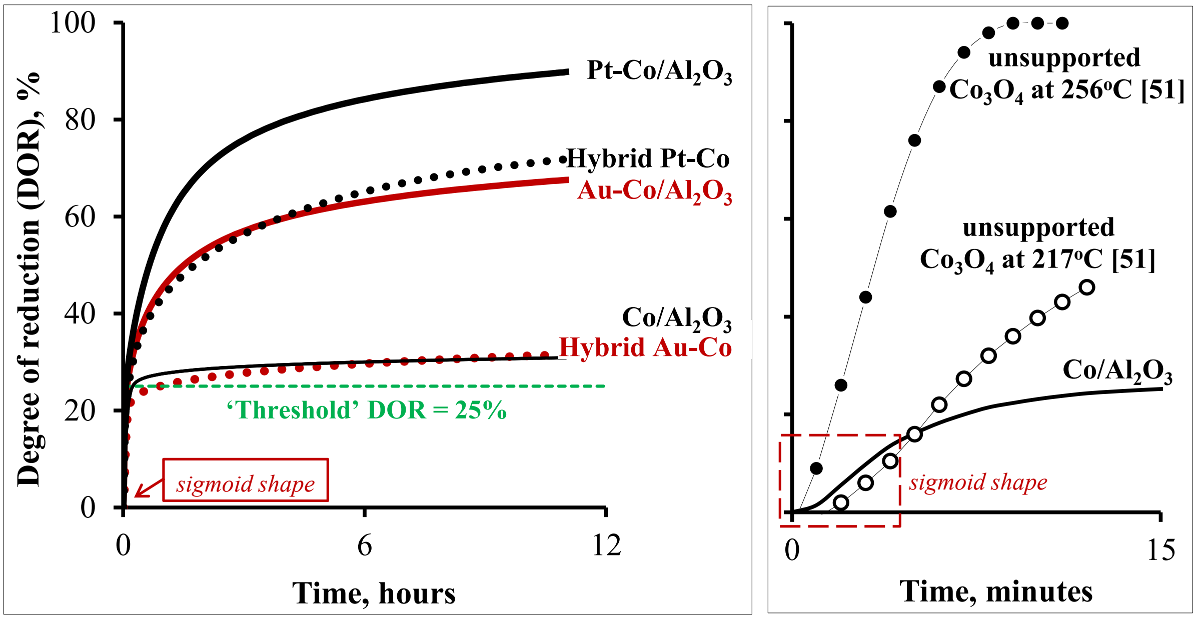

Figure 5.5-2: ***Left:*** Reduction curves of samples in the Au-Co and Pt-Co systems during isothermal reduction in H_2 at 350°C as determined from thermogravimetric analyses. ***Right:*** Reduction curve of Co/Al_2O_3 overlaid with those of bulk Co_3O_4 during isothermal reduction at various temperatures from Batley et al. [51].

Interestingly, Co/Al_2O_3 rapidly attained the threshold DOR of 25% despite a low final DOR of 30.9% (Fig. 5.5-2). The threshold DOR was attained in the first 14 minutes, but it took an additional 10.6hours to reach the final DOR of 30.9%. Hence, the reduction rate from 25% → 30.9% was a factor of 200 slower than that from 0% → 25%. Based on the ideal two-step reduction of an ideal single Co_3O_4 crystallite presented in Scheme 5.5-1 (assuming that Co_3O_4 and Co^0 can not co-exist), it was apparent that attaining a 25% degree of reduction, which incidentally corresponds to ideal $Co_3O_4 \rightarrow CoO$ reduction was facile, while the kinetics of $CoO \rightarrow Co^0$ reduction were severely hindered.

Consider Figure 5.5-2: *Right*, in which the reduction curve Co/Al_2O_3 is overlaid with those of bulk unsupported Co_3O_4. The reduction curves of the bulk Co_3O_4 particles were obtained at lower reduction temperatures of 217°C and 256°C [51]. Even at the lower temperatures, the reduction rate of Co_3O_4 in the absence of a support was significantly faster and only slowed down as complete reduction was approached. This indicated that the kinetics of bulk $Co_3O_4 \rightarrow CoO$ versus bulk $CoO \rightarrow Co^0$ did not differ as substantially as they did in supported cobalt oxides in the Co/Al_2O_3 sample.

The reduction curves of bulk Co_3O_4 suggest that the rapid decline in the reduction rate of Co/Al_2O_3 at the threshold DOR of 25% was likely to have been induced by the Al_2O_3 support. In particular, it appears that the stabilising effect of the support affected the reduction of the CoO intermediate to a greater extent than Co_3O_4. The curve of a hypothetical Co/Al_2O_3 sample in which Al_2O_3 affected the kinetics of both $Co_3O_4 \rightarrow CoO$ and $CoO \rightarrow Co^0$ reduction to the same extent was imagined free of the rapid decline in the reduction rate after the threshold DOR of 25% was attained. The curve of this hypothetical sample would thus mimic that of bulk Co_3O_4. From Figure 5.5-2: Left, it was apparent that the catalysing effect of the promoters became more pronounced after the threshold DOR, when the promoters seemed to help overcome the drastic decline in the rate. In fact, the promoters appeared to better align the reduction curve of Al_2O_3-supported Co_3O_4 with that of the bulk Co_3O_4 samples that were devoid of metal-support interactions (MSIs).

Arnoldy & Moulijn [9] used the concept of polarisation to explain the stabilising effect of Al_2O_3 on supported CoO. According to these authors, the covalent character of the Co-O bond (based on Fajans' Rules [52-53]) means that it can be polarised by Al^{3+} ions in the support. Polarisation increases the effective charge of Co and thus the lattice energy, which results in the need for higher reduction temperatures for supported cobalt oxides. In accordance with this argument, it is suggested that the polarisation of the Co-O bonds by Al^{3+} ions would be even greater in the CoO intermediate oxide, which possesses 25% fewer O atoms than Co_3O_4.

The stronger negative influence of oxidic supports on CoO reduction compared to Co_3O_4 reduction has been reported in other literature [17-20, 54]. Using Co/Al_2O_3, Wang & Chen [20] reported that while Co_3O_4 → CoO reduction was facile, the reduction of CoO → Co^0 was more difficult and was greatly influenced by the metal-support interactions especially in small crystallites. Similar deductions were determined by Sexton et al. [54] who found that Kieselguhr supported Co_3O_4 reduced easily but CoO reduction was kinetically hindered. Sexton et al. also found that MgO and ThO_2 promoters could retard the reduction kinetics of CoO but had a limited effect on the easily reducible Co_3O_4.

Finally, it was noteworthy that the reduction curves of the bulk Co_3O_4 in Figure 5.5-2: *Right* displayed the sigmoid shape that is characteristic of the induction step of the nucleation-growth kinetic model (and/or autocatalysis) for the reduction of transition metals oxides (Sec. 2.2.4.2). The induction period is the early region of the reduction curves that is characterised by very low reduction rates as the active sites for H_2 activation are generated. The proposed induction period is highlighted in Figures 5.5-2: *Right* & *Left.* Incidentally, the reduction curves of the Al_2O_3 supported samples also showed the sigmoid shape, which is consistent with an increase in the rate as the reduction proceeds, in accordance with the nucleation-growth kinetic model (and/or autocatalysis). It must be cautioned that based on the literature in Section 2.2.4.2, there is great debate on the kinetics that govern the reduction of transition metal oxide particles. It is also unclear whether the kinetic models presented for metal oxide particles and unsupported crystallites would apply to the reduction of supported cobalt nano-crystallites.

5.5.1.3 Effect of promoters on the rate of reduction

The curves of the differential reduction rates as a function of time and DOR are shown in Figure 5.5-3: *Top* and *Bottom* respectively. Note that with regard to the x-axes, *time* is shown for the initial 15 (out of 720) minutes, while the *DOR* corresponds to the 12-hour reduction in its entirety. It was interesting to note that the bell-shaped curves of the differential reduction rates as a function of the DOR were also consistent with the nucleation-growth/autocatalytic model as suggested by the sigmoid reduction curves in Figure 5.5-2.

In Figure 5.5-3: *Top*, the bulk Co_3O_4 sample exhibited the highest maximum differential reduction rate, and its curve was characterised by a discrete reduction peak, with the reaction complete after only 10 minutes. The reduction profiles of the Al_2O_3 supported samples were also characterised by a single sharp reduction peak in the promoted samples, while the peaks in the Co/Al_2O_3 and Hybrid Au-Co were much broader, shorter and less refined. Therefore, the maximum differential reduction rate increased as follows: (Co/Al_2O_3 ≈ Hybrid Au-Co) < Hybrid Pt-Co < Au-Co/Al_2O_3 < Pt-Co/Al_2O_3. The higher differential reduction rates in the presence of the reduction promoters were evidence of faster reduction kinetics compared to the unpromoted sample. However, unlike the bulk Co_3O_4 sample in which complete reduction was attained (i.e. the differential reduction rate declined to 0), the reduction rates of the supported samples continued to decline to very low values until the programmed end of the H_2 Stage of the thermogravimetric analysis. As such, the main reduction peaks of the supported samples were accompanied by long tails that persisted for 12 hours.

For the Al_2O_3 supported samples, the curves of the reduction rates as a function of the degree of reduction (DOR) in Figure 5.5-3: *Bottom* were characterised by 3 stages: the first was an initial increase to reach a maximum reduction rate, followed by a rapid decline until the threshold DOR of 25%, after which the decline in the rate continued, albeit at very low rates. The low rates were observed as extended tails similar to those obtained in the curves of the reduction rate as a function of time (Fig. 5.5-3: *Top*). The reduction rates of the supported samples declined greatly at the threshold DOR of 25% probably because of the slow kinetics of $CoO \rightarrow Co^0$ reduction, caused by stabilisation of the CoO intermediate by Al^{3+} ions in the support. In comparison, the reduction rate of the bulk unsupported Co_3O_4 (at 256°C) did not show the decline at the threshold DOR but increased until at a DOR of approximately 50%, after which it decreased until complete reduction was attained. It was hypothesized that the reduction rate of bulk Co_3O_4 sample did not decline/tail to very low values once the threshold DOR of 25% was achieved because it was not subject to metal-support interactions.

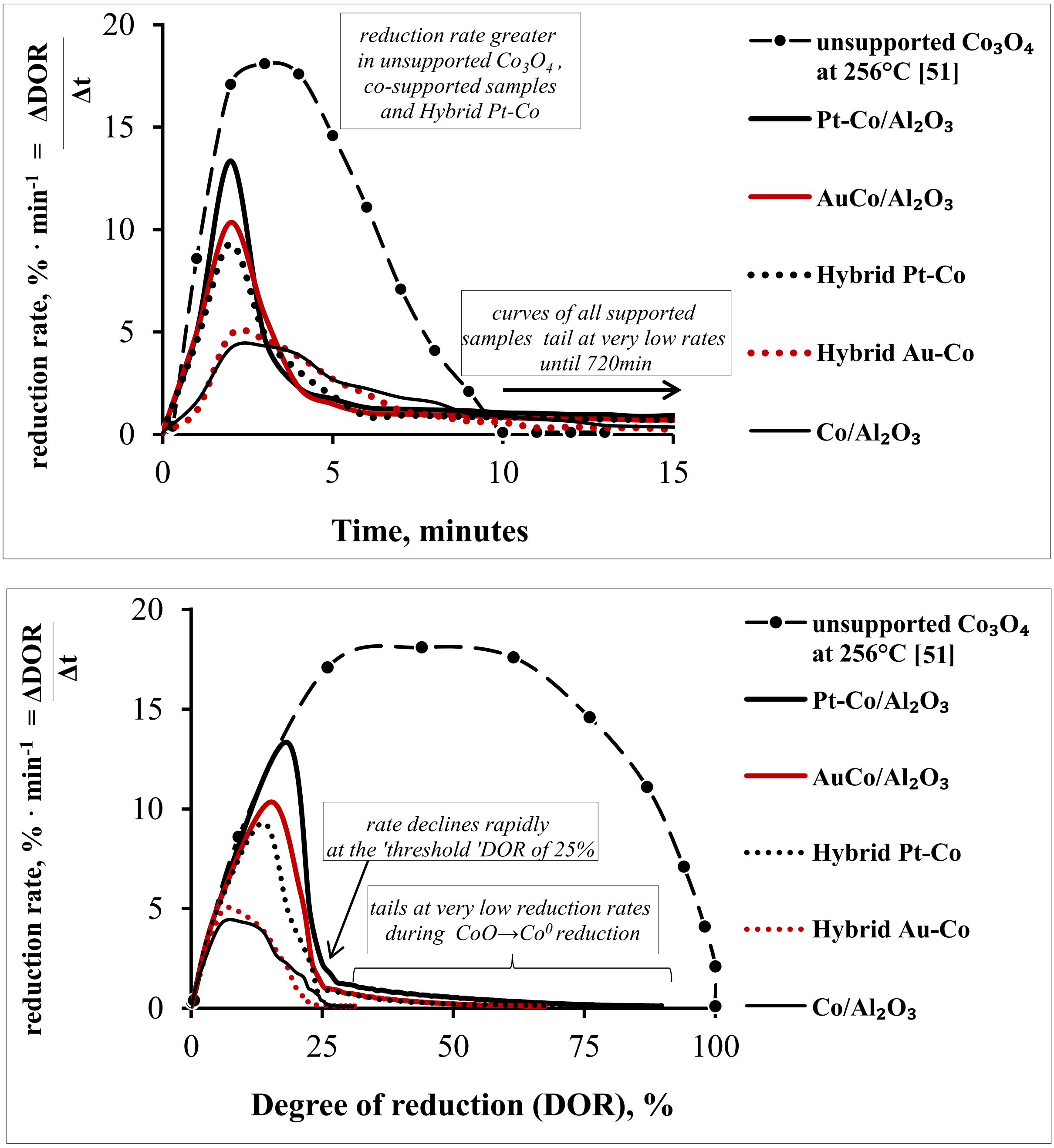

Figure 5.5-3: ***Top:*** Differential reduction rates as a function of time. ***Bottom:*** Differential reduction rates as a function of the degree of reduction.
NB: Only the initial 15 minutes of the time axis are shown (top) while the values of DOR axis (bottom) correspond to the 12 hours over which reduction occurred.

Table 5.5-2 includes the values of the maximum differential reduction rate, the more modest differential reduction rates at the threshold DOR of 25%, and the very low differential reduction rates just before the activation was terminated at 12 hours. Despite the very low overall reduction rates at the threshold DOR, the promoted samples still had an advantage, which coupled with the total reduction time of 12 hours resulted in significantly improved values of DOR. Nevertheless, complete reduction was not attained by any of the catalyst samples. Also included in Table 5.5-2 is the estimated additional time that would have been required for the samples to attain complete reduction at 350°C in H_2, based on the very low reduction rates obtained at the end of the 12-hour activation. This estimated time is hypothetical and assumes that complete reduction can actually be attained in all samples i.e. that all cobalt is actually reducible.

The additional times required were 4.8h (Pt-Co/Al_2O_3), ~40h (Hybrid Pt-Co and Au-Co/Al_2O_3) and 1-3weeks for Co/Al_2O_3 and Hybrid Au-Co. The advantage of the Pt and Au promoters is clearly demonstrated.

Table 5.5-2: Additional time (+Δt) required to attain complete reduction in H_2 at 350°C.

	DOR at 12h, %	**Differential reduction rate, %·min^{-1}**			**+Δt, hours* for DOR=100%**
		Maximum	**at threshold DOR=25%**	**at 12h**	
Co/Al_2O_3	30.9	3.8	2.9 x 10^{-1}	2.1 x 10^{-3}	550
Hybrid Pt-Co	71.8	9.2	8.4 x 10^{-1}	12 x 10^{-3}	40
Pt-Co/Al_2O_3	89.8	13	22 x 10^{-1}	36 x 10^{-3}	4.8
Hybrid Au-Co	31.3	4.8	3.0 x 10^{-1}	6.0 x 10^{-3}	190
Au-Co/Al_2O_3	67.5	10	12 x 10^{-1}	13 x 10^{-3}	43

*assuming differential reduction rate at the end of the 12-hour activation remains constant until reduction is complete.

5.5.2 Effect of Pt and Au promoters during the isothermal activation process studied by in situ XRD

In situ XRD analyses were carried out in an Anton Paar XRK-900 reaction chamber. The objective was to analyse the effects of Au and Pt on the evolution of Co_3O_4, CoO, and Co^0 phases during the isothermal reduction.

5.5.2.1 The effect of promoters on the degree of reduction (DOR)

The diffractograms of the reduced catalysts are shown in Figure 5.5-4. The overall trend in the extent of reduction was (Co/Al_2O_3 ≈ Hybrid Au-Co) < Hybrid Pt-Co < $Au-Co/Al_2O_3$ < $Pt-Co/Al_2O_3$.

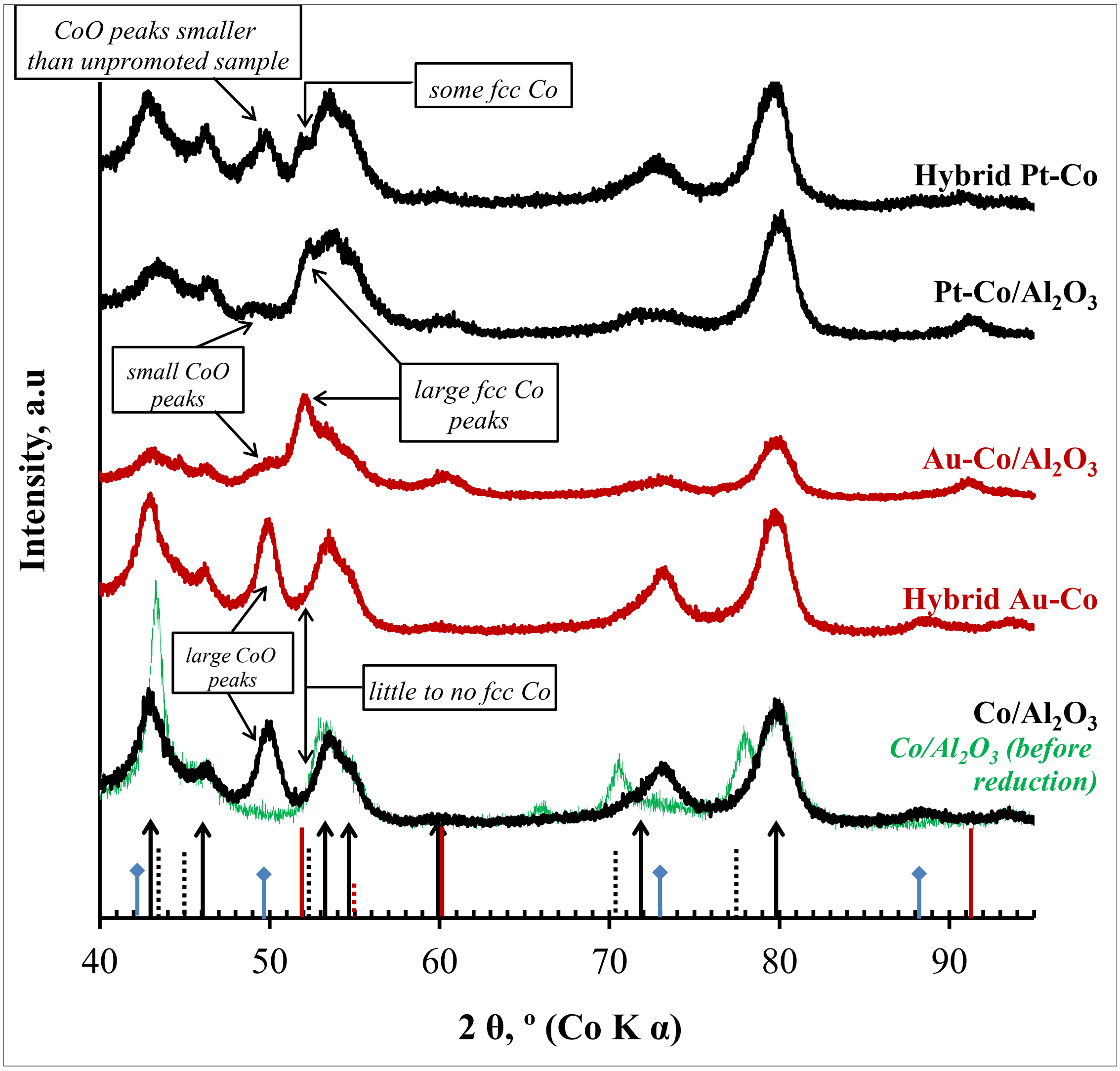

Figure 5.5-4: In situ XRD collected after reduction in H_2 at 350°C. The diffractogram of Co/Al_2O_3 before reduction is overlaid with that of the reduced sample. γ-Al_2O_3 (→); Co_3O_4 (.....); CoO (—◆ blue); fcc Co (—); and hcp Co (.....).

All samples (except Au-Co/Al_2O_3) were diluted with Al_2O_3 to obtain the higher Al_2O_3/Co ratio in the hybrid samples (see Fig. 5.5-4). It must be emphasized that preliminary TPR analyses had showed that dilution with Al_2O_3 did not affect the reducibility (Appendix E3). In any case, dilution with Al_2O_3 was done in order to facilitate the Rietveld refinement process of the multiple diffractograms (120+) obtained from the in situ analyses because the Co/Al ratio would have been the same across the board. However, the Au-Co/Al_2O_3 analysis was carried out last, and dilution with Al_2O_3 omitted because use of the XRK-900 reaction chamber lowered the XRD signal intensity. Unfortunately, the lower signal intensity was disadvantageous to quantification using Rietveld refinement particularly because the larger Al_2O_3 peaks overlapped greatly with the relatively small adjacent fcc Co peaks. Due to omission of dilution with the Al_2O_3 support, the fcc Co peak at $2\theta = 51.7^o$ was more visible in the diffractogram of Au-Co/Al_2O_3 as can be observed in Figure 5.5-4.

In both catalyst systems, CoO and Co^0 were the only observable cobalt phases following the 12-hour activation in H_2. Only fcc Co was observed, and no peaks corresponding to hexagonal close packed (hcp) Co were present in any of the samples. The predominance of fcc Co was consistent with the literature. fcc Co is regarded as the more thermodynamically stable cobalt phase for crystallites in the size range used in this study [55, 56].

In the **Pt-Co Catalyst System**, the size of the peaks corresponding to CoO at $2\theta = 49.7^o$ increased as follows: Pt-Co/Al_2O_3 < Hybrid Pt-Co < Co/Al_2O_3 while the reverse trend was observed for the fcc Co peaks at $2\theta = 51.7^o$, i.e. Co/Al_2O_3 << Hybrid Pt-Co < Pt-Co/Al_2O_3. The reducibility of the unpromoted Co/Al_2O_3 sample was poor because the dominant cobalt phase was CoO while no peaks corresponding to fcc Co were observed in its diffractogram. Pt greatly improved the reducibility of cobalt oxides in the co-supported sample, while the reducibility in the hybrid sample also improved although some CoO persisted even after 12 hours in H_2.

In the **Au-Co Catalyst System,** the sizes of the CoO peaks increased as follows: Au-Co/Al_2O_3 << (Hybrid Au-Co ≈ Co/Al_2O_3**)**, while fcc Co peaks were only observed with Au-Co/Al_2O_3. Therefore, cobalt oxides in Au-Co/Al_2O_3 experienced improved reducibility as evidenced from the large fcc Co peaks, and very low residual CoO. In contrast, the diffractogram of reduced Hybrid Au-Co was very similar to that of Co/Al_2O_3, which was in agreement with their comparable degrees of reduction based on TGA and TPR.

Rietveld refinement using TOPAS® was used to determine the composition and crystallite sizes of the cobalt species in the calcined and reduced samples (Table 5.5-3). While no crystalline metallic cobalt was detected in the Co/Al_2O_3 and Hybrid Au-Co samples, the quantity of metallic Co^0 in Hybrid Pt-Co, Pt-Co/Al_2O_3 and Au-Co/Al_2O_3 was determined as 25%, 89%, and 74.6% respectively. The greater metallic content of the Pt containing samples was attributed to the catalysing effect of Pt, and concurred with the results from TPR and TGA. The higher quantity of Co^0 in Hybrid Pt-Co compared to Co/Al_2O_3 suggested that Pt catalysed the formation of metallic cobalt via a remote-control mechanism such as hydrogen spillover. Although the Au promoter increased the metallic content in the Au-Co/Al_2O_3 sample, its lower affinity for H_2 activation and subsequent spillover resulted in the poor reducibility of the Hybrid Au-Co sample in which the spillover pathway was longer and involved multiple interfaces.

An ideal contraction in the crystallite diameter of 75% is expected when Co_3O_4 reduces to Co^0 in accordance with relative molar volumes (Eq. 5.5-3). The Co^0 crystallite size diameters in Pt-Co/Al_2O_3 and Au-Co/Al_2O_3 decreased in line with the expected contraction. However, the sizes in Hybrid Pt-Co increased from 12.7nm Co_3O_4 crystallites to the 15nm Co^0 crystallites. There was no reason to expect a greater degree of Co^0 sintering in the hybrid samples compared to the co-supported samples, and reduction promoters reportedly have little to no effect on the crystallite sizes of Co on highly interacting supports like Al_2O_3 (Sec. 2.3.2). Consequently, it was hypothesized that the Rietveld refinement may have suffered a greater degree of uncertainty due to the smaller Co^0 peaks and the poorer X-ray signal intensity from use of the Anton Paar XRK-900 reaction chamber.

Table 5.5-3: Composition and crystallite sizes of the Co phase in the calcined samples and after isothermal reduction in H_2 at 350°C.

	Calcined		**Reduced**			
	Composition, %	***Crystallite size, nm***	***Composition*, %***		***Crystallite size, nm***	
	Co_3O_4		CoO	Co^0	CoO	Co^0
Co/Al_2O_3	100	12.7	100	0	9.4	-
Hybrid Pt-Co	100	12.7	75±2.5	25±2.5	7.9±0.1	15±1.1
$Pt\text{-}Co/Al_2O_3$	100	14.5	11.0	89.0	10.5	10.3
Hybrid Au-Co	100	12.7	100	0	10.2	-
$Au\text{-}Co/Al_2O_3$	100	15.7	25.4	74.6	8.0	9.4

*Composition is based on only the crystalline phases detected by XRD. Further more peak overlap of Co^0 peaks with Al_2O_3 peaks likely hindered their detection during the Rietveld Refinement.

$$d_{Co^0} \approx 0.75 \cdot d_{Co_3O_4} \qquad \textbf{Equation 5.5-3}$$

It is worth noting that the Co^0 crystallite size diameters in Table 5.5-3, which were determined from the XRD data were consistent with the particle sizes measured during the TEM analysis in Section 5.1.2 in which the Co^0 crystallite sizes (following a 400°C reduction) were ca. 10nm in Co/Al_2O_3, $Pt\text{-}Co/Al_2O_3$ and $Au\text{-}Co/Al_2O_3$.

5.5.2.2 Evidence in support of a threshold degree of reduction (DOR)

Figure 5.5-5 shows the intensities of the characteristic peaks of Co_3O_4, CoO and Co^0 as a function of time during the isothermal activation process, i.e. $I_i = f(t)$. The figures were generated from the diffractograms taken in the course of the in situ reduction process. The results in Figure 5.5-4 were therefore the final diffractograms from the in situ reduction.

Co/Al_2O_3: For Co/Al_2O_3, the drop in the intensity of Co_3O_4 coincided with an increase in that of CoO in accordance with the 2-step reduction. The intensity of CoO reached a maximum at approximately 1 hour on stream, after which it declined by just 4.6% on completion of the analysis. Incidentally, the intensity at the expected 2θ value of fcc Co (51.7°) increased by approximately 6.1% in the same period. As discussed with Figure 5.5-4, distinct fcc Co peaks were never observed in the diffractogram of reduced Co/Al_2O_3. However, the subtle decline in the intensity of CoO corresponded well with the increase in the intensity at 2θ=51.7°, which suggested some CoO → Co reduction. The quantity of Co^0 formed was probably very low, and any small peaks at 2θ=51.7° were likely to have been enshrouded in the adjacent

Al_2O_3 peaks (2θ=53.4° & 54.8°). Due to the low quantities, the Co^0 phase may have also lacked 3-dimensional long range order, which would have limited its XRD visibility. Support for the presence of a metallic, albeit non-XRD visible phase was later obtained under reaction conditions, where Fischer-Tropsch products where observed to form immediately following exposure of activated Co/Al_2O_3 to syngas (Chapter 6). Similar observations regarding Fischer-Tropsch product formation despite XRD invisible Co^0 were made by Clapham [57]. Although a small change in the quantity of Co^0 was observed, the quantity was so low and below detection for the Rietveld Refinement process (using TOPAS® software) used to determine the compositions shown in Table 5.5-3.

The variation of the peak intensities as a function of time concurred with the thermogravimetric analyses, which showed that reduction to a threshold DOR of 25% was facile and occurred rapidly following exposure to H_2, but further reduction was very slow (Fig. 5.5-2). In fact, the rapid increase in the intensity of CoO as a function of time was resonant with the fast increase of the threshold DOR to 25%. In addition, the very slow, minimal increase in intensity of fcc Co at 2θ=51.7° was resonant with the kinetically hindered increase in the TGA reduction curves from 25% to the final value of 30.9%, which took over 10hours. The data from in situ XRD therefore supported the hypothesis that the rapid reduction to reach the threshold DOR of 25% was indeed due to $Co_3O_4 \rightarrow CoO$ reduction, while the kinetically hindered reduction that followed was due to $CoO \rightarrow Co^0$. The hindered reduction of CoO was deduced to result from greater stabilisation by the Al_2O_3 support.

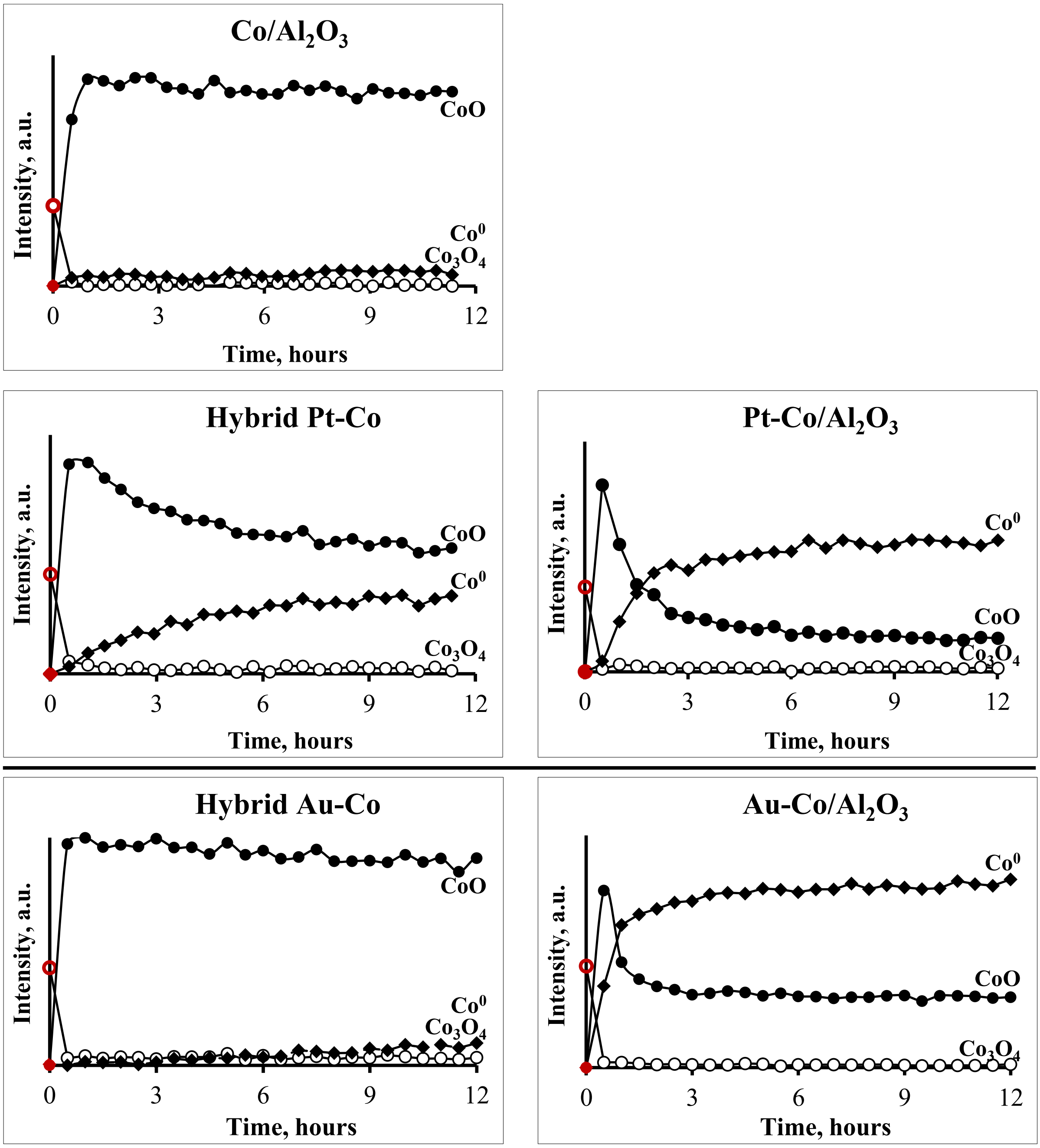

Figure 5.5-5: In situ XRD peak intensities of CoO (49.7°), Co_3O_4 (70.3°) and fcc Co (51.7°) as a function of time during the isothermal reduction (350°C) in pure H_2.

Pt-Co Catalyst System: In the Pt containing catalysts, the peak intensity of Co_3O_4 decreased *slightly* faster than that of the unpromoted Co/Al_2O_3 sample, which was indicative of a slight catalysing effect on the reduction kinetics of Co_3O_4→CoO. The catalysing effect of Pt was more obvious with regard to the intensities of the CoO and Co^0 peaks. In **Hybrid Pt-Co,** the intensity of CoO rose to a maximum in the initial half hour, after which it declined at an increasingly slow rate until reduction was terminated, while the intensity of the Co^0 peak increased gradually with time. The trends with **Pt-Co/Al_2O_3** were similar, except that the intensity of CoO declined more rapidly, and to a greater extent, while that of Co^0 increased more rapidly to reach a value that was 30% greater than in Hybrid Pt-Co. Therefore, Pt had a minimal effect on the Co_3O_4 reducibility but greatly improved the CoO→Co^0 reduction kinetics.

Au-Co Catalyst System: With **Hybrid Au-Co**, the curves of the peak intensities as a function of time were almost identical to those of Co/Al_2O_3 in agreement with the values of DOR from the TGA (31.3% and 30.9%). In contrast, the intensity of fcc Co in **Au-Co/Al_2O_3** started to increase just 30 minutes into the reduction analysis, which indicated an almost instantaneous two-step reduction rate of $Co_3O_4 \rightarrow CoO \rightarrow Co^0$. The near instantaneous reaction was consistent with the high differential reduction rates determined for Au-Co/Al_2O_3 and the Pt containing samples during the thermogravimetric analyses (Table 5.5-2).

The curves of peak intensity as a function of time were complementary to the reduction curves obtained during the thermogravimetric analyses (see Fig. 5.5-2), and helped decipher the relationship between the two-step reduction and the calculated values of DOR. The in situ XRD data supported the hypothesis developed from the TGA that: Pt and Au not only increased the overall $Co_3O_4 \rightarrow Co^0$ reduction rate, but the root of the catalysing effect was facilitating the cobalt crystallites to exceed the threshold DOR of 25%. Ultimately, Pt and Au helped overcome the stabilising effect of Al_2O_3 on the CoO intermediate.

5.5.2.3 Effect of promoters on the rate of reduction

The curves of the peak intensities as a function of time, $I_i = f(t)$, (Fig. 5.5-5) were used to establish how quickly the reduction of Al_2O_3-supported cobalt oxides proceeded in the presence of Pt and Au. Scheme 5.5-2 shows the two-step consecutive reduction where kinetic constants k_1 and k_2 correspond to $Co_3O_4 \rightarrow CoO$ and $CoO \rightarrow Co^0$ reduction respectively. A correlation can be assumed between the peak intensity and the concentration of each reducing oxide, $I_i = f([i])$. Therefore, it is conceivable that the reduction rate is a function of the rate constant, concentration of the reducing oxide and hydrogen partial pressure, $dI_i/dt = f(k, [i], P_{H2})$. k_1 and k_2 could therefore be calculated by assuming that each reduction rate was 1st order with the reducing oxide and hydrogen, $dI_i/dt = k \cdot I_i \cdot P_{H2}$, which if H_2 is in excess simplifies to $dI_i/dt = k \cdot I_i$.

$$\mathbf{Co_3O_4} \xrightarrow{k_1} \mathbf{3CoO} \xrightarrow{k_2} \mathbf{3Co^0}$$

$$I_i = f(t) \quad ; \quad I_i = f([i]) \quad \textbf{AND} \quad \frac{d[i]}{dt} = f(k, [i], P_{H_2})$$

if 1st order

$$\frac{dI_i}{dt} = k \cdot I_i \cdot P_{H_2}$$

and if H_2 is in excess:

$$\frac{dI_i}{dt} = k \cdot I_i$$

Where: i = Co_3O_4 or CoO

k = 1st order rate constant

[i] = concentration of species i

I_i = peak intensity of species i in the in situ XRD-TPR diffractograms

Scheme 5.5-2: The rate of the two consecutive reactions that comprise the reduction of Co_3O_4.

Based on the literature, it is acknowledged that the kinetics of metal oxide reduction are not only governed by rate constants and the concentration of the reactants, but also by the concentration of the water co-product and complex relationships between H_2 activation, O removal, nucleation, and the formation of intermediate oxides i.e. $\frac{dI_i}{dt}$ = f (k, [i], P_{H2}, P_{H2O}, f_{model}([i]), where f_{model}([i]) is a function based on a gas-solid reduction model such as the Avarmi-Erofeev [50, 58]. Therefore, defining the reduction as first order was only used as an analogy to describe the shapes of the curves of intensity as a function of time, I_i = f (t). The observed curves in Figure 5.5-5 are typical of consecutive reactions. Consequently, the assumption of first order kinetics as detailed in Scheme 5.5-2 simply provides a provisory means to quantify the influence of the reduction promoters on the two-step/consecutive reaction. The assumption that the reduction of metal oxide proceeds with pseudo first order kinetics when H_2 is in excess as detailed in Scheme 5.5-2 is also supported by the work of Richardson et al. during NiO reduction [59].

The calculated rate constants are shown in Table 5.5-4. The rate for constant CoO → Co^0 reduction (k_2) was several orders of magnitude less than that for Co_3O_4 → CoO (k_1). The reduction of $Co_3O_4 \rightarrow CoO$ (k_1) even in unpromoted **Co/Al_2O_3** was facile, and so only a slight increase in the corresponding rate constant was realised in the presence of the promoters. In contrast, the rate constant of $CoO \rightarrow Co^0$ reduction (k_2) in **Hybrid Pt-Co**, **Pt-Co/Al_2O_3** and **Au-Co/Al_2O_3** were 15, 61 and 47 times that of the unpromoted Co/Al_2O_3 sample respectively. Like in previous analyses, the enhancement introduced by **Hybrid Au-Co** was not considered to be statistically different from Co/Al_2O_3.

Table 5.5-4: Rate constants of $Co_3O_4 \rightarrow CoO$ (k_1) and $CoO \rightarrow Co^0$ reduction (k_2) determined from curves of the peaks intensities of CoO (49.7°), Co_3O_4 (70.3°) and Co^0 (51.7°) as a function of time during the isothermal activation process.

	1st order rate constants	
	$Co_3O_4 \rightarrow CoO$	**$CoO \rightarrow Co^0$**
Co/Al_2O_3	k_1	k_2 (= $0.0015k_1$)
Hybrid Pt-Co	$1.1k_1$	$15k_2$
Pt-Co/Al_2O_3	$1.3k_1$	$61k_2$
Hybrid Au-Co	$1.2k_1$	$2.0k_2$
Au-Co/Al_2O_3	$1.4k_1$	$47k_2$

The overall trend in the values of k_2, which described the rate at which the catalytically active Co^0 phase was formed, could thus be used to quantify the catalysing effect that Au and Pt promoters had on the reduction of supported cobalt oxides. The values of k_2 increased as follows: (Co/Al_2O_3 ≈ Hybrid Au-Co) < Hybrid Pt-Co < Au-Co/Al_2O_3 < Pt-Co/Al_2O_3, which was consistent with the expectations from the TGA in the previous section.

The large discrepancy between the rate constants, i.e. $k_1 >> k_2$ was noteworthy because numerous sources report that activation energy for $Co_3O_4 \rightarrow CoO$ (k_1) is actually greater than that for $CoO \rightarrow Co^0$ (k_2). Lin & Chen [58] calculated activation energies of -94 and -83 $kJ \cdot mol^{-1}$ respectively, which may imply slower kinetics of Co_3O_4 reduction. However, it must be kept in mind that rate constants are functions of both the activation energy *Ea* and the Arrhenius constant *A* as detailed below.

$$\mathbf{Co_3O_4} \xrightarrow{\substack{k_1,\\ Ea_1,\\ A_1}} \mathbf{CoO} \xrightarrow{\substack{k_2,\\ Ea_2,\\ A_2}} \mathbf{Co^0}$$

$$k_1 = A_1 \cdot exp^{-Ea_1/RT} \quad \text{OR} \quad k_2 = A_2 \cdot exp^{-Ea_2/RT}$$

$$k_1 >>> k_2$$

BUT

$$Ea_1 > Ea_2 \quad [58]$$

Therefore, it was tentatively hypothesized that the severely hindered $CoO \rightarrow Co^0$ reduction in Al_2O_3 supported cobalt oxides was not due to differences in the activation energy, but to differences in the Arrhenius constants.

$$A_1 >>> A_2$$

The deduction of a greater Arrhenius constant for the $CoO \rightarrow Co^0$ reduction step is consistent with the literature in which gas-solid reaction models were used to describe the reduction kinetics of cobalt oxides. Higher values of the Arrhenius constant have been reported by Lin & Chen [58]. Lin & Chen [58] fitted the TPR profiles of 18%Co/SiO_2 to a number of reduction models including the ‘2-D and 3-D nucleation models according Avarmi-Erofeev, unimolecular decay, and the 3-D diffusion according to Jander. In all cases, it was determined that the Arrhenius constant for $Co_3O_4 \rightarrow CoO$ reduction was 10^2 to 10^3 times that of $CoO \rightarrow Co^0$ reduction. Although the authors did not provide a mechanistic explanation for the discrepancy, it is suggested that different mechanisms may govern the reduction steps in the two-step reduction.

5.5.3 Effect of Pt and Au promoters during the isothermal activation process studied by quasi-in situ XPS

Quasi-in situ XPS analyses completed the multifaceted approach used to study the effects of the Pt and Au reduction promoters during the standard activation process. While the isothermal TGA and in situ XRD analyses provided information on bulk characteristics, XPS was more sensitive to the effects of the promoters on the surface of the reduced samples. The catalyst preparation process for the XPS analyses commenced with *ex situ* reduction in a test unit, after which the reduced samples were transferred to the spectrometer via a glove box. Consequently, only the reduced samples could be analysed. This was in contrast to the TGA and in situ XRD analyses that allowed for documentation of the changes in the catalyst composition as a function of time during the 12-hour activation process.

The Co 2p regions of the XPS spectra of the activated samples are shown in Figures 5.5-6 and 5.5-7. In Figure 5.5-6, the spectra of the reduced samples are overlaid with those of the calcined samples. The characteristic Co 2p doublet (Co $2p_{3/2}$ and Co $2p_{1/2}$) due to spin-orbit splitting [3] was observed for all samples. In elemental Co, the main photoelectron lines are present at 793eV (Co $2p_{1/2}$) and 778eV (Co $2p_{3/2}$). Following reduction, the shapes of the doublet changed, and the main photoelectron lines shifted towards the binding energy of elemental Co from the characteristic positions of Co_3O_4, which were at approximately +3eV greater than elemental Co. Furthermore, the Co $2p_{3/2}$ peaks of Hybrid Pt-Co and Pt-Co/Al_2O_3 exhibited shoulders close to the binding energy of elemental Co. The shake-up satellites also got stronger and closer to the main elemental photoelectron lines. As discussed in Section 5.1.1, the binding energy of the relevant cobalt species increases as follows: $Co^0 < Co^{2+} < Co^{3+}$. While the shake-up satellites are not present with Co^0, they are more intense for Co^{2+} and closer to the main elemental photoelectron lines i.e. +5eV (Co^{2+}) versus +10eV (Co^{3+}). In summary, the shift of the peaks of all samples to lower binding energies, *and* the stronger and closer (to the elemental photoelectron lines) shake-up satellites were indicative of the reduction of $Co_2^{3+}Co^{2+}O_4^{2-} \rightarrow Co^{2+}O^{2-}$, while the shoulders at the Co $2p_{3/2}$ peaks were indicative of $Co^{2+}O^{2-} \rightarrow Co^0$ reduction.

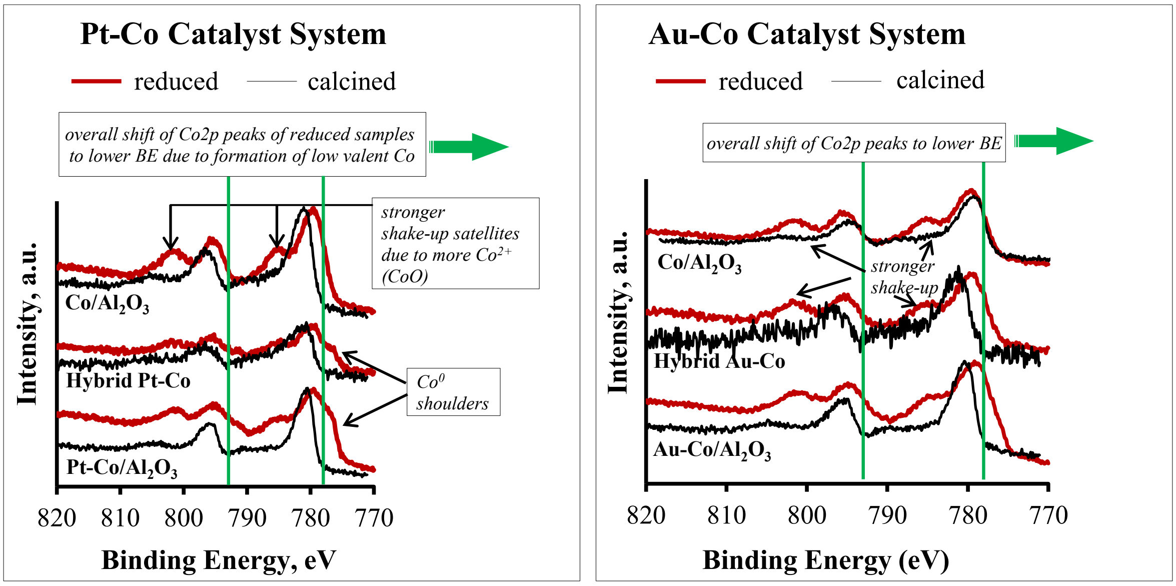

Figure 5.5-6: Co 2p regions of the XPS spectrum of reduced samples. The spectra are overlaid with those of the calcined samples to highlight changes that occurred following reduction. Main photoelectron lines for elemental Co indicated by broken vertical lines at 793eV (Co $2p_{1/2}$) and 778eV (Co $2p_{3/2}$).

Figure 5.5-7 shows Co 2p peaks that have been deconvoluted using Gaussian peaks based on Co^0 foil, CoO, Co_3O_4 and $CoAl_2O_4$ reference compounds from Moodley [60]. The Gaussian peaks therefore corresponded to Co^0, Co^{2+}, and to the shake-up satellites. Gaussian peaks were not assigned to Co^{3+} species because the thermogravimetric analyses (Sec. 5.5.1) and the in situ XRD diffractograms (Sec. 5.5.2) indicated that CoO (Co^{2+}) was the only form of oxidic cobalt present following the 12-hour activation process. **Co/Al_2O_3** exhibited Co 2p peaks that corresponded well with Co^{2+} compounds such as $CoAl_2O_4$ and CoO [60]. This was based on the stronger shake-up satellites compared to the calcined sample, and the fact that there was no shoulder corresponding to Co^0 at the Co $2p_{3/2}$ peak.

In the **Pt-Co Catalyst System**, the sizes of the CoO Gaussian peaks decreased as follows: Co/Al_2O_3 > Hybrid Pt-Co > Pt-Co/Al_2O_3, and the sizes of the Co^0 Gaussian peaks decreased as follows: Pt-Co/Al_2O_3 > Hybrid Pt-Co > Co/Al_2O_3. It was thus deduced that the reducibility was greatest for Pt-Co/Al_2O_3 and lowest for Co/Al_2O_3.

In the **Au-Co Catalyst System**, the Co 2p peaks in Hybrid Au-Co were very similar to those of Co/Al_2O_3, in agreement with the TPR, TGA and in situ XRD analyses. The main Co 2p photoelectron lines of Au-Co/Al_2O_3 were shifted to lower binding energies and the shake-up satellites were weaker compared to the unpromoted Co/Al_2O_3, which was indicative of a greater content of Co^0.

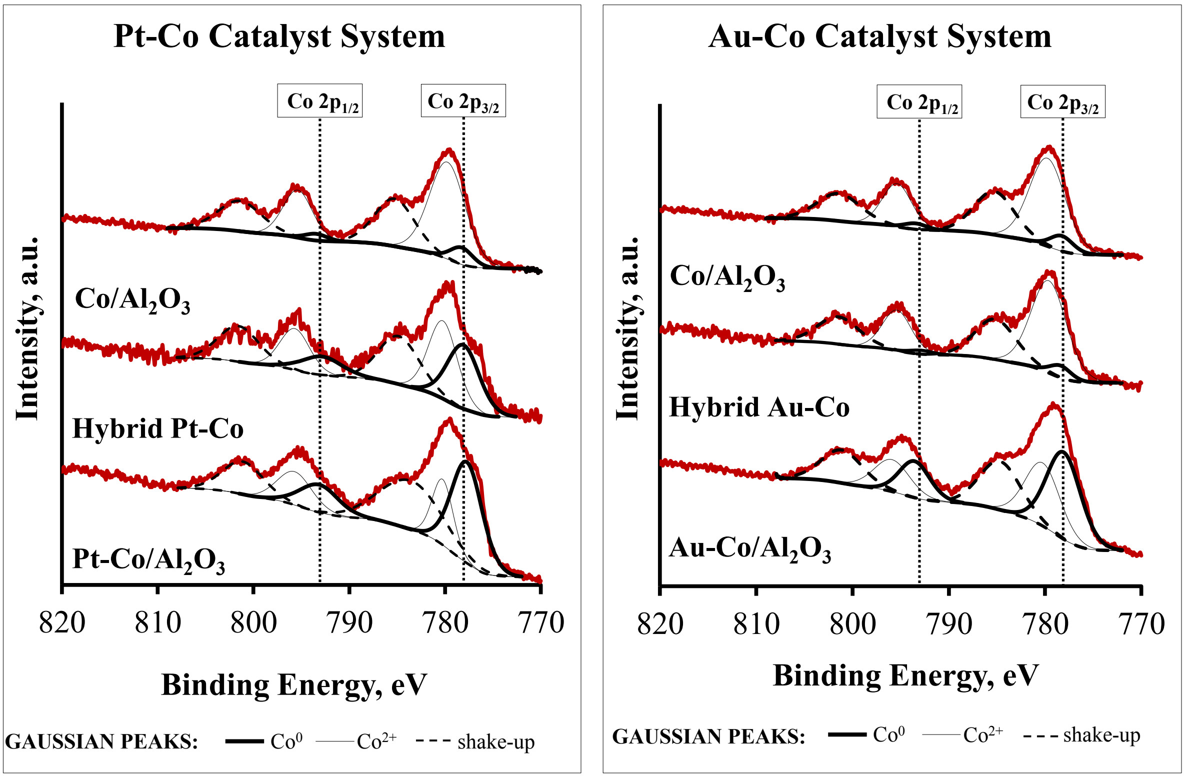

Figure 5.5-7: Co 2p regions of the XPS spectrum of reduced samples. The spectra have been deconvoluted with Gaussian peaks to highlight contributions from Co^{2+}, Co^0 and shake-up satellites. Main photoelectron lines for elemental Co indicated by broken vertical lines at 793eV (Co $2p_{1/2}$) and 778eV (Co $2p_{3/2}$).

Table 5.5-5 includes the amount of surface Co^0 quantified using the areas of the Gaussian peaks at the elemental Co$2p_{3/2}$ photoelectron line in Figure 5.5-7. The extent of reduction based on the composition of Co^0 (% Area) increased as follows: (Hybrid Au-Co ≤ Co/Al_2O_3) < Hybrid Pt-Co < Au-Co/Al_2O_3 < Pt-Co/Al_2O_3.

It must be reiterated that the best fit Gaussian peaks were used, so the indicated values are *mathematically* accurate but do not necessarily corresponded to reality. Nevertheless, the trends in the surface specific metal content correlated with the values of the degree of reduction calculated from the thermogravimetric analyses (Sec. 5.5.1), and the compositions obtained from Rietveld refinement of in situ XRD data (Sec. 5.5.2). The greater metallic character of Pt-Co/Al_2O_3 and Au-Co/Al_2O_3 was attributed to direct promoter → Co spillover compared to the less efficient process in the hybrid samples, where the hydrogen pathway involved traversing multiple interfaces and longer distances to reach the Co species on adjacent support particles. The catalysing effect of Pt was superior to Au because the reducibility of both the Pt-Co/Al_2O_3 and the Hybrid Pt-Co samples were enhanced, while the Au promoter only improved the reducibility of the co-supported Au-Co/Al_2O_3 sample.

Table 5.5-5: Ratio of Co^0/Co^{2+} Gaussian peaks and % area of the Co^0 peaks at the Co $2p_{3/2}$ main photoelectron line following the isothermal activation process at 350°C.

	Gaussian peaks	
	Area ratio Co^0/Co^{2+}	***Area of Co^0 peak*** %
Co/Al_2O_3	0.1	10
Hybrid Pt-Co	0.9	48
Pt-Co/Al_2O_3	2.3	70
Hybrid Au-Co	0.08	7.4
Au-Co/Al_2O_3	1.3	57

XPS is a surface sensitive technique with a probing depth of 1.4-6nm [3, 60], and contributed to the overall picture of the catalysing effect of Pt and Au promoters during the reduction of supported cobalt oxides. In situ XRD analyses indicated that promoters increased the quantity of Co^0 in the bulk structure of supported cobalt oxides, while XPS confirmed that there was also a greater quantity of Co^0 on the surfaces of the cobalt crystallites. Since the active sites for reaction are present on the surface of the catalyst, the larger quantity of the desired Co^0 active phase in Hybrid Pt-Co, Pt-Co/Al_2O_3 and Au-Co/Al_2O_3 was expected to result in improved Fischer-Tropsch activity.

5.5.4 Consolidation of the effect of Pt and Au promoters on the reduction of cobalt oxides during the isothermal activation

5.5.4.1 The promoting effects of reduction promoters

The multifaceted approach that was employed to study the reduction of Al_2O_3 supported cobalt oxides suggested that the promoting effects of the Au and Pt promoters might be categorised into two:

- *Improved overall Co_3O_4 → Co^0 reduction:* The ability to catalyse the overall reduction of $Co_3O_4 \rightarrow Co^0$, resulting in high reduction rates as a function of time.

- *Improved CoO → Co^0 reduction:* The ability to partially alleviate the negative stabilising effect of Al_2O_3 on supported cobalt oxides, especially on CoO. Without a promoter, a sharp decline in the reduction rate occurred after a threshold degree of reduction of approximately 25% due to the hindered reduction of CoO.

Improved overall Co_3O_4 → Co^0 reduction: In this instance, the promoting effect of the Pt and Au is most likely linked to the role of H_2 in the rate limiting step(s) of the reduction of Co_3O_4. This promotion therefore occurs whether Co_3O_4 crystallites are supported or not. For example, Batley et al. [51] found that Pt catalysed the reduction of *bulk* Co_3O_4 in a 0.5% Pt/Co_3O_4 sample.

The improvement in the overall $Co_3O_4 \rightarrow Co^0$ reduction in the presence of promoters was supported by the much higher values of degree of reduction (DOR) obtained from TGA (Sec. 5.5.1), higher quantity of metallic Co^0 determined from Rietveld refinement of in situ XRD data (Sec. 5.5.2), and higher quantity of surface Co^0 determined from quasi-in situ XPS analyses (Sec. 5.5.3). In unpromoted Co/Al_2O_3, reduction is slow because the surface of cobalt oxides shows very little activity for H_2 activation. H_2 activation occurs instead at nucleation centres, which may be defects such as two adjacent metal atoms with an oxygen (O) vacancy between them (Sec. 2.2.4.2). Therefore, H_2 activation first occurs at defects to form active H species that can reduce nearby cobalt species, after which reduction to metallic Co^0 may proceed autocatalytically [17, 28, 38], with CoO as a stable intermediate. However, when a reduction promoter is present, its surface can activate H_2 readily, after which the H species may spillover to the cobalt oxides for reduction. Therefore, formation of activated hydrogen species for the reduction of cobalt oxides via spillover must be more kinetically favoured than via direct activation at the nucleation sites of the cobalt oxides. This was mostly likely the case with Hybrid Pt-Co, Pt-Co/Al_2O_3, and Au-Co/Al_2O_3.

Improved CoO → Co^0 reduction: TGA and in situ XRD indicated that the reduction of CoO was particularly hindered, which was attributed to the greater stabilisation by the Al_2O_3 support. From the TGA curves of the *DOR as a function of time* and the *differential reduction rates as a function of time and DOR*, it was apparent that the catalysing effect of the promoters became easier to decipher *after* the threshold degree of reduction of 25%. The threshold degree of reduction corresponded to the removal of 25% of O from the structure of Co_3O_4, which marked the commencement of CoO → Co^0 reduction. On the other hand, the calculated reduction rates of the two-step consecutive reduction of Co_3O_4 using the in situ XRD data suggested that the promoters only slightly increased the Co_3O_4 → CoO reaction rate, but increased the CoO reduction rate to a significant extent. Therefore, although promoters helped improve the overall reduction of $Co_3O_4 \rightarrow Co^0$, the root of the catalysing effect was facilitating the cobalt crystallites to exceed the thresholdDOR of 25%. Ultimately, Pt and Au helped cobalt oxides to overcome the detrimental stabilising effect of the metal support interactions.

- ***The use of a multifaceted approach to quantify the effects of promoters***

The results of the **Au-Co/Al_2O_3** versus **Hybrid Pt-Co** during the TPR and TGA versus the in situ XRD analyses were interesting to consider. Au-Co/Al_2O_3 and Hybrid Pt-Co had comparable values of DOR from the TGA analyses (Sec. 5.5.1) and the TPR profiles of these samples were observed to terminate at the same temperatures (Sec. 5.4.1), which suggested that the samples had comparable reducibilities. However, the in situ XRD data (Sec. 5.5.3) showed that the Au-Co/Al_2O_3 sample contained 3 times as much metallic Co^0 than the Hybrid Pt-Co sample, which indicated that it was in fact better reduced. The Fischer-Tropsch tests in the subsequent chapter also provided evidence for the greater metallic character of Au-Co/Al_2O_3; Au-Co/Al_2O_3 had up to 3 times the mass-based activity of Hybrid Pt-Co in the initial stages of the reaction.

The different metallic character despite comparable values of DOR between Au-Co/Al_2O_3 and Hybrid Pt-Co highlighted the complexity surrounding the two-step reduction of Co_3O_4. In addition, these results highlighted the inadequacy of using only the 'degree of reduction/DOR' to quantify the catalyst reducibility. The DOR assumes that Co_3O_4 reduces directly to Co^0, without factoring in the formation and complexity introduced by the stable CoO intermediate. As discussed with the TGA results, the calculated DOR is cumulative over the multiple crystallites contained in a single sample and is not necessarily representative of each individual crystallite as implied by a two-step ideal reduction sequence. The multiple crystallites of varying sizes and varying extents of interaction with the promoter and support limited the likelihood that all crystallites in a sample could attain the same DOR simultaneously. Consider the fact that despite comparable values of DOR, in situ XRD data showed that Au-Co/Al_2O_3 had a Co^0/CoO composition of 3/1, while Hybrid Pt-Co had the *reverse* composition of Co^0/CoO of 1/3. It was unclear why Au-Co/Al_2O_3 and Hybrid Pt-Co had different quantities of metallic Co^0. It is hypothesized that the physicochemical differences between the samples, particularly the interaction/proximity of the promoter to the Co species may have altered the specific reduction kinetics.

These results highlighted the inadequacy of using only the DOR to describe the improvement in the cobalt reducibility in the presence of reduction promoters as is frequently done in the literature. The degree of reduction is most useful with metal oxides that do not typically reduce via a stable intermediate such as CuO and NiO [61-63]. The formation of a stable CoO reduction intermediate, which is further stabilised by interaction with the Al_2O_3 support results in the more complex reduction of Co_3O_4. Therefore, the reduction of Co_3O_4 can not be accurately described by a single value of the DOR because it results in two stable reduction products, i.e. CoO and Co^0.

Therefore, the multifaceted approach employed in this study, which not only involved determination of the DOR using TGA, but also quantifying the reduction products using XRD and XPS was fundamental to the understanding of the operation of the reduction promoters.

5.5.4.2 Proposed steps of reduction promotion via spillover in co-supported and hybrid catalysts

Scheme 5.5-3 shows illustrations of how the Pt and Au promoters in the co-supported catalysts are proposed to catalyse the reduction of Co_3O_4. The operation of the reduction promoter begins with adsorption of H_2 molecules from the gas phase, followed by dissociation of the hydrogen on the metal surface (step 1). Numerous spillover hydrogen species have been proposed in the literature, including H^+, H^+-H^- ion pairs, atomic H and H_3^+ ions (Sec. 2.4.2). However, H_2 almost exclusively adsorbs dissociatively on transition and noble metal surfaces especially at the temperatures at which the activation pre-treatment occurs, so it was hypothesized that the spillover hydrogen species from the reduction promoter were atomic hydrogen/protons.

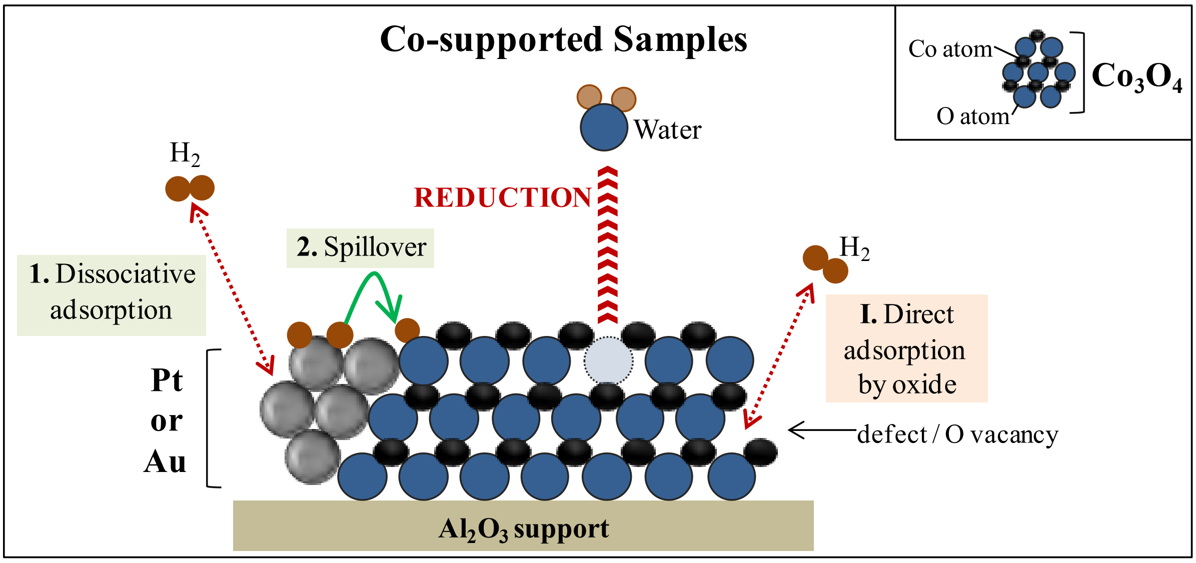

Scheme 5.5-3: An illustration of how the reduction of cobalt oxides is conceived to occur in Pt-Co/Al_2O_3 and Au-Co/Al_2O_3. Only a single spillover step occurs as indicated by the green arrow, which involves traversing the promoter/cobalt interface.

H species then proceed to spillover across the promoter cobalt interface (step 2), and can then react with the atomic O in the structure of the cobalt oxides to form water. After formation of sufficient O vacancies, the structure is expected to initially crystallise into a stable CoO nuclei, after which Co^0 nuclei are expected to form following further removal of O. Reduction via spillover competes with direct gas phase adsorption and activation by the cobalt oxides (step I). Based on the literature on the reduction of transition metal oxides (Sec.

2.4.2.2), the H_2 activation sites on the surface of the cobalt oxides are depicted as two Co atoms with an O vacancy between them (i.e. a defect).

Due to the higher reactivity of metal surfaces, spillover from the promoter is more kinetically favourable, and results in the improved reduction seen with Pt and Au promoters. The kinetics of the spillover step were also believed to have been facilitated by direct promoter-Co contact because the pathway of hydrogen in the co-supported samples would require only a single spillover step across the promoter/Co interface (step 2). However, an alternative spillover pathway that involves migration across the Al_2O_3 support also exists if the promoter and cobalt crystallites are not in direct physical contact.

Reduction promotion in the hybrid samples was hypothesized to occur according to Scheme 5.5-4.

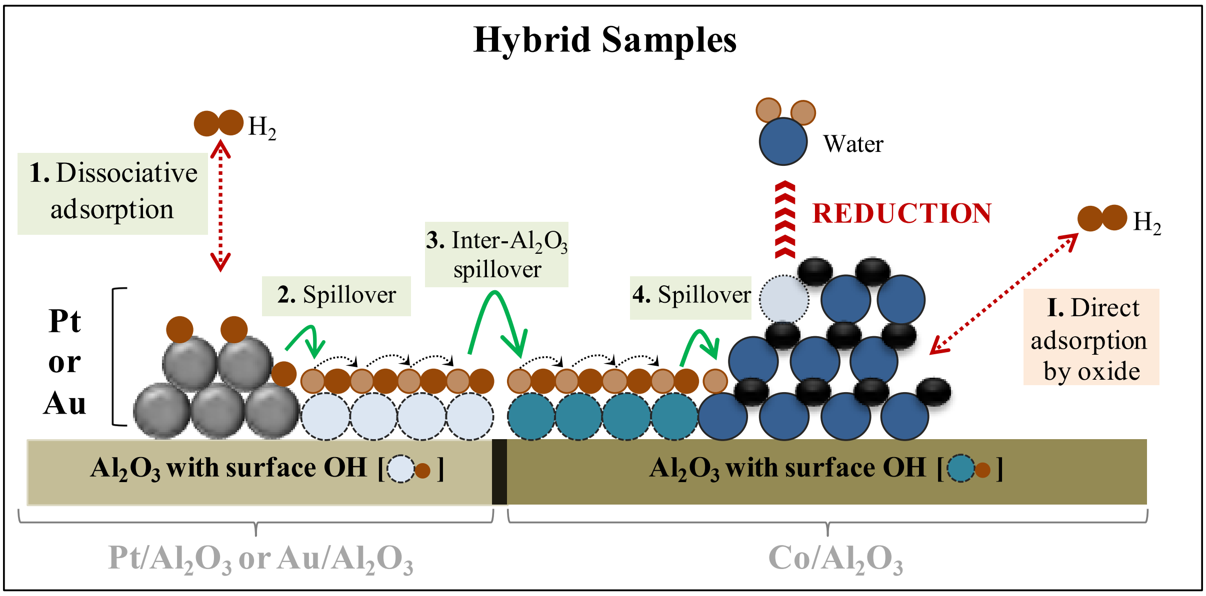

Scheme 5.5-4: An illustration of how the reduction of cobalt oxides is conceived to occur in Hybrid Pt-Co and Hybrid Au-Co. The promoter and Co_3O_4 crystallites are present on adjacent Al_2O_3 support particles. There are a minimum of 3 spillover steps including Promoter→Al_2O_3, inter-Al_2O_3 and Al_2O_3→Co as indicated by the green arrows. Developed using deductions made by Luo & Epling [64] and Conner & Falconer [65].

This figure is a composite of deductions made during a range of spillover studies including Luo & Epling [39], Conner & Falconer [40] and Carley [66]. Following dissociation on the promoter surface, the first spillover step of H species is across the promoter/Al_2O_3 interface (step 2). This is then followed by migration along the Al_2O_3 support via interaction with the hydrogen-bonded surface hydroxyl groups. According to the 'bucket-brigade' model, hydrogen is transferred by associating with the hydrogen-bonded network of hydroxyl groups via a Grotthuss-type mechanism. Mobility in this manner is high because only the charge of the hydrogen is transferred, rather than its mass (see Sec. 2.4.5). This movement is illustrated by the short broken arrows, while hydrogen-bonded hydroxyl groups are depicted as oxygen atoms associated with two hydrogen atoms.

The second spillover step in the pathway of the hybrid catalysts (step 3) arises to allow H species to cross the inter-alumina interface. Spillover H then migrates over the 2nd Al_2O_3 particle to reach Co_3O_4, where the final spillover step (step 4) occurs across the Al_2O_3/Co interface and prior to reaction with the oxides. The need for a minimum of at least 3 spillover steps (steps 2-4), and the greater separation between the promoter and cobalt oxides was believed to have lowered the efficiency of H transfer and resulted in the lower reducibility compared to the co-supported samples.

The driving force for spillover from the promoter to the cobalt oxides was hypothesized to be the concentration gradient between the promoter surface and that of the cobalt oxides. The surface of the promoters was easily saturated with hydrogen that was desired by the cobalt oxides that had a comparatively low reactivity with H_2.

5.5.4.3 Formation rates, energy and mechanism of activated hydrogen for the reduction of cobalt oxides via hydrogen spillover

Scheme 5.5-5 is a simple model of the proposed elemental steps involved in the formation of activated hydrogen during the reduction of **Pt-Co/Al_2O_3**. Scheme 5.5-5 was developed from a study of H_2 bronze formation in Pt/MoO_3 by Regalbuto [67].

S_0 and S_1 are the hydrogen adsorption sites on the Pt and the Co_3O_4 surfaces respectively. Activated hydrogen, $H \cdot S_1$, is a form of atomic hydrogen adsorbed on the surface of the Co_3O_4. $H \cdot S_1$ may be formed by direct dissociative adsorption from the gas phase by the surface of the cobalt oxides. The rate constant for this adsorption is shown as k_{ads}. The corresponding elementary equation is shown as (a).

$H \cdot S_1$ may also be formed by hydrogen spillover from the Pt surface. In the presence of Pt, H_2 first adsorbs on S_0 sites on the Pt surface. This occurs reversibly as indicated by the forward and reverse adsorption constants, k_1 and k_2, and expressed by equation (b). The adsorbed form of atomic hydrogen on Pt is $H\cdot S_0$, which may then spillover to S_1 sites on the oxide to form $H\cdot S_1$. $H\cdot S_1$ may then react with O in the bulk of the oxide. The spillover rate constant is depicted as k_{sp}. The spillover step, expressed as equation (c), leaves the sites of Pt (S_0) vacant for subsequent hydrogen adsorption. Unlike hydrogen adsorption on Pt, the spillover step is depicted as irreversible with only the forward rate constant k_{sp} because H is desired by the oxides for the reduction. It is thus proposed that in this case, the reverse spillover step rate constant would be insignificant in comparison to k_{sp}.

Unpromoted reduction	*Pt promoted reduction*
(a) $H_2 + 2S_1 \xrightarrow{k_{ads}} 2H\cdot S_1$	**(b)** $H_2 + 2S_0 \underset{k_2}{\overset{k_1}{\longleftrightarrow}} 2H\cdot S_0$
	(c) $H\cdot S_0 + S_1 \xrightarrow{k_{sp}} S_0 + H\cdot S_1$

Scheme 5.5-5: The elementary steps involved in the generation of activated hydrogen, $H\cdot S_1$, for reduction of cobalt oxides. S_0 sites are on the Pt, while S_1 sites are on the surface of the cobalt oxides. $H\cdot S_1$ can be formed from direct adsorption from the gas phase (far left) and via hydrogen spillover mechanism from Pt. Developed from Kim & Regalbuto [67].

In order for Pt to catalyse the reduction of cobalt oxides in **Pt-Co/Al_2O_3**, the rate of hydrogen activation via spillover must be greater than direct H_2 activation from the gas phase as shown in Equation 5.5-4. The expressions in Equation 5.5-4 were derived from the elementary step equations in Scheme 5.5-5. $r_{spillover}$ is the rate of hydrogen spillover defined as step (c) in Scheme 5.5-5. $r_{spillover}$ is a function of the spillover rate constant (k_{sp}), the Pt surface coverage by hydrogen ($C_{H\cdot S0}$) and the concentration of vacant sites on the receiving cobalt oxide surface ($Cv_{H\cdot S1}$). r_{ads} is the rate of the gas phase hydrogen adsorption by cobalt oxides. r_{ads} is a function of the adsorption constant (k_{ads}), the partial pressure of hydrogen (P_{H2}) and the square of the concentration of the vacant sites on the receiving cobalt oxide surface ($Cv_{H\cdot S1}{}^2$). r_{ads} is based on the elementary step (a) in Scheme 5.5-5. The concentration of the vacant sites, $Cv_{H\cdot S1}$, is squared because two adjacent sites are required for each adsorbing H_2 molecule, i.e. H_2 adsorbs dissociatively.

$$(r_{spillover})_{Pt} = (k_{sp} \cdot C_{H\cdot S_0} \cdot Cv_{S_1})_{Pt} \qquad \textbf{Equation 5.5-4}$$

$$r_{ads} = k_{ads} \cdot P_{H_2} \cdot Cv_{S_1}{}^2 \qquad \textbf{Equation 5.5-5}$$

The surfaces of the oxides of transition metals show very little activity for H_2 activation and in fact, sites that are active for H_2 activation (nucleation centres/defects/O vacancies) need to be formed before the reduction proceeds (Sec. 2.2.4.2). When a Pt promoter is present, H_2 activation need not occur at nucleation centres/defects (which is very slow) but may occur on the Pt surface. Since H_2 activation occurs readily on the Pt surface, it is suggested that Pt catalysed the reduction of the cobalt oxides by facilitating a high surface concentration of active H species via hydrogen spillover. Thus, spillover was more kinetically favourable than gas phase adsorption.

$$(r_{spillover})_{Pt} > r_{ads}$$

$$(k_{sp} \cdot C_{H\cdot S_0} \cdot Cv_{S_1})_{Pt} > k_{ads} \cdot P_{H_2} \cdot Cv_{S_1}{}^2$$

In **Hybrid Pt-Co**, it is suggested that the multiple of interfaces that hydrogen needed to navigate decreased the efficiency with which activated hydrogen for the reduction reaction ($H\cdot S_1$) was generated. The formation of activated hydrogen via spillover in Hybrid Pt-Co may be adapted from that of Pt-Co/Al_2O_3 (Equation 5.5.4) where k_{sp}' is the lumped overall rate constant for spillover from Pt to Co across the multiple interfaces.

$$(r_{spillover})_{Hyb,Pt} = (k_{sp}{}' \cdot C_{H\cdot S_0} \cdot Cv_{S_1})_{Hyb,Pt} \qquad \textbf{Equation 5.5-6}$$

However, the various techniques used in this indicated that even this less efficient pathway, spillover in Hybrid Pt-Co was more kinetically favourable than direct H_2 adsorption by cobalt oxides as illustrated below.

$$(r_{spillover})_{Hyb,Pt} > r_{ads}$$

$$(k_{sp}' \cdot C_{H \cdot S_0} \cdot Cv_{S_1})_{Hyb,Pt} > k_{ads} \cdot P_{H_2} \cdot {Cv_{S_1}}^2$$

Furthermore, various analyses showed that Pt-Co/Al_2O_3 had a better reducibility than Hybrid Pt-Co as illustrated below.

$$(r_{spillover})_{Pt} > (r_{spillover})_{Hyb,Pt} > r_{ads}$$

$$(k_{sp} \cdot C_{H \cdot S_0} \cdot Cv_{S_1})_{Pt} > (k_{sp}' \cdot C_{H \cdot S_0} \cdot Cv_{S_1})_{Hyb,Pt} > k_{ads} \cdot P_{H_2} \cdot {Cv_{S_1}}^2$$

It may thus be proposed that the spillover rate constant in Pt-Co/Al_2O_3 (k_{sp}) is greater than the lumped spillover rate constant (k_{sp}') in the Hybrid Pt-Co catalyst as shown in Equation 5.5-7.

$$k_{sp} > k_{sp}' \qquad \textbf{Equation 5.5-7}$$

The differences between the two catalyst systems highlighted the impact that a reduction promoter's affinity for H_2 activation had on the extent of reduction of supported cobalt oxides. Since **Au-Co/Al_2O_3** improved the reducibility of cobalt oxides, Au most likely had a more competitive rate of $H \cdot S_1$ formation via spillover compared to direct activation by cobalt oxides. The spillover rate expression in Au-Co/Al_2O_3 may be derived the same as that of Pt-Co/Al_2O_3 shown earlier as Equation 5.5-4. However, where the Pt surface was depicted as S_0, the Au surface is depicted as $S_{0,g}$. In addition, while the spillover rate constant from Pt was depicted as k_{sp}, that from Au is depicted as $k_{sp,g}$. Therefore:

$$(r_{spillover})_{Au} = (k_{sp,g} \cdot C_{H \cdot S_{0,g}} \cdot Cv_{S_1})_{Au} \qquad \textbf{Equation 5.5-8}$$

From various analyses, it was apparent that the reduction of Au-Co/Al_2O_3 was less facile than Pt-Co/Al_2O_3 and accordingly, the rate of H_2 activation and subsequent spillover from Au was likely lower than with Pt according to Equation 5.5-9.

$$(k_{sp} \cdot C_{H\cdot S_0} \cdot Cv_{S_1})_{Pt} \quad > \quad (k_{sp,g} \cdot C_{H\cdot S_{0,g}} \cdot Cv_{S_1})_{Au}$$

$$(k_{sp} \cdot C_{H\cdot S_0})_{Pt} \quad > \quad (k_{sp,g} \cdot C_{H\cdot S_{0,g}})_{Au}$$ **Equation 5.5-9**

Equation 5.5-9 highlights the role of Au surface coverage by hydrogen ($C_{H\cdot S_{0,g}}$) versus the Pt surface coverage by hydrogen ($C_{H\cdot S_0}$). The surface coverage by hydrogen is expected to increase with a metal's affinity for H_2 activation. H_2 dissociates relatively easily and atomic hydrogen has a moderate-to-strong binding energy on Pt but H binding is weaker and dissociation is highly activated on Au surfaces [41]. In fact, the low reactivity of Au surfaces means that hydrogen adsorption is limited to low coordinated atoms at defects, corners and along edges, which are more prevalent in smaller crystallites, and hence the need for small gold particles in the range of ca.3nm (see Sec. 5.1.2). It could thus be hypothesized that the rate at which H_2 was adsorbed and spilled over to the cobalt oxides was lower with Au surfaces because of the lower affinity for H_2 adsorption.

The expression for **Hybrid Au-Co** may also be derived from that of Au-Co/Al_2O_3 (Equation 5.5-8). $k_{sp,g}'$ is the <u>lumped overall rate constant</u> for spillover from Au to Co across the multiple interfaces.

$$(r_{spillover})_{\,Hyb,Au} \; = \; (k_{sp,g}{}' \cdot C_{H\cdot S_{0,g}} \cdot Cv_{S_1})_{Hyb,Au}$$ **Equation 5.5-10**

Hybrid Au-Co did not show a statistical improvement in reducibility compared to the unpromoted Co/Al_2O_3 sample as illustrated below.

$$(r_{spillover})_{\,Hyb,Au} \approx \; r_{ads}$$

$$(k_{sp,g}{}' \cdot C_{H\cdot S_{0,g}} \cdot Cv_{S_1})_{Hyb,Au} \; \approx \; k_{ads} \cdot P_{H_2} \cdot {Cv_{S_1}}^2$$

However, the reducibility in Hybrid Au-Co was much lower than the Hybrid Pt-Co sample as illustrated in Equation 5.5-11.

$$(r_{spillover})_{Hyb,Pt} > (r_{spillover})_{Hyb,Au}$$

$$(k_{sp}{}' \cdot C_{H\cdot S_0} \cdot Cv_{S_1})_{Hyb,Pt} > (k_{sp,g}{}' \cdot C_{H\cdot S_{0,g}} \cdot Cv_{S_1})_{Hyb,Au}$$

$$(k_{sp}{}' \cdot C_{H\cdot S_0})_{Hyb\ Pt} > (k_{sp,g}{}' \cdot C_{H\cdot S_{0,g}})_{Hyb\ Au} \qquad \textbf{Equation 5.5-11}$$

As mentioned previously, $k_{sp}{}'$ and $k_{sp,g}{}'$ in Equation 5.5-11 are the *lumped overall spillover rate constants* for spillover from Pt and Au respectively. These constants include hydrogen migration across multiple interfaces and surface in the hydrogen pathway of the Hybrid samples, i.e. promoter → Al_2O_3 spillover, inter-alumina spillover, Al_2O_3 → Co spillover as well as migration along the Al_2O_3 support as illustrated in Scheme 5.5-4. With Hybrid Pt-Co, the rate of spillover and ultimately cobalt reduction was enhanced by milling, which improved surface continuity i.e. $k_{sp}{}'$ was improved by increasing the inter-alumina contact area. However, despite the greater surface continuity, Au did not improve the reducibility of cobalt oxides in Hybrid Au-Co.

The results from both catalyst systems are therefore summarised in Table 5.5-6. According to a reduction promotion mechanism based on hydrogen spillover, it was deduced that direct Au→ Co spillover was kinetically advantageous for reduction, albeit less so than direct Pt → Co spillover.

The least favourable spillover pathway was that in Hybrid Au-Co which incorporated both H_2 activation on Au followed by 'Au → Al_2O_3 ⇒ Al_2O_3 →Co' spillover. The corresponding pathway in Hybrid Pt-Co was kinetically advantageous for reduction, but needed to be improved by milling the support to improve surface continuity, which in turn increased the lumped spillover rate constant k_{sp}'.

Table 5.5-6: Rate of formation of activated hydrogen '$H{\cdot}S_1$' and the corresponding impact on the reducibility

Spillover pathway	Rate of formation of activated hydrogen '$H{\cdot}S_1$' for reduction of cobalt oxides	Improved reducibility?
Pt → Co	$(r_{spillover})_{Pt} > r_{ads}$	Y
Au → Co	$(r_{spillover})_{Au} > r_{ads}$	Y
Pt → Al_2O_3 → Al_2O_3 → Co	$(r_{spillover})_{Hyb,\,Pt} > r_{ads}$	Y
Au → Al_2O_3 →Al_2O_3 → Co	$(r_{spillover})_{Hyb,\,Au} \approx r_{ads}$	N

The catalysing effect of Au and Pt reduction promoters on the reduction of cobalt oxides may be represented using the energy level diagram in Scheme 5.5-6. Gas phase activation by the cobalt oxides is depicted in green, and is the most kinetically hindered. H_2 activation in the hybrid samples may also be advantageous but necessitates spillover across a number of interfaces and surface migration over the Al_2O_3 supports (black). Direct promoter → Co spillover offers the most kinetically favourable pathway for H_2 activation for the reduction of cobalt oxides (red). This assignment is supported by Khodakov et al. [68] where the activation energy for Co^0 formation decreased from 130kJ/mol in unpromoted 15%Co/Al_2O_3 to 60kJ/mol with 0.1%Pt.

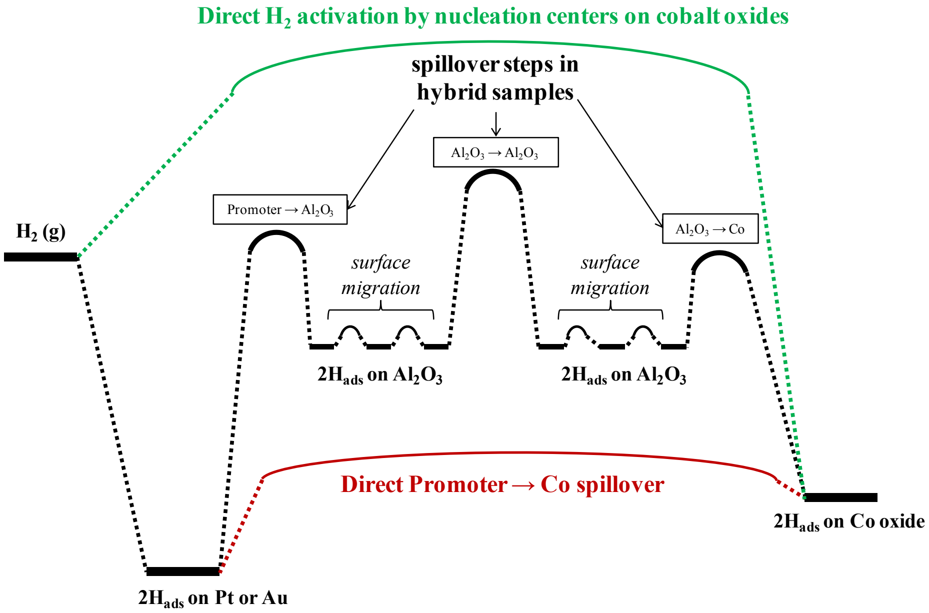

Scheme 5.5-6: A comparison of the energies of H_2 activation via direct adsorption (Co/Al_2O_3), via direct promoter → Co spillover in co-supported samples and via platinum → $Al_2O_3 \Rightarrow Al_2O_3$ → Co spillover in hybrid samples [69].

In the energy level diagram, surface migration is depicted as fast, with a low energy barrier because spillover H does not physically migrate but rather triggers a knock-on effect, which causes the net displacement of hydrogen along the hydrogen-bonded chain of surface OH groups (Sec. 2.4.5). Note that although surface migration of spillover hydrogen species along Al_2O_3 has been suggested to involve the 'bucket-brigade' model, no literature that addresses the processes that govern $Al_2O_3 \Rightarrow Al_2O_3$ spillover has so far been found, even though it has been observed in other studies [16, 31]. $Al_2O_3 \Rightarrow Al_2O_3$ spillover is depicted as a highly energetically hindered reaction in the energy level diagram because preliminary analyses in Section 5.3 showed that no effects of spillover were observed in the hybrid Pt-Co sample unless the Al_2O_3 support was milled to enhance surface continuity and thus increase the inter-alumina surface area.

The rate-limiting step during **nucleation-growth-autocatalytic** model for the reduction of transition metal oxides has been attributed to H_2 activation as depicted in the energy level diagram. From the literature, nucleation-growth-autocatalytic reduction of transition metal oxides is characterised by sigmoid curves of the degree of reduction as a function of time,$DOR = f(t)$, and bell-shaped curves of the reduction rate as a function of the degree of reduction, $\frac{dDOR}{dt} = f(DOR)$ (Sec. 2.2.4.2). Sigmoid reduction curves and bell-shaped curves of the differential reduction rate were indeed obtained with all the catalysts used in this study (Sec. 5.5.1). This indicated that the reduction rate increased with time despite the constant activation temperature of 350°C, which was thus suggestive, but not evidence, of reduction according to the nucleation-growth-autocatalytic model, instead of the shrinking core model.

Autocatalysis: The concept of autocatalysis during the reduction of Co_3O_4 presents an interesting scenario in which to analyse the role played by Pt as a reduction promoter. The reduction of transition metal oxides is said to be autocatalytic because it is catalysed by low valent metal atoms, which are active for hydrogen activation [9]. The reaction is thus self-catalysed because the quantity of low valent Co atoms (Co^{2+} and Co^0) increases as reduction proceeds. Therefore, the implication of autocatalytic reduction of Co_3O_4 in unpromoted Co/Al_2O_3 is that the initial quantity of Co^0 formed during reduction proceeds to act as a reduction promoter for other crystallites. Physical mixtures of the metal and metal oxides have been observed to reduce faster for Fe^0 + iron oxides and Mo^0 + molybdenum oxide systems [70-72]. Therefore, it may be expected that in promoted catalysts, the Co^0 autocatalyst competes with the Pt or Au promoter. However, the results from this study indicated that the promoted samples still attained higher values of DOR, which implied that Pt and Au were still advantageous for the reduction of cobalt oxides. Therefore, Pt and Au seemed to have provided more kinetically favoured pathways for reduction despite autocatalysis.

Direct promoter-Co interaction: Besides maximising the efficiency of promoter → Co spillover, the role of direct promoter-Co co-ordination/interaction must be considered with regard to the improved reducibility observed with the co-supported samples. It is well known that Pt-Co coordination readily occurs in Pt-Co/Al_2O_3. In fact, Pt-Co coordination has been reported even when catalysts are sequentially impregnated as done in this study [5, 40, 74, 75]. Recent work by Bartholomew et al. [40] showed that for the Pt-Co/Al_2O_3, this intimate contact is achieved regardless of whether the Co and Pt are sequentially or co-deposited provided they are calcined together. Iglesia et al. [73] suggested that intimate contact between the promoter and Co was required to observe the reduction promotion.

In a study of the reduction of CuO, Gentry et al. [76] suggested that the improved reducibility in the presence of Pd was due to both hydrogen spillover and extra nucleation centres resulting from non-specific distortion of the CuO lattice by Pd. A similar explanation may apply to Pt-Co/Al_2O_3, in which Pt-Co coordination readily occurs because Pt may be incorporated in the bulk of the cobalt crystallite, and/or on its surface as atomic Pt as proposed by Jacobs et al. [5, 74]. A possible bimetallic/electronic effect could include distortion of the surface of cobalt oxides to create defects/nucleation centres, which would in turn increase the rate of hydrogen activation on the surface of the oxides and facilitate reduction. Therefore, Pt-Co coordination may have also contributed to the improved reducibility of Pt-Co/Al_2O_3 but the Hybrid Pt-Co sample demonstrated that reduction promotion could also be achieved remotely.

With regard to the Au-Co Catalyst System, direct Au-Co co-ordination may also be considered especially because Hybrid Au-Co, in which the Au and Co were separate, did not show any improved reducibility. However, Jacobs et al. [24] used EXAFS studies to deduce that for the most part, Au-Co coordination did not exist in a 5.05%Au-15%Co/Al_2O_3. Au and Co formed separate phases and it is thus suggested that gold's catalysing effect on the reduction of cobalt oxides was more likely due to a hydrogen spillover effect than an electronic/ligand effect.

5.6 References

[1] G.P. Glaspell, P.W. Jagodzinski, A. Manivannan, J. Phys. Chem. B. 108 (2004) 9604–9607.

[2] J. Case, “Gold catalysts prepared by ion exchange for use in ethylene glycol oxidation: An exploratory study”, Masters’ Thesis, University of Cape Town, South Africa, 2008.

[3] J.W. Niemantsverdriet, Spectroscopy in Catalysis, John Wiley & Sons, 2007.

[4] A. Feller, M.Claeys, E. van Steen, J. Catal. 185 (1999)120–130.

[5] T. Jermwongratanachai, G. Jacobs, W.D. Shafer, V.R.R. Pendyala, W. Ma, M. K. Gnanamani, S. Hopps, G.A. Thomas, B. Kitiyanan, S. Khalid, B. H. Davis, Catal. Today 228 (2014) 15–21.

[6] W.F.Stickle, P.E. Sobol, K. D. Bomben. Handbook of X-ray Photoelectron Spectroscopy, Vol. 40, Perkin Elmer, Eden Prairie, 1992.

[7] D. Schanke, S. Vada, E.A. Blekkan, A.M. Hilmen, A. Hoff, A. Holmen. J. Catal. 156 (1995) 85–95.

[8] S.A.A. Mansour, Mater. Chem. Phys. 36 (1994) 317-323.

[9] P. Arnoldy, J.A. Moulijn, J. Catal. 93 (1985) 38-54.

[10] J.H.A. Martens, H.F.J. van't Blik, R. Prins, J. Catal. 97 (1986) 200–209.

[11] H.F.J. van’t Blik, R. Prins, J. Catal. 97(1986)188-190.

[12] C. Ehrhardt, M. Gjikaj, W. Brockner, Thermochim. Acta 432 (2005) 36-40.

[13] A. Małecki, A. Małecka, R. Gajerski, B. Prochowska-Klisch, and A. Podgórecka. J. Therm. Anal. Calorim. 34 (1988) 203-209.

[14] M. P. Rosynek, C. A. Polansky, Appl. Catal. 73(1991) 97-112.

[15] J. van de Loosdrecht, S. Barradas, E.A. Caricato, N.G. Ngwenya, P.S. Nkwanyana, M.A.S. Rawat, B.H. Sigwebela, P.J. van Berge, J.L.Visagie, Top. Catal. 26 (2003) 121-127.

[16] A.M. Hilmen, D. Schanke, A. Holmen, Catal. Lett. 38 (1996) 143-147.

[17] G. Jacobs, Y. Ji, B.H. Davis, D. Cronauer, A.J. Kropf, C.L. Marshall, Appl. Catal. A: Gen. 333 (2007) 177–191.

[18] A.Y. Khodakov, J. Lynch, D. Bazin, B. Rebours, N. Zanier, B. Moisson, P. Chaumette. J. Catal. 168 (1997) 16-25.

[19] A.Y. Khodakov, W. Chu, P. Fongarland, Chem. Rev.107 (2007) 1692-1744.

[20] W.-J. Wang , Y.-W. Chen, Appl. Catal. 77 (1991) 223–233.

[21] R.L. Chin, D.M. Hercules, J. Phys. Chem. 86 (1982) 360-367.

[22] J.T. Richardson, L.W. Vernon, J. Phys. Chem. 62 (1958) 1153-1157.

[23] Y.Zhang, D. Wei, S. Hammache, and J. G. Jr Goodwin, J. Catal. 188 (1999) 281-290;

[24] G. Jacobs, M.C. Ribeiro, W. Ma, Y. Ji, S. Khalid, P.T. Sumodjo, B.H. Davis, Appl. Catal. A: Gen. 361 (2009) 137-151.

[25] G. Jacobs, T.K. Das, Y. Zhang, J. Li, G. Racoillet, B.H. Davis, Appl. Catal. A: Gen. 233 (2002) 263-281.

[26] T. Jermwongratanachai, G. Jacobs, W. Ma, W.D. Shafer, M.K. Gnanamani, P. Gao, B. Kitiyanan, B.H. Davis, J.L.S. Klettlinger, H.Y. Chia, D.C. Cronauer, A.J. Kropf, C.L. Marshall (2013). Appl. Catal. A: Gen. 464 (2013) 165– 180.

[27] W. Ma, G. Jacobs, R. Keogh, D.B. Bukur, B.H. Davis. Appl. Catal. A: Gen. 437 (2012) 1-9.

[28] F. Diehl, A. Y. Khodakov, Oil Gas Sci. Technol.– Rev. IFP 64 (2009) 11-24.

[29] F. Morales, B. M. Weckhuysen, Catalysis (R. Soc. Chem.) 19 (2006) 1-40.

[30] S.K. Beaumont, S. Alayoglu, C. Specht, W.D. Michalak, V.V. Pushkarev, J. Guo, N. Kruse, G.A. Somorjai, J. Am. Chem. Soc. 136 (2014) 9898−9901.

[31] P. Baeza, M. Villarroel, P. Avila, A.L. Agudo, B. Delmon, F.J. Gil-Llambías, Appl. Catal. A: Gen. 304 (2006) 109–115.

[32] S. Degen, “McCrone Micronising Mill Methods”, Undergraduate Research Project. University of Wisconsin (Whitewater), USA, 2007.

[33] E.V. Buhrke, D. K. Smith, (Eds) A practical Guide for the Preparation of Specimens for X-ray Flourescence and X-ray Diffraction Analysis, John Wiley and Sons Inc, 1998.

[34] A.M. Hilmen, D. Schanke, K.F. Hanssen, A. Holmen, Appl. Catal. A: Gen. 186 (1999) 169-188.

[35] P.H. Bolt, “Transition metal–aluminate formation in alumina-supported model catalysts”, PhD Thesis, University of Utrecht, The Netherlands, 1994.

[36] K. Jalama, N. J. Coville, D. Hildebrandt, D. Glasser, L. L. Jewell, Top. Catal. 44 (2007) 129-136.

[37] N. Ahmad, S.T. Hussain, B. Muhammad, J.A. Anderson, N. Ali, S.M. Abbas, in: Proceedings of 2013 10th International Bhurban Conference on Applied Sciences & Technology (IBCAST) Islamabad, Pakistan, 2013.

[38] G. Jacobs, M. C. Ribeiro, W. Ma, Y. Ji, S. Khalid, P. T. Sumodjo, B. H. Davis, Appl. Catal. A: Gen. 361 (2009) 137-151.

[39] K. Jalama, N. J. Coville, H. Xiong, D. Hildebrandt, D. Glasser, S. Taylor, A. Carley, J. A. Anderson, G. J. Hutchings, Appl. Catal. A: Gen. 395 (2011) 1–9.

[40] K.M. Cook, H.D. Perez, C.H. Bartholomew, W.C. Hecker, Appl. Catal. A: Gen. 482 (2014) 275–286.

[41] J. Greeley, M. Mavrikakis, J. Phys. Chem. B 109 (2005) 3460-3471.

[42] J.F. Cevallos Candau, W.C. Jr Conner, J. Catal. 106 (1987) 378-385.

[43] J.B. Peri, J. Phys. Chem. 69 (1966) 211-219.

[44] J.B. Peri, R.B. Hannan, J. Phys. Chem. 64 (1960) 1526–1530.

[45] R. Kramer, M. Andre, J. Catal. 58 (1979) 287-295.

[46] S. Storsæter, Ø. Borg, E.A. Blekkan, A. Holmen, J.Catal. 231 (2005) 405-419.

[47] G. Jacobs, P.M. Patterson, T.K. Das, M. Luo, B.H. Davis, Appl. Catal. A: Gen. 270 (2004) 65-76.

[48] J. Li, X.Zhan, Y. Zhang, G. Jacobs, T.Das, B.H Davis, Appl.Catal. A: Gen. 228 (2002) 203-212.

[49] P.J. van Berge, J. van de Loosdrecht, J. Barradas, A. M. van der Kraan, Catal. Today 58 (2000) 321-334.

[50] J. Wimmers, P. Arnoldy, J.A. Moulijn. J. Phys. Chem. 90 (1986) 1331-1337.

[51] G.E. Batley, A. Ekstrom, D.A. Johnson, J. Catal. 34 (1974) 368-375.

[52] K. Fajans, Naturwiss. 11 (1923) 165-172.

[53] K. Fajans, G. Joos, Z. Phys. 23(1924) 1-46; K. Fajans, Z. Kristallogr. 61 (1924) 18-48.

[54] B.A. Sexton, A.E. Hughes, T.W. Turney, J. Catal. 97(1986) 390-406.

[55] E. van Steen, M. Claeys, M. E. Dry, J. van de Loosdrecht, E.L. Viljoen, J. L.Visagie,. J. Phys. Chem. B 109 (2005) 3575-3577.

[56] O. Kitakami, H. Sato, Y. Shimada, F. Sato, M. Tanaka, Phys. Rev. B 56 (1997)13849-13854.

[57] B. Clapham, “The Development of an In-Situ X-Ray Diffraction Cell for Fischer-Tropsch Catalyst Characterisation”, Masters’ Thesis, University of Cape Town, South Africa, 2012.

[58] H.-Y. Lin, Y.-W. Chen, Mater. Chem. Phys. 85 (2004) 171–175.

[59] J.T. Richardson, R. Scates, M.V. Twigg, Appl. Catal. A: Gen. 246 (2003) 137-150.

[60] D.J. Moodley, “On the Deactivation of Cobalt-based Fischer-Tropsch Synthesis Catalysts”, PhD Thesis, Eindhoven University of Technology, The Netherlands, 2008.

[61] J.A. Rodriguez, J.Y. Kim, J.C. Hanson, M. Perez, A.I. Frenkel, Catal. Lett. 8 (2003) 247-254.

[62] J.A. Rodriguez, J.C. Hanson, A.I. Frenkel, J.Y. Kim, M. Pérez, J. Am. Chem. Soc. 124 (2002) 346-354.

[63] J.Y. Kim, J.A. Rodriguez, J.C. Hanson, A.I. Frenkel, P. L. Lee. J. Am. Chem. Soc. 125 (2003) 10684-10692.

[64] J.-Y. Luo, W.S. Epling, Appl. Catal. B: Environ. 97 (2010) 236-247.

[65] W.C. Jr Conner, J.L. Falconer, Chem. Rev. 95 (1995)759-788.

[66] A.F. Carley, H.A. Edwards, B. Mile, M.W. Roberts, C.C. Rowlands, J. Chem. Soc. Faraday Trans. 90 (1994) 3341-3346.

[67] J.-G. Kim, J. R. Regalbuto, J. Catal. 139 (1993) 175-190.

[68] W. Chu, P.A. Chernavskii, L. Gengembre, G.A. Pankina, P. Fongarland, A.Y. Khodakov J. Catal. 252 (2007) 215-230.

[69] M. de Beer, A. Kunene, D. Nabaho, M. Claeys, E. van Steen, J. S. Afr. Inst. Min. Metall. 114 (2014) 157-165.

[70] R.P. Viswanath, B. Viswanathan, M.V.C. Sastri, React. Kinet. Catal. Lett. 2 (1975) 51-56.

[71] M.V.C. Sastri, R. P. Viswanath, B. Viswanathan, Int. J. Hydr Energy 7 (1982) 951-955.

[72] J. Sloczynski, J. Solid State Chem. 118 (1995) 84-92.

[73] E. Iglesia, L. S. Soled, R. A. Fiato, G. H. Via, J. Catal. 143 (1993) 345–368.

[74] G. Jacobs, J.A.Chaney, P.M. Patterson, T.K. Das, J.C. Maillot, B.H. Davis, J. Synchrotron Rad. 11 (2004) 414-422.

[75] M.D. Shannon, C. M. Lok, J.L. Casci, J. Catal. 249 (2007) 41–51.

[76] S. J. Gentry, N. W. Hurst, A. Jones, J. Chem Soc. Faraday Trans. 1 (1981) 603-619.

Chapter 6

Hydrogen Spillover from Au and Pt Promoters during the Fischer-Tropsch Synthesis

6.1 Carbon monoxide Conversion

Catalyst testing under Low-Temperature Fischer-Tropsch conditions was carried out at 220°C and 20 barg (Sec. 4.3). H_2 and CO were mixed in a ratio of 2:1 and fed at a Gas Hourly Space Velocity (GHSV) of $1200ml\cdot(min\cdot gCo)^{-1}$ (NTP) to a packed bed reactor containing an already activated catalyst. To prevent temperature runaways, the reactor temperature at start-up was ramped at 1°C/min from 150°C to 220°C. As a result, actual reaction conditions were only realised after 1.5 hours on stream and only then was on-line analysis of the permanent gases including H_2, CO, CH_4, CO_2 and N_2 (reference gas) via the GC-TCD started. Off-line GC-FID analysis of the gaseous hydrocarbon product begun as soon as quasi steady-state conversions were observed with the GC-TCD.

Figure 6.1-1 shows the curves of CO conversion as a function of time on stream for the various catalysts. For the **Pt-Co catalyst system**, the trend in CO conversion with time was as follows: Pt-Co/Al_2O_3 > Hybrid Pt-Co > Co/Al_2O_3. A similar trend was observed for H_2 conversion, with the H_2/CO usage ratios in the range of 2.1-2.2. The trend in the CO conversion was maintained with time even though Pt-Co/Al_2O_3 exhibited a large loss in activity of approximately 37%, most of which was in the initial 15 hours on stream.

With the **Au-Co catalyst system**, the trend in CO conversion with time was as follows: Au-Co/Al_2O_3 > (Hybrid Au-Co ~ Co/Al_2O_3). Unlike with the Pt-Co catalyst system, Hybrid Au-Co did not show any improvement in catalyst activity compared to the unpromoted Co/Al_2O_3. This was consistent with the results from catalyst activation in the preceding chapter where it was observed that although Au in Au-Co/Al_2O_3 increased the quantity of metallic Co^0 after reduction, Hybrid Au-Co did not show an improvement in the reducibility compared to Co/Al_2O_3.

Therefore, the overall trend in CO conversion with time on stream for both catalyst systems was as follows: (Pt-Co/Al_2O_3 ≈ Au-Co/Al_2O_3) >> Hybrid Pt-Co > (Hybrid Au-Co ≈

Co/Al_2O_3). This overall trend was consistent with expectations from the TGA, in situ XRD and quasi in situ XPS analyses that showed that the co-supported catalysts had the highest values of the degree of reduction (DOR) and contained the greatest amount of metallic Co^0 in the bulk and on the catalyst surface.

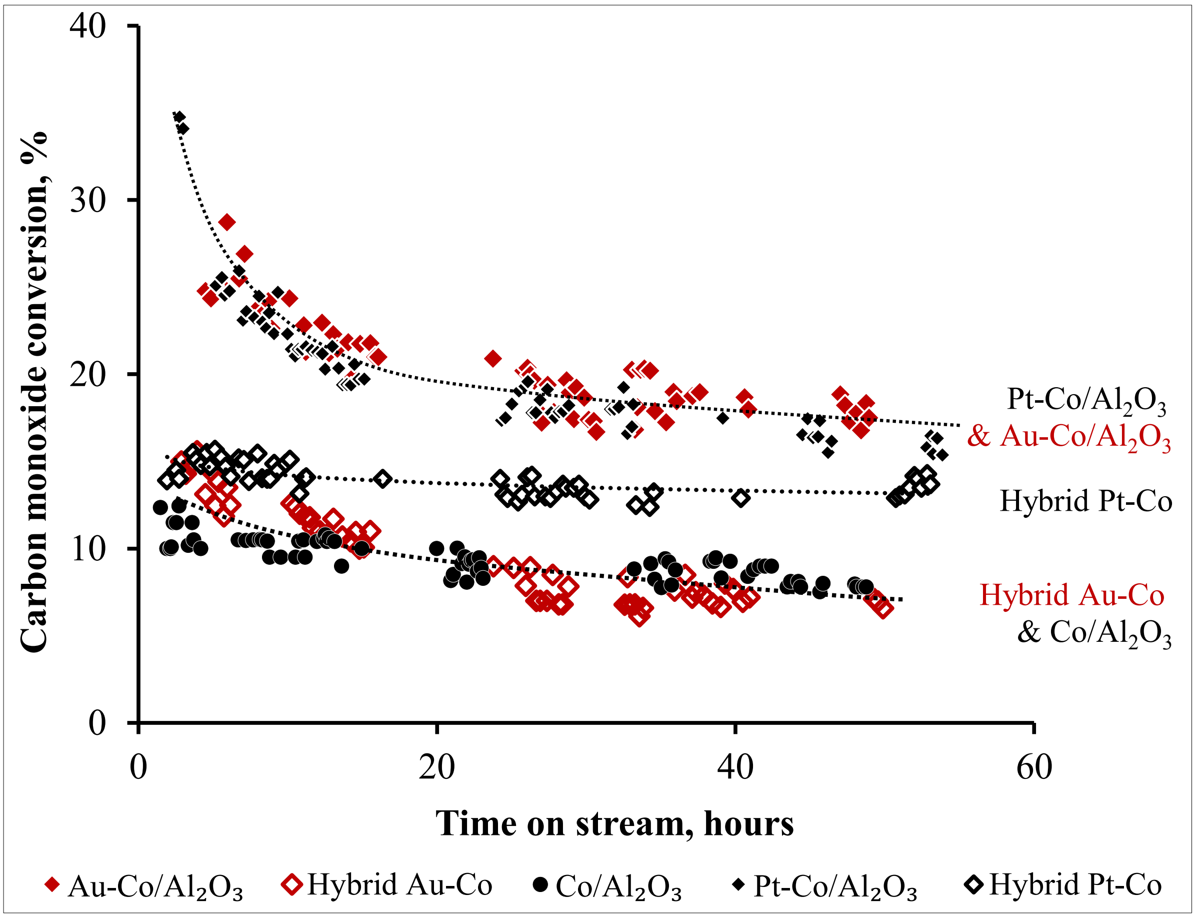

Figure 6.1-1: Change in carbon monoxide conversion with time on stream. $GHSV_{syngas}$=1200ml·(min·gCo)$^{-1}$ at 220°C, 20 barg and H_2/CO ratio of 2.

- ***'Deactivation' of catalysts under reaction conditions***

All catalysts were observed to deactivate most rapid with initial time on stream (Fig. 6.1-1). This trend was similar to the observations made by van Berge et al. and Khodakov et al. shown in Figures 2.2-1 and 2.2-2.

The deactivation rates were calculated according to Equation 6.1-1 [1], and are listed in Table 6.1-1. For all samples, the loss in activity was greatest immediately after start-up and slowed to a relatively low rate after 18 hours, at which point quasi-steady state was assumed.

$$Deactivation\ rate\ \left(\%/_{h}\right) = \frac{X_{CO,t_2} - X_{CO,t_1}}{t_2 - t_1}$$ **Equation 6.1-1**

Table 6.1-1: Deactivation rate constants at various time intervals on stream.

	Deactivation rate, %/h	
	4 – 24 h	**24 – 48 h**
Co/Al_2O_3	-0.3	-0.16
Hybrid Pt-Co	-0.07	-0.03
Pt-Co/Al_2O_3	-0.40	-0.10
Au-Co/Al_2O_3	-0.33	-0.12
Hybrid Au-Co	-0.19	-0.07

The Fischer-Tropsch reaction starts with a 'clean' catalyst surface, but proceeds to generate multiple reactive and unreactive species (e.g. carbonaceous species) after a series of turnovers. Therefore, it is not surprising that the catalyst activity shows an apparent decline in the period following exposure to syngas because the presence of other species would naturally led to a decline in the active surface that was available purely for H_2 and CO adsorption. Thus, a portion of the decline in activity of all samples was probably product related.

The deactivation rate of Pt-Co/Al_2O_3 and Au-Co/Al_2O_3 especially in the initial 24 hours was higher than the unpromoted Co/Al_2O_3 and hybrid samples, which suggested that Pt and Au promoters increased the rate at which cobalt deactivated. This is in agreement with the literature on promoted cobalt catalysts, where a higher deactivation rate may be observed in the presence of reduction promoters [1]. The adverse effect of promoters may stem from the higher conversion, which increases the rate of deactivation by both carbon deposition and oxidation from higher water partial pressures [1]. Therefore, the apparent increase in the deactivation rate is not necessarily a direct effect of the promoter, but rather a secondary effect of the higher reducibility and higher conversion. The effects of the higher conversion must be decoupled from the observed deactivation rate to accurately determine the effects of promoters on the deactivation rate. One way in which this may be achieved is to compare deactivation of promoted and unpromoted cobalt-based catalysts at the same conversion [1]. Unfortunately, this was not carried out because deactivation was outside the scope of this study and would have required extended times on stream.

Finally, it is noted that most of the literature that specifically addresses the deactivation of cobalt-based catalysts (Sec. 2.2.3) is based on extended periods on stream from 600 hours to 150 days compared to 48-60 hours on stream in this study. Nonetheless, it was hypothesized that the deactivation mechanisms that are identified as the initial or fast were more likely to have dominated due to the short times. A detailed analysis of the potential deactivation mechanisms was attempted and is provided in Appendix F1.

6.2 Conversion and Selectivity of Pt/Al_2O_3 and Au/Al_2O_3 under Fischer-Tropsch Conditions

At the selected reaction conditions, the CO conversions of the Pt/Al_2O_3 and Au/Al_2O_3 samples were too low to be accurately quantified using the GC-TCD. Instead, the GC-FID analyses were used to determine the CO conversion as 0.02% for Pt/Al_2O_3 and 0.047% for Au/Al_2O_3. However, the CO conversion determined in this manner was based only on the hydrocarbon formation and was thus 'CO_2 free', which implied that no $CO \rightarrow CO_2$ conversion occurred via the water-gas-shift (WGS) reaction.

In any case, the low amounts of CO_2 that may have been produced by the very low metal loading (0.5%) in monometallic promoter catalysts were impossible to detect. This was due to a large degree of dilution of the reactor product stream *upstream* of the GC-TCD by the N_2 reference gas, and the Ar stream used to maintain the system pressure (Sec. 4.3). Matsuzaki et al. [2] used 5.2%Pt/SiO_2 at comparable reaction conditions (20bar, $H_2/CO=2$, 250°C), and found the CO_2 selectivity to be 29-32%, and the rest C_1 (CH_4 and CH_3OH). Sakurai & Haruta [3] also reported high activity for the WGS reaction (CO_2 selectivities of 30-50%) during CO hydrogenation on various supported Au catalysts (50bar, $H_2/CO=2$, 250°C). Based on the findings by Matsuzaki et al. [2] and Sakurai & Haruta [3], it was estimated that the overall CO conversions of both monometallic promoter catalyst samples would have been approximately 30% greater than the CO_2-free CO conversions.

The GC-FID chromatograms of the Au/Al_2O_3 and Pt/Al_2O_3 samples are shown in Figure 6.2-1. Determination of the product distribution was non-trivial because of the very low peak intensities. Nevertheless, it can be seen that the product of Au/Al_2O_3 was predominantly C_1-C_3. On the other hand, that of Pt was highly olefinic and Pt appeared to favour more chain growth since it exhibited carbon numbers of up to about C_6. The higher selectivity towards longer hydrocarbon chains observed with Pt/Al_2O_3 was in accordance with the deduction by van Santen et al. [4] that the strong Pt-C bond makes it suitable for chain growth.

The FID chromatogram of Au/Al_2O_3 displayed an extra unusual peak in the boiling point region of C_1-C_2, which was tentatively attributed to acetylene ($HC{\equiv}CH$). Acetylene is hardly observed in the Fischer-Tropsch product of transition metals (Co, Fe) because the high electron density around the triple carbon bond results in a very strong adsorption to metal surfaces, which causes it to rapidly hydrogenate to ethylene [5]. Acetylene adsorbs more strongly than CO and ethylene ($H_2C=CH_2$). In fact, the high strength of acetylene adsorption has been exploited by co-feeding it with syngas at temperatures as low as 120°C. Even at this low temperature, acetylene initiates chain growth more easily compared to ethylene, which is highly reactive but adsorbs less strongly [5]. It was thus hypothesized that the lower reactivity of the Au surface may have allowed the acetylene intermediate to desorb despite its high electron density. Therefore, the ease with which acetylene desorbed was in line with the low selectivity towards longer chained hydrocarbons because few species would have been present on the Au surface for chain growth.

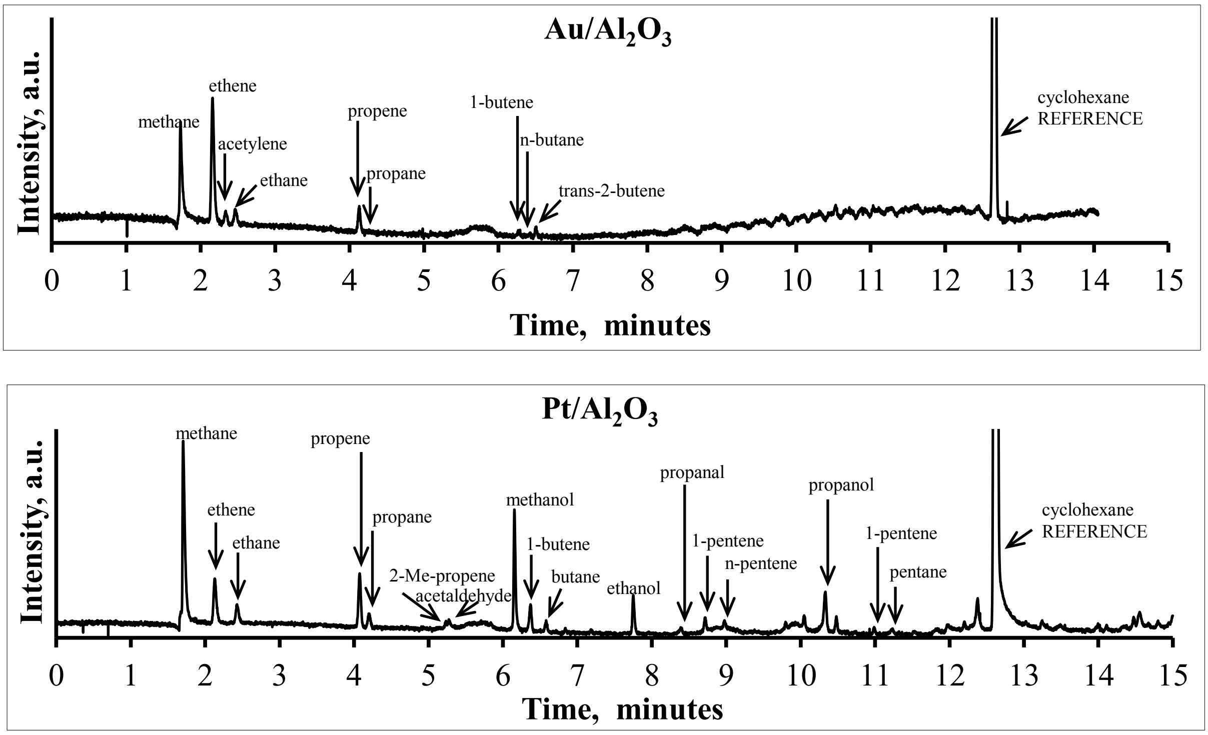

Figure 6.2-1: GC-FID chromatograms of the gas phase Fischer-Tropsch products. $GHSV_{syngas}$=48000ml·(min·gMe)$^{-1}$ at 220°C, 20barg and H_2/CO ratio of 2. ***Top:*** Au/Al_2O_3. ***Bottom:*** Pt/Al_2O_3.

The calculated product selectivities of Pt/Al_2O_3 and Au/Al_2O_3 are shown in Table 6.2-1. At 37.6%, the CH_4 selectivity Au/Al_2O_3 was greater than that of Pt/Al_2O_3 at 31.9%. On the other hand, Pt/Al_2O_3 was highly selective towards oxygenates: methanol and ethanol constituted almost 20% of the overall product selectivity, while the oxygenate selectivity in the C_1-C_3 fractions ranged from 45.6 to 54.7%. The high selectivity towards oxygenates was in agreement with Matsuzaki et al. [2] who also observed that SiO_2 supported Pt catalysts were highly selective towards methanol. On the contrary, no oxygenates were observed in the product distribution of Au/Al_2O_3 even though Sakurai & Haruta [3] reported that supported Au catalysts were highly selective towards methanol. Sakurai & Haruta [3] tested Au catalysts at a much higher pressure of 50bar, which may have contributed to the differences in activity and product selectivities with this study.

Table 6.2-1: Product selectivity of Au/Al_2O_3 and Pt/Al_2O_3 at Low Temperature Fischer-Tropsch conditions.

	X_{CO}, %	**Overall product selectivity, %C**				**Oxygenate content, %C**		
		CH_4	C_2+	MeOH	EtOH	C_1	C_2	C_3
Pt/Al_2O_3	0.02	31.9	56	14.7	5.1	45.6	43.9	54.7
Au/Al_2O_3	0.047	37.6	62.4	-	-	-	-	-

The ASF plots and the olefin selectivity as a function of carbon number are shown in Figures 6.2-2 and 6.2-3 respectively. The ASF plot of the Pt/Al_2O_3 sample was resonant with that of the typical Fischer-Tropsch product, with the CH_4 selectivity disproportionately greater than predicted by the chain growth probability. The ASF chain growth probability (α) of the Pt/Al_2O_3 was determined from the slope of the ASF plot, from C_3-C_6, as 0.5, while the α value of the Au/Al_2O_3 sample was determined as 0.4.

The product of Pt/Al_2O_3 was highly olefinic, and the olefin selectivity displayed features typically observed with Fischer-Tropsch product including a lower C_2 olefin selectivity due to its higher reactivity, and a decrease in the olefin selectivity with carbon number. The trends in the olefin selectivity of Au/Al_2O_3 were less clear but the C_2 olefin selectivity was greater than that of Pt, which suggested that C_2 species on the Au surface was less reactive. This was consistent with the fact that a peak attributed to acetylene was observed.

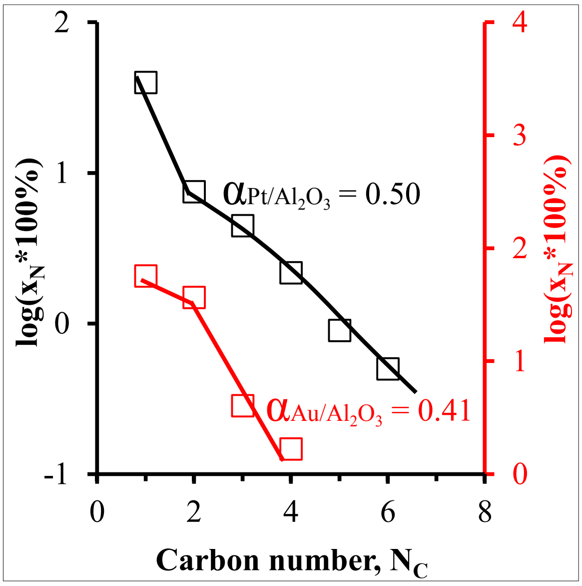

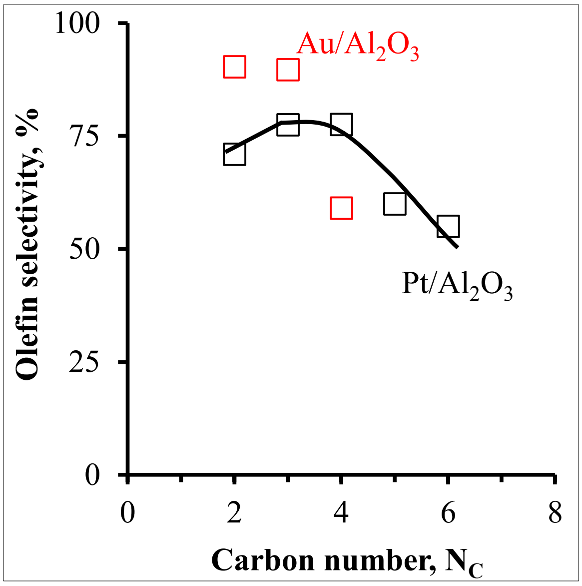

Figure 6.2-2: ASF Distribution of the hydrocarbon product of Pt/Al_2O_3 and Au/Al_2O_3.

Figure 6.2-3: Olefin selectivity in the hydrocarbon product of Pt/Al_2O_3 and Au/Al_2O_3. The selectivity was determined only in the olefin+paraffin fraction and excluded oxygenates.

Table 6.2-2 includes the activation energy for CO dissociation and adsorption energies of molecular CO on Au, Pt and Co surfaces available from van Santen et al. [4].

Table 6.2-2: Activation energy for CO dissociation and adsorption energies of molecular CO on Au, Pt and Co surfaces [4].

		Ea for CO dissociation at low coverage (kJ·mol^{-1})	**Adsorption energies of atop adsorbed molecular CO (kJ·mol^{-1})**
Au	fcc	581	-28
Pt	fcc	419	-154
Co	fcc	251	- 171

While the CO adsorption energy of Pt is just lower than on Co, the barrier for CO dissociation on Pt is 1.7 times greater. According to van Santen et al. [4], Pt surfaces are characterised by a high selectivity for chain growth by CH_x monomers due to a strong Pt-C bond but the high energy barrier for CO dissociation makes Pt unsuitable for the commercial Fischer-Tropsch reaction. High CO dissociation barriers result in CH_x monomers forming too slowly. Therefore, Pt had a high selectivity towards short-chained hydrocarbons because the rate of CH_x hydrogenation was high relative to the CH_x formation from CO dissociation, which resulted in few CH_x species for incorporation into growing chains [4].

The behaviour of Au towards CO was deduced to be different from that of Pt because Au showed lower chain growth. From Table 6.2-2 the activation energies for CO dissociation on fcc structures increase as follows: Au >> Pt > Co, and adsorption energies of atop adsorbed CO as follows: Co > Pt >>> Au. These metrics suggest that Au is unsuitable for use as a Fischer-Tropsch catalyst. Firstly, the low adsorption energy of CO on Au means that the Au-CO bond is weak making Au less suitable for chain growth, which is in contrast to the case of Pt [4]. Secondly, the high CO dissociation energy is resonant with Pt, whereby CO dissociates too slowly to form C_1 monomers, which favours hydrogenation over incorporation into growing chains. The low CO adsorption energy is consistent with the case of acetylene, which was deduced to adsorb weakly despite the triple bond because of the low reactivity of Au. Due to the low reactivity of Au surfaces towards H_2 (see Table 5.4-1) and CO, adsorption on Au crystallites is limited to low coordinated atoms along edges, corners, interfacial sites with the support and defects [6]. Therefore, the activity of the Au/Al_2O_3 sample was facilitated by the use of gold crystallites of ca. 3nm, which have a greater fraction of the low co-ordinated surface atoms required for reaction.

6.3 Cobalt Time-Yield and Apparent site-time yield: The Effects of Pt and Au

The cobalt-time yield was determined as the number of moles of CO converted in each second per mole of cobalt present in the catalyst (Eq. 6.3-1). The apparent site-time yield (STY) was defined as the number of moles of CO converted in each second per mole of metallic cobalt present on the catalyst surface (Eq. 6.3-2). The moles of metallic cobalt present on the surface were determined using data from the H_2 chemisorption measurements (Sec. 4.2.7).

$$Cobalt - time\ yield\ (s^{-1}) = \frac{X_{CO,t} \cdot \dot{N}_{CO}}{N_{Cobalt}}$$ **Equation 6.3-1**

$$Apparent\ site - time\ yield\ (s^{-1}) = \frac{X_{CO,t} \cdot \dot{N}_{CO}}{H_{ads,chem}}$$ **Equation 6.3-2**

Where:

$X_{CO,t}$ = CO conversion at time *t*

$\dot{N}_{CO}$= specific molar flow rate of CO (mmol/gCo·s)

N_{Cobalt} = total number of moles of Co in catalyst (mmolCo)

$H_{ads,chem}$ = number of moles of atomic H adsorbed per mole of Co. Determined using H_2 chemisorption (mmolH/gCo). Ratio of atomic H to surface Co^0=1.

The values of the cobalt-time yield and apparent STYare shown in Table 6.3-1. It was noted that both values were dependent on the conversion, which changed with time on stream. Nevertheless, it was expected that like with the conversion in Fig. 6.1-1, the general trends between the samples would be maintained regardless of time. Included in the table are values of the degree of reduction (DOR) determined from TGA, the CO conversion at 24hours and the results from H_2 chemisorption from which the quantity of surface metal species following activation was determined. The CO conversion at 24 hours on stream and the dispersion were used to calculate the values of the cobalt-time yield and apparent STY. The raw data from the H_2 chemisorption analyses is included in Appendix F2.

Table 6.3-1: Cobalt-time yield, apparent site-time yield and dispersion of the various catalysts.

	Cobalt-time yield x 10^3 s^{-1}	**Apparent Site-time yield x 10^3 s^{-1}**	**DOR’ %^{A}**	**X_{CO} at 24h, %**	**H_{ads}:Co^B**	**H_{ads}:Au OR H_{ads}:Pt^C**	**Dispersion i.e. H_{ads}:Co^D**
Au/Al_2O_3	-	-	-	0.05	-	0.27	-
Pt/Al_2O_3	-	-	-	0.02	-	0.37	-
Co/Al_2O_3	4.8	45	30.9	9.5	0.032		0.032
Hybrid Pt-Co	6.6	51	71.8	13	0.042	0.37	0.039
Pt-Co/Al_2O_3	9.2	91	89.8	19	0.034	0.37	0.031
Hybrid Au-Co	4.5	40	31.3	8.9	0.035	0.27	0.033
Au-Co/Al_2O_3	9.0	97	67.5	20	0.029	0.27	0.028

A: Degree of reduction (DOR) using TGA data in Sec. 5.5.1. Assumption is direct $Co_3O_4 \rightarrow Co^0$ reduction

B: From H_2 chemisorption. Units are mmolH:mmolCo. The ratio of atomic H to the total moles of Co in the sample. For this ratio, it is assumed that all the H chemisorbed only on the cobalt surface.

C: From H_2 chemisorption. Units are mmolH:mmolPt OR mmolH:mmolAu. The ratio of atomic H to the total moles of the promoter in the co-supported or hybrid sample. Ratio assumed to be the same as that in monometallic samples.

D: From H_2 chemisorption. Units are mmolH:mmolCo. The ratio of atomic H to the total moles of Co in the sample excluding the H that was estimated to have chemisorbed on promoter according to **C**.

The cobalt-time yield increased as follows: (Co/Al_2O_3 ≈ Hybrid Au-Co) < Hybrid Pt-Co << (Pt-Co/Al_2O_3 ≈ Au-Co/Al_2O_3) according to Table 6.3-1. The cobalt-time yield increased with the degree of reduction, and was thus dependent on the total quantity of the catalytically active phase (Co^0) following the 12-hour activation in H_2. The higher cobalt-time yield of the Co/Al_2O_3 catalyst in the presence of Pt and Au promoters is a widely observed and ascribed to the higher quantity of Co^0 formed following catalyst activation [1, 7].

However, catalyst activity is not a function of the overall quantity of cobalt as defined by cobalt-time yield, but rather the quantity of surface metallic cobalt as described by the apparent STY in Table 6.3-1. The apparent STY increased as follows: (Co/Al_2O_3 ≈ Hybrid Au-Co) < Hybrid Pt-Co << (Pt-Co/Al_2O_3 ~ Au-Co/Al_2O_3). Although Hybrid Pt-Co was determined to have a higher apparent STY than Co/Al_2O_3, the difference of just 12% was not considered statistically relevant because of the numerous measurements and associated uncertainties involved in the calculation of this value. However, the apparent STYs of Pt-Co/Al_2O_3 and $Au-Co/Al_2O_3$ were more than twice the apparent STY of the unpromoted sample. These high values indicated that a synergy arose when Co and the promoter were co-supported and/or in direct physical contact.

The apparent STY, cobalt-time yield, and CO conversion are represented as curves in Figure 6.3-1 to better illustrate the synergistic effects observed in the presence of Pt and Au promoter in $Pt-Co/Al_2O_3$ and $Au-Co/Al_2O_3$.

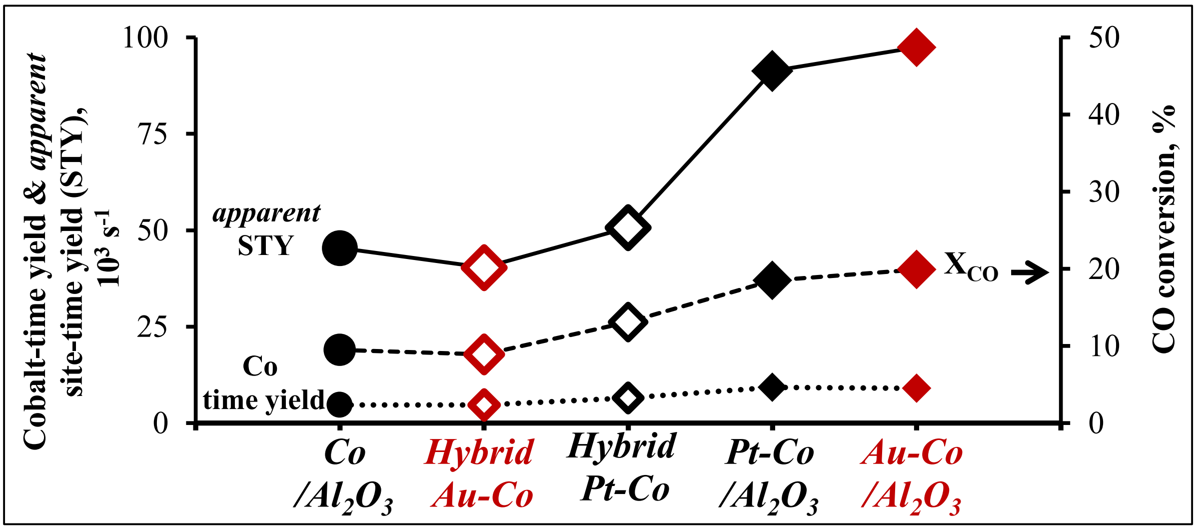

Figure 6.3-1: Cobalt-time yield, apparent site-time yield (STY), and CO conversion in the Platinum-Cobalt System (**black**) and the Gold Cobalt System (**red**).

6.3.1 Apparent site-time yield versus the true intrinsic site-time yield of Co^0

The apparent STY as defined in Equation 6.3-1 is the active site based activity and is synonymous with the turnover frequency or turnover number. However, the active site based activity is based on H_2 chemisorption data where isotherms were collected under non-reactive conditions (Sec. 4.2.7), so one of the major assumptions surrounding its use was that the quantity of the active sites remained constant following exposure to syngas and with time on stream. However, Schanke et al. [8] stated that reactions that involve CO and hydrocarbons generate unreactive material on the catalyst surface, so that only a fraction of the active area determined using H_2 chemisorption is actually available for reaction. Thus, the site-time yield for purposes of the current study was termed ‘apparent’. The true intrinsic STY of Co is that obtained when the effects of surface coverage of non-reactive material on the catalyst surface are decoupled from the apparent STY.

The higher apparent STY in the presence of reduction promoters was corroborated by various literature sources that studied samples with high promoter-to-cobalt mass ratios i.e. higher than used commercially [8-10]. Unfortunately, the complexity of the Fischer-Tropsch reaction and the intricate composites that constitute the various types of catalysts means that there is little agreement and understanding of the cause of the higher apparent STY in the presence of reduction promoters. In fact, some authors report that the active site-based activity of Co is not at all affected in the presence of promoters. The lack of consensus is compounded by the fact that many studies of promoted cobalt catalysts do not even report values of the active site-based activity, and instead chose to determine just the cobalt-time yield (mass-based) despite the fact that Fischer-Tropsch reaction is dependent on the surface of the cobalt catalyst rather than its bulk.

However, a body of literature exists that has used evidence from Steady-State Isotopic Transient Kinetic Analysis (SSITKA) of methanation to establish that even though the apparent STY increases in the presence of noble metal promoters, the <u>true intrinsic STY</u> of Co^0 remains unaffected [8, 9, 11]. These studies show that a constant intrinsic STY of Co^0 is obtained when the effects of coverage are decoupled from those of the apparent STY. The higher apparent STY in the presence of reduction promoters is instead attributed to a greater coverage of reactive intermediates (CH_X) in the presence of noble metal reduction promoters. Unfortunately, SSITKA of methanation studies are carried at atmospheric pressure (1-2 bar, H_2/CO = 7-10, 210-220°C) to study CH_4 formation instead of at commercial Fischer-Tropsch conditions, which has likely hindered their wider acceptance. Nevertheless, these studies assert that the obtained results are applicable at standard FT conditions (high pressure, lower H_2/CO ratio) since CH_4 and C_5+ hydrocarbons are formed from the same CH_x reactive intermediate [8, 9, 11]. The formation of methane and longer chained hydrocarbons from the same CH_x intermediate is also asserted by van Santen et al. [4].

The mechanism by which Pt and other reduction promoters increase the coverage of reactive species is not explicitly clear from the reviewed SSITKA studies [8, 9, 11]. Schanke et al. [8] did suggest that lower coverage of reactive intermediates required for the Fischer-Tropsch product might arise because a portion of the surface is blocked by unreactive species or is simply unoccupied. In line with this suggestion, Iglesia et al. [10] postulated that the higher active site-based activity with 0.26%Ru-23%Co/TiO_2 (and SiO_2) catalysts was because Ru helped stabilise Co^0 sites against deactivation during initial turnovers. Ru was suggested to have a 'cleaning' effect due to its high ability to activate H_2, and thus remove O and carbon deposits from the Co^0 surface.

6.3.2 Effects of direct promoter-cobalt interaction

Ideally, analyses of the behaviour of the hybrid samples versus that of Co/Al_2O_3 allows for isolation of the remotely controlled promoter effects such as hydrogen spillover. On the other hand, the behaviour of the hybrid versus the co-supported samples allows for quantification of the remote-control promotion effects against effects that arise from direct promoter-cobalt interaction. Unfortunately, decoupling the contribution of these effects by analysis of the cobalt-time yield or apparent STY was non-trivial.

A recent study by de Beer [12] investigated the active site-based activity by systematically increasing the extent of interaction between Co and the promoter (using a strong electrostatic adsorption preparation method) while maintaining a promoter/Co atomic ratio in 0.5 (Pt or Au)%-10%Co/SiO_2. The importance of an interaction between the promoter and Co was evidenced by a disproportionate increase in the active site based activity in the samples with the most intimate promoter-Co interaction. The results by de Beer [12] were consistent with the synergistic effect of Pt and Au in the co-supported samples versus the hybrid samples in which the promoter and cobalt were separated (Fig. 6.3-1).

As discussed in the preceding chapter, Pt-Co co-ordination occurs readily in Pt-Co/Al_2O_3 provided the catalyst is calcined after preparation, while Au and Co in Au-Co/Al_2O_3 have been found to form separate phases [1,13-18]. The contrasting behaviour of these promoters is consistent with the 'Green's-function linear-muffin-tin-orbitals method' calculations by Norskov et al. [19]. Norskov et al. showed that the surface segregation energies at the close packed Co surface were greater with Au atoms (-0.76eV) versus Pt atoms (-0.38eV). The surface energies per atom were also determined to decrease as follows 1.07eV (Co) > 1.03eV (Pt) > 0.72eV (Au). The higher surface segregation energy of Au atoms on Co means that the two metals are less likely to alloy. In fact, the lower surface energy per Au atom suggests that it would preferentially deposit on the surface of metallic Co to decrease the overall surface energy of the bimetallic crystallite. Pt on the other hand is likely to alloy more easily with Co based on the low surface segregation energy, while its lower surface energy means that it may preferentially deposit on the surface of Co as observed by Somorjai et al. [20] although it has been suggested that Pt might be imbedded in the structure of Co crystallites [17]. In any case, the deduction of spillover from Pt and Au in the preceding chapter means that at least some crystallites need to exist on the Co surface in order to access molecular H_2 from the gas phase during the reduction.

Regardless of the differences in Pt-Co versus Au-Co coordination, the cleaning effect proposed by Iglesia et al. [10] to explain the observed synergistic (ruthenium) promoter effect implies that it is the quantity and not the quality of Co^0 active sites that is maintained at greater values when the promoter is present. According to Iglesia, this effect is based on the reducing behaviour of the promoter rather than an effect on the intrinsic chemical behaviour of the Co that would otherwise arise from an electronic/bonding effect.

These deductions are supported by the recent studies by Somorjai et al. [20, 21] who used CO_2 methanation as a probe reaction for the Fischer-Tropsch synthesis to study the mechanistic role of Pt (see Sec. 2.4.3.2). The model catalysts included adjacent but physically separated Pt and Co nanoparticles supported on MCF-17 mesoporous SiO_2. An illustration of the model catalysts was included in Figure 2.4-2. A synergy in the apparent STY was also obtained with adjacent Pt and Co nanoparticles versus the pure Co nanoparticles despite Pt and Co separation, and was attributed to the cleaning of the cobalt surface by Pt. The authors suggested that Pt's reactivity towards H_2 resulted in a hydrogen spillover action under reaction conditions. Spillover provided the cleaning action via removal of near surface or even subsurface oxygen/oxides that accumulate on the cobalt surface following C-O bond breaking [20].

Therefore, the synergy observed in the apparent STY of $Pt\text{-}Co/Al_2O_3$ and $Au\text{-}Co/Al_2O_3$ can be explained by the cleaning effect due to hydrogen spillover from the promoter. The results from the various SSITKA of methanation studies and the work by Somorjai strongly suggest that direct promoter-Co coordination/bimetallic effects need not exist in order to observe the synergistic effect introduced by promoters. However, it is suggested that direct promoter-cobalt interaction plays an important role in facilitating the hydrogen spillover process. In Chapter 5, the importance of direct promoter-cobalt contact for the spillover process was emphasized by the assertion that it provides the most efficient pathway for spillover hydrogen transfer i.e. direct Pt → Co or Au → Co, and the same case may arise under Fischer-Tropsch conditions. This ties-in with the fact that no synergistic effect of the apparent STY was observed with hybrid samples because the spillover pathway was less efficient.

6.3.3 H_2 activation and spillover by Pt and Au under Fischer-Tropsch conditions

It is worth noting that during the reduction pre-treatment, the hydrogen acceptor surface (Co_3O_4) was much less active for H_2 activation than the promoter surface, which boosted spillover as a competitive source of activated hydrogen for the reaction. In contrast, under reaction conditions, the metallic Co^0 surface itself is active for H_2 activation. Naturally, the effects of spillover are easier to isolate when the accepting surface (e.g. Co_3O_4) shows little to no activity for H_2 activation compared to when the accepting surface is metallic (e.g. Co^0), and is itself active for dissociative H_2 adsorption.

Spillover hydrogen from the promoter is imagined to create a hydrogen-rich microenvironment in an isolated region around the Co crystallites. This could result in a number of consequences such as the cleaning effect by removing O and carbon deposits from the Co^0 surface, and possibly a more hydrogenated product. Greater hydrogenation would be characterised by a higher paraffin/olefin ratio, lower chain growth probability, and selectivity towards shorter hydrocarbon chains that could arise from the higher local H/C ratio; these characteristics were indeed observed in the presence of promoters in this study (Sec. 6.4). It may also be conceived that spillover would have the same effects as a higher partial pressure of H_2 on the reaction kinetics. An increase in the H_2 partial pressure has generally been reported to correlate positively with the reaction rate within a range of conditions (see Sec. 2.2.1). This is in accordance with the kinetic expressions for the Fischer-Tropsch reaction on cobalt (see Eq. 2.2-1 to 2.2-4). Therefore, it is conceivable that the Fischer-Tropsch rate on Co would also increase due to the higher localised hydrogen partial pressure.

- ***Effect of the Water-Gas Shift (WGS) reaction***

In Section 6.2, it was suggested that Pt and Au might have catalysed the water-gas shift reaction under Fischer-Tropsch conditions. In fact, both Pt and Au promoters have been cited as the cause of the higher amount of CO_2 in the promoted Co/Al_2O_3 catalyst, and some studies have cited the WGS reaction as a cause of the higher extent of hydrogenation in the promoted catalysts [15, 22]. Therefore, under Fischer-Tropsch conditions, the relationship between hydrogen and the promoter is more complex compared to during reduction because the WGS reaction may also be involved. The H_2 produced from the WGS reaction may have a similar effect as spillover hydrogen since it would also result in an increase in the localised H_2/CO ratio.

The low levels of CO_2 could not be directly quantified using the GC-TCD as explained in Section 6.2. Nonetheless, the H_2/CO ratio in the product of the various samples showed the following trend at a CO conversion of ca. 12.3%: 2.03 in Hybrid Au-Co > 2.08 in Co/Al_2O_3> 2.1 in Hybrid Pt-Co > 2.2 in Pt-Co/Al_2O_3 > 2.4 in Au-Co/Al_2O_3. A higher H_2/CO ratio in the product may be an indication of WGS activity. It was apparent that besides Hybrid Au-Co, the presence of Pt and Au increased the WGS activity, which was highest in Au-Co/Al_2O_3. It was interesting that Hybrid Au-Co showed very little WGS activity, i.e. had the lowest H_2/CO ratio in the product. If indeed the WGS activity originated from only the presence of Au, then the expectation was that even Hybrid Au-Co would have exhibited an increased quantity of H_2/CO in the product. The fact that the ratio was highest in Au-Co/Al_2O_3 suggested that Au was not solely responsible for observed differences in the product H_2/CO ratio. It is possible that that the higher H_2/CO ratio in the product (and thus higher CO_2 formation) occurs via an alternative pathway in the presence of Pt and Au. Jacobs et al. [15] suggested that the Pt promoter in Pt-Co/Al_2O_3 could facilitate the dehydrogenation of formates, i.e. R(HCOO), during a steam-assisted decomposition reaction. It is conceivable that this formate decomposition would occur more readily on surfaces in which the promoter and cobalt were in close proximity since the formate intermediates would be adsorbed on the Co surface. The formation of formates was not observed in this study.

○ *CO poisoning of platinum*

The case of CO poisoning of **Pt** to the detriment of H_2 adsorption must be considered with respect to hydrogen spillover in the presence of syngas. CO poisoning of Pt to the detriment of hydrogenation reactions is well known and has been a subject of numerous publications related to Proton Exchange Membrane fuel cells (PEMFCs) [23-28] and hydrogenation of olefins such as ethylene [30, 31]. CO poisoning occurs because it binds more strongly than hydrogen to Pt surfaces [25, 26]. The heat of adsorption of CO on Pt is about 1.5 times that of H_2 [27]. According to Vogel et al. [25], in PEMFCs, even very small concentrations of CO may saturate the surface of the Pt catalyst to the exclusion of hydrogen, and so the CO concentration in the operation of PEMFCs must be maintained <50ppm for commercial operations [28]. Somorjai et al. [30] also found that the hydrogenation of ethylene on Pt nano-particles supported on Al_2O_3 was hindered in the presence of CO. They suggested that due to CO poisoning, the reaction was instead catalysed by the Pt-Al_2O_3 support interface at which CO was easily hydrogenated and thus interfacial sites could be free for the hydrogenation reaction [30, 31].

The inhibition of the Pt surface by CO was thought to have had unfavourable consequences for Pt → Co spillover under Fischer-Tropsch conditions compared to during the reduction. During catalyst activation in pure H_2, Pt active sites were available for H_2 activation with limited competition from other molecules. During the LTFT reaction, the CO in syngas could have effectively blocked a large portion of the Pt surface for H_2 adsorption and subsequent spillover. The detrimental effect of CO on H_2 activation and spillover was imagined to be greater in the hybrid sample in which the Pt/Co separation was great and the efficiency of spillover transfer already poor even under pure H_2 conditions as deduced from the lower reducibility of Hybrid Pt-Co in Chapter 5. Based on the observed synergy in the promoted catalysts, it was inferred that H_2 activation and spillover proceeded, albeit at subdued rates. H_2 adsorption could have been favoured on alternative sites such as at the Pt-Al_2O_3 interface as suggested by Somorjai et al. [30, 31]. Besides reaction at the metal/support interface, it is well known that the maximum CO coverage on Pt ranges between 0.5-0.75ML [32-36]. This is also the case with other metals including Fe and Co [8, 37]. The lower saturation coverage of CO may have left some sites available for adsorption of other species such as hydrogen, which has a saturation coverage close to 1ML on Pt and other metal surfaces [8, 37, 38].

In the **Au-Co catalyst system**, detrimental effects of CO poisoning were not expected due to the low strength of adsorption of most molecules on the Au surface and also the fact that Au is a well-known CO oxidation catalyst (Sec. 2.3.2).

- ***The effect of adsorbed hydrocarbons***

Spillover under reaction conditions needed to occur on a catalyst surface that was probably covered with a layer of liquid hydrocarbons over/through which spillover hydrogen species would have needed to diffuse in order to access Co active sites. It is unclear whether the presence of hydrocarbons would have hindered hydrogen spillover especially in the case of the hybrid samples where hydrogen migration needed to occur over extensive areas of the support that were now covered by hydrocarbons.

Spillover has been observed to occur in heavily coked samples [39] and in fact, hydrocarbons can act as bridges to facilitate interfacial spillover [40], resulting in a higher overall spillover rate.

6.3.4 Consolidation

It is hypothesized that the synergistic effect of Pt and Au promoters on the apparent STY can occur remotely, albeit more efficiently when the promoter and Co are in direct physical contact, without the need for an electronic interaction/ligand effect. The observed increase in the apparent STY with Pt-Co/Al_2O_3 and Au-Co/Al_2O_3 was because the promoters facilitated a higher surface coverage of reactive intermediates through the cleaning effect of spillover hydrogen. Spillover is imagined to generate a hydrogen-rich microenvironment around the cobalt crystallites and thus have effects similar to those obtained at high H_2/CO ratios.

The basis for the higher apparent STY in (Pt or Au)-Co/Al_2O_3 compared to the corresponding hybrid samples was conceived to lie in the physicochemical dissimilarities, and more specifically, in the great separation that had been introduced between the promoter and cobalt. Close interaction between the promoter and cobalt was important for the synergistic effect because a similar increase in apparent STY was not observed with the hybrid catalysts.

The case of Au-Co/Al_2O_3 is interesting and provides support for the fact the proximity of the promoter to the cobalt, rather than their co-ordination/bimetallic interaction is important for the synergistic promoter effect on the apparent STY. Au-Co/Al_2O_3 exhibited an apparent STY that was comparable to that of Pt-Co/Al_2O_3 despite the literature indicating that Au and Co probably form separate phases while Pt and Co were more likely to interact. Therefore, comparable activities of these samples indicated that the promoter-cobalt bonding/co-ordination was not vital to obtain the high values of apparent STY. Rather, high values of apparent STY may also be obtained if the promoter and cobalt are adjacent but in separate phases without an electronic interaction. This observation is noteworthy and contradicts the assertion made by Iglesia et al. [10] that although the (Ru) promoter did not affect the chemical behaviour of Co, a well-mixed bimetallic particle with intimate Ru-Co contact was required to observe the synergy in the apparent STY. Iglesia et al. [10] stated that intimate interaction in the 0.14%Ru-11%Co/TiO_2 sample was attained during calcination.

Finally, it is suggested that using the site-time yield to assess the activity of the Au and Pt promoted cobalt catalysts is inadequate because under Fischer-Tropsch conditions, a large portion of the catalyst surface may actually be covered by unreactive species, with only a limited part available for reaction [8]. To accurately analyse hydrogen spillover versus electronic/bimetallic effects, additional analyses such as SSITKA of methanation would be required to eliminate the effects of different surface coverage.

6.4 The effects of Pt and Au promoters on the product distribution of Co/Al_2O_3

The results obtained from the hydrocarbon product analyses were analysed as a function of time on stream, and compared at a similar conversion. Only the gas-phase hydrocarbon products were collected in ampoules for quantification using the off-line GC-FID (see Sec. 4.3). It is well known that the product distribution of the cobalt-based LTFT catalyst is dependent on the activity and so different catalysts can only be accurately compared at similar levels of conversion [1, 41].

6.4.1 ASF distribution

The Anderson-Schulz-Flory (ASF) distributions as a function of carbon number are shown in Figure 6.4-1. The ASF distributions were typical of cobalt-based catalysts and showed the frequently observed deviations from the ideal ASF kinetics including higher amounts of C_1, and a minima at C_2. The high selectivity of C_1 has been attributed to formation of CH_4 from multiple pathways while the low selectivity of C_2 is related to the higher readsorption probability of the C_2 olefin compared to higher α-olefins [43, 44], which facilitates its disproportionate incorporation into growing chains.

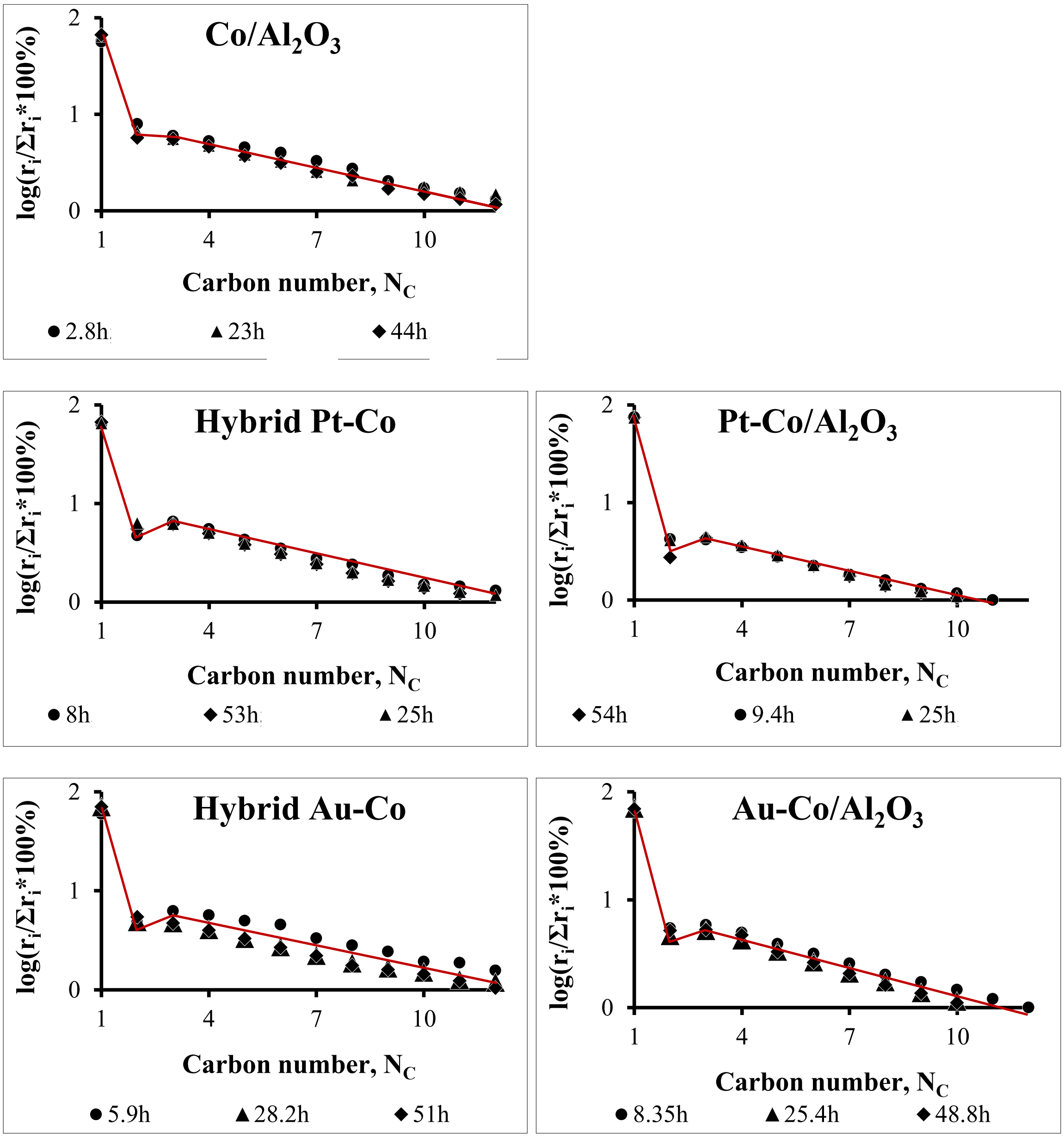

Figure 6.4-1: ASF distribution of the gas-phase hydrocarbon product at various times on stream. Red curve added to highlight trends.

6.4.2 Methane (CH_4) selectivity

Figure 6.4-2 shows the CH_4 selectivity of samples as a function of time on stream. The CH_4 selectivity of all samples was higher than predicted by ASF kinetics, which is typical of cobalt-based catalysts. A number of reasons have been proposed for the deviation of CH_4 from the ideal kinetics such as formation from specific C_1 species that do not incorporate into growing chains [45-47], and formation on distinct active sites [45-47].

With all samples, CH_4 selectivity increased with time so that after start-up when the conversion was at its highest, selectivity was at its lowest. These trends concurred with those reported by Jacobs et al. [1], van Berge et al. [48, 49], and Khodakov et al. [50]. The results from Khodakov et al. were illustrated in Figure 2.2-2. Khodakov et al. suggested that the trends with time on stream might be an effect of catalyst deactivation, which results in changes in the ratios of metallic Co^0 to oxides, mixed Co/support compounds and other species that are typically present under reaction conditions. Although Co^0 is the active phase for reaction, it is suggested that the other oxidic or even carbidic cobalt phases may take part in side and/or secondary reactions including WGS, isomerisation, reinsertion, and hydrogenolysis [50]. During studies of pre-treatment atmospheres, Bukur et al. [51] also suggested that high CH_4 selectivity was related to the presence of different cobalt phases including CoO, Co_xC and other interactions between cobalt and polymeric carbon.

Over the 48+ hours on stream, CH_4 selectivities were in the range of 15-30% and compared well with the literature at the same reaction conditions, i.e. 220°C, 20 bar and $H_2/CO=2$; $X_{CO}=10\text{-}50\%$. Khodakov et al. [50] reported selectivities in the range 8-15% on unpromoted Co/Al_2O_3, Jacobs et al. [15] using $0.5\%Pt\text{-}25\%Co/Al_2O_3$ obtained selectivities of up to 11%, and Jalama et al. [22] reported selectivities of up to 28% with Au promoters on various supports.

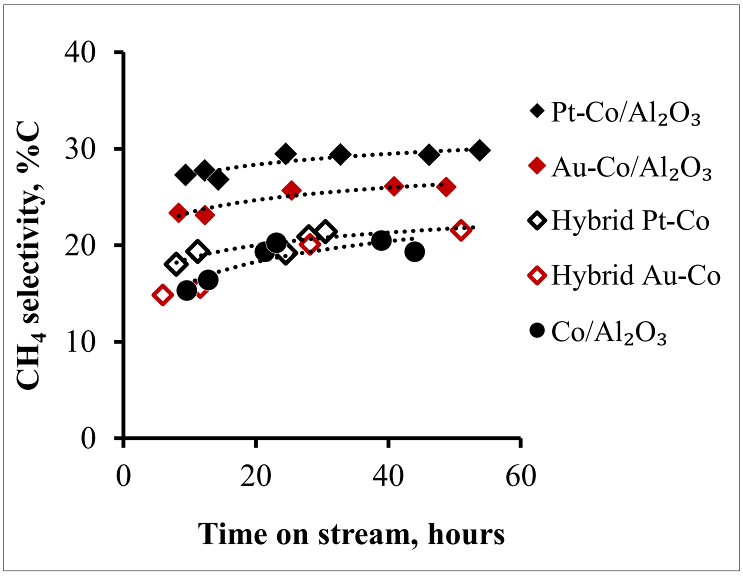

Figure 6.4-2: Methane selectivity as a function of time on stream.

The CH_4 selectivities at a conversion of ca. 12.3% are shown in Table 6.4-1. The trend in the CH_4 selectivity was as follows: Pt-Co/Al_2O_3 > Au-Co/Al_2O_3 > (Hybrid Pt-Co ≈ Hybrid Au-Co ≈ Co/Al_2O_3). The higher values with Au-Co/Al_2O_3 and Pt-Co/Al_2O_3 were consistent with the frequently reported effect of the higher hydrogenation activity in Pt promoted catalysts [1, 8, 15, 42, 52] and Au promoted catalysts [22].

Table 6.4-1: CH_4 selectivity at a CO conversion of ca. 12.3%.

Sample	CH_4 selectivity, %C
Co/Al_2O_3	21
Hybrid Au-Co	20
Hybrid Pt-Co	21
Au-Co/Al_2O_3	26
Pt-Co/Al_2O_3	30

Various reasons have been proposed to explain the enhanced hydrogenation activity in the presence of Pt, Au and other noble metal promoters. It may be that the effect is multifaceted and caused by several factors including hydrogen spillover, the enhanced WGS reaction (or formate decomposition), the prevalence of small Co crystallites, and the use of chlorinated precursors.

- **Hydrogen spillover:** The role of hydrogen spillover has been discussed with regard to the synergistic effect in Section 6.3. A spillover effect has been proposed to explain the high CH_4 selectivity in the presence of Pt promoters [15, 52, 53].

- **Water-Gas Shift:** Jacobs et al. [15] suggested that the high spillover rate and WGS activity of Pt/Al_2O_3 (as evidenced by higher CO_2 selectivity) increased the H/C ratio, resulting in deleterious CH_4 production. An alternative pathway for CO_2 and H_2 formation was proposed with respect to the high activity of Pt for the decomposition of formate – R(HCOO) (see Sec. 6.3.3).
- **Small Co^0 crystallites:** Some literature sources have singled out the smaller average Co^0 crystallite sizes, which are frequently obtained with Pt and other noble metal promoted Co catalysts on weakly interacting supports such as SiO_2 and TiO_2 [8, 42, 52]. Noble metal promoters reportedly aid the reduction of small Co crystallites and other highly dispersed Co^0 species that would otherwise remain oxidic, but this in turn increases the CH_4 selectivity for which small Co^0 species (<5nm) were found to show greater selectivity [54-57]. However, according to Diehl & Khodakov [33], modification of the Co^0 crystallite size by Pt and other noble metals is rarely observed for strongly interacting supports like Al_2O_3 [1, 8, 11, 15].
- **Chlorinated precursors:** The use of chlorinated precursors during catalyst preparation has also been cited as a cause of high CH_4 selectivity. Using Ru-Co/Al_2O_3, Kogelbauer et al. [11] showed that the CH_4 selectivity of the sample prepared using $Ru(NO)(NO_3)_3$ was 3.4% higher than the unpromoted sample, but 7% greater when a chlorinated $RuCl_3$ precursor was used. A similar increase in CH_4 was obtained with a catalyst prepared using a HCl solution (instead of an aqueous solution) of $Ru(NO)(NO_3)_3$ during impregnation of Co/Al_2O_3. Chloride ions were suggested to facilitate a detrimental restructuring of the Co surface, which resulted in the slightly higher CH_4 selectivity.

o ***CH_4 selectivity of Pt-Co/Al_2O_3***

A number of effects may have contributed to the high CH_4 selectivity of Pt-Co/Al_2O_3. The selectivity was predictably high because the Pt loading of 0.5% exceeded the 0.1% ideal level beyond which detrimental hydrogenation activity is pronounced according to Diehl & Khodakov [42].

A hydrogen spillover effect was supported by the fact that a synergistic effect of Pt was observed in the apparent STY of Pt-Co/Al_2O_3, which was double that of the unpromoted Co/Al_2O_3. Based on deductions from SSITKA of methanation studies [8, 9, 11] and results reported by the group of Somorjai [20], it was hypothesized that the higher apparent STY was due to spillover hydrogen from Pt (see Sec. 6.3). Therefore, it could be argued that spillover also modified the localised H_2/CO ratio, to result in a higher selectivity to hydrogenated products such as CH_4 [15, 52, 53].

The role of Pt in enhancing the water-gas shift activity and in that way increasing the localised H_2/CO ratio could not be directly established but was inferred from the product H_2/CO ratio. The H_2/CO ratio in the product of Pt-Co/Al_2O_3 was 5.8% higher than in the unpromoted sample, which suggested some water-gas shift activity, or alternatively, formate decomposition activity as suggest by Jacobs et al. [15].

With regard to crystallite size and its effect on CH_4 selectivity [54-56], Rietveld refinement of the XRD diffractograms of the reduced samples showed that the crystallite size in Pt-Co/Al_2O_3 decreased from Co_3O_4 (14.4nm) → Co^0 (10.3nm), while in Co/Al_2O_3, it decreased from Co_3O_4 (12.7nm) → CoO (9.4nm). XRD did not detect any Co^0 in reduced Co/Al_2O_3 as detailed in Table 5.5-3, but if a contraction in the size of CoO was assumed, then the Co^0 crystallites in Co/Al_2O_3 would have been <9.4nm. Therefore, Pt-Co/Al_2O_3 would in fact have had the larger Co^0 average crystallite size, and by this reasoning should have the lower CH_4 content. Furthermore, it has been discussed that Pt use with strongly interacting supports like Al_2O_3 does not typically result in a decrease in Co^0 crystallite size [42], and so the likelihood of the high CH_4 selectivity being a consequence of a high prevalence of small crystallites was low. Nonetheless, as much as XRD indicated an average crystallite size, it must be kept in mind that very small crystallites (<30Å) would not have been detected and thus their contribution was excluded from the average XRD crystallite size.

With respect to the use of a chlorinated Pt precursor, use of $Pt[(NH_3)_4]Cl_2.H_2O$ was also expected to increase the CH_4 selectivity. Indeed, broad XPS scans revealed very small Cl 2s and Cl 2p ions in calcined Pt/Al_2O_3 and Pt-Co/Al_2O_3, which persisted even after reduction (Fig. 6.4-3).

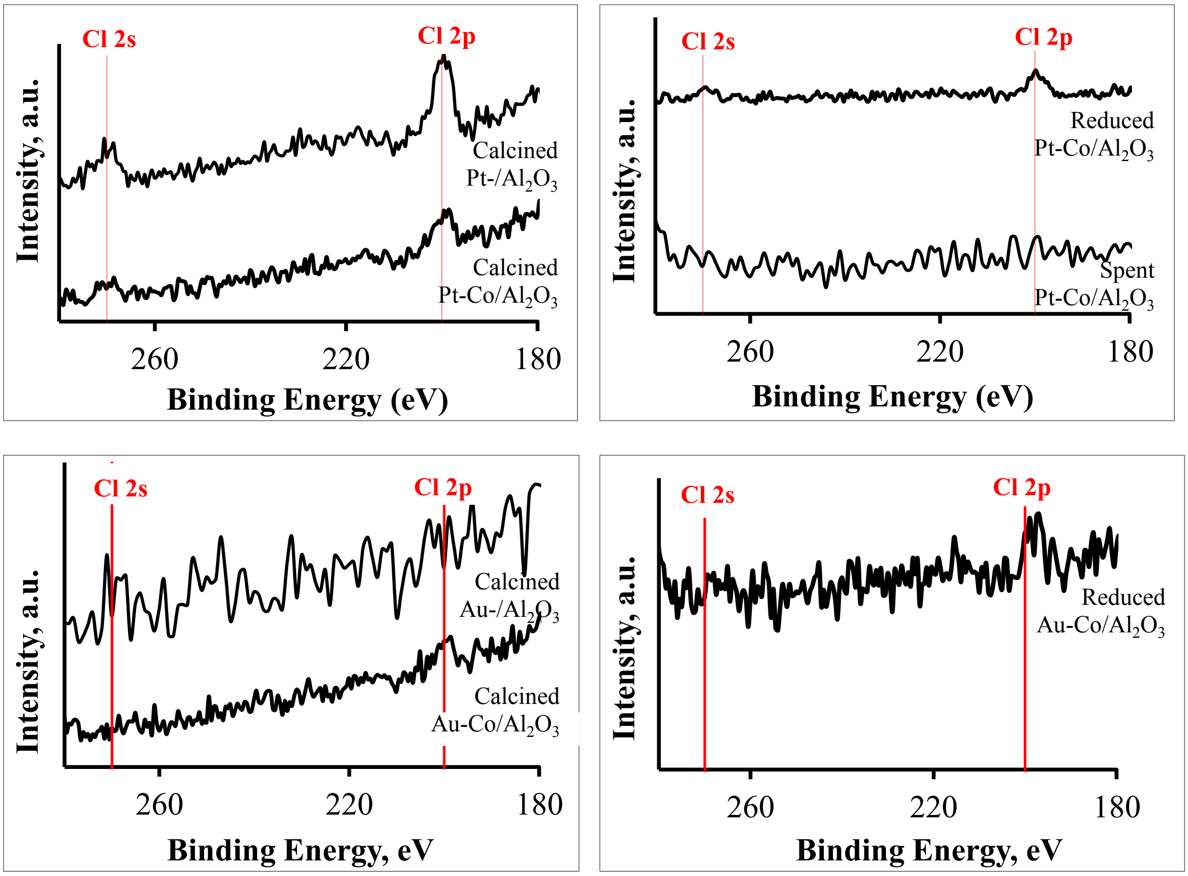

Figure 6.4-3: XPS scans in the Cl 2s and Cl 2p regions of various calcined and reduced Pt and Au containing samples. ***Top row***: Pt-Co catalyst system. ***Bottom row:*** Au-Co catalyst system.

A similar observation was made with the Au-Co catalyst system in which a chlorinated precursor was used. The increase in CH_4 due to the very low quantities of chlorine detected was thought to have been small, i.e. <10% greater than the unpromoted sample based on deductions by Kogelbauer et al. [11]. From the literature, increases in CH_4 selectivity as high as 31% have been observed with non-chlorinated precursors [15], and so the use of $Pt[(NH_3)_4]Cl_2.H_2O$ was not thought the lone contributor to the 47% increase in CH_4 selectivity observed with Pt-Co/Al_2O_3.

- ***CH_4 selectivity of Au-Co/Al_2O_3***

The same deductions put forward for Pt-Co/Al_2O_3 applied to Au-Co/Al_2O_3. The high CH_4 selectivity in the presence of Au could be explained by hydrogen spillover, which is supported by the synergistic effect of Au on the apparent STY.

Concerning the water-gas shift reaction, the H_2/CO ratio in the product of Au-Co/Al_2O_3 was 10.6% greater than that in Co/Al_2O_3, which suggested some water-gas shift activity. Au-Co/Al_2O_3 had the highest product H_2/CO ratio of all samples. The chlorinated precursor used with Au may have also contributed to the CH_4 selectivity based on XPS scans (see Fig. 6.4-3).

Au-Co/Al_2O_3 however resulted in a lower CH_4 selectivity than the equivalent Pt-Co/Al_2O_3 catalyst when compared at a similar conversion in Table 6.4-1. This was consistent with the lower activity for dissociative H_2 adsorption on Au versus Pt surfaces, which also resulted in the lower reducibility reported in Chapter 5.

- ***CH_4 selectivities of the Hybrid Catalyst Samples***

The hybrid samples presented an interesting context for assessing the contribution of Pt and Au to the CH_4 selectivity. These samples allowed for exclusion of electronic/bimetallic/ligand effects between the promoter and Co, and elimination of the effects of Cl^- ions on the Co^0 surface because the chlorine would have been isolated to the promoter constituent.

Hybrid Pt-Co: From CH_4 selectivities in Table 6.4-1, it was apparent that Pt in the hybrid sample did not affect the CH_4 selectivity. This is consistent with the results of activity where the apparent STY of Hybrid Pt-Co was not statistically different from that of Co/Al_2O_3. Therefore, although the effects of spillover were readily observable during reduction, spillover in this sample did not appear to occur as readily under reactive conditions. The efficiency of the Pt → Al_2O_3 → Al_2O_3 → Co spillover pathway appeared even lower than that of the more direct Pt → Co pathway in Pt-Co/Al_2O_3 potentially due to the presence of CO on poisoning of Pt as discussed previously (Sec. 6.3.3). Under LTFT conditions, the Hybrid Pt-Co catalyst may behave in a manner similar to Hybrid Au-Co during reduction, when it was deduced that the low activity for H_2 activation on Au, and the inefficient spillover pathway over multiple interfaces resulted in uncompetitive spillover rates to catalyse the reduction (Chapter 5).

Nevertheless, deductions from Somorjai et al. [20, 21] on separated Pt and Co nano-particles strongly suggest that spillover from Pt to Co might occur under reaction conditions. The advantage of this study was although Pt and Co nano-particles were physically separated, the nanoparticles were still present on the same continuous support surface (see Fig. 2.4-2).

Surface continuity and proximity most likely allowed for more efficient Pt to Co spillover in contrast to the structure of Hybrid Pt-Co. The importance of surface continuity for spillover was highlighted during the development of the catalyst systems in the Section 5.3.

Hybrid Au-Co: The Au surface in the hybrid sample did not improve the reducibility of cobalt oxides, and was not expected to behave much different from unpromoted Co under Fischer-Tropsch conditions.

6.4.3 C_5+ selectivity

The C_5+ selectivity as a function of time on stream is shown in Figure 6.4-4, and Table 6.4-2 shows the C_5+ selectivities of the various samples at a CO conversion of ca. 12.3%. The C_5+ selectivity was determined using Equation 6.4-1, which incorporated GC-FID results with a product range defined as C_1 to C_{100}. Only the composition up until C_{10} to C_{13} could be quantified using the GC-FID, so higher carbon numbers were obtained by extrapolation using the C_4-C_{10} chain growth probability (α). As discussed previously, it is often observed that the chain growth probability (α) increases between C_{10} and C_{20}, and so the use of Equation 6.4-1 and the C_4-C_{10} value of α most likely resulted in a lower estimation of the C_5+ selectivity.

$$C_5\text{+ selectivity} = 100\% - (C_{1\text{-}4}\text{ selectivity}) \qquad \textbf{Equation 6.4-1}$$

The trend in C_5+ selectivity was the inverse of the CH_4 selectivity and increased as follows: (Pt-Co/Al_2O_3 ≈ Au-Co/Al_2O_3) < Hybrid Pt-Co < (Hybrid Au-Co ≈ Co/Al_2O_3). The same arguments presented for the high CH_4 selectivity were applicable, so the Au and Pt doped Co/Al_2O_3 samples, which exhibited higher extents of hydrogenation activity also had the lowest selectivity to high molecular weight products. Therefore, the high hydrogenation activity facilitated by Pt and Au increased CH_4 selectivity but was ruinous to the C_5+ selectivity and counterproductive to the ultimate goal of wax production in the LTFT process. This result is an affirmation of the limited amount of Pt in the industrial catalyst, which not only results in catalyst cost savings but also prevents the undesired low C_5+ selectivity.

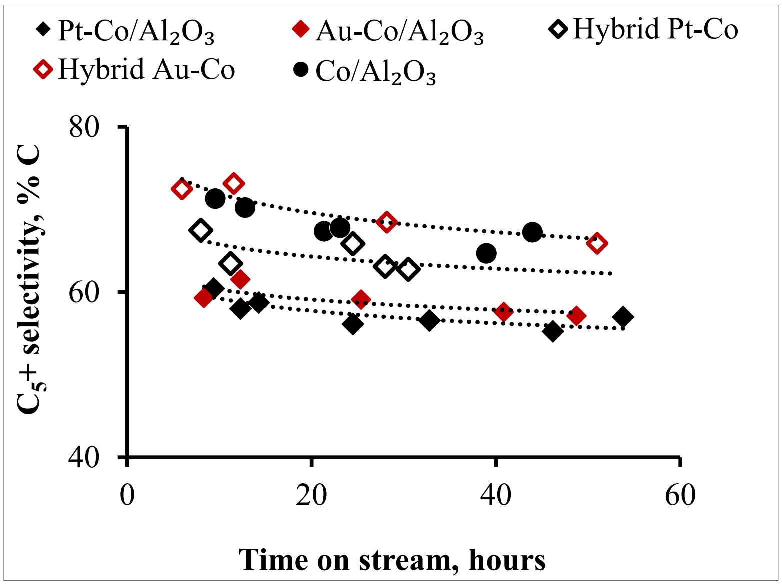

Figure 6.4-4: C_5+ selectivity as a function of time on stream.

Table 6.4-2: CH_4 and C_5+ selectivity at a CO conversion of ca. 12.3%.

Sample	**CH_4 selectivity, %C**	**C_5+ selectivity, %C**
Co/Al_2O_3	21	65
Hybrid Au-Co	20	68
Hybrid Pt-Co	21	63
$Au-Co/Al_2O_3$	26	57
$Pt-Co/Al_2O_3$	30	57

6.4.4 Chain growth probability (α)

The carbon number dependence of the ASF chain growth probability (α) at different times on stream is shown in Figure 6.4-5. The minimum α value was obtained with C_2, after which C_4+ chains exhibited a relatively constant α value. These results are consistent with a Fischer-Tropsch product [45, 58].

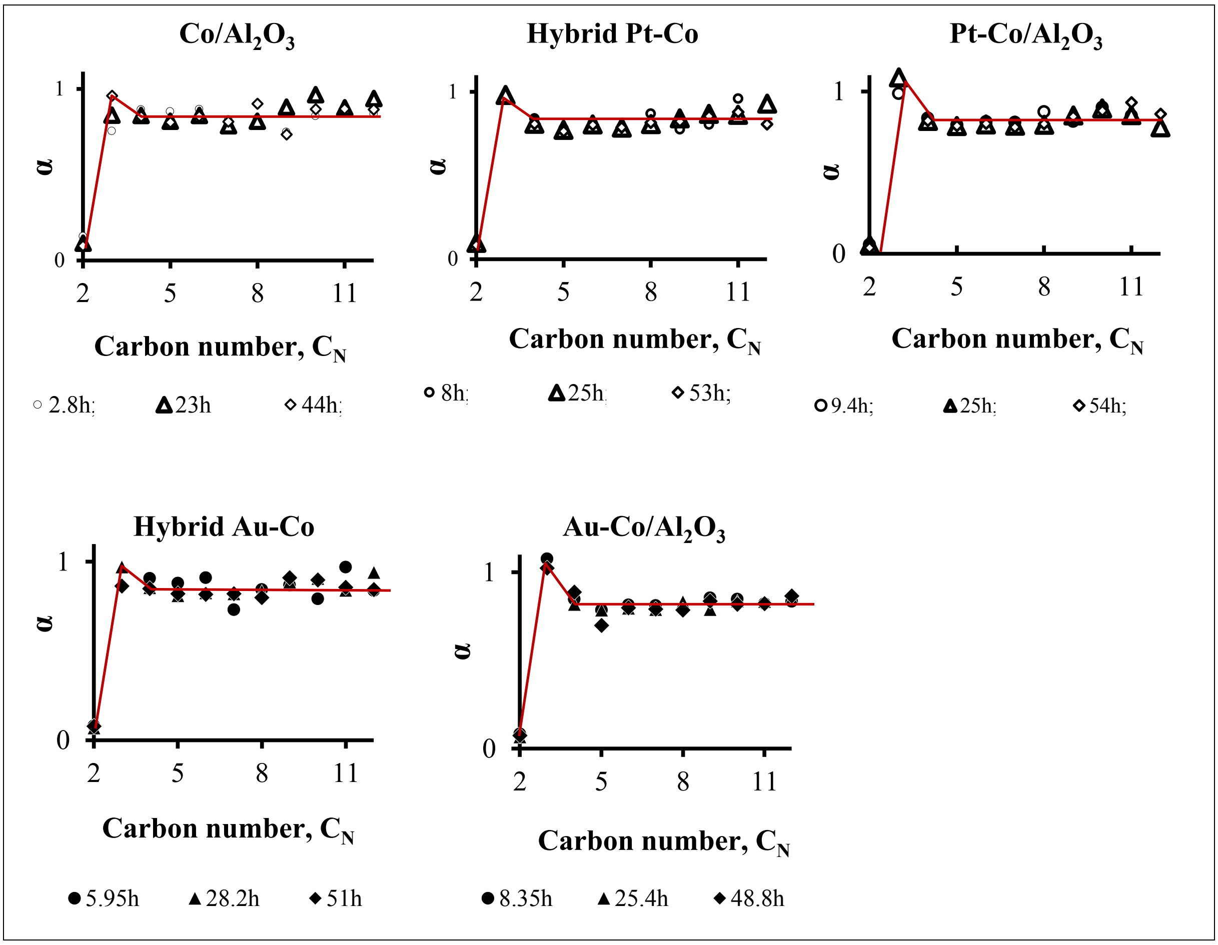

Figure 6.4-5: Carbon number dependence of the chain growth probability at various times on stream (hours). Red curve added to highlight trends.

The C_{4-10} chain growth probabilities are shown as a function of time in Figure 6.4-6. α values were determined from the slope of the ASF Distribution of the gas-phase hydrocarbon product (see Fig. 6.4-1). The C_{12}+ fraction was not included in the determination of α because it was poorly represented in the (gas phase) GC-FID spectra. C_{12} and higher molecular weight hydrocarbons were not well represented because they also constituted the liquid phase of the reactor product, which remained in the hot trap and was not analysed. Furthermore, a small portion of the light hydrocarbon product $<C_{10}$ would have also remained in the hot trap, which introduced some error in the calculated α values.

The values of α varied within a narrow range of <5%, which made trends more difficult to decipher. α values appeared to decrease with time, concurrently with a rise in CH_4 selectivity and drop in C_5+ selectivity. Like with CH_4, the change in the C_5+ selectivity with time on stream may be related to the declining activity and decrease in the quantity of active cobalt relative to oxidic cobalt and other cobalt phases present in a working catalyst that result in the prevalence of side reactions [50, 51].

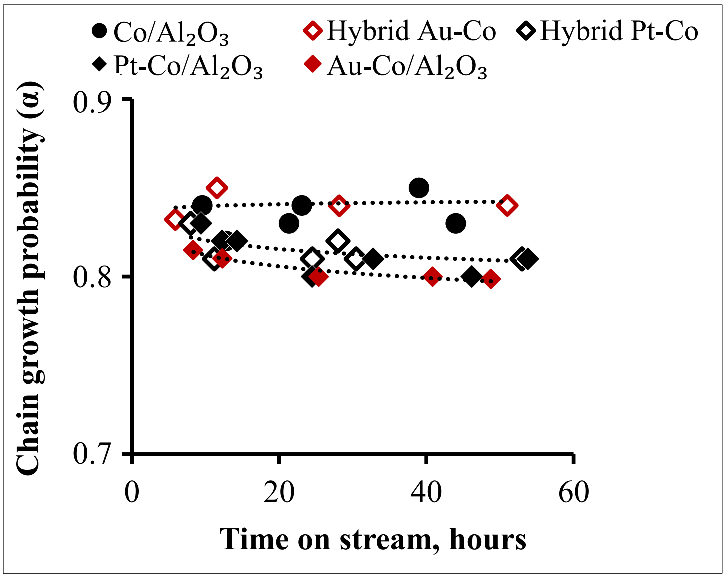

Figure 6.4-6: Chain growth probability (α) as a function of time on stream.

The chain growth probabilities of the various samples at the same CO conversion of ca. 12.3% are shown in Table 6.4-3. It was apparent that doping Co with Pt or Au was detrimental to chain growth, which was highest with Co/Al_2O_3 and lowest with for <u>$Au-Co/Al_2O_3$</u> and <u>$Pt-Co/Al_2O_3$</u>.

Table 6.4-3: CH_4 and C_5+ selectivities and chain growth probability (α) at a CO conversion of ca. 12.3%.

Sample	CH_4 selectivity, %C	C_5+ selectivity, %C	Chain growth probability (α)
Co/Al_2O_3	21	65	0.85
Hybrid Au-Co	20	68	0.84
Hybrid Pt-Co	21	63	0.82
$Au\text{-}Co/Al_2O_3$	26	57	0.80
$Pt\text{-}Co/Al_2O_3$	30	57	0.81

The expected effect of reduction promoters can be illustrated using Scheme 6.4-1 from Claeys & van Steen [58], which depicts ideal chain growth on the catalyst surface during the Fischer-Tropsch reaction, where a hydrocarbon species may grow, or desorb as an olefin (by H abstraction) or alternatively desorb as a paraffin (by H addition). By increasing the localised H:C ratio, promoters would have suppressed chain growth i.e. lowered the α values by increasing the probability of desorption (d_P) to form paraffins via hydrogen addition.

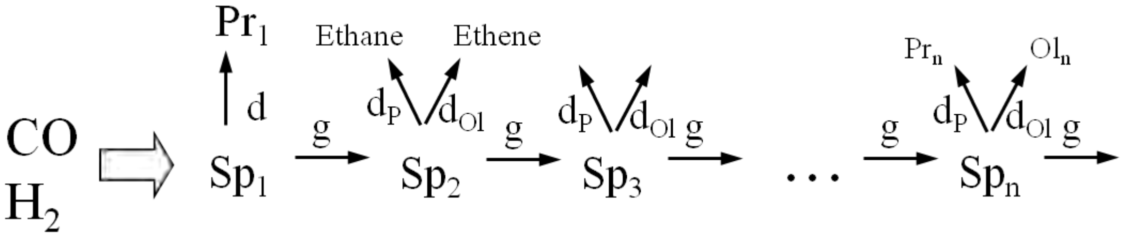

Scheme 6.4-1: Ideal chain growth including desorption as and olefin or paraffin. Adapted from Claeys & van Steen [58].
Sp_n = species with carbon number equal to *n*, d = desorption, g = growth, d_P = desorption as paraffin, d_{Ol} = desorption as olefin, Pr_n = paraffin with carbon number equal to n.

Like with the cases of catalyst activity, CH_4 and C_5+ selectivity, the behaviour of **Hybrid Pt-Co** and the unpromoted sample were similar and did not allow for conclusive deductions. The chain growth probability of **Hybrid Au-Co** was similar to that of the unpromoted sample in accordance with the poor activity of Au for H_2 activation and subsequent spillover during reduction, and the lack of a synergistic effect on the apparent STY.

6.4.5 Olefin selectivity

Although 1-olefins are considered primary products of the Fischer-Tropsch reaction (Sec. 2.1), they are reactive and may readsorb and undergo subsequent hydrogenation to the corresponding paraffin, take part in chain growth to longer hydrocarbon chains or undergo double bond shift. Scheme 6.4-2 from Claeys and van Steen [58] shows the typical secondary reactions that 1-olefins may undergo under Fischer-Tropsch conditions. The double bond shift reaction occurs if readsorption is non-terminal and is undesirable because it does not lead to further chain growth.

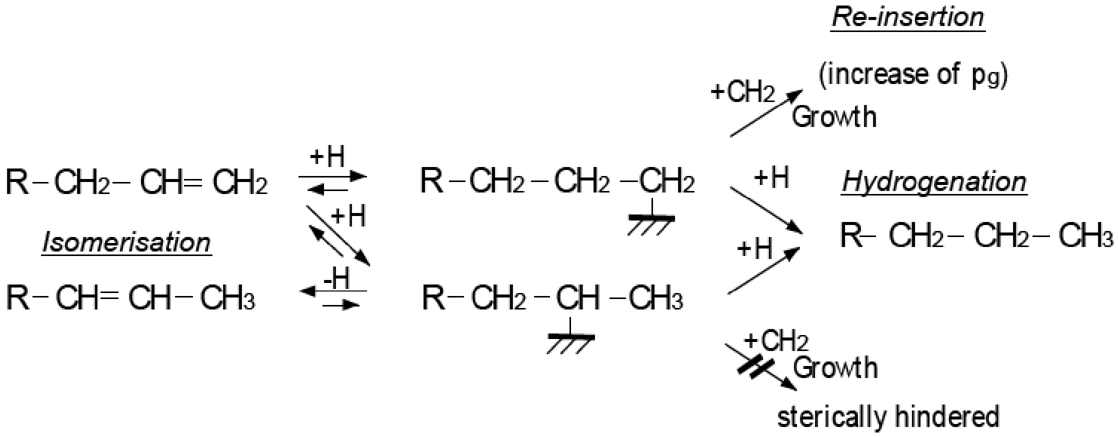

Scheme 6.4-2: Major secondary reactions of 1-olefins during the Fischer-Tropsch reaction. Non-terminal readsorption of a 1-olefin, followed by double bond shift does not result in chain growth [58].

Figure 6.4-7 shows the olefin selectivity as a function of carbon number at various times on stream. The carbon number dependence of the olefin content of all samples showed an increase from C_2 to maxima at C_3-C_4, followed by a gradual decrease with chain length. This peculiar behaviour is due to the high reactivity of the C_2 olefin compared to higher α-olefins [1, 43, 44, 58], which allows for its disproportionate incorporation into growing chains. The decline of olefin selectivity with carbon length is said to be a consequence of the chain length dependent solubility and diffusivity in the liquid (wax) surrounding the catalyst particles, both of which increase the extent of 1-olefin readsorption [43, 58-61].

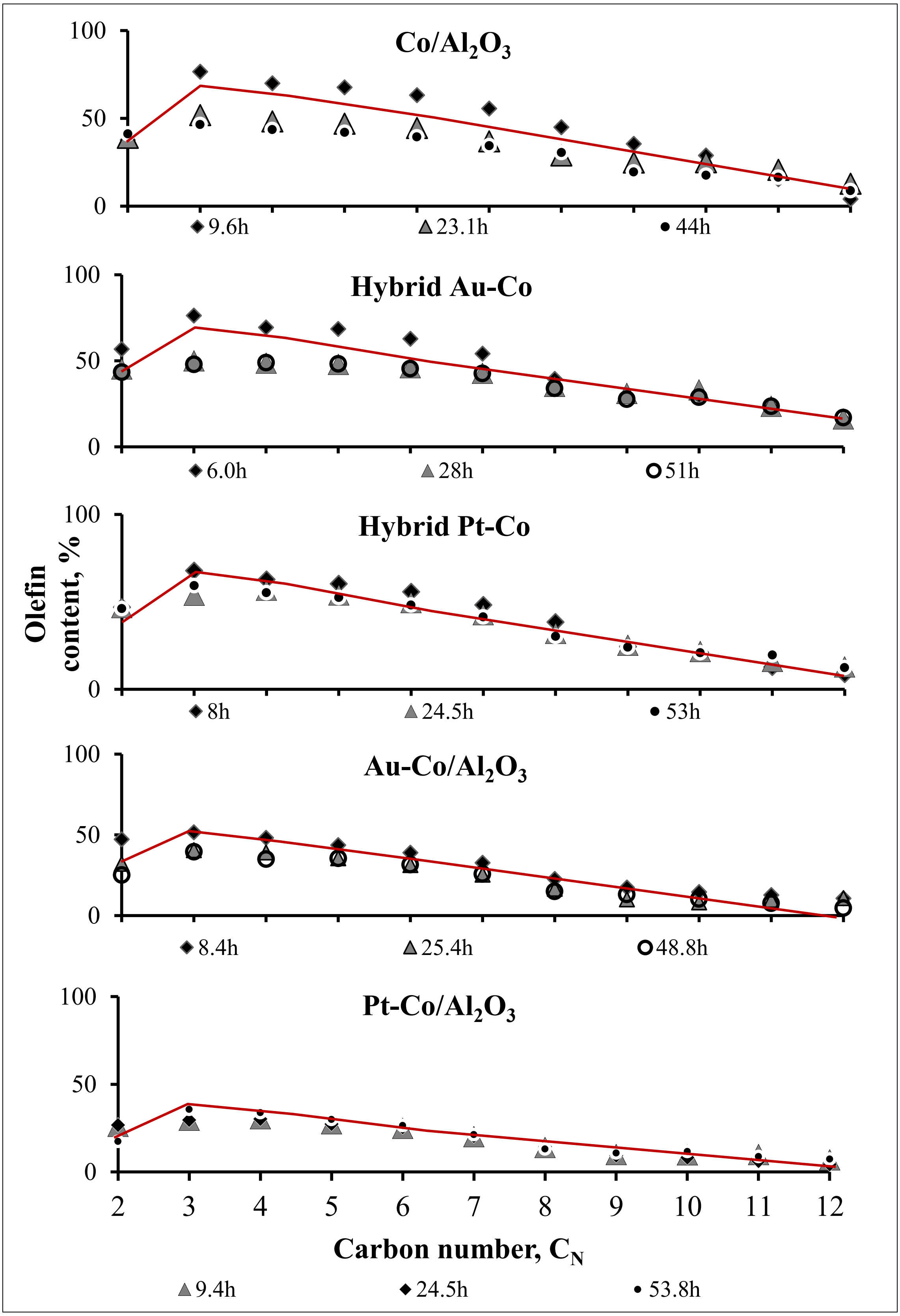

Figure 6.4-7: Olefin selectivity as a function of carbon number at various times on stream (hours). Red curve added to highlight trends.

Figure 6.4-8 includes graphs of the C_2, C_3, and C_5 olefin selectivity as a function of time. Generally, the olefin content at these three carbon numbers decreased with time, which also pointed to a common increase in H_2 availability relative to that of CO with time on stream.

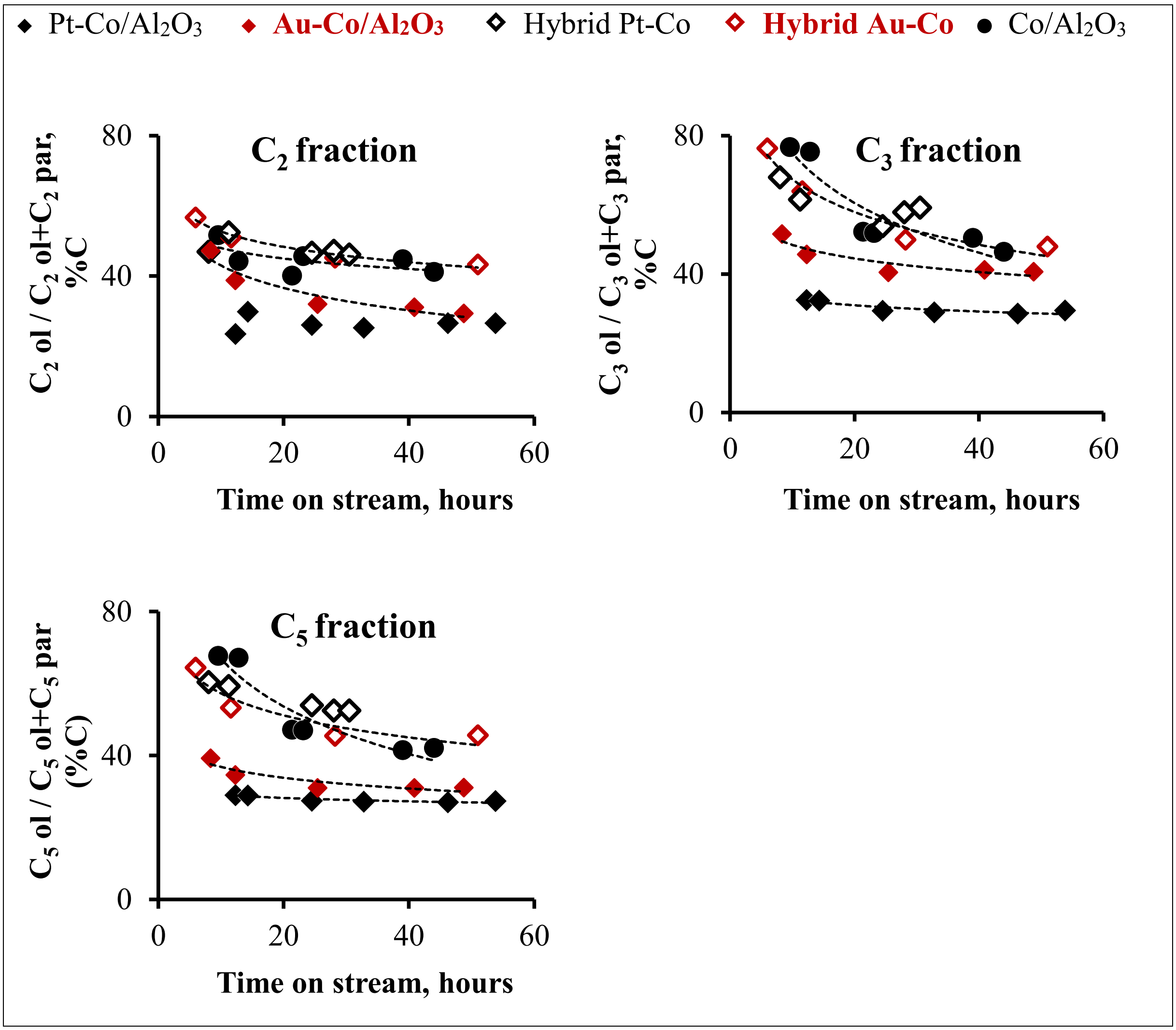

Figure 6.4-8: Olefin selectivity in C_2, C_3, and C_5 fractions as a function of time on stream.

The olefin selectivities at a CO conversion of ca. 12.3% for the various catalysts are included in Table 6.4-4. The olefin content increased as follows: ($Au-Co/Al_2O_3$ ~ $Pt-Co/Al_2O_3$) << (Co/Al_2O_3 ≈ Hybrid Au-Co ≈ Hybrid Pt-Co). Pt and Au appeared to decrease the olefin selectivity (and in turn increase the paraffinicity of the product) but only when co-supported with Co/Al_2O_3 rather than in the hybrid samples.

Table 6.4-4: Olefin selectivity, CH_4 and C_5+ selectivity and chain growth probability (α) at a CO conversion of ca. 12.3%.

Sample	**CH_4 selectivity, %C**	**C_5+ selectivity, %C**	**α**	**Olefin selectivity, %**		
				C_2	***C_3***	***C_5***
Co/Al_2O_3	21	65	0.85	45	50	42
Hybrid Au-Co	20	68	0.84	45	50	46
Hybrid Pt-Co	21	63	0.81	46	59	53
$Au-Co/Al_2O_3$	26	57	0.80	29	41	31
$Pt-Co/Al_2O_3$	30	57	0.81	27	30	27

From the literature, it was confirmed that the olefin selectivities of $Au-Co/Al_2O_3$ and $Pt-Co/Al_2O_3$, especially at high promoter/Co ratios as used in this study are typically lower than the unpromoted sample [1, 22]. At a conversion of ca. 23%, Jacobs et al. [1] observed that C_2 and C_3 olefin contents in $0.5\%Pt-25\%Co/Al_2O_3$ were 39% and 21% lower than in the corresponding unpromoted sample. Jalama et al. [22] also observed a decrease in the olefin selectivity with $5\%Au-10\%Co/Al_2O_3$ although the catalysts in the study were not compared at the same CO conversion. The decreased olefin selectivity in the presence of the promoters is in line with the general increase in H_2 availability due to a possible spillover mechanism (Table 6.4-4). Promoters increase the CH_4 selectivity, decrease the C_5+ selectivity, and decrease the probability of chain growth.

Although detrimental to C_5+ selectivity and chain growth probability, the increased H_2 availability when Co is in close proximity to Au and Pt may provide protection against deactivation by carbon deposition, which is less prevalent when the olefin content is low [62]. This suggestion ties in with the assertion that the promoters activate hydrogen, which can spillover to the Co^0 surface for a cleaning effect that prevents accumulation of unreactive deleterious carbonaceous species that accumulate of the surface of Fischer-Tropsch catalysts over time [20, 21]. Unfortunately, extended periods on stream are required to make conclusions regarding deactivation, and it was difficult to draw conclusions from the literature on deactivation specifically due to carbon and carbonaceous species because no study that benchmarks promoted against unpromoted samples was found. The most comprehensive study found on deactivation specifically due to carbon and carbonaceous species used only a Pt promoted Co/Al_2O_3 [63, 64].

6.4.6 Double-bond isomerisation

The 2-olefin/1-olefin (2-ol/1-ol) ratios in the C_4 and C_5 fractions as a function of time are shown in Figure 6.4-9. Since 1-olefins are considered the primary reaction products, this ratio allows for analysis of the effect of promoters on the extent of secondary reactions and/or internal olefin isomerisation [1]. According to Schulz & Claeys [45], during the Fischer-Tropsch synthesis, 2 olefins are almost exclusively formed from secondary reactions.

Generally, the extent of isomerisation increased with time on stream, except for Hybrid Au-Co, which decreased suddenly between 0-12 hours (i.e. unsteady state) before it proceeded to increase gradually from 12h+ in line with the other samples. These results are consistent with the increase of H_2 availability relative to CO with time on stream as deduced for CH_4, C_5+ selectivity and olefin selectivity. Double bond isomerisation occurs when 1-olefins readsorb non-terminally. From Scheme 6.4-1 depicting the secondary reactions of 1-olefins, it may be observed that hydrogen is required for the readsorption to occur.

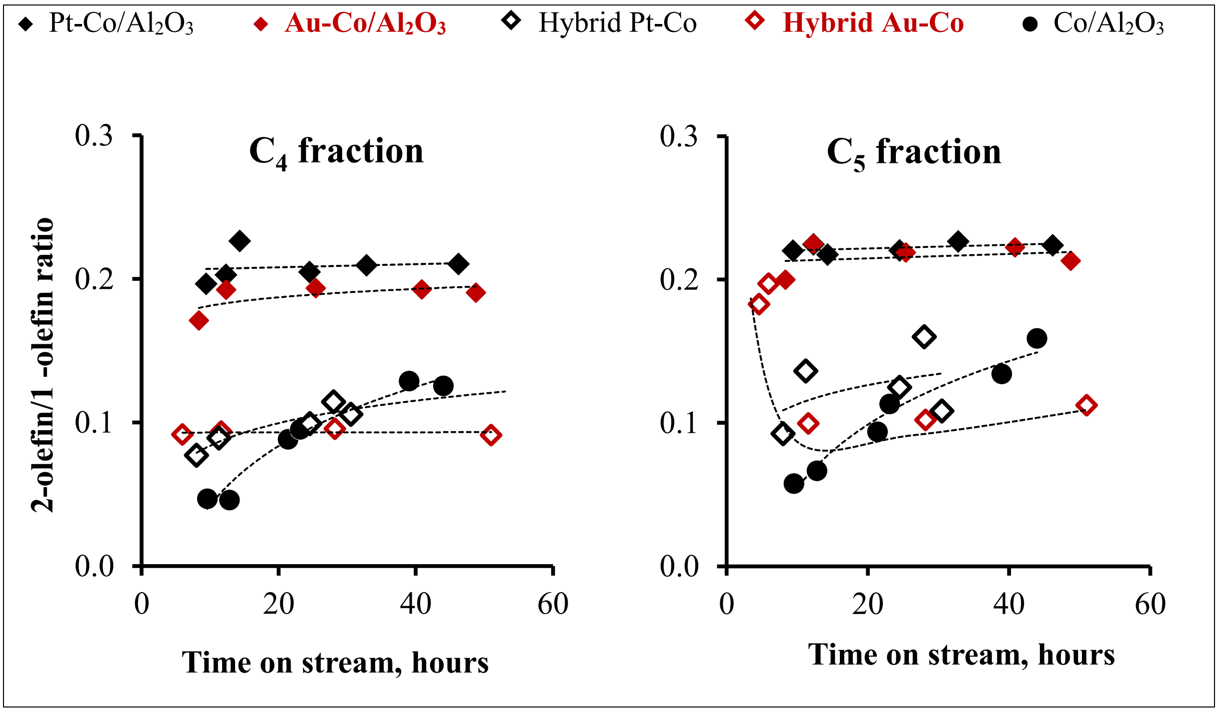

Figure 6.4-9: 2-olefin/1-olefin (2-ol/1-ol) ratios in the C_4 and C_5 fractions as a function time.

The 2-ol/1-ol ratio for the various samples at a conversion of ca. 12.3% are shown in Table 6.4-5. The level of double-bond isomerisation increased as follows: (Co/Al_2O_3 ~ Hybrid Au-Co ~ Hybrid Pt-Co) > ($Au-Co/Al_2O_3$ ~ $Pt-Co/Al_2O_3$). The level of the double-bond isomerisation was twice as high in the presence of Au and Pt promoters but only when co-supported with Co. The behaviour of the hybrid samples was similar to Co/Al_2O_3. The higher level of double bond isomerisation in the Pt-Co/Al_2O_3 and Au-Co/Al_2O_3 samples was therefore consistent with the higher extent of secondary readsorption in these samples since the availability of hydrogen was a prerequisite for double bond isomerisation.

Table 6.4-5: 2-olefin/1-olefin ratio, olefin selectivity, CH_4 and C_5+ selectivity, chain growth probability at a CO conversion of ca. 12.3%.

Sample	**CH_4 selectivity, %C**	**C_5+ selectivity, %C**	**α**	**Olefin selectivity, %**			**2ol:1ol ratio**	
				C_2	*C_3*	*C_5*	*C_4*	*C_5*
Co/Al_2O_3	21	65	0.85	45	50	42	0.13	0.13
Hybrid Au-Co	20	68	0.84	45	50	46	0.10	0.10
Hybrid Pt-Co	21	63	0.81	46	59	53	0.11	0.11
Au-Co/Al_2O_3	26	57	0.80	29	41	31	0.19	0.21
Pt-Co/Al_2O_3	30	57	0.81	27	30	27	0.21	0.22

It was also noted that double bond isomerisation could also occur on the acid sites of the support. The use of chlorinated precursors increases the catalyst surface acidity, which could in turn increase the level of double-bond isomerisation [50, 42, 65]. As discussed earlier, XPS scans showed that very low quantities of Cl^- ions persisted after both calcination and even isothermal reduction of Pt-Co/Al_2O_3 and Au-Co/Al_2O_3 (see Fig. 6.4-2). It is possible that Cl^- ions could have increased the surface acidity of Al_2O_3 and contributed somewhat to the higher 2-olefin selectivity in Pt-Co/Al_2O_3 and Au-Co/Al_2O_3. Nevertheless, XPS showed that the levels of Cl^- were very low, and it was thus expected that they made only a minor contribution.

6.4.7 Consolidation

- ***Product selectivity with time on stream***

With time on stream, the CH_4 selectivity and 2-ol/1-ol ratio increased while the C_5+ selectivity, chain growth probability, and olefin selectivity decreased. Collectively, these trends pointed to a common increase in H_2 availability relative to that of CO with time on stream and were attributed to the change in the composition of the various Co species that may arise on the surface of a working catalyst. Although not Fischer-Tropsch active, other Co phases besides Co^0 may be responsible for side reactions.

- ***Effects of hydrogen spillover from Au and Pt on product selectivity***

In the Au-Co/Al_2O_3 and Pt-Co/Al_2O_3 samples, the CH_4 selectivity and 2olefin/1olefin ratio increased while the C_5+ selectivity, chain growth probability, and olefin selectivity decreased compared to the unpromoted sample. These trends were consistent with expectations of a hydrogen spillover contributing to at least a portion of the enhanced hydrogenation activity in the presence of the promoters. Spillover from Pt in the Hybrid Pt-Co and from Au in Hybrid Au-Co most likely did not occur competitively/successfully. This was attributed to the low affinity of Au for hydrogen dissociation and possible blockage of a large portion of the Pt surface by CO, which in turn diminished the concentration of active sites available for hydrogen adsorption.

Even though spillover was advantageous to the apparent STY, the increase in hydrogen availability in the presence of Pt and Au promoters was disadvantageous because it decreased the chain growth probability, resulting in a scenario that was in fact undesirable for the Low Temperature Fischer-Tropsch process. Generally, the hydrogen availability is pronounced at noble metal promoter loadings greater than 0.1% [42] and so detrimental effects to the Fischer-Tropsch product selectivity are actually minimised by the very low Pt loadings used in the commercial catalyst [20]. The ideal reduction promoter would be one that was cheap, facilitated reduction, improved the STY, and suppressed the CH_4 selectivity in favour of C_5+ without negatively affecting the lifetime of the cobalt catalyst. Ruthenium has been shown to fit these criteria [10, 43, 59] except for its high cost and low availability. However, a recent publication by Jacobs et al. [15] suggests that silver may be the panacea in this context because a 0.256%Ag-25%Co/Al_2O_3 catalyst showed superior activity and selectivity when tested against 0.5%Pt-25%Co/Al_2O_3 at near commercial operating conditions.

In a review of promoters for cobalt-based catalysts, Morales & Weckhuysen [66] proposed that promoter effects could be split into three categories, namely: structural, electronic, and synergistic effects. "Structural promoters affect the formation and stability of the active phase of a catalyst material, electronic promoters directly affect the elementary steps involved in each turnover on the catalyst, while synergistic promotion indirectly [affects] the behaviour of the active cobalt phase, by changing the local reaction environment of the active site as a result of chemical reactions performed by the promoter element itself." Therefore, the effect of Au and Pt in improving the reducibility of cobalt was a form of structural promotion, while the effect observed during the Fischer-Tropsch reaction was most likely to have been synergistic.

6.5 References

[1] W. Ma, G. Jacobs, R. Keogh, D.B. Bukur, B.H. Davis, Appl. Catal. A: Gen. 437 (2012) 1-9.

[2] T. Matsuzaki, K. Takeuchi, T.-A Hanaoka, H. Arawaka, Y. Sugi, Appl. Catal. A: Gen. 105 (1993) 159-184.

[3] H. Sakurai, M. Haruta, Appl. Catal. A: Gen. 127 (1995) 93-105.

[4] R.A. van Santen, I.M. Ciobica, E. van Steen, M.M. Ghouri, Adv. Catal. 54 (2011) 127-187.

[5] Y. Zhang, L. Hou, J.W. Tierney, I. Wender, Energy Fuels 21 (2007) 640-645.

[6] G. Bond, C. Louis, D.T. Thompson (Eds.), Catalysis by Gold, Vol. 6, Imperial College Press, London, 2006.

[7] G. Jacobs, M.C. Ribeiro, W. Ma, Y. Ji, S. Khalid, P. T. Sumodjo, B.H. Davis, Appl. Catal. A: Gen. 361 (2009) 137-151.

[8] D. Schanke, S. Vada, E.A. Blekkan, A.M. Hilmen, A. Hoff, A. Holmen, J. Catal. 156 (1995) 85–95.

[9] S. Vada, A. Hoff, E. Ådnanes, D. Schanke, A. Holmen, Top. Catal. 2 (1995) 155-162.

[10] E. Iglesia, S.L. Soled, R.A. Fiato, G.H. Via, J. Catal. 143 (1993) 345–368.

[11] A. Kogelbauer, J.G. Jr Goodwin, R. Oukaci, J. Catal. 160 (1996) 125–133.

[12] M. de Beer, "Deposition of Au/Pt on Co/SiO2 for Fischer-Tropsch Synthesis", Masters Thesis, University of Cape Town, South Africa, 2014.

[13] G. Jacobs, J.A. Chaney, P. M. Patterson, T.K. Das, J.C. Maillot, B.H. Davis, J. Synchrotron Rad. 11 (2004) 414-422.

[14] L.Guczi, D. Bazin, I. Kovacs, L. Borko, Z. Schay, J. Lynch, P.Parent, C. Lafon, G. Stefler, Z. Koppany, I. Sajo, Top. Catal. 20 (2002) 129-139.

[15] T. Jermwongratanachai, G. Jacobs, W. Ma, W.D. Shafer, M.K. Gnanamani, P. Gao, B. Kitiyanan, B.H. Davis, J.L.S. Klettlinger, H. Y. Chia, D.C. Cronauer, A.J. Kropf, C.L. Marshall, Appl. Catal. A: Gen. 464 (2013) 165-180.

[16] T. Jermwongratanachai, G. Jacobs, W.D. Shafer, V. R. R. Pendyala, W. Ma, M. K. Gnanamani, S. Hopps, G.A. Thomas, B. Kitiyanan, S. Khalid, B. H. Davis, Catal. Today 228 (2014) 15-21.

[17] M.D. Shannon, C.M. Lok, J.L. Casci, J. Catal. 249 (2007) 41-51.

[18] K.M. Cook, H.D. Perez, C. H. Bartholomew, W.C. Hecker, Applied Catalysis A: General 482 (2014) 275–286.

[19] A. V. Ruban, H. L. Skriver, J. K. Nørskov, Phys. Rev. B 59 (1999): 15990-16000.

[20] S.K. Beaumont, S. Alayoglu, C. Specht, W.D. Michalak, V.V. Pushkarev, J. Guo, N. Kruse, G.A. Somorjai, J. Am. Chem. Soc. 136 (2014) 9898-9901.

[21] S.K. Beaumont, S. Alayoglu, C. Specht, N. Kruse, G.A. Somorjai, Nano Lett. 14 (2014) 4792-4796.

[22] K. Jalama, N.J. Coville, H. Xiong, D. Hildebrandt, D. Glasser, S. Taylor, A. Carley, J. A. Anderson, G.J. Hutchings, Appl. Catal. A: Gen. 395 (2011) 1-9.

[23] X. Cheng, Z. Shi, N. Glass, L. Zhang, J. Zhang, D. Song, Z.-S. Liu, H. Wang, J. Shen. J. Power Sources 165 (2007) 739-756.

[24] K.A. Thrush, J.M. White, Appl. Surf. Sci. 24 (1985) 108-120.

[25] W. Vogel, J. Lundquist, P. Ross, P. Stonehart, Electrochim. Acta 20 (1975) 79-93.

[26] J. J. Baschuk, X. Li, Int. J. Energy Res. 25 (2001) 695-713.

[27] G. Postole, A. Auroux, Int. J. Hydrogen Energy 36 (2011) 6817-6825.

[28] A.S. Chellappa, C.M. Fischer, W. J. Thomson, Appl. Catal. A: Gen. 227 (2002) 231-240.

[29] M.E. Levin, M. Salmeron, A.T. Bell, G.A. Somorjai, J. Catal. 106 (1987) 401-409.

[30] K.S. Hwang, M. Yang, J. Zhu, J. Grunes, G.A. Somorjai, J. Molecular Catal. A: Chem. 204 (2003) 499-507.

[31] R.M. Rioux, R. Komor, H. Song, J. D. Hoefelmeyer, M. Grass, K. Niesz, P. Yang , G.A. Somorjai, J. Catal. 254 (2008) 1-11

[32] S. Baldelli, A.S. Eppler, E. Anderson, Y.-R. Shen, G.A. Somorjai, J. Chem. Phys. 113 (2000) 5432-5438.

[33] P. Inkaew, "Electrochemistry of carbon monoxide on platinum single-crystal surfaces", PhD Thesis, Texas Tech University, USA, 2008.

[34] N. R. Avery, J. Chem. Phys. 74 (1981) 4202-4203.

[35] B. Shan, Y Zhao, J. Hyun, N. Kapur, J.B. Nicholas, K. Cho, J. Phys. Chem. C 113 (2009) 6088-6092.

[36] A.D. Allian, K. Takanabe, K.L. Fujdala, X. Hao, T.J. Truex, J. Cai, C. Buda, M. Neurock, E. Iglesia, J. Am. Chem. Soc. 133 (2011) 4498-4517.

[37] P. van Helden "Initial steps of the Fischer-Tropsch synthesis on Fe(100): The role of hydrogen", PhD Thesis, University of Cape Town, South Africa, 2008.

[38] R. Woods, J. Electroanal. Chem. Interfacial Electrochemistry 49 (1974) 217-226.

[39] J.M. Parrera, E.M. Traffano, J.C. Musso, C.L. Pieck, Stud. Surf. Sci. Catal. 17 (1983) 101-108.

[40] R. Prins, V. K. Palfi, M. Reiher, J. Phys. Chem. C 116 (2012) 14274−14283.

[41] F. Morales, E. de Smit, F.M.F. de Groot, T. Visser, B.M. Weckhuysen. J.Catal. 246 (2007) 91-99.

[42] F. Diehl, A.Y. Khodakov, Oil Gas Sci. Technol.-Rev. IFP 64 (2009) 11-24.

[43] E. Iglesia, S.C. Reyes, R.J. Madon, J. Catal. 129 (1991) 238.

[44] I. Puskas, B. L. Meyers, J. B. Hall, Catal. Today 21 (1994) 243-251.

[45] H. Schulz, M. Claeys. Appl. Catal. A: Gen. 186 (1999) 71-90.

[46] H. Schulz, E. van Steen, M. Claeys, Stud. Surf. Sci. Catal. 81 (1994) 455-460.

[47] H. Schulz, E. Steen van, M. Claeys, Top. Catal. 2 (1995) 223-234.

[48] P.J. van Berge, R.C. Everson, Stud. Surf. Sci. Catal. 107 (1997) 207-212.

[49] P. J. van Berge, J.van de Loosdrecht, J.L. Visagie, U.S. Patent 6 835 690, 2004.

[50] A.Y. Khodakov, W. Chu, P. Fongarland, Chem. Rev. 107 (2007) 1692-1744.

[51] Z. Pan, M. Parvari, D.B. Bukur, Top. Catal. 57 (2014) 470-478.

[52] N. Tsubaki, S. Sun, K. Fujimoto, J. Catal. 199 (2001) 236-246.

[53] S. Sun, K. Fujimoto, Y. Yoneyama, N. Tsubaki, Fuel 81 (2002) 1583-1591.

[54] A.Y. Khodakov, Catal. Today 144 (2009) 251-257.

[55] G.L. Bezemer, J.H. Bitter, H.P.C.E. Kuipers, H. Oosterbeek, J.E. Holewijn, X. Xu, F. Kapteijn, A.J. van Dillen, K.P. de Jong, J. Am. Chem. Soc. 128 (2006) 3956-3964.

[56] G.L. Bezemer, U. Falke, A.J. van Dillen, K.P. de Jong, Chem. Commun. (2005) 731-733.

[57] H. Karaca , O.V. Safonova, S. Chambre, P. Fongarland, P. Roussel, A. Griboval-Constant, M. Lacroix, A.Y. Khodakov, J. Catal. 277 (2011) 14–26.

[58] M. Claeys, E. van Steen, Stud. Surf. Sci. Catal 152 (2004) 601-680.

[59] E. Iglesia, S.L. Soled, R.A. Fiato, J. Catal. 137 (1992) 212-224

[60] C.G. Visconti, E. Tronconi, L. Lietti, R. Zennaro, P. Forzatti, Chem. Eng. Sci. 62 (2007) 5338-5343.

[61] E. Kuipers, C. Scheper, J. Wilson, I. Vinkenburg, H. Oosterbeek, J. Catal. 1996 (158) 288 –300.

[62] J.-H. Lee, S.-K. Lee, Ihm, Appl. Catal. 36 (1988) 199-207.

[63] D.J. Moodley, “On the Deactivation of Cobalt-based Fischer-Tropsch Synthesis Catalysts”, PhD Thesis, Eindhoven University of Technology, The Netherlands, 2008.

[64] D.J. Moodley, J. van de Loosdrecht, A.M. Saib, M.J. Overett, A.K. Datye, J.W. Niemantsverdriet, Appl. Catal. A: Gen. 354 (2009) 102-110.

[65] S. Bessell, Appl. Catal. A: Gen. 96 (1993) 253-268.

[66] F. Morales, B.M. Weckhuysen, Catalysis 19 (2006) 1-40.

Chapter 7

Concluding Remarks

This study sought to explicate the operation of Pt and Au promoters for the Co/Al_2O_3 catalyst by decoupling hydrogen spillover effects from those that require direct promoter-cobalt coordination. The study also sought to contribute to the limited body of literature on Au as a hydrogenation catalyst and promoter for cobalt. The use of Au presents an intriguing context in which to study spillover because it has been observed to segregate from Co crystallites with which Pt readily co-ordinates. Pt and Au are also divergent with regard to their reactivity since Au is considerably less active for the dissociative adsorption of H_2 and CO compared to Pt. The effect of these nuances on the reducibility, catalyst activity and selectivity, and particularly their relationship to hydrogen spillover was a fundamental interest in this study.

Hybrid catalysts as model systems for the promoted cobalt-based catalyst

Hybrid catalysts, which comprised loose mechanical mixtures of monometallic cobalt and promoter samples were successfully developed for this study. The development of the hybrid catalysts was non-trivial and provided evidence that surface continuity was a fundamental requirement for the operation of reduction promoters. The catalysing effect of Pt on the reduction of cobalt oxides was not observed during TPR of Hybrid Pt-Co when the catalysts were prepared using large Al_2O_3 support particles. On the other hand, dramatic evidence of the reduction promotion effect was obtained after the support particles were milled to <20μm, and it was suggested that finer support particles mimicked extended surfaces due to the higher inter-particle surface areas. This observation provided evidence of hydrogen transportation via surface migration because hydrogen transfer from Pt to Co by other means, such as via gas-phase transportation, would not have been dependent on the surface continuity.

Hydrogen spillover during the reduction of Pt and Au promoted Co/Al_2O_3 catalysts

The overall trend in the reducibility was determined as follows:

$$(Co/Al_2O_3 \approx \text{Hybrid Au-Co}) < \text{Hybrid Pt-Co} < Au\text{-}Co/Al_2O_3 < Pt\text{-}Co/Al_2O_3$$

The $Pt\text{-}Co/Al_2O_3$ and $Au\text{-}Co/Al_2O_3$ samples had the highest extents of reduction, and it was deduced that the direct promoter → Co spillover pathway was the most kinetically favourable for hydrogen transfer. Direct hydrogen spillover from the promoters occurred more competitively than hydrogen activation by the cobalt oxides, which allowed Au and Pt promoters to catalyse the reduction of the cobalt oxides. Compelling evidence for the improved reducibility of Hybrid Pt-Co was also obtained, which indicated that direct Pt-Co coordination was not required for the reduction promotion effect. However, in this instance, hydrogen migration necessitated spillover across multiple interfaces, which decreased the efficiency of spillover compared to the direct promoter → Co spillover pathway in $Pt\text{-}Co/Al_2O_3$.

Au improved the reducibility of $Au\text{-}Co/Al_2O_3$, but a corresponding effect was not obtained with Hybrid Au-Co. Au is less reactive towards H_2, and it was suggested that the catalysing effect was more adversely affected by Au/Co separation because of the severely diminished flux of spillover hydrogen compared to Pt.

During the **TPR analyses**, it was observed that the high temperature peak assigned to the reduction of non-stoichiometric cobalt aluminate species completely disappeared with Hybrid Pt-Co. This deduction was significant because it demonstrated that the mixed cobalt-alumina complexes often observed in the reduction profile of Co/Al_2O_3 do not actually form during calcination, but rather during the TPR analysis. This result also suggested that intimate interaction (physical and/or chemical) with the cobalt was not required to prevent the formation of mixed oxides.

No improvement in the reducibility of the hybrid samples was observed when water vapour was co-fed during TPR analyses because water enhanced the metal support interactions, which counteracted any effects of enhanced spillover. However, the presence of Pt and Au helped counter the water-induced formation of Co species that were completely irreducible in the temperature range of up to 950°C.

The multifaceted approach used to study **catalyst activation in H_2** was used to confirm that supported Co_3O_4 reduced via the formation as CoO as a stable intermediate, and that the

Al_2O_3 support had a stabilising effect on CoO, which was detrimental to the overall reducibility. $Co_3O_4 \rightarrow CoO$ reduction occurred easily even in the unpromoted sample, while the $CoO \rightarrow Co^0$ reduction kinetics were severely hindered. Using TGA in conjunction with in situ XRD analyses, this hindrance was observed as a threshold degree of reduction of ca. 25% that was quickly attained by the unpromoted Co/Al_2O_3 sample, but after which the reduction kinetics slowed significantly. The operation of Pt and Au promoters only slightly improved the already facile $Co_3O_4 \rightarrow CoO$ reduction, but greatly increased the reduction rate of $CoO \rightarrow Co^0$. Therefore, the root of the promotion effect was deduced to be the facilitation of the cobalt crystallites to exceed the threshold DOR of 25% by overcoming the detrimental stabilising effect of the support.

The synergistic effect of hydrogen spillover on the cobalt activity

$Pt\text{-}Co/Al_2O_3$ and $Au\text{-}Co/Al_2O_3$ had the highest cobalt-time yields in accordance with their high extents of reduction but exhibited a two-fold increase in the apparent STY compared to the unpromoted sample. The role of spillover hydrogen was again invoked during the Fischer-Tropsch reaction, this time providing a 'cleaning' effect on the cobalt surface via the removal of near surface or even subsurface oxygen/oxides that accumulate on the cobalt surface following C-O bond breaking. High coverage of reactive intermediates explained the higher apparent STY, and thus the intrinsic activity of the Co^0 active sites was not necessarily enhanced by co-ordination with the promoters. Despite the improved reducibility, the effects of spillover hydrogen under reactive conditions were significantly diminished in Hybrid Pt-Co. It is suggested that CO adsorption blocked off a large portion of the Pt surface, which in turn diminished the concentration of active sites available for hydrogen adsorption. The effect of the fewer adsorption sites on the spillover flux was compounded by the great Pt/Co separation in Hybrid Pt-Co compared to $Pt\text{-}Co/Al_2O_3$ in which Pt and Co were in close proximity.

The effects of hydrogen spillover on the product selectivity

Hydrogen spillover was corroborated by the enhanced selectivity towards hydrogenated products when compared at a similar level of conversion. The presence of Au and Pt promoters had a distinct effect on the apparent hydrogen (versus CO) availability under reaction conditions, which was characterised by higher CH_4 selectivity, lower C_5+ selectivity, lower olefin selectivity, lower values of the chain growth probability (α) and higher extent of double-bond isomerisation. The higher availability of hydrogen in the presence of promoters was imagined to create a hydrogen-rich microenvironment around the cobalt crystallites, which would result in the similar effects as using syngas with a higher H_2/CO ratio.

A synergism rather than an electronic effect was supported by the fact that Au-Co/Al_2O_3 exhibited an apparent STY that was comparable to that of Pt-Co/Al_2O_3 despite the literature indicating that Au and Co probably form separate phases while Pt and Co were more likely to interact. However, no corresponding synergism was observed with the hybrid samples, which was in contrast to the action of the promoters in catalysing the reduction, where strong evidence for a spillover effect was obtained. Therefore, the effect of Pt and Au promoters during the Fischer-Tropsch reaction could only be tentatively attributed to synergistic effects since electronic effects could not be ruled out.

Recommendations

It is proposed that further research of the effects of these promoters would benefit from a study in which model hybrid catalysts were used, such as well-defined separated nanoparticles of the promoter and the cobalt on a single continuous support surface. Such a study would eliminate the effect of the extensive surface migration and crossing of the interface across adjacent discontinuous support particles that were deduced to be detrimental to the migration of hydrogen in the Hybrid Pt-Co and Hybrid Au-Co samples. The use of transient experiments such as SSITKA of methanation to decouple the effects of surface coverage from the intrinsic site-time yield of Co is recommended to substantiate the deduction that the effects in the promoted samples were indeed synergistic rather than electronic. Finally, the study would benefit from Fischer-Tropsch tests with extended times on stream in order to investigate the effect of promoters on the deactivation rate by carbonaceous species because this could be used as a confirmation of the cleaning effect of spillover hydrogen.

In conclusion, the systematic investigation of the hydrogen spillover phenomenon using hybrid catalysts at commercially relevant conditions was successfully carried out in this study. Thus far, no comparable investigation of the hydrogen spillover phenomenon using these catalyst systems during both reduction and under real reactive conditions has been encountered in the published literature.

Appendices

Contents

Appendix E

E1. Hydrogen spillover during the Reduction of 0.25wt%Pt Promoted 10wt%Co/TiO_2 Catalysts

E1.1 Preparation of Titania Supported Catalysts

The preparation procedures for both the cobalt and platinum catalysts described in Section 4.1 were repeated by replacing the alumina support with titania (Degussa P25, SA = 50 m^2g^{-1}). The titania support was first modified by calcination in an oven at 700°C for 16 hours.

E1.2 Catalyst Characterisation of Prepared Samples

Figure E1.1 shows the X-ray diffractograms of the TiO_2 support before it was calcined at 700°C (prior to catalyst preparation). Included are calcined samples of the samples in the Pt-Co Titania systems. The cobalt phase was identified as Co_3O_4, no Pt peaks were observed, and the pure TiO_2 support was observed to undergo a phase change after calcination at 700°C.

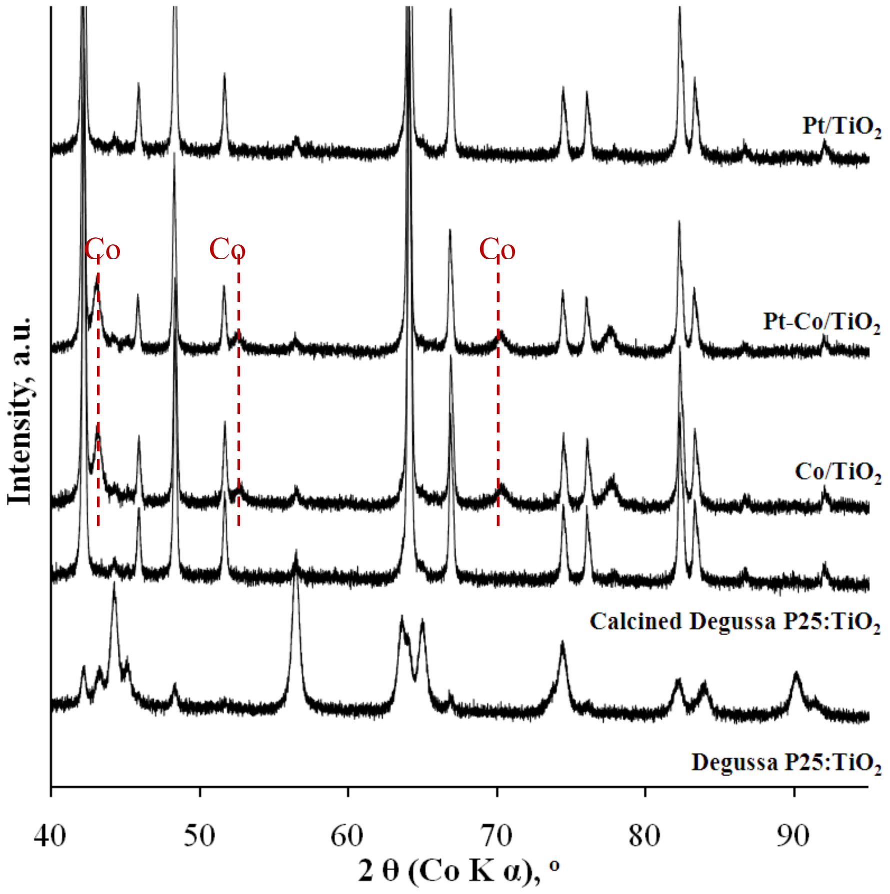

Figure E1.1: X-ray Diffractograms of the Degussa P25 TiO_2, calcined Degussa P25 TiO_2, and calcined samples in the Platinum-Cobalt-Titania System.

E1.3 Characterisation of the Reduction Behaviour of Pt Promoted Co/TiO_2 using H_2 Temperature-Programmed Reduction

The profiles obtained during the TPR analysis of the Platinum-Cobalt-Titania catalyst system supported on **calcined Degussa P25 (support particle size < 20µm)** are shown in Figure E1.2 from which the reducibility of the samples was deduced to have increased as follows: Co/TiO2 < Hybrid Pt-Co/TiO_2 < Pt-Co/TiO_2. While the unpromoted sample continued to reduce even after 560°C, the reduction of Hybrid Pt-Co was complete at 390°C, which was only 30°C after that of the co-supported Pt-Co/TiO_2. Therefore, Figure E1.2 suggested that direct Pt/Co co-ordination was not actually required to obtain a higher degree of reduction in in line with a hydrogen spillover reduction mechanism

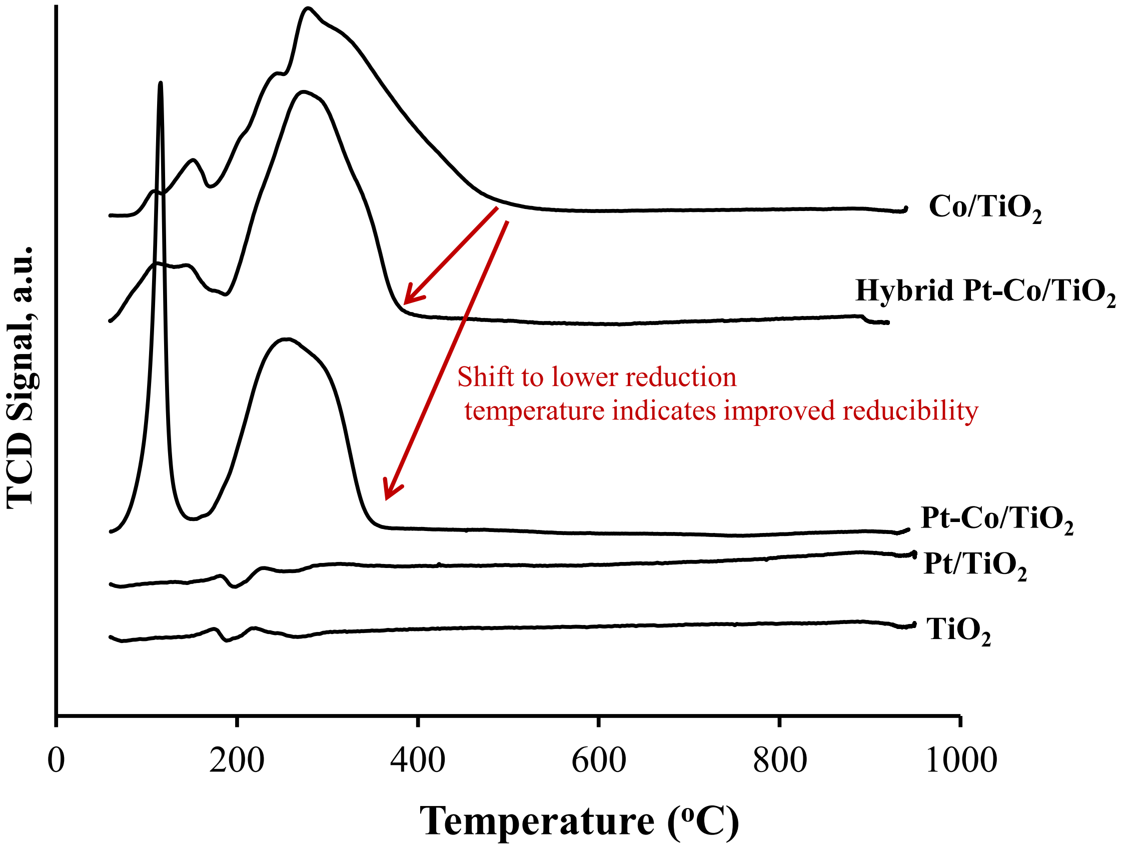

Figure E1.2: TPR profiles of 10%Co/TiO_2, Hybrid Pt-Co/TiO_2 and Pt-Co/TiO_2 prepared on Degussa P25 TiO_2.

E2. Thermogravimetric Analysis (TGA) of Al_2O_3 during the Isothermal Activation Process

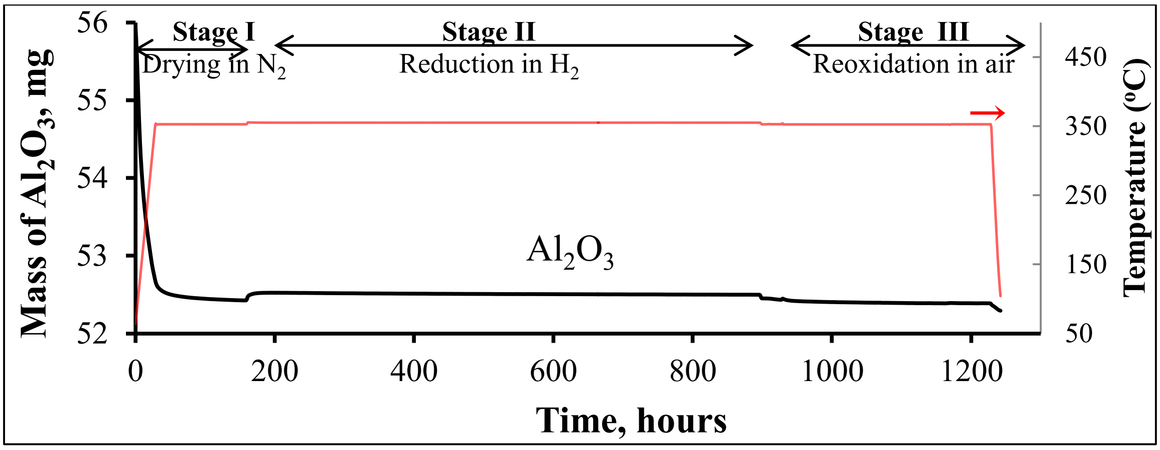

Figure E2.1: Thermogravimetric Analysis (TGA) profile of Al_2O_3 during the isothermal activation at 350°C. Sample drying carried out in pure N_2, reduction carried out in pure H_2, and re-oxidation step carried out in synthetic air. All flow rates maintained at $1000 ml \cdot min^{-1} \cdot g_{Co}^{-1}$ and temperature ramped at 10°C/min.

E3. Temperature Programmed Analysis (TPR) of Co/Al_2O_3 versus $CoAl_2O_3 + Al_2O_3$

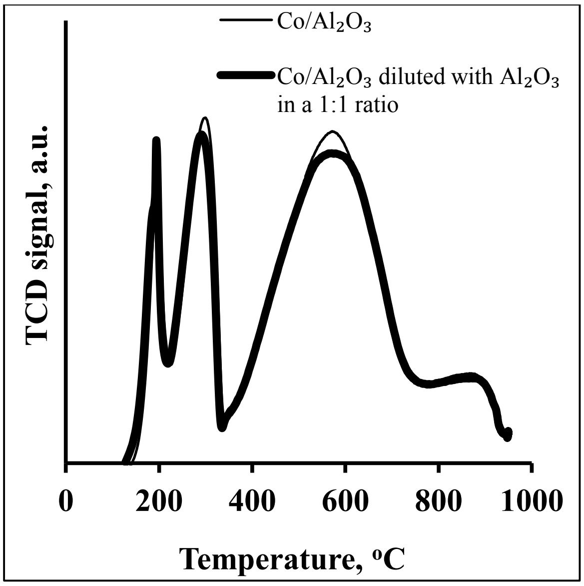

Figure E3.1: TPR profiles of Co/Al_2O_3 and a sample of Co/Al_2O_3 diluted with Al_2O_3 in a 1/1 mass ratio (milled Al_2O_3). No effect of dilution is observed in the appearance of the profile.

Appendix F

F1. Causes of 'deactivation' of catalysts under reaction conditions

- ***Reconstruction of the Co^0 surface by CO***

The rapid loss in activity attributed to surface reconstruction of Co^0 on exposure to CO in syngas has been observed with Co/Al_2O_3 immediately after start-up (TOS < 1 hour) at reaction conditions similar to those used in this study (Fischer, 2012). Surface reconstruction could have indeed contributed to the loss in activity of the samples in this catalyst system during the initial exposure to the CO in syngas. However, the effect could not be quantified as it was obscured by the slow temperature ramp at start-up, during which changes in activity could not be assessed because no GC-TCD data was collected.

- ***Reoxidation and/or sintering of cobalt crystallites***

Reoxidation (bulk or surface) followed possibly by sintering has been identified as one of the causes of initial deactivation in industrial cobalt catalysts (see Sec. 2.3). Furthermore, the presence of reduction promoters such as Pt has been observed to increase the rate at which reoxidation occurs (at high $H_2O:H_2$ ratios) (Jacobs et al., 2004). However, the low conversions used in this study (<30%), high Co metal loadings and fairly large Co crystallite sizes were expected to have kept the susceptibility to reoxidation fairly low.

- ***Deactivation by heavy wax and carbonaceous deposits***

It has been suggested that the rapid deactivation of cobalt catalysts at start-up may arise due to the generation of heavy wax and subsequent blockage of narrow catalyst pores (see Section 2.3). However, Sie & Krishna (1999) who used data from various Co & Fe catalysts to generate a Thiele-Wheeler plot found that intra-particle heat and mass transport limitations would only arise for catalyst particles greater than 500μm in contrast to the <120μm particles used in this study. Furthermore, in a review of cobalt-based catalysts, Khodakov et al. (2007) found that generally, internal mass and heat transport limitations could be ignored for particles smaller than 200μm. During preliminary studies, external mass transport limitations were eliminated after it was determined that CO conversion was not affected by the *linear velocity* but rather the GHSV.

Deactivation from the build-up of unreactive carbonaceous species was more likely to have occurred with this catalyst system. However, Moodley (2008) reported that the build-up of these unreactive species is very slow and its effect only measureable after extended periods on stream. In spite of the short times on stream in this study, XPS scans in the Carbon (C) 1s region of spent and the calcined samples of Co/Al_2O_3 and Pt-Co/Al_2O_3 were carried out and the spectra are shown in Figure F1. The spent catalysts were obtained at the end of a Fischer-Tropsch test following a passivation treatment (Sec. 4.3). No further treatment of the catalysts was carried out prior to the XPS analyses. Due to the presence of carbon species in the atmosphere, XPS analyses always reveal a corresponding peak at 284.5eV. Other forms of carbon like high molecular weight hydrocarbons and polymeric carbon identified as possible sources of deactivation result in a distortion of the C 1s peak, which can be used to shed light on their identity. Peaks at 283.6eV, 284.6 eV and 284.8 eV may be attributed to carbidic carbon, C-C bonds, and graphite respectively (Nakamura et al., 1988 and Moodley, 2008). However, Moodley (2008) cautioned that the close binding energies of the carbon species hinders their accurate identification.

Since the chemical nature of the carbon species on the catalyst samples was unknown, peak deconvolution was carried out via a ‘black-box’ approach using a combination of Gaussian curves. The C 1s peaks in the spent samples was asymmetric which indicated that that they were composed of a number of carbon species from both the atmospheric carbon and hydrocarbons formed under reaction conditions. An additional peak at a higher binding energy of approximately 289eV was present with the spent samples, which corresponded to a C-O bond. This was most likely from adsorbed CO species form during the CO_2 passivation treatment or possible oxygenates, although the latter is less likely due to the low quantities observed using GC-FID.

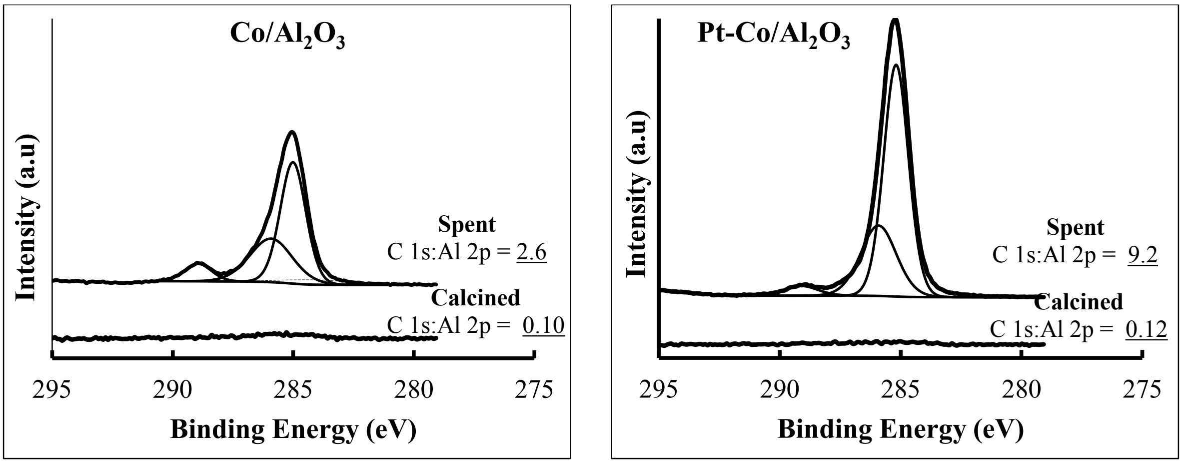

Figure F1: (Left) Carbon 1s regions of the calcined and spent Co/Al_2O_3 and (Right) Carbon 1s regions of the calcined and spent Pt-Co/Al_2O_3.

For quantification purposes, the ratio of the C 1s: Al 2p peaks was used to compare the freshly prepared to the spent samples to obtain the values included in Figure F1. For the Co/Al_2O_3 sample, this value changed from 0.1 to 2.6 versus the Pt-Co/Al_2O_3 sample where it changed from 0.11 to 9.2. These results indicated that there was a larger quantity of heavy hydrocarbons present on the Pt-Co/Al_2O_3 surface although it was not clear whether they might have contributed to the observed decline in activity because their exact chemical composition was unknown. However, it is conceivable that these carbonaceous species may have covered up a portion of the active Co^0 surface area and led to the observed decline in the activity of all catalyst samples.

○ ***Poisoning***

Poisoning of the catalysts may have arisen from either syngas or from the catalyst components during preparation. The syngas used in this study was produced by blending gas from Hydrogen 5.0 (99.999%: Air Liquide) with Carbon monoxide (99.97-100%: Afrox). The impurities reported by the suppliers included: O_2, H_2O, C_nH_m, Ar, and N_2, but none was a common poison for cobalt active sites.

Other poisons that may have been introduced downstream of the syngas cylinders included Ni- and Fe- carbonyls from the reaction of CO with the main gas lines or stainless steel body of the test-unit. These metal carbonyls form at approximately 200°C (Rep et al., 2007) and could decompose on the active cobalt surface and block active sites. Fe and Ni carbonyls are also highly active for unwanted side reactions such methanation. For this study, it was thought that the SiC layer that was present just above the catalyst bed in the fixed bed reactor would have acted as a guard bed onto which any Fe or Ni carbonyls decomposed. Nonetheless, broad XPS scans of the spent catalyst samples were analysed and found to be free of peaks corresponding to Ni (855eV) and Fe 2p (710eV). It was deemed unlikely that poisons present in syngas had contributed to the deactivation observed during the Fischer-Tropsch reaction.

REFERENCES

Fischer N., "Preparation of nano and Angstrom sized cobalt ensembles and their performance in the Fischer-Tropsch synthesis", PhD Thesis, University of Cape Town, South Africa, 2011.

Jacobs, G., Chaney, J. A., Patterson, P. M., Das, T. K., Maillot, J. C., & Davis, B. H. (2004). Fischer-Tropsch synthesis: study of the promotion of Pt on the reduction property of Co/Al_2O_3 catalysts by in situ EXAFS of Co K and Pt LIII edges and XPS. Journal of Synchrotron radiation, 11(5), 414-422.

Khodakov Andrei Y., Wei Chu, and Pascal Fongarland: 2007 'Advances in the Development of Novel Cobalt Fischer-Tropsch Catalysts for Synthesis of Long-Chain Hydrocarbons and Clean Fuels. Chemical Reviews', 107 (5), 1692-1744.

Moodley D.J., J. van de Loosdrecht, A.M. Saib, M.J. Overett, A.K. Datye, J.W. Niemantsverdriet: 2009, 'Carbon deposition as a deactivation mechanism of cobalt-based Fischer–Tropsch synthesis catalysts under realistic conditions'. Applied Catalysis A: General, 354 (1–2), 102–110.

Nakamura, J., Toyoshima, I., & Tanaka, K. I.: 1988, 'Formation of carbidic and graphite carbon from CO on polycrystalline cobalt', Surface Science, 201(1), 185-194.

Rep M., Cornelissen R.L., Clevers S. 2007, 'Methanol Catalyst Poisons: A literature Study'. CCS B.V Energie-advies. Report IND07002 06.25 Chrisgas Versie 1.1. http://lnu.se/polopoly_fs/1.37212!Methanol%20Catalyst%20Poisons%20-%20A%20Literature%20Study%20(CCS).pdf

Sie, S. T., & Krishna, R.: 1999, 'Fundamentals and selection of advanced Fischer–Tropsch reactors', Applied Catalysis A: General, 186(1), 55-70.

F2. H_2 Chemisorption on reduced samples at 125°C following the 12 hour activation reduction in pure H_2 at 350°C

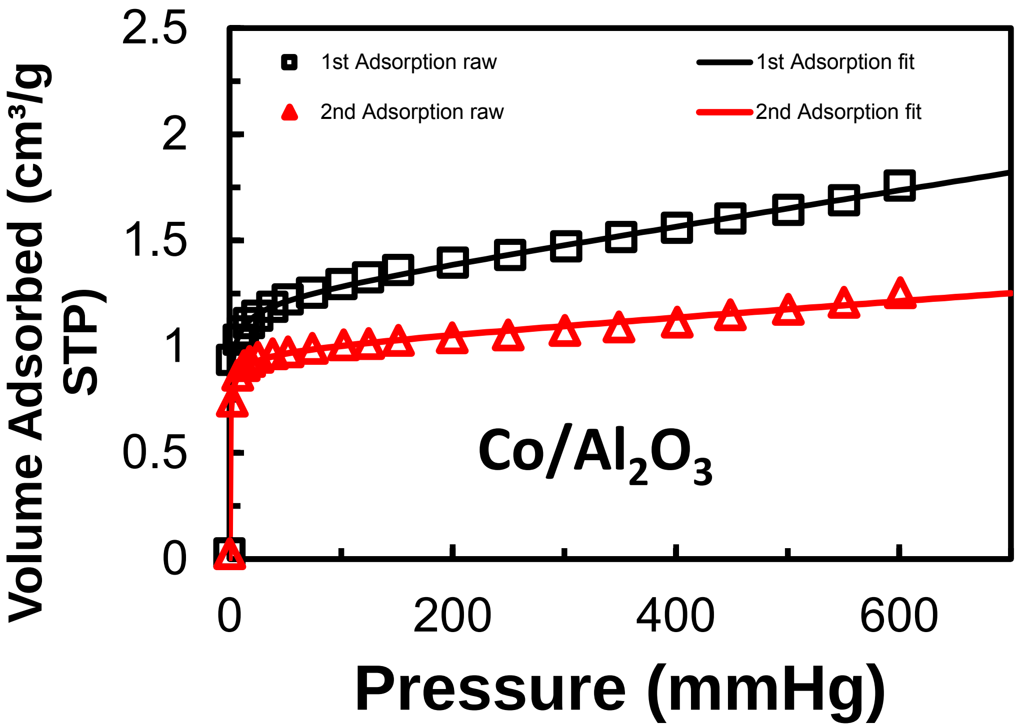

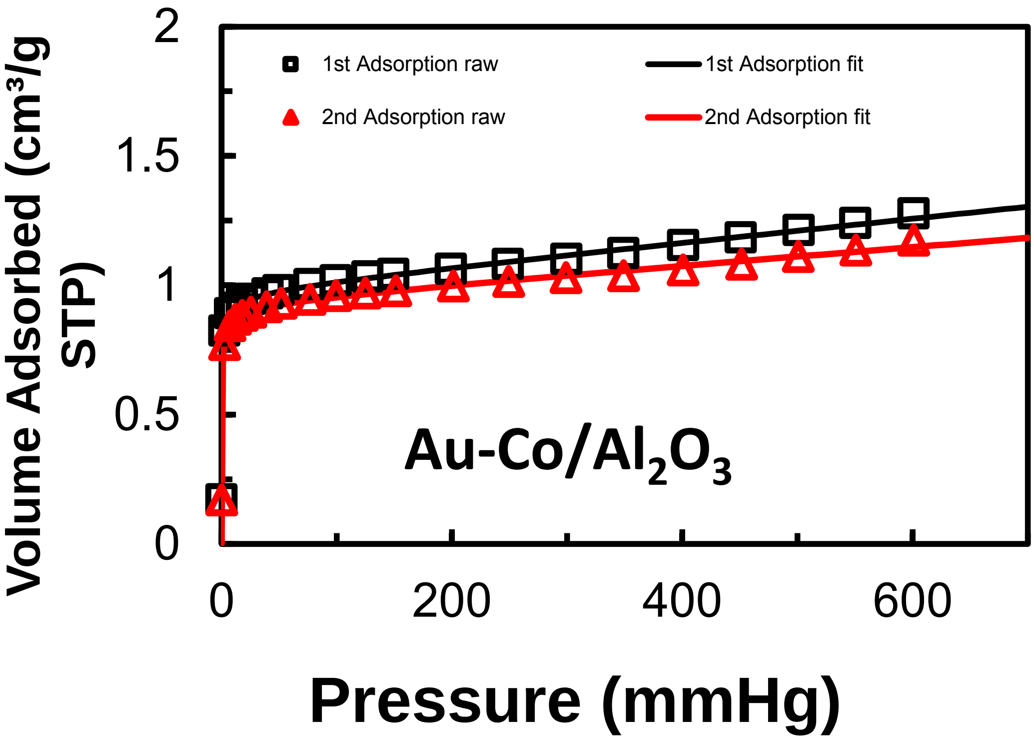

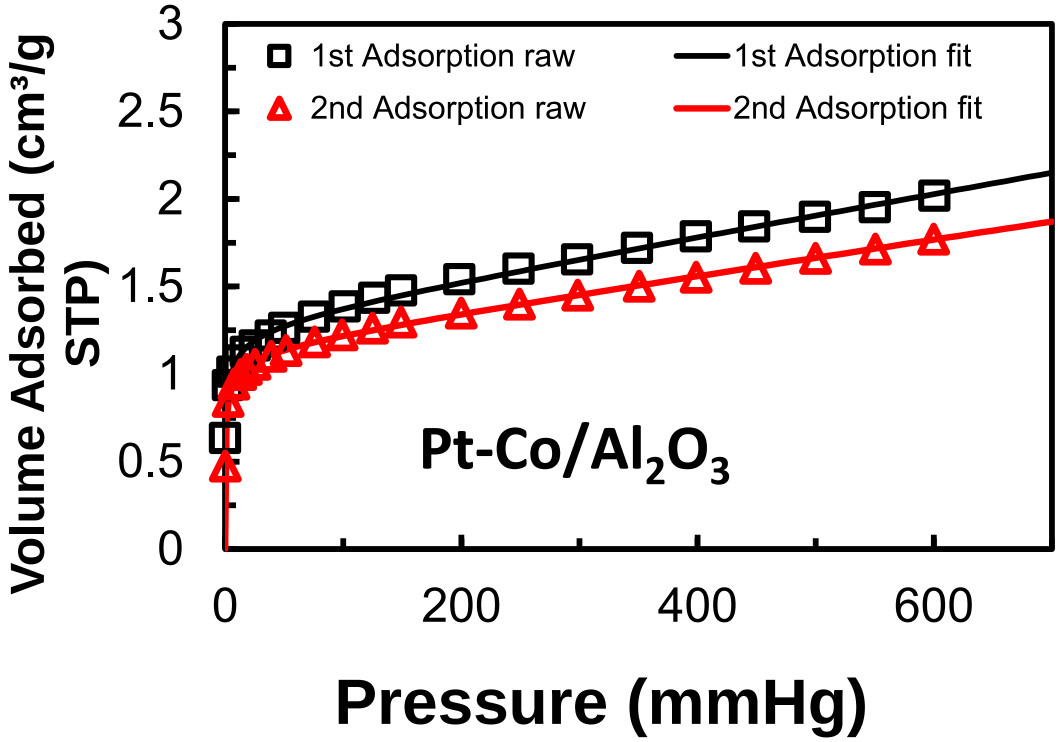
Volume Adsorbed (cm³/g STP)
3
2.5
2
1.5
1
0.5
0
0
200
400
600
Pressure (mmHg)
1st Adsorption raw
2nd Adsorption raw
1st Adsorption fit
2nd Adsorption fit
Pt-Co/Al2O3

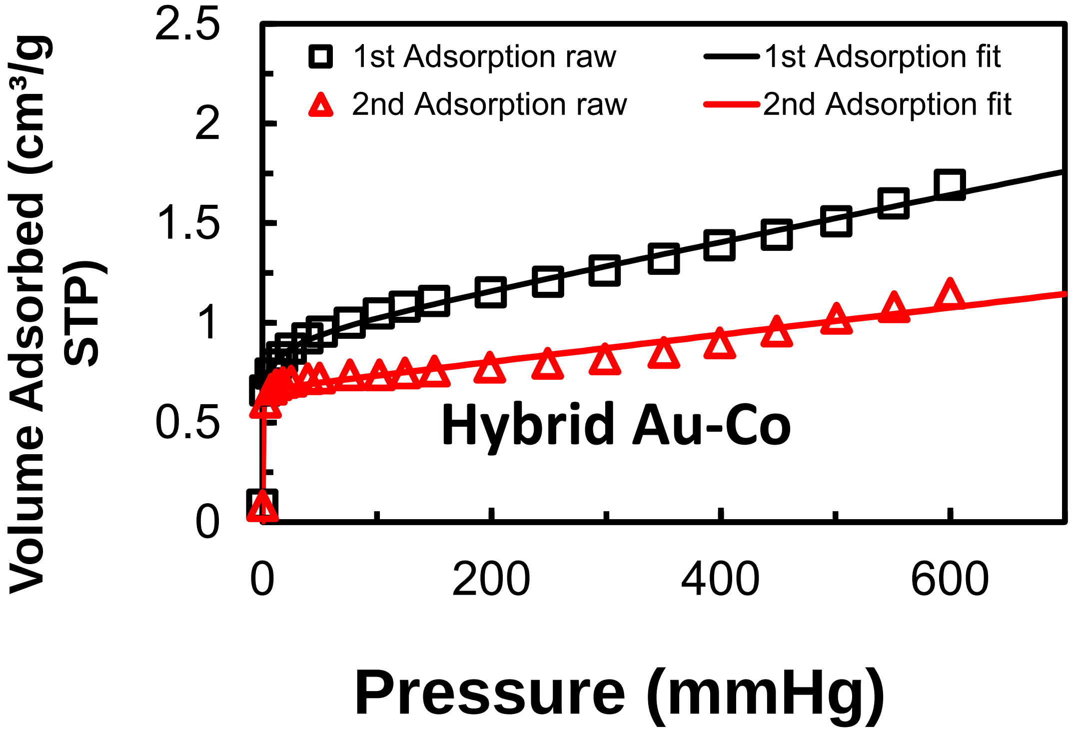
Volume Adsorbed (cm³/g STP)
2.5
2
1.5
1
0.5
0
0
200
400
600
Pressure (mmHg)
1st Adsorption raw
2nd Adsorption raw
1st Adsorption fit
2nd Adsorption fit
Hybrid Au-Co

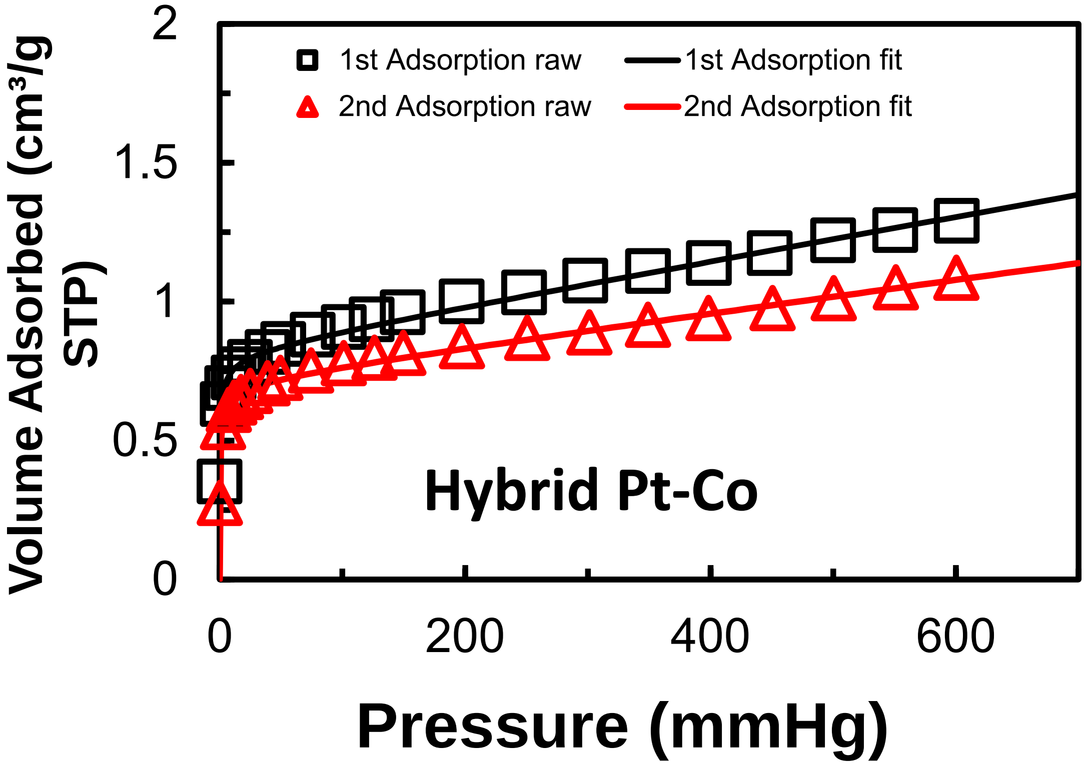
Volume Adsorbed (cm³/g STP)
Pressure (mmHg)
0
0.5
1
1.5
2
0
200
400
600
1st Adsorption raw
2nd Adsorption raw
1st Adsorption fit
2nd Adsorption fit
Hybrid Pt-Co

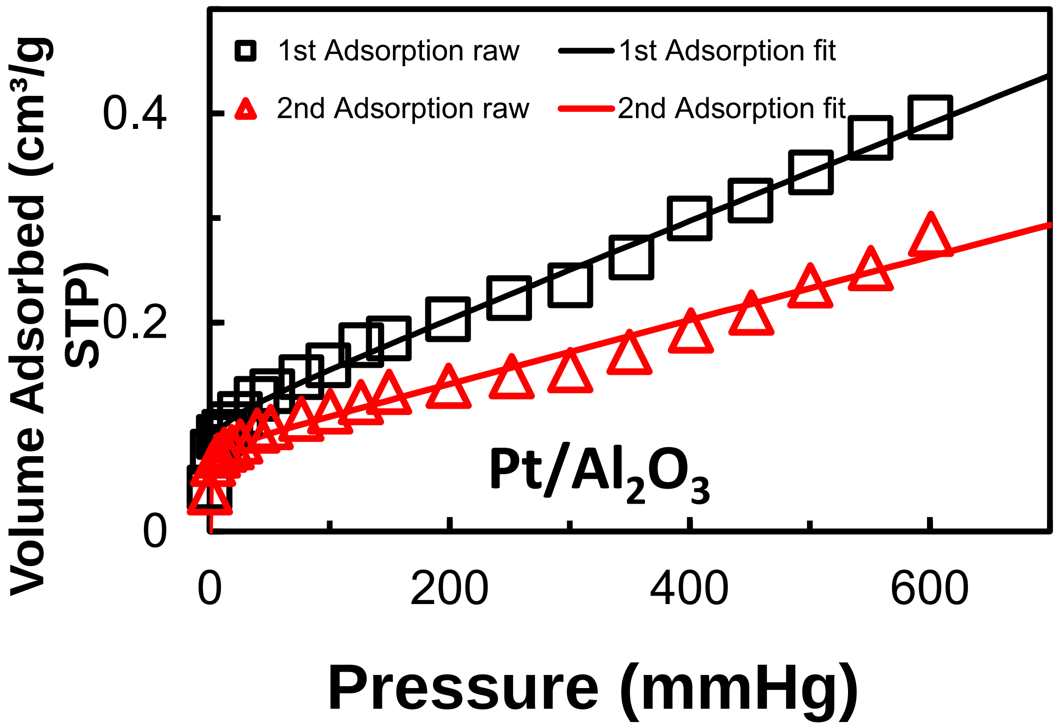
Volume Adsorbed (cm³/g STP)
Pressure (mmHg)
0
0.2
0.4
0
200
400
600
1st Adsorption raw
2nd Adsorption raw
1st Adsorption fit
2nd Adsorption fit
Pt/Al$_2$O$_3$

F3. H_2 versus CO chemisorption on reduced samples

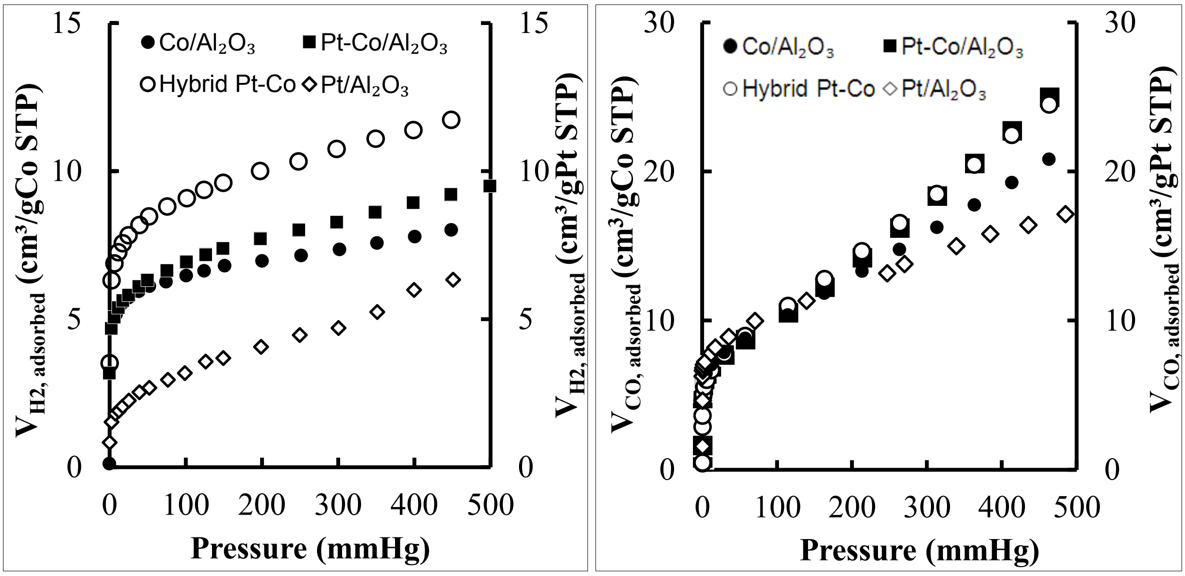

Figure F3: Platinum Cobalt System. ***Left***: H_2 chemisorption at 125°C following the 12-hour isothermal reduction in pure H_2 at 350°C. ***Right***: CO chemisorption at 35°C following the 12-hour isothermal reduction in pure H_2 at 350°C.